

N 7 6 - 1 4 0 8 8

NASA-CR-144902

CASE FILE
COPY

ANALYTICAL EVALUATION OF ILM SENSORS

By

Raymond J. Kirk
C. Edward Johnson
Douglas Doty

October 1975

Distribution of this report is provided in the interest of information exchange. Responsibility for the contents resides in the author or organization that prepared it.

Supplement to
Final Report

Prepared under Contract No. NAS1-13489 by

HONEYWELL INC.

Systems and Research Center
Minneapolis, Minnesota

for

NATIONAL AERONAUTICS AND SPACE ADMINISTRATION

ANALYTICAL EVALUATION OF ILM SENSORS

**Supplement to
Final Report**

Contract NAS1-13489

**Systems and Research Center
Honeywell Inc.**

1. Report No. NASA CR- 144902		2. Government Accession No.		3. Recipient's Catalog No.	
4. Title and Subtitle Analytical Evaluation of ILM Sensors (Supplement)				5. Report Date October 1975	
				6. Performing Organization Code	
7. Author(s) Raymond J. Kirk, C. Edward Johnson, and Douglas Doty				8. Performing Organization Report No. F-2132	
				10. Work Unit No.	
9. Performing Organization Name and Address Honeywell Inc. Systems & Research Center Minneapolis, MN. 55413				11. Contract or Grant No. NAS1-13489	
				13. Type of Report and Period Covered Final Report(Supplement)	
12. Sponsoring Agency Name and Address NASA Langley Research Center Hampton, VA 23665				14. Sponsoring Agency Code	
15. Supplementary Notes					
16. Abstract <p>Functional requirements and operating environment constraints for an Independent Landing Monitor for aircraft landings in Cat. II/III weather conditions are identified and translated into specific sensing requirements. State-of-the-art capabilities of radar, TV, FLIR, multilateration, microwave radiometry, interferometry, redundant MLS and nuclear sensing concepts are evaluated and compared to the requirements. Concepts showing the best ILM potential are identified in Volumes I and II of this series. This document identifies three specific concepts: bistatic radar, complex interferometry, and circular synthetic aperture.</p>					
17. Key Words (Suggested by Author(s)) Independent Landing Monitor Radar Landing Aids Microwave Interferometry Landing Aids Bistatic Radar Circular Synthetic Aperture				18. Distribution Statement Unclassified - Unlimited	
19. Security Classif. (of this report) Unclassified		20. Security Classif. (of this page) Unclassified		21. No. of Pages 186	
				22. Price*	
Suppl. to Vol. I&II					

Foreword

This report completes the documentation of the Analytical Evaluation of Various Potential Sensors for Use in an Independent Landing Monitor (ILM) for Conventional Take-off and Landing (CTOL) Aircraft study performed under National Aeronautics and Space Administration Contract NAS 1-3489 for Langley Research Center. Documentation of the main body of the study is contained in CR-132687, Analytical Evaluation of ILM Sensors, September 1975. This supplemental report documents the analysis and evaluation of three additional sensing concepts.

Honeywell Inc. Systems and Research Center performed this study program under the technical direction of Mr. R. J. Kirk. The program was conducted during the period of July, 1974 to October, 1975. Gratitude is extended to NASA/Langley Research Center for their technical guidance and direct assistance through our technical monitor, Mr. W. T. Bundick.

In addition to the authors, Mr. J. E. Luoma of Honeywell made valuable contributions to the study.

TABLE OF CONTENTS

	Page
SUMMARY	1
SECTION I INTRODUCTION	3
SECTION II SUMMARY OF RESULTS	7
Airborne Bistatic Thinned Array Radar	8
Concept Description	8
Summary of Capabilities	9
Complex Interferometer/DME	12
Concept Description	12
Summary of Capabilities	14
Synthetic Circular Aperture System	15
Concept Description	15
Summary of Capabilities	19
Conclusions	21
Recommendations	23
SECTION III DETAILED ANALYSES	25
Bistatic Radar Application Analysis for ILM	25
Introduction	25
Analysis	26
Radar Parameters	26
Software Scenario	26
Analytical Considerations	30
Results	41
Comments on ILM Application	49
Analysis of Space Diversity Interferometers for ILM	53
Introduction	53
Analysis	54
MADGE Parameters	54
Software Scenario	55
Analytical Considerations	62
Evaluation	64
Results	69
Comments on ILM Application	112
Analysis of a Circular Synthetic Aperture System for ILM	116
Introduction	116
Conceptual Description	116
Geometrical Considerations	118
Background	119
Accuracies and Precision	123

TABLE OF CONTENTS (Continued)

		<u>Page</u>
	Location Corridor	124
	Corridor Triangulation	124
	Geometrical Shape Orientation	127
	Conceptual Implementations	132
	ILM Applications	138
SECTION IV	REFERENCES	145
SECTION V	APPENDICES	147
	Appendix A Determination of Array Gain Characteristics ...	147
	Appendix B Computer Program for the Analysis of Specular..	159
	Multipath in an Interferometer	
	Appendix C English Translation of Reference 6.....	171

LIST OF FIGURES

<u>No.</u>	<u>Title</u>	<u>Page</u>
1	Airborne Bistatic Thinned Array Radar	10
2	Complex Interferometer/DME	13
3	Variation 1 of Circular Synthetic Aperture System	17
4	Variation 2 of Circular Synthetic Aperture System	18
5	Scan Distribution Loss	36
6	Fluctuation Loss vs Detection Probability	37
7	Standard Deviation of Clutter Component	39
8	T_i , Time Between Samples	40
9	Scan Distribution Loss and Related Losses vs Number of Scans	43
10	Summary of Power Detection Ratio (LN-66 Minimum)	44
11	Summary of Power Detection Ratio (LN-66) Maximum)	45
12	Summary of Power Detection Ratio (AVQ-30X Minimum)	46
13	Summary of Power Detection Ratio (AVQ-30X Maximum)	47
14	Bistatic Radar ILM Application	50
15	Effective Elevation Array Connections	55
16	Flat Surface	58
17	Samoa Airport	59
18	Hangar Scenario	60
19	Box Canyon or Fjord	61
20	Antenna Field Pattern Plot Vertical Array	65
21	Antenna Field Pattern Plot Horizontal Array	66
22	Location of Equipments for MADGE ILM Application	113
23	Antenna Grating Lobe Pattern Representation	117
24	Vector Diagram of U and V	121
25	Angular Uncertainty as Function of Elevation Angle	122
26	Linear Uncertainties for $\Delta \theta = \Delta \psi$ ($\psi = 45^\circ$)	126
27	Location Corridor Site Geometry for Corridor Intersection	128
28	Relationship of Range and Azimuth Precision	129
29	Geometry for Derivation of Guidance and Position from Known Ground Points	130
30	Factor to Derive Range Precision for Geometrical Shape Orientation	133
31	Azimuthal Error as Function of Geometry Point Separation	134
32	Elevation Angular Deviations as Function of Geometry Point Separation	135
A-1	3-Dimensional Axis for Antenna Field Conventions	148
A-2	Normalized Antenna Gain Profile (Azimuth)	150
A-3	Normalized Antenna Gain Profile (Elevation)	151
A-4	K' as Function of Element Spacing	156
B-1	Multipath Geometry	160
C-1	Rotating Antenna Geometry	172
C-2	Transmitting Antenna Reference Frame	174
C-3	Transparency Function	176
C-4	Vector Relationship	184
C-5	Amplitude Modulation Through Antenna Rotation	184
C-6	Apodization Effects	185

LIST OF TABLES

<u>No.</u>	<u>Title</u>	<u>Page</u>
1	Typical Radar Transmitting Parameters	27
2	Receiving Array Parameters	28
3	Analytical Weather Cases	29
4	X-Band Backscattering Cross Section	29
5	Radar Return Power Ratios (Smooth Concrete Runway) . . .	31
6	Radar Return Power Ratios (Rough Concrete Runway) . . .	32
7	Summary of Multiple Pulse Loss Factors	42
8	MADGE System Parameters	56
9	Scenario Test Situations	57
10	Modified MADGE Parameters	115
11	Geometrical Configuration Considerations	125
12	Mission Applications for Astrolabe Concept as an Independent Monitor	136
13	Equipment Summary for ILM Applications	142

SUMMARY

ANALYTICAL EVALUATION OF ILM SENSORS (Supplement)

Raymond J. Kirk
C. Ed Johnson
Douglas Doty
Honeywell Inc.

This report is a supplement to CR-132687, Analytical Evaluation of ILM Sensors, September 1975. It documents the analysis and evaluation of the capabilities of three specific sensing concepts to meet the necessary functional requirements and operational environment for an Independent Landing Monitor (ILM) which will provide the flight crew with an independent assessment of the operation of the primary landing system during Category II/III operations. The three concepts are; an airborne bistatic radar, a complex interferometer/DME combination and a rotating synthetic aperture system. Functional requirements and environmental conditions for the ILM application are documented in CR-132687.

Using our baseline functional requirements, the most critical need for the ILM appears in the landing sequence at 1000 to 2000 meters from threshold (middle marker) through rollout. Each of the concepts evaluated in this report show potential of becoming feasible ILM concepts. The complex interferometer/DME concept has been developed as a Cat. II landing aide and with increases to the ground equipment complex should also be capable of some Cat. III ILM functions. The other two concepts are in early development stages at this time.

SECTION I

INTRODUCTION

The technology required for automatic landing of conventional fixed-wing aircraft using the VHF Instrument Landing System (ILS) and highly redundant flight control systems in Category III Conditions has been demonstrated many times. However, the introduction of this capability into general usage has been limited. One reason for the limited use of autoland systems has been the lack of a monitoring system operating independently from the primary guidance system. Independent operation would allow the pilot to assess the performance of the autoland system and the aircraft situation relative to the runway under conditions of low visibility and/or allow the pilot to manually land the aircraft in the event of failures in a fail-passive autoland system. This independent monitoring function should serve to build up the pilot's confidence in low visibility landings and permit the reduction of the flight control system from a fail-operational automatic unit to a fail-passive system with manual backup capability. The Independent Landing Monitor (ILM) is here defined to include the sensors, signal processors, and displays needed to provide the pilot with information to assess his situation and either make a missed approach or proceed in with the manual landing.

The primary objective of the ILM study was to evaluate analytically the capabilities of various generic sensor concepts to meet the functional requirements for an Independent Landing Monitor.

To evaluate the capabilities of the various sensing concepts over a range of ILM requirements, the functions required of the ILM were defined for a basic configuration and for three configurations of increasing complexity:

- a. Basic - The ILM shall provide information to allow determination of aircraft position (elevation, azimuth, range) with respect to the runway down to a wheel altitude of 12 feet. The accuracy of the position information should be adequate to monitor the approach with a Category III Microwave Landing System (MLS) as the primary guidance system.

- b. Case I - The requirements for the basic system configuration are extended to touchdown and through rollout to provide guidance to the aircraft through the full landing sequence. Heading with respect to end of runway should be provided with an accuracy of 0.1° .
- c. Case II - Add the detection of obstacles, such as aircraft and ground vehicles on or near the runway to the Basic and Case I configuration functions. Detection of obstacles should be at a range sufficient to permit execution of a missed approach.
- d. Case III - Meet the Basic, Case I, Case II requirements through the use of a real-world perspective image of the runway and its surroundings. The image should be of sufficient quality to provide position, rate of change of position, and attitude information to the pilot in a form analogous to the visual cues available during VFR approach and landing.

This report documents an add-on analysis effort to the ILM study which was initiated after compilation of the final report was completed. The add-on effort consisted of analysis and evaluation of three specific sensing concepts for ILM not included in the primary study and summation of the results.

The final report for the primary study is titled "Analytical Evaluation of ILM Sensors", CR-132687, Sept. 1975. It contains a description of the study technical approach, summary of results, detail description of ILM functional requirements and operational environment, analysis and evaluation on twenty potential ILM sensing concepts and further refinement on six concepts considered feasible.

This add-on effort utilized the technical approach, functional requirements and operational environment and some of the computer programs and data already documented in CR-132687. This is not duplicated here and readers should refer to that report for this information. References to specific sections of that report are contained where applicable in this document.

This report contains two major sections for ease of reading. A summary of results section provides a brief description of the three ILM sensing concepts reviewed, a summary of their capabilities and constraints and conclusions and recommendations. The second section contains the documentation for the detail analysis and results for each of the three concepts.

SECTION II SUMMARY OF RESULTS

Landing safety and reliability, independent of terminal area weather conditions, is a goal towards which the air transport industry is striving. The benefits to passengers, the airlines and the military are clear. To this end, fail-operational landing systems are minimum requirements for achieving all-weather landing capabilities. The systems, utilizing an accurate and reliable microwave landing system as the primary landing aid, form the basis for the FAA's and ICAO's plans to make Category III operations available at a limited number of high density airports in the 1980's.

To date, fail-operational systems for Category III conditions have required highly-redundant fail-operational flight control systems and high reliability landing aids in fully automatic configurations. An alternative approach to the fully automatic configurations is to utilize a fail-passive flight control system and primary landing aid with an independent back-up landing aid and manual flight control. The fail-passive primary landing system permits the use of dual redundancy rather than the more costly triple or quad redundancy of an automatic fail-operational system. The back-up independent landing monitor (ILM) with manual takeover capability upgrades the system from fail-passive to fail-operational.

The intent of the Analytical Evaluation of ILM Sensors study was to survey potential sensors and sensing concepts to determine their utility as the independent landing aid and to identify the limits or conditions under which they would fulfill one or more of the required functions. Development of a baseline set of functional requirements and environmental operating conditions for an ILM and

evaluation of the feasibility of twenty different sensing concepts to meet these requirements was undertaken in the study and is documented in Reference 1.

The intent of this add-on effort was to analyze and evaluate against the same baseline criteria three additional specific sensing concepts. Each of these concepts appeared on preliminary examination to be potentially feasible ILM candidates, but were identified after completion of the technical effort on the primary study. Evaluation of the three concepts to meet the criteria of Reference 1 is reported here.

The three concepts are an airborne bistatic thinned array radar under development by Hughes Aircraft, Inc. with the tradename "BISTAR", a complex interferometer/DME system in late development as a Category II landing aide by M.E.L., Ltd. with the tradename "MADGE", and a rotating antenna synthetic circular aperture device under development at ONERA with the tradename "Astrolabe".

AIRBORNE BISTATIC THINNED ARRAY RADAR

Concept Description

This airborne ILM concept uses bistatic radar techniques to achieve improvements in resolution. Airborne radars commonly use the same antenna for both transmit and receive. In this case, the transmit antenna is mounted in the nose of the aircraft and scans through the required coverage with a relatively broad beam antenna pattern. A thinned array of receiving elements spread across the wing generates a multi-lobe receiving pattern with each lobe having high azimuth resolution. The superposition of the scanned transmit antenna pattern and the receiving pattern results in a high resolution azimuth scan. Because a separate

transmit antenna is used, the wing elements can be separated by approximately one-half of the transmit antenna diameter rather than a fraction of the wavelength. This results in on the order of 20-30 receiving elements on the wing rather than hundreds of transmit-receive elements as would be required for an equivalent monostatic antenna array.

A sketch of the concept is shown in Figure 1. The system is an air-derived concept and could be a completely airborne system although passive ground augmentation to enhance the runway outline may be desirable. The frequency of operation could be X, Ku, or Ka band. A key feature of this concept is the ability to serve other functions, such as weather detection, in addition to the ILM function. Thus, frequency selection may depend also on these other modes.

The simplest display for use with the bistatic thinned array radar concept is a sector PPI image using range-azimuth format. Techniques to generate a perspective image with this concept should be explored.

Summary of Capabilities

The analysis showed this application has potential for providing high resolution direct imaging of the runway during approach in severe rain, snow, or zero visibility fog. Direct imaging of the runway is limited to within 5Km even for high contrast runway detection without enhancement. Specific results are itemized below:

1. Lowest backscattering cross-sections provide inadequate background to runway backscattering cross-section ratio contrast, ΔB , and background to precipitation clutter, B_g/C , to detect the runway unless circular polarization is used for clutter reduction and degraded range resolution is used to decrease the noise bandwidth. With these assumptions, approximate detection ranges for 20 db contrast (runway to background backscattering cross-section ratio) are:

Weather	Detection Range, 23m runway
16mm/hr Rain	1.9 km
9mm/hr Snow	2.0 km
Fog, zero visibility	1.9 km

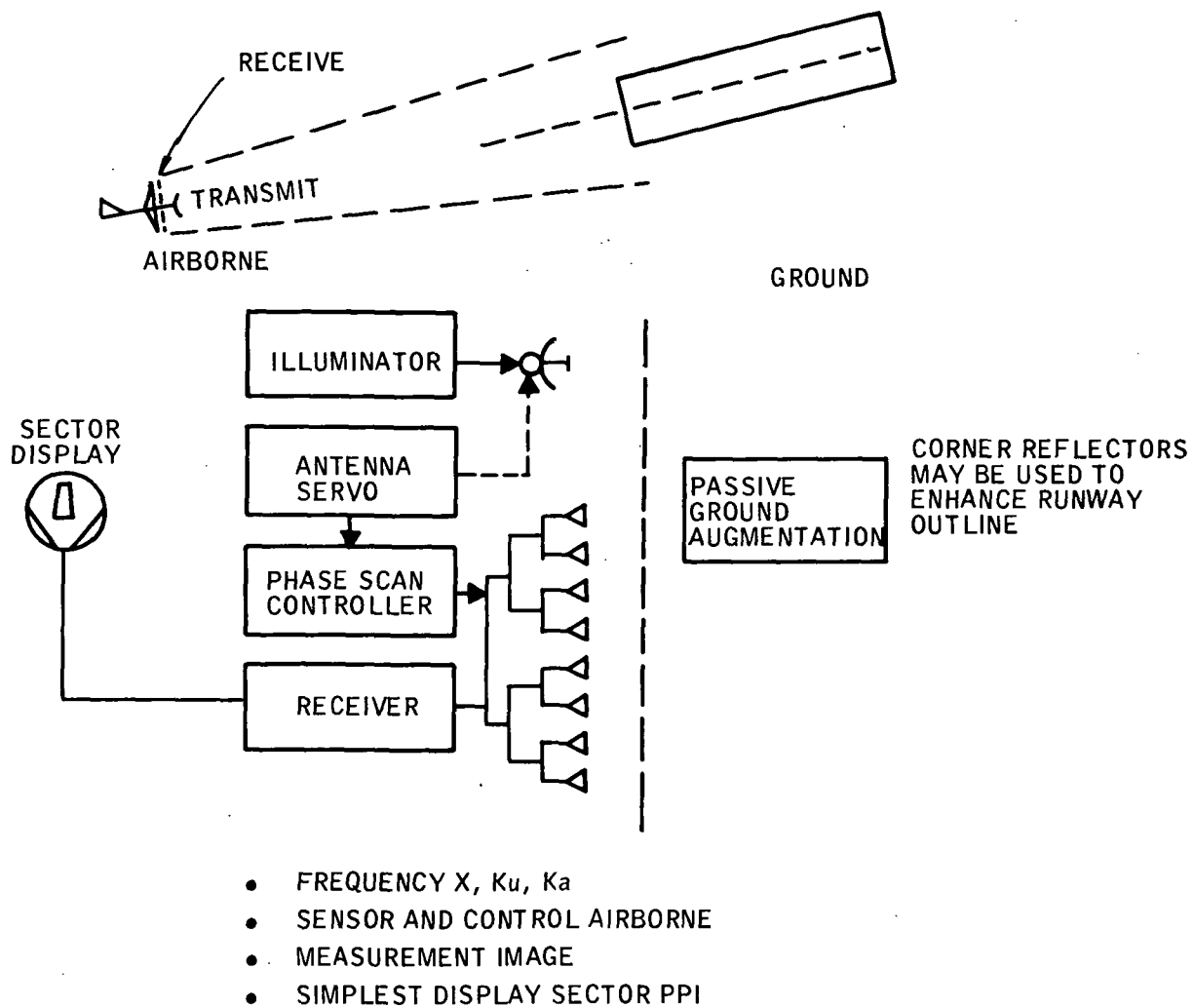


Figure 1. Airborne Bistatic Thinned Array Radar

2. Runway images derived by passive reflector enhancement or imaging of cultural objects such as runway lights or other objects with approximately one square meter scattering cross-sections can be detected with the extended detection ranges shown:

Weather	Detection Range
16mm/hr Rain	2.6 km
9mm/hr Snow	3.0 km
Fog, zero visibility	2.8 km

3. Higher backscattering cross-sections allow further utilization of the high resolution capabilities of the Marconi illuminator with the array receiving system. For this case, a runway-to-background backscattering cross-section ratio contrast of 35 dB was analyzed. The approximate detection ranges are:

Weather	Detection Range, 23m runway
16mm/hr Rain	4.1 km
9mm/hr Snow	5.4 km
Fog, zero visibility	4.4 km

4. The limitations above for the 23 meter runway are due to the runway to background contrast. This contrast of 35 dB is approximately the maximum allowable based on the 33 dB sidelobes measured for the array (Reference 2). Using this as the limiting case, assuming 6 dB B_g/C minimum required for detection, the maximum precipitation rates may be derived for the detection of a 23 meter runway at 1 nm and 2 nm. These maximum rates are derived from the approximate expression Clutter Power, $C \propto R^{1.6}$, where R is the precipitation fall rate in mm/hr. (Reference 1)

Maximum Precipitation Rates for 23 meter Runway Detection

1NM	Rain	67 mm/hr
	Snow	59 mm/hr
2NM	Rain	20 mm/hr
	Snow	17 mm/hr Equivalent Water

5. For comparison, the Ka band perspective imaging radars examined in Reference 1 show detection ranges of 1 to 1.5 km and 1 to 2 km for the conditions of itemized results 1 and 2, respectively. Thus, nearly a factor of 2 improvement in range is shown. However, it is still well below desired ranges.

COMPLEX INTERFEROMETER/DME

Concept Description

This concept uses interferometric techniques to generate elevation/azimuth angle data and DME techniques for range measurements in the landing sequence. A sketch and block diagram of the concept is shown in Figure 2. The aircraft equipment consists of an interrogator and a receiver-decoder. Interrogations are initiated by the aircraft system to the ground transponder. The interrogation message is received by the transponder and the elevation and azimuth angle antenna units on the ground. The elevation and azimuth units utilize complex space diversity interferometer arrays to accurately measure angles to the interrogating aircraft in the presence of multi-path signals. The angle data is transferred to the transponder and transmitted back to the aircraft as part of the response. Range is measured on the aircraft by measuring the time from interrogation to response.

Frequency of operation used is C-band. Measurements consist of range-to-touchdown and azimuth/elevation angles. The simplest display will be steering commands and range-to-go to touchdown.

The particular application analyzed here is the MADGE system, developed by the MEL Equipment Co. Ltd, Sussex, England. It utilizes a space diversity interferometer to obtain elevation data, a standard interferometer with a special array ambiguity resolution technique to obtain azimuth, and a pulse DME to obtain range. The previous analysis of Independent Landing Monitor techniques employing interferometers (Reference 1) concluded that they could not be used, due to the extreme phase distortions caused by multipath reflections. These distortions prevented correct ambiguity resolution of a long baseline interferometer with a short baseline inter-

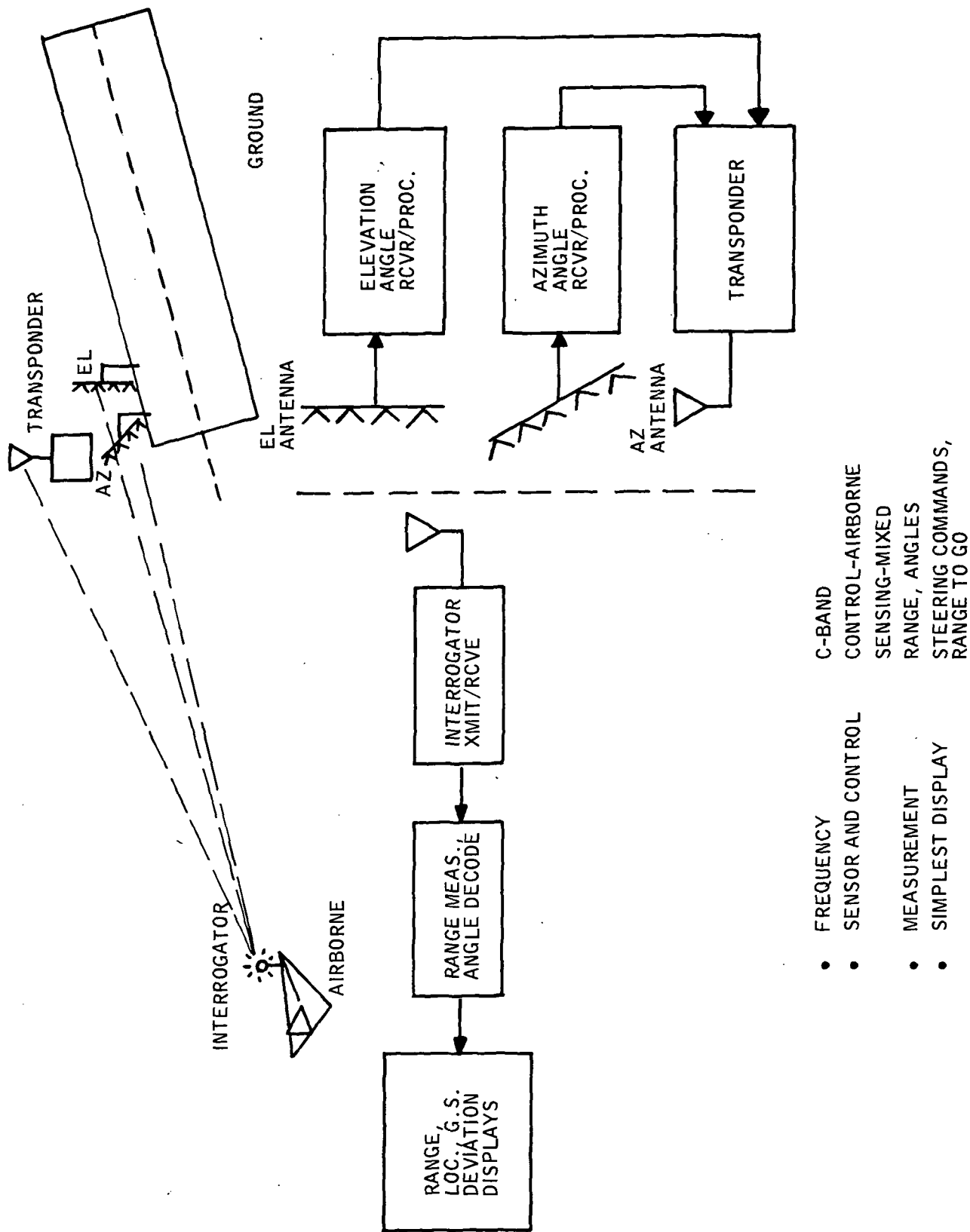


Figure 2. Complex Interferometer/DME

ferometer, since the short baseline unit did not have enough accuracy to determine the correct grating lobe of the long baseline unit.

By using an array of interferometer pairs, and recursively resolving ambiguities from a shorter baseline to a slightly longer baseline, correct ambiguity resolution can be obtained for arrays of any length. Further reduction in multipath caused errors can then be obtained by averaging the results of interferometers at different positions. The MADGE system is currently configured as a Category II landing aid and, thus, is not designed to meet all of the ILM requirements. This analysis examines the feasibility of extending the design concept to meet Category III requirements.

Summary of Capabilities

Space diversity has been shown to be an effective technique for the reduction of specular multipath errors in an interferometer. The MADGE elevation array shows errors of less than 10 mrad even in severe multipath conditions when operated as a focused array. The current MADGE system is apparently operated in an unfocused manner, but range estimates to allow focusing could be made available with minor change in system operation. The 10 mrad error exceeds the allowable 1.2 mrad error for an MLS elevation unit, but is close enough that proper site selection should yield an acceptable system.

Two fixes were attempted.

- o Stuffing the array with additional antennas, keeping the spacing between antennas of a pair constant.
- o Extending the array by 4 more antennas, maintaining the array spacing constant and thereby increasing the spacing between antennas of a pair by a ratio of 3/2.

Stuffing the array did not yield any improvement in performance. Extending the array provided a slight increase in accuracy, bounding the error below 7.5 mrad rather than 10 mrad. Thus, neither of these particular fixes are sufficient to provide Category III performance in a severe multipath environment.

The MADGE azimuth unit does not utilize space diversity for multipath protection. In the cases examined, which were severe multipath situations, the azimuth unit had errors large enough to cause ambiguity resolution errors. The azimuth unit does have some multipath protection, and would probably be adequate in a less severe environment. It would be better to use a space diversity array similar to the elevation unit to insure operation in any multipath environment.

In the box canyon environment, an elevation type array operated as an azimuth unit showed better performance, holding peak errors to 13 mrad rather than the 18 mrad of the normal MADGE azimuth unit. More importantly, the space diversity array is capable of providing correct ambiguity resolution in the presence of multipath distortions of this magnitude, whereas the standard MADGE azimuth array is not.

In all cases using a space diversity array, large multipath errors tend to be highly oscillatory with a mean error much smaller than the peaks of the oscillation. Since no filtering is employed in the computation of these multipath errors, it is likely that the errors could be reduced to a much more acceptable value if filtering were employed. For example, in the case of the extended elevation array at a 1° glide slope in the Samoan airport environment, the peak errors are about ± 7.5 mrad, whereas the mean error is .02 mrad. This is certainly an acceptable multipath error component.

The MADGE equipment as it now exists is not capable of Category III operation. Severe multipath environments can cause errors to exceed the limits for CAT III equipment, focusing errors cause excessive geometric biases, and the system is not configured to provide roll out guidance. The following changes should be made to MADGE to provide a workable Category III equipment:

- o The interferometer arrays should be focused.
- o The azimuth array should be replaced with a space diversity array.

SYNTHETIC CIRCULAR APERTURE SYSTEM

Concept Description

An independent landing monitor concept called ASTROLABE is being developed by ONERA

in France. In this system the two angular coordinates, elevation and azimuth angles, are obtained by 2-dimensional phase modulation of a microwave carrier, induced by the continuously rotating motion of a pair of antennas.

A conventional interferometer array consisting of two elements separated by several wavelengths has high angular resolution within an ambiguous lobe structure created by the grating lobe pattern. Resolving the ambiguity consists of determining which of the many possible lobes contains the real target. Rotating the array provides ambiguity resolving capability since the grating lobes are not evenly spaced in angle. The cross-correlation of the received signal parameters with the theoretical signal parameters based on the rotating geometrical grating lobe structure provides a high-precision angle determining capability. The scheme is conceptually simple but difficult to apply because of the complexity of the 2-dimension cross-correlation processing requirement which is characteristic of synthetic aperture systems. Optical processing techniques are used in many synthetic aperture systems because of the 2-dimensional transform characteristics of lens systems. Although digital techniques are applicable, system costs are much higher because of the fast sampling speed, high computation rates, and large mass storage requirements of a near real-time system. ONERA personnel have patented a rather simple and comparatively economical optical system that provides a high precision signal processing capability that is applicable for real-time display of angle proportional information for either ground or aircraft installation. Current displays used in the development tests give a visual display of the location of the correlation point whose position is representative of the angular coordinates referenced to the rotating array.

Several different system concepts using the Astrolabe principle are possible and are discussed in Section III. Two concepts were considered representative and examined in more detail in the analysis: variation 1, an Astrolabe rotating receiving array on the aircraft with several beacon transmitters highlighting the runway extremities to provide a real-time perspective display of the runway extent and variation 2, an Astrolabe rotating receiving array on the ground with an aircraft beacon and a two-way DME/information data link providing near real-time cockpit indications of aircraft approach corridor azimuth and elevation angular coordinates and range-to-go. The two variations are shown in Figures 3 and 4.

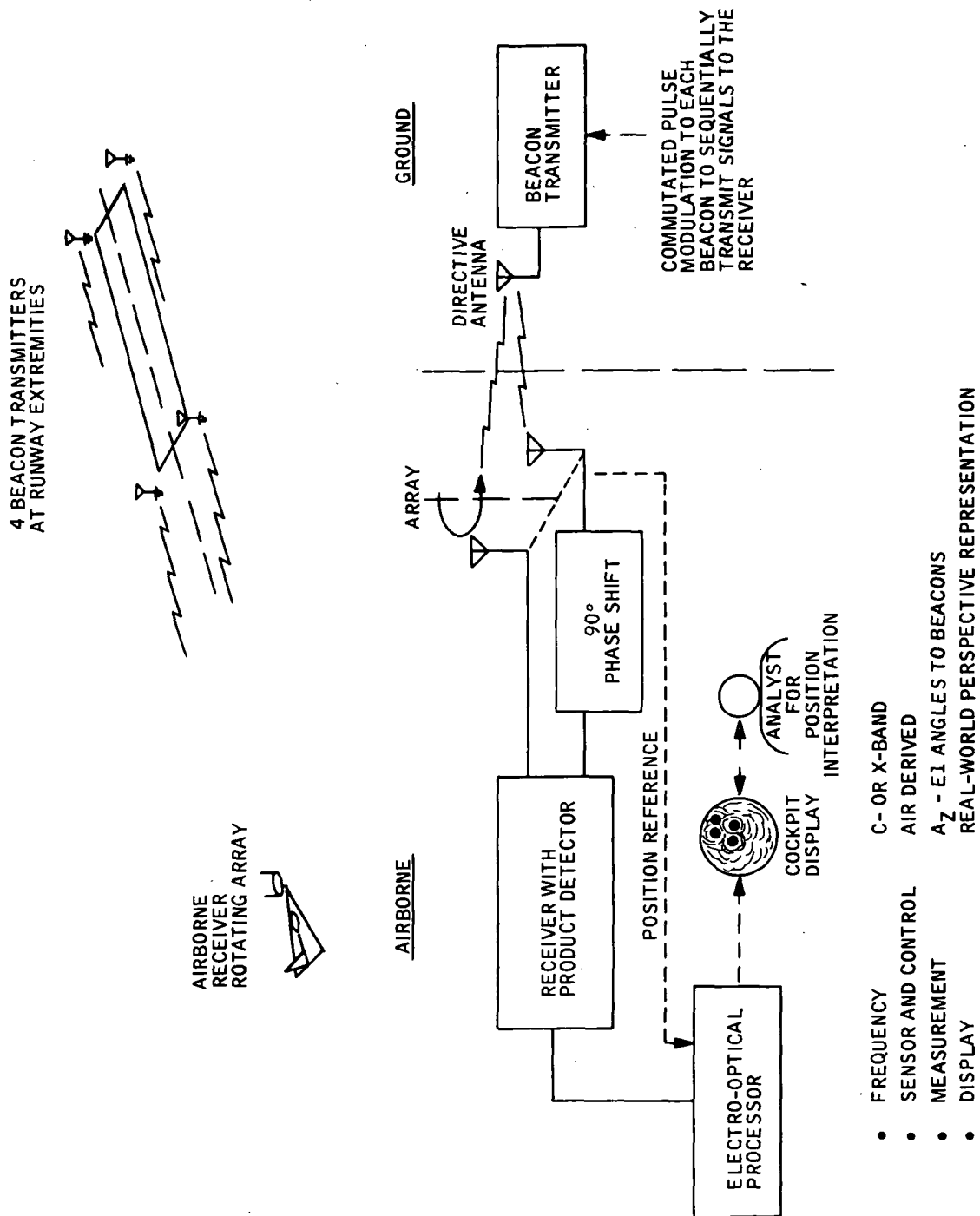
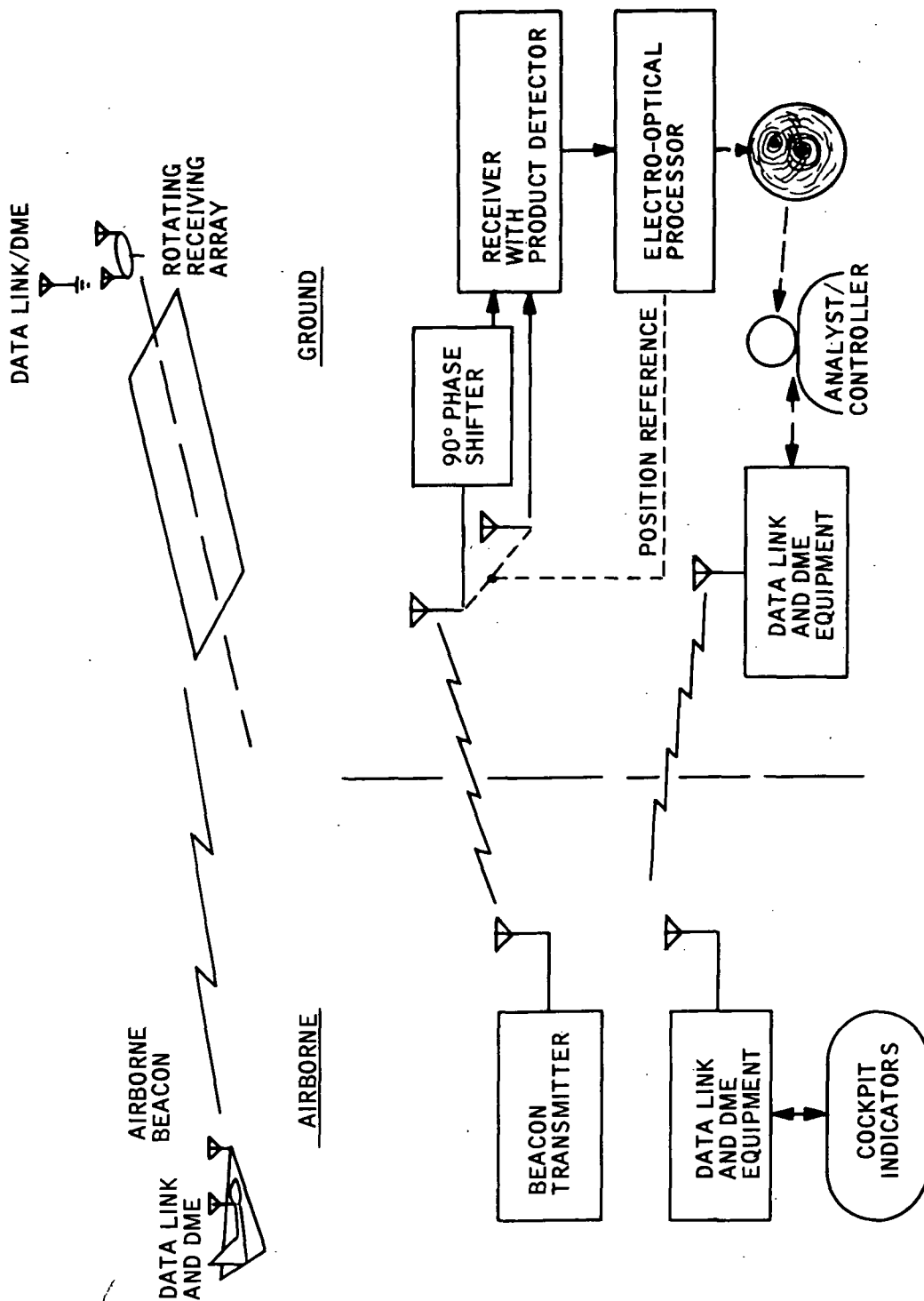


Figure 3. Variation 1 of Circular Synthetic Aperture System



- FREQUENCY
- SENSOR AND CONTROL
- MEASUREMENTS
- DISPLAY
- C- OR X-BAND
- GROUND DERIVED WITH DATA LINK TRANSFER
- A_Z - E1 AND RANGE
- COCKPIT INSTRUMENTS

Figure 4. Variation 2 of Circular Aperture System

Summary of Capabilities

The concepts used in the Astrolabe system show potential for use as an ILM. Reference 1 contains the desired ILM angular accuracy specification of 0.10° to 0.12° for 2σ accuracy. To assure 2σ accuracy of 0.12° with Astrolabe would require element separations of approximately $R/\lambda=80$ which would require spinning element separations (R) of approximately 3 meters at X-band and 0.8 meters at K_a -band. The selection of frequency for the transmissions is somewhat arbitrary although it should be recalled from Reference 1 that approximately $(1.3 \times R_{\max} \text{ (Km)})$ dB more power is required for K_a -band operation than X-band operation in heavy rain (16mm/hr). For example, guidance or position determination at a range of 8 Km would require over 10 dB (10 times) more power at K_a -band than at X-band for the same receiver signal to noise ratio.

It is conceivable, however, since an 80 cm element separation would be possible in the nose of a commercial aircraft, that K_a -band operation of a spinning antenna in the aircraft for high accuracy angle determination would be feasible. This configuration would have the requirement for stabilization of the spinning antenna to eliminate high frequency roll, pitch, and yaw angular deviations to achieve the required high accuracies. A gimballed system for the spinning antenna (with the spinning elements generating the gyroscopic stability platform) could be used with sensors to derive smoothed aircraft to antenna reference angles to relate derived angles to the aircraft reference frame.

Multipath errors consist of two types: direct multipath terms which are unresolvable from true targets over short observation times and cross-product multipath terms that originate from the product detector which are resolvable over relatively short (less than one second at X-band) integration times. Analysis shows the cross-product terms are reducible by at least 12 dB but the direct multipath terms are left to the expertise of the display analyst for removal. The multipath problem therefore favors ground receivers and analysts since the multipath geometry would be more familiar and predictable. A pilot would see a somewhat different display to interpret at each airport.

Comments on ILM applications up to this point have been general for nearly any configuration. When multiple systems are used in an effort to attain location by triangulation or geometrical shape orientation, several other considerations are

necessary.

Multiple ground receiving locations were shown to require large separations (2 to 4 Km). These wide separations seriously hinder displaced ground receiving sites since the triangulation function must be performed centrally. Either multiple receivers, receiver processors, and analysts or multiple receivers with IF or detected IF signals relayed to a central processing and analysis center would be required resulting in a costly configuration.

Configurations with airborne receivers and displaced ground transmitters have the same problem of wide separation of ground antennas for high accuracy although the analysis is centralized to the aircraft. The wide separations necessary for ranging accuracies necessarily limit the achievable angular accuracies. This effect coupled with multipath problems will degrade performance such that any multiple configuration will be of questionable use for flare, touch-down, and roll-out information.

The multiple ground antenna configurations, although capable of providing high accuracy results prior to flare maneuvers are not practical ILM's because of the complexity of the analysis, interpretation, and triangulation requirements. If the high accuracy requirements can be waived it would be feasible to use variation 1 (Figure 3) where the imagery (4 beacon points) would be representative of the four corners of the runway and presented to the aircrew in the form of a pseudo real-world perspective image for a VFR type of approach. This application would require the spinning (or a stepped Wollenweber array) receiving antenna in the aircraft. Decreased accuracy requirements would negate requirements for a stabilized antenna platform. Beacon location (point) accuracies on the display to the order of 1° should be achievable. Suitability of a four-point image of the runway for guidance to the pilot was not determined in this study.

A high accuracy ILM application at a reduced cost when compared to the multiple ground antenna configurations would consist of a combination of a single beacon transmitter on the aircraft, a spinning receiving antenna on the ground, and an interrogator/response TOA (time-of-arrival) ranging capability incorporated into the ground-to-aircraft data link for relaying angular information to the aircraft.

This system would provide high precision approach corridor information (azimuth and elevation angle along with precise range-to-go as described in reference 1, ILM Multilateration Sensor section). It should be pointed out that this combination of sensors would benefit from the most accurate capabilities of both techniques: Astrolabe precision angle referencing without triangulation techniques and its associated accuracy degradation and high precision ranging by TOA multilateration techniques without GDOP (Geometrical Dilution of Precision) inherent in multilateration angle determination. This concept should be capable of providing 2 sigma angular accuracies of 0.1° and ranging accuracies to a few meters which are consistent with ILM requirements.

CONCLUSIONS

1. The use of a large thinned array receiving antenna in the airborne bistatic radar concept provides a significant resolution improvement over a comparable monostatic radar. Part of this improvement can be traded off for the ILM problem through reduction of operating frequency from Ka-band to X-band with a corresponding drop in atmospheric signal attenuation. This allows the system to operate at reduced output power and, thus, reduced transmitter costs. This cost advantage is offset, however, by the cost of the wing-mounted phased array. Total system cost of the X-band bistatic radar and the K_a-band imaging radar would be approximately the same. Since runway detection range of both radars is approximately the same due to similar beamwidths, the advantages of the X-band bistatic system become subjective; quality of function (weather radar and ILM) and the availability of more equipment expertise since X-band technology is more developed than K_a-band technology.

These advantages are at the expense of increased installation design costs. From preliminary examination, it appears feasible to install the thinned array antennas in the wings of most commercial aircraft. However, each aircraft type will probably require its own unique installation design.

2. The complex interferometer/DME combination (MADGE) shows a potential of meeting Category III accuracy requirements for ILM, however, as currently configured (designed for Category II operations) it does not meet the accuracy requirements. Analysis of the elevation antenna array and signal processing showed this concept

can suppress multipath interference and provide angular accuracies equivalent to MLS to within 200 to 300 meters aircraft to ground antenna ranges. Use of the elevation concept for both azimuth and elevation angle measurements and addition of a second set of antennas to provide flare, touchdown and rollout guidance should satisfactorily meet the Basic and Case I ILM requirements. Use of radar altitude beyond runway threshold for flare and location of the azimuth antenna at the stop end of the runway should eliminate the need for the second set of antennas.

3. Analysis of the circular synthetic aperture concept (Astrolabe) showed azimuth-elevation angular measurements of sufficient accuracy (0.1°) could be achieved over the desired ILM operating range. Use of multiple beacon configurations to measure range through triangulation were not satisfactory and it was concluded DME must be included in the concept to provide an independent range-to-go measurement.

Electro-optical processing is used to cross-correlate the received signal with a reference pattern to generate a pseudo-real world display of the azimuth-elevation direction to the signal sources from the receiver. Multipath sources, interference rings and other noise sources also appear on the display with human interpretation required to identify the desired signal source. We concluded this type of display may be feasible for a ground controller where each aircraft approach would generate a similar looking display. A display of this type in the aircraft would show a different noise pattern at each airport requiring longer response time by the operator for interpretation. Further signal processing may also be feasible to electronically measure azimuth/elevation angles with output to a more common guidance display.

4. Comparative costs for the three systems in this report and the feasible ILM concepts of Reference 1 were generated internally through comparisons to like equipments. They are based on 1974/1975 costs and do not represent specific manufacturer inputs. These costs and weights of the airborne units are as follows:

	<u>Airborne Cost</u>	<u>Grd. Cost</u>	<u>Airborne Wt.</u>
Bistatic Radar	\$62K	-	82 kgms
Complex Interferometer/DME	\$13K	\$41K	8 kgms
Circular Synthetic Aperture (variation 2)	\$15K	\$23K	8 kgms

RECOMMENDATIONS

1. We can not recommend a specific sensing concept which stands above all others from our analysis in meeting the ILM requirements. We have identified several concepts, including the three in this report and six in Reference 1, which show potential capability to meet at least part of our baseline ILM requirements. Each system is costly and/or will require major development efforts before becoming operational in addition to each having unique problem areas ranging from the human interface to installation difficulties both on the ground and in the aircraft.

Radars, operating in the X to K_a-band, have potential for meeting to some degree each of the major ILM functions examined: approach, landing and rollout guidance, obstacle detection, and real world imagery. With reduced environmental extremes and possible enhancement of runway/background differences, development of useful operational systems should be feasible.

Several concepts: multilateration, redundant MLS, complex interferometry, synthetic circular aperture, provide greater approach coverage and higher accuracy for the ILM functions of approach, landing, and rollout guidance than the radars but provide no capability for obstacle detection or real world imagery. Selection of one of these concepts as an ILM requires reliance on another set of equipment or operational procedures to cover the obstacle avoidance function and verification of crew acceptance of the non-real world guidance display (cross-pointers, synthetic image, etc.) for the confidence building function.

2. As discussed in the recommendations of Reference 1, there is no clear consensus of opinion in the industry on the functional usage or purposes of an ILM. This study started with the baseline ILM function of landing monitor for a Configuration K, MLS-equipped aircraft. Using this function, the associated ILM sensing

requirements are generated by the possible Category III environmental and operational landing conditions.

We were unable in this study, due to time allotted, to explore in detail other possible functions of an ILM or frequency of occurrence considerations of the various environmental/operational conditions leading to extreme sensing requirements. These factors must be analyzed and traded off with the potential sensing concepts before an optimal concept can be selected for any user.

SECTION III

DETAIL ANALYSES

BISTATIC RADAR APPLICATION ANALYSIS FOR ILM

Introduction

A bistatic radar uses separate transmitting and receiving antennas such that scattered incident energy may be received at angles other than the incidence angle, Receiving antennas incapable of handling large transmitter powers may be used, or arrays may be thinned with resulting grating lobes being removed by selection of the second antenna. This application is of the latter type, using a special phased array receiving system (Reference 2). This application has several advantages which will be presented later.

The previous analysis of Independent Landing Monitors (ILM's) using radar techniques (Reference 1) concluded that X-band radiation had the potential for adequate penetration of Category III weather conditions (very short or "zero" visibility) but did not have the capability for high resolution because of the large physical size of a monostatic radar antenna. This bistatic application allows a large physical receiving antenna for high resolution at X-band by locating array elements (individual antennas) along the lower edge of a wing. The receiving function is simplified by "thinning" the array (removing array elements) such that fewer array elements are used while maintaining the long array length for high resolution. Fewer array elements (16 to 32 elements) make it possible to perform the receiver heterodyning at the array elements and thus minimize transmission line losses and simplify routing of the array signals through the wing structure by replacing the RF waveguides with IF cabling. Thinning the array does create the problem of ambiguous grating lobes of the receiving array, however, by properly selecting array element spacings to match the transmitting antenna, it is possible to place the receiving grating lobes in the nulls of the transmitting radiation pattern. This concept is the application analyzed by this report.

A representative scenario for the ILM application is an aircraft during straight-in approach to a 4000 meter runway during adverse weather conditions (Reference 1). The aircraft is on a 3° glideslope with a 5° nose up attitude relative to the glideslope and a velocity of 75 m/sec (145 kts). The analysis describes the expected

signal power ratios as a function of:

Range

Weather Conditions

Runway and Surrounding Culture Scattering Cross Sections

Equipment Parameters

The specific parameters that were used in the analysis for each of the above factors are described in the following paragraphs.

Analysis

The analysis of the bistatic radar application was performed with the same considerations that were used in the previous ILM analysis so that comparisons could be made with previous results. The same analytic software routines were used for deriving single-pulse return power ratios and the additional factors considered in Reference 1 were reviewed. The single-pulse results and the additional factors are discussed in detail in Paragraph C below. The parameters and environmental factors considered in the software analysis are defined and reviewed in Paragraphs A and B respectively.

A. Radar Parameters

Two specific radars were analyzed as illuminators for a bistatic application. Parameters typical of a Marconi LN-66 radar were used because of previous bistatic tests of this very short pulse, high PRF radar (Reference 2). For comparison, a stock RCA AVQ-30X weather radar as an illuminator was analyzed since this radar is already available on some aircraft. The parameters used in the analysis are summarized in Table 1. Table 2 lists the receiving system parameters. The array and receivers as described in Reference 2 were analyzed due to their apparent applicability for aircraft mounting.

B. Software Scenario

The software previously developed (see Reference 1 for description) was used for the single-pulse return power calculations. The basic four most adverse weather cases of each type of weather (2 fog, 1 rain, and 1 snow) were used to determine the radar penetrability. The four cases are summarized in Table 3. The X-band backscattering cross-sections, γ , in dBSM (dB referenced to one

Table 1. Typical Radar Transmitting Parameters
(References 1 and 2)

Radar System	Marconi LN-66 (BISTAR System)	RCA AVQ-30X
Band	X-band	X-band
Frequency	9.4 GHz	9.4 GHz
Power	12 kw	65 kw
PRF	5000	200
Pulsewidth	40 nanoseconds	5 microseconds
Antenna Gain	33 dB	35 dB
1st Sidelobe (H) (rel. to main lobe)	-21 dB	-30 dB
1st Sidelobe (V) (rel. to main lobe)	-21 dB	-30 dB
Az Beamwidth (one-way)	2.3°	2.9°
El Beamwidth (one-way)	3.6°	5.2°
Scan Parameters		
Scan Sector	60° ($\pm 30^\circ$)	180° ($\pm 90^\circ$)
Scan Rate	1200°/second	45°/second
Images Per Second	20 images/second	1/4 image/seconds

Table 2. Receiving Array Parameters
(Reference 2)

Array Element

Flared Slot

Max Gain - 20 dB*

Az Beamwidth 60° (see Figure A-2a)

El Beamwidth 7° (see Figure A-2b)

Array, linear

$$\begin{aligned} \text{Max Gain*} &= 5.8 \text{ dB} + 10 \log_{10} \frac{nd}{\lambda} - 10 \log_{10} K' \\ &= 20.2 \text{ dB} \end{aligned}$$

$$\left(\frac{d}{\lambda} = 7.5, \text{ so } K' \approx 6.5 \right)$$

Number of Elements, $n = 32$

Array Length 7.7 m (25 feet)

Az Beamwidth 0.23°

El Beamwidth 7.0°

1st Sidelobe (H), -30 dB

No sidelobes on the Elevation Pattern

Receiver

Noise Figure 9 dB

$$\text{Noise Bandwidth, } B, \text{ Hz} = \frac{1}{\text{Transmitter Pulsewidth (sec)}}$$

*See Appendix A for Derivation

Table 3. Analytical Weather Cases

Weather Case	Description	Density or Fall Rate	Altitude
D 1.3	Heavy Rain	16 mm/hr	ground to 1500 m
D 2.4	Radiation Fog	4g/m ³ , zero visibility	ground to 60 m
D 3.4	Evaporation Fog	4g/m ³ , zero visibility	ground to 1500 m
D 4.3	Heavy Snow	9 mm/hr (equivalent water)	ground to 3000 m

Table 4. X-Band Backscattering Cross-Section, σ , dBSM

Asphalt	-56 to -45
Concrete	-61 to -38
Grass	-42 to -5
Snow	-43 to -29

square meter) are listed in Table 4. The extreme values for grass backgrounds and a 23 meter wide runway were used to derive the results in Paragraphs D.2. The remaining parameters and expressions are identical to the previous analysis.

C. Analytical Considerations

The computer runs provided the single-pulse results shown in Tables 5 and 6. The very low backscattering cross-sections assumed for the results of Table 5 prompted the use of circular polarization for precipitation clutter reduction (25 dB reduction for rain and 16 dB reduction for snow). Additionally a modification of the Marconi LN-66 was run to test the feasibility of degrading resolution to increase grass background returns. This modification, designated XRADAR, has identical parameters to the LN-66 except the pulsewidth was increased (decreasing the receiver bandwidth) by a factor of 5 (to 200 nano-seconds) and the receiving array was shortened to 16 elements (12.5 foot length, beamwidth of 0.46°). This resulted in a decrease in array gain of 6 dB, an increase in footprint and clutter volume by 10 dB and a decrease in receiver noise bandwidth by 7 dB (1/5).

Several additional factors were considered as modifiers of the single-pulse results to account for statistical and dynamic properties of complex multiple-pulse returns and the display or monitoring functions. The factors considered in the previous ILM sensor analysis were reviewed and the terms appropriate or significant to the bistatic scenario are discussed in this section.

L_j - Scanning Loss

The losses due to scanning of the antennas are of three origins.

L_{j1} - loss incurred because the scan rate is too fast or the PRF is too low to receive at least one pulse return from each resolution element.

L_{j2} - loss due to mis-tracking between the two separately scanned antennas.

Table 5. Radar Return Power Ratios for a smooth concrete ($\gamma = -61$ dBSM) runway surrounded by short dry grass or snow ($\gamma = -42$ dBSM) (circular polarization for precipitation clutter reduction is assumed)

	Weather Case D 1.3 Heavy Rain (16 mm/hr)				Weather Case D 2.4 Radiation Fog				Weather Case D 3.4 Evaporation Fog				Weather Case D 4.3 Snow (9 mm/hr Equivalent water) Marconi LN-66, XRADAR, RCA AVQ-30X			
	Marconi LN-66, X RADAR, RCA AVQ-30X				Marconi LN-66, XRADAR, RCA AVQ-30X				Marconi LN-66, XRADAR, RCA AVQ-30X				Marconi LN-66, XRADAR, RCA AVQ-30X			
1 NM (1853m)	ΔB	19.5	14.3	19.5	19.5	14.3	19.5	19.5	14.3	19.5	19.5	14.3	19.5	14.3	19.5	19.5
	S/B _g	33.3	20.7	1.8	33.3	20.7	1.8	33.3	20.7	1.8	33.3	20.7	1.8	33.3	20.7	1.8
	S/N	14.7	13.0	35.1	15.3	13.7	35.8	14.6	12.9	35.0	15.6	14.0	36.1	15.6	14.0	36.1
	S/C	39.5	26.9	7.2	39.5	26.9	7.2	39.5	26.9	7.2	39.5	26.9	7.2	39.5	26.9	7.2
	B _g /N	-18.6	-7.7	33.3	-18.0	-7.0	34.0	-18.7	-7.8	33.2	-17.7	-6.7	34.3	-17.7	-6.7	34.3
Resolution Cell Size	B _g /C	6.2	6.2	5.4	6.2	6.2	5.4	6.2	6.2	5.4	6.2	6.2	5.4	6.2	6.2	5.4
	C/N	-24.8	-13.9	27.9	-24.8	-13.9	27.9	-24.8	-13.9	27.9	-24.8	-13.9	27.9	-24.8	-13.9	27.9
		6m x 30m x 1.5m*	30m x 3m*	750m x 1.5m*	6m x 30m x 1.5m*	30m x 3m*	750m x 1.5m*	6m x 30m x 1.5m*	30m x 3m*	750m x 1.5m*	6m x 30m x 1.5m*	30m x 3m*	750m x 1.5m*	6m x 30m x 1.5m*	30m x 3m*	750m x 1.5m*
		1.5m*	3m*	1.5m*	1.5m*	3m*	1.5m*	1.5m*	3m*	1.5m*	1.5m*	3m*	1.5m*	1.5m*	3m*	1.5m*
		8.3	3.3	8.3	8.3	3.3	8.3	8.3	3.3	8.3	8.3	3.3	8.3	8.3	3.3	8.3
3 NM (5560m)	S/B _g	31.5	15.9	0.6	31.5	15.9	0.6	31.5	15.9	0.6	31.5	15.9	0.6	31.5	15.9	0.6
	S/N	-4.0	-8.6	16.5	-1.0	-5.2	19.5	-3.1	-7.8	17.3	-0.5	-5.1	19.9	-0.5	-5.1	19.9
	S/C	33.0	17.4	0.6	33.0	17.4	0.6	33.0	17.4	0.6	33.0	17.4	0.6	33.0	17.4	0.6
	B _g /N	-35.5	-24.1	15.9	-32.5	-21.5	18.9	-34.6	-23.7	16.7	-32.0	-21.0	19.3	-32.0	-21.0	19.3
	B _g /C	1.5	1.5	0.0	1.5	1.5	0.0	1.5	1.5	0.0	1.5	1.5	0.0	1.5	1.5	0.0
Resolution Cell Size	C/N	-36.6	-25.6	15.9	-36.6	-25.6	15.9	-36.6	-25.6	15.9	-36.6	-25.6	15.9	-36.6	-25.6	15.9
		6m x 30m x 4.5m*	30m x 9m*	750m x 4.5m*	6m x 30m x 4.5m*	30m x 9m*	750m x 4.5m*	6m x 30m x 4.5m*	30m x 9m*	750m x 4.5m*	6m x 30m x 4.5m*	30m x 9m*	750m x 4.5m*	6m x 30m x 4.5m*	30m x 9m*	750m x 4.5m*
		4.5m*	9m*	4.5m*	4.5m*	9m*	4.5m*	4.5m*	9m*	4.5m*	4.5m*	9m*	4.5m*	4.5m*	9m*	4.5m*
		2.3	1.2	2.3	2.3	1.2	2.3	2.3	1.2	2.3	2.3	1.2	2.3	2.3	1.2	2.3
		27.2	11.8	-3.6	27.2	11.8	-3.6	27.2	11.8	-3.6	27.2	11.8	-3.6	27.2	11.8	-3.6
8 NM (14825m)	S/N	-25.1	-29.0	-4.7	-18.1	-22.7	2.4	-21.6	-26.2	-1.2	-17.4	-22.3	2.8	-17.4	-22.3	2.8
	S/C	24.4	8.8	-7.9	-18.6	-34.5	1.2	-45.3	-39.0	2.4	19.2	3.6	-13.1	19.2	3.6	-13.1
	B _g /N	-52.3	-42.5	-1.1	-45.3	-34.5	1.2	-48.8	-39.0	2.4	-44.8	-34.1	6.4	-44.8	-34.1	6.4
	B _g /C	-2.8	-3.0	-4.3	-2.8	-3.0	-4.3	-2.8	-3.0	-4.3	-2.8	-3.0	-4.3	-2.8	-3.0	-4.3
	C/N	-49.0	-38.5	3.3	-49.0	-38.5	3.3	-49.0	-38.5	3.3	-49.0	-38.5	3.3	-49.0	-38.5	3.3
Resolution Cell Size		6m x 30m x 12m*	30m x 24m	750m x 12m*	6m x 30m x 12m*	30m x 24m	750m x 12m*	6m x 30m x 12m*	30m x 24m	750m x 12m*	6m x 30m x 12m*	30m x 24m	750m x 12m*	6m x 30m x 12m*	30m x 24m	750m x 12m*
		12m*	24m	12m*	12m*	24m	12m*	12m*	24m	12m*	12m*	24m	12m*	12m*	24m	12m*
		8.3	3.3	8.3	8.3	3.3	8.3	8.3	3.3	8.3	8.3	3.3	8.3	8.3	3.3	8.3
		31.5	15.9	0.6	31.5	15.9	0.6	31.5	15.9	0.6	31.5	15.9	0.6	31.5	15.9	0.6
		-4.0	-8.6	16.5	-1.0	-5.2	19.5	-3.1	-7.8	17.3	-0.5	-5.1	19.9	-0.5	-5.1	19.9

* Array focusing required

Terms: ΔB - signal variation in dB as the 23m runway is swept by the antennas
 S - signal power returned by a 1 m² target
 B_g - maximum signal power returned by the ground (background only)
 C - signal power returned by the precipitation
 N - receiver thermal noise power

Table 6. Radar Return Power Ratios in dB for a rough concrete runway ($\gamma = -38$ dBsm) surrounded by 8" to 10" vegetation ($\gamma = -5$ dBsm)

	Weather Case D 1.3 Heavy Rain		Weather Case D 2.4 Radiation Fog		Weather Case D 3.4 Evaporation Fog		Weather Case D 4.3 Snow (9mm/hr)	
	Marconi LN-66 RCA AVQ-30X		Marconi LN-66 RCA AVQ-30X		Marconi LN-66 RCA AVQ-30X		Marconi LN-66 RCA AVQ-30X	
1 NM (1853m)	ΔB	33.0	33.0	33.0	33.0	33.0	33.0	33.0
	S/B _g	-3.7	-35.2	-35.2	-35.2	-35.2	-35.2	-35.2
	S/N	14.7	35.1	35.8	35.0	15.6	36.1	36.1
	S/C	14.5	-17.8			18.3	-14.1	-14.1
	B _g /N	18.4	70.3	71.0	70.2	19.3	71.3	71.3
Resolution Cell Size	B _g /C	18.2	17.4			22.0	21.1	21.1
	C/N	0.2	52.9			-2.7	50.2	50.2
		6m x	750m x					
		1.5m*	1.5m*					
3 NM (5560m)	ΔB	14.1	14.1	14.1	14.1	14.1	14.1	14.1
	S/B _g	-5.5	-36.4	-36.4	-36.4	-5.5	-36.4	-36.4
	S/N	-4.0	16.5	19.5	17.3	-0.5	56.3	56.3
	S/C	8.0	-24.4			11.7	-20.6	-20.6
	B _g /N	1.5	52.9	55.9	53.7	5.0	56.3	56.3
Resolution Cell Size	B _g /C	13.5	12.0			17.2	15.8	15.8
	C/N	-12.0	40.9			-11.8	40.5	40.5
		6m x	750m x					
		4.5m*	4.5m*					
8 NM (14825m)	ΔB	3.9	3.9	3.9	3.9	3.9	3.9	3.9
	S/B _g	-9.8	-40.6	-40.8	-40.8	-9.8	-40.8	-40.8
	S/N	-25.1	-4.7	2.4	-1.2	-17.6	2.8	2.8
	S/C	-0.6	-32.9			3.2	-29.1	-29.1
	B _g /N	-15.3	35.9	43.2	39.6	-7.8	43.6	43.6
Resolution Cell Size	B _g /C	9.2	7.7			13.0	11.7	11.7
	C/N	-24.5	28.2			-20.8	31.9	31.9
		6m x	750m x					
		12m*	12m*					

*Array Focusing Required

Terms: ΔB - signal variation in dB as the 23m runway is swept by the antennas
 S - signal power returned by a 1 m² target
 B_g - maximum signal power returned by the ground (background only)
 C - signal power returned by the precipitation
 N - receiver thermal noise power

L_{j3} - loss from electronically scanned phased array, the gain decreases as approximately $|\cos \theta|$ for θ measured from broadside.

For a beamwidth of 0.23° , the Marconi radar as presented in Reference 2 has been modified to transmit one pulse per resolution element and 20 independent pulses for each resolution element (one per scan) per second allowing the possibility of direct CRT display. (Independence will be shown later.) The RCA radar has a sufficiently slow scan that one pulse is radiated each 0.225° or approximately once each resolution element of the 0.23° array. This is coincidentally convenient, however, only one return from each resolution element occurs every 4 seconds. This data is too slow for direct viewing without display storage such as a scan converter or storage tube in the display. L_{j1} is thus negligible although the effects of the slow sample rate will be evident in other factors.

Mis-tracking between the two antennas is not a serious factor since both illuminating (transmitting) antenna beamwidths are at least a factor of 10 wider than the phased array. Reference 2 and Appendix A demonstrate that weighted amplitudes and/or non-linear element spacings can reduce sidelobe (and grating lobe) levels such that spurious returns can be suppressed to at least 30 dB below the receiving array mainlobe. As long as the phased array can track the illuminating antenna within approximately 1° , L_{j2} will be negligible.

The loss due to electrically scanning the phased array θ degrees from broadside is approximately $|\cos \theta|$. At the scan limits, this would be about a 1.5 dB reduction in gain. Large crab angles necessitated by high cross-winds may require operation in this region. Other effects that would require consideration in this region would be degraded beamwidth (beamwidth is proportional to $\frac{1}{|\cos \theta|}$) and array length across which the propagating short time-duration return pulse must propagate. The receiving array length and transmitter pulse-width for this analysis were acceptable. (e.g. a 40 nanosecond pulse could be detected by nearly all elements of a 25 meter length array at θ as large as 30° ($\frac{3 \times 10^8 \text{ m/sec} \times 4 \times 10^{-8} \text{ sec}}{\sin 30^\circ} \approx 24\text{m}$). L_{13} is negligible for targets

directly ahead and approximately a 1.5 dB loss for targets at the scan limits of the Marconi radar. Operation of the RCA system beyond 30° would cause larger losses, however, operation at such extreme angles is not envisioned for ILM's at this time.

L_a - Sensor Losses due to aircraft motion and instabilities.

The high resolution (0.23°) capabilities of the receiving array will dictate that stabilization is required since rms angular yaw rates of approximately 0.8 degrees/sec with deviations of several degrees were identified in the previous study (Reference 1). Tracking of the yaw instabilities within approximately the beamwidth (0.25°) is possible with on-board instrument sensors. Pitch and roll sensor inputs are similarly required. L_a is thus assumed negligible, provided display stabilization is incorporated using aircraft instrument sensors.

L_d - Scan Distribution Loss

The derivation of scan distribution loss will follow the same assumptions as the previous analysis; specifically, the bistatic ILM display will occupy a small amount of aircrew workload time resulting in only a couple of seconds for aircrew viewing during each required reference of the ILM display. The display integration is thus limited to a few seconds and the number of pulses (samples) and independent scans forming the reference display image are bounded by those few seconds. The Marconi illuminator may provide approximately 40 samples of each resolution element in 40 scans (20 scans per second) while the RCA system would provide only one sample (if at all) in the same time interval. In view of this rather severe restriction, we'll assume the scan limits of the RCA radar are modified to $\pm 30^\circ$ at the same scan rate (a relatively minor modification) such that up to two samples may be received in the same two second time interval. Recall from the previous study that scan distribution loss is derived (from Reference 3) by holding the cumulative probability of detection, P_c , constant in the expression:

$$P_c = 1 - (1 - P_d)^j \quad (1)$$

where P_c - cumulative probability of detection in j scans
 P_d - single scan probability of detection

The variation of single scan probability of detection, P_d , as a function of increasing number of scans, j , results in a decreasing S/N requirement. As the number of scans increases, the number of pulses available for integration in each scan decreases, offsetting the decreasing S/N required. The effect of the trade-off between single scan and multiple scans is shown in Figure 5. The scan distribution loss L_d is relative to direct integration of all possible pulses (assumed correlated within one scan and uncorrelated between successive scans) falling within the interval of consideration.

L_f - Fluctuating Signal Loss

The fluctuations of the pulse returns contribute losses, L_f , as a function of number of pulses integrated and probability of detection. Swerling and Schwartz have characterized the effects and the loss as a function of probability of detection is shown in Figure 6.

L_{c1} - Collapsing Loss

Four types of collapsing loss are considered in the bistatic system: noise, L_{c11} ; beam, L_{c12} ; range, L_{c13} ; and display, L_{c14} .

The noise collapsing loss, L_{c11} , arises from noise sources within parallel receiver channels adding coherently. Sources would include effects such as local oscillator noise at the mixers of parallel receiver channels to the phased array adding at IF. The effects are reducible by circuit techniques (e.g., balanced mixers) and minimizing the coherency of the noise prior to summation by adjusting the noise path lengths as described in Reference 2. Careful adherence to proper noise limiting techniques should allow reduction of L_{c11} to negligible levels.

The beam collapsing loss, L_{c12} , is considered in part by the analytic software beam considerations which generate beam patterns representative of typical patterns to add in contributions from sidelobes and grating lobes. Other effects such as beam pattern distortions during operational flights due to effects of flaps or landing gear deployment can only be speculatively considered pending operational tests of the actual array. Assume the array is mounted as far out on the wing as possible to remove the nose wheel and engine nacelles

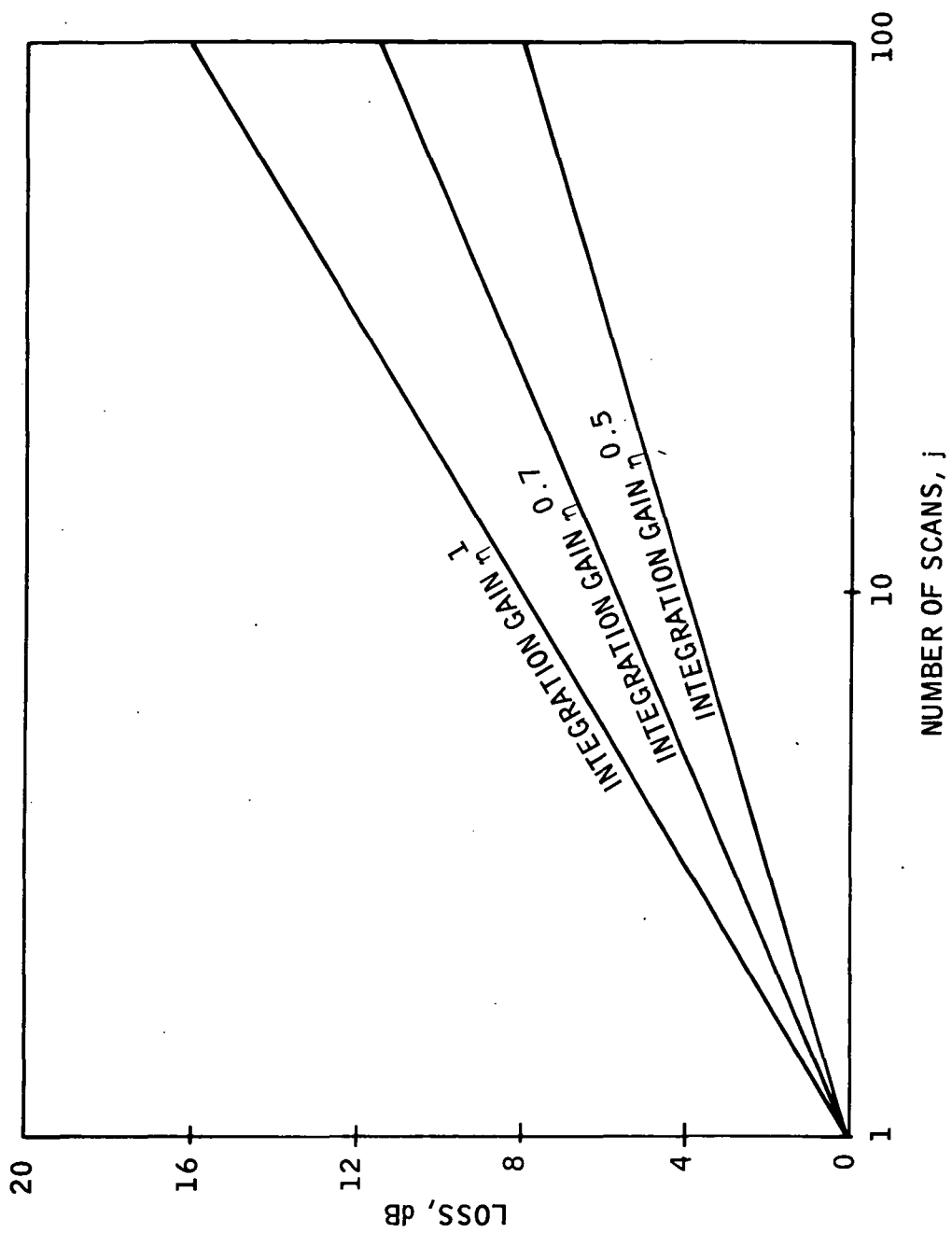


Figure 5. Scan Distribution Loss

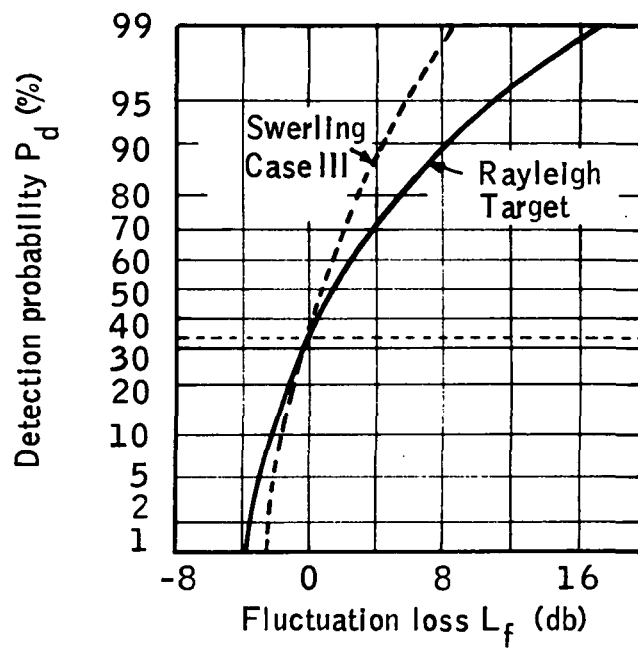


Figure 6. Fluctuation Loss vs Detection Probability

as far as possible from the array scan coverage and as far back on the wing as possible to minimize pattern blockage by the leading edge flaps. This configuration should minimize beam collapsing loss, L_{c12} , resulting in only a slight increase in precipitation clutter return caused by "knife-edge" diffraction along the lower edge of the flaps. This diffraction distortion of the antenna pattern would tend to increase the vertical beamwidth (collecting more precipitation clutter due to increased vertical dimension of the clutter cell), however the nearly vertical distortion would not degrade resolution since the vertical angle reference is established through ranging and knowledge of aircraft altitude and glide slope. Since the precipitation clutter will be shown to be substantially less than background returns, the effect of this loss should be small.

The range collapsing losses, L_{c13} , due to returns from ambiguous ranges at high PRF is expected to be severe due to the extreme variations in backscattering cross-sections. The previous analysis suggested variable PRI's as a solution for integrating out this effect. Reference 2 also suggests pulse-to-pulse beam agility although this implementation would require an electronically-scanned phased array illuminator or several transmitting antennas. Variable or staggered PRI is recommended to minimize L_{c13} to acceptable levels.

L_{c14} , the display collapsing loss is minimized by providing appropriate cockpit instrument sensor inputs so that effects of yaw and roll image distortions can be minimized to the appropriate sensor accuracy. Typical gyro/servo accuracies of nearly 0.25° would be in close agreement with array resolutions.

L_i - Integration Loss

The integration loss (relative to n^1 integration gain) is a function of the integration efficiency of the display/display processing and the pulse return correlation functions. Figures 7 and 8 from Reference 1 provide the correlation information for background and precipitation returns. The display is assumed to integrate correlated pulses with an efficiency of $n^{0.7}$ = integration gain (Reference 1), uncorrelated as $n^{0.5}$. The correlation data shows that the background and precipitation clutter are essentially uncorrelated from pulse to pulse as the standard deviation of doppler velocity within 10 km is within

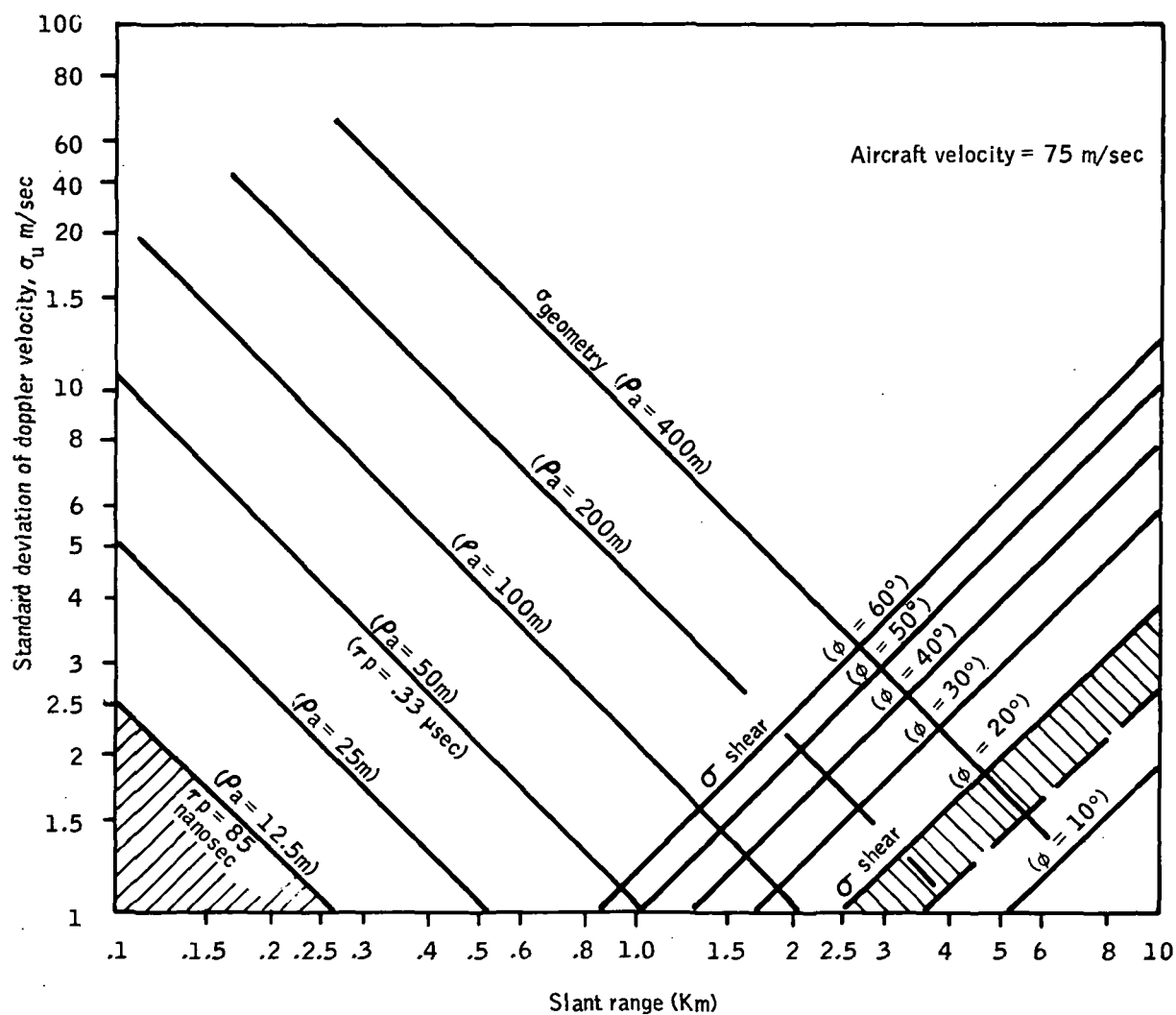


Figure 7. Standard Deviations of Clutter Component

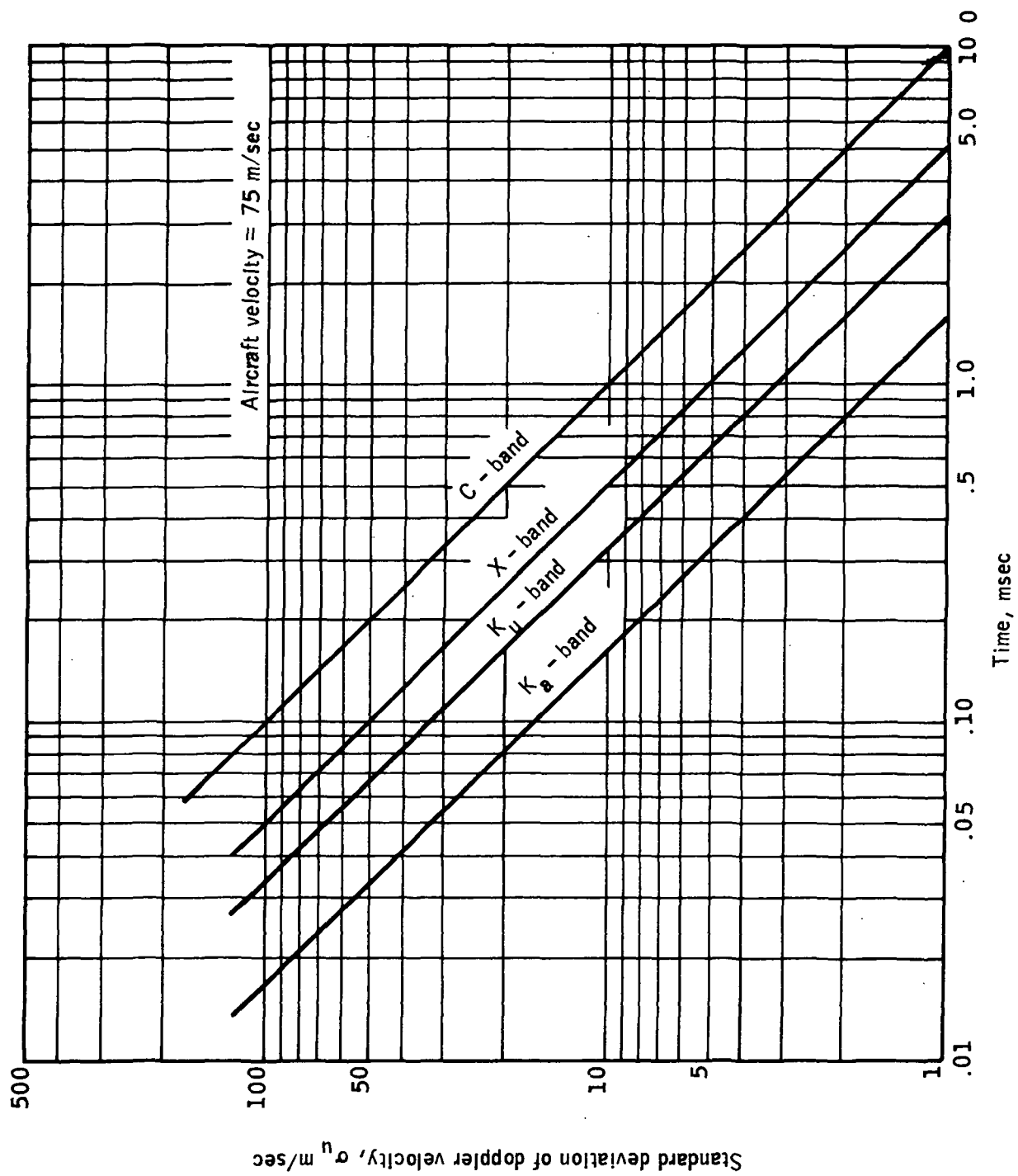


Figure 8. T_i , Time Between Samples

1.5 m/sec which is the region of inseparable combined turbulence, shear, and ground wind doppler velocity components.

D. Results

The overall results of the single pulse and multiple pulse factors define a set of complex system requirements needed to minimize the loss factors presented previously. A summary of the loss terms is presented in Table 7 and Figure 9. The multiple pulse effects are insignificant compared to the magnitude of the individual pulse power ratios. Tables 5 and 6 are summarized in the graphs in Figures 10 through 13. The graphs have curves labeled to show the most significant mechanisms contributing to the curve. Thus, if $B_g \gg S$ and $C \ll N$ the curve approaches B_g/N . The different slopes evident in the curves are usually indicative of differing dominant terms at near and far ranges. The ΔB reference curve is derived from the convoluted power return maximum variation from the runway and background as the runway is scanned. Thus, in order to "detect" the runway the range must be less than the range at which the ΔB reference curve crosses the +6dB minimum detection threshold.

The analysis showed the application has potential for providing high resolution direct imaging of the runway during approach in severe rain, snow, or zero visibility fog. Specific results are itemized below:

1. Lowest backscattering cross-sections provide inadequate contrast, ΔB , and background to precipitation clutter, B_g/C , to detect the runway unless circular polarization is used for clutter reduction and degraded resolution is used to decrease the noise bandwidth. With these assumptions, approximate detection ranges for 20 dB contrast (runway to background) are: (XRADAR results)

Weather	Detection Range, 23m Runway
16 mm/hr Rain	(1.9 km)
9 mm/hr Snow	(2 km)
fog, zero visibility	(1.9 km)

Table 7. Summary of Multiple Loss Factors

Loss Term	Marconi LN-66	Radar	RCA AVQ-30X
L_j , scanning L_a , sensor L_{nf} , near field L_d , scan distribution L_f , fluctuating signal L_{cl} , collapsing L_i , integration, target L_i , integration, background L_i , integration, precipitation	Negligible Negligible Small, contained in L_f 7dB for target, 5 dB for clutter* -2 dB* Reducibly Small 4.8dB ($n_{dB}^{.7} = 11.2$ dB) (40 pulses) 8 dB ($n_{dB}^{0.5} = 8$ dB also) 8 dB ($n_{dB}^{0.5} = 8$ dB also)		Negligible Negligible Small, contained in L_f 0 to 2 dB* (1 or 2 pulses) 8 to 4 dB* (1 or 2 pulses) Reducibly Small 0 to -3 dB (1 or 2 pulses) 0 to -1.5 dB (1 or 2 pulses) 0 to -1.5 dB (1 or 2 pulses) * .90 probability of detection
Summary for .9=Pc Target Background Precipitation Noise**	gain 6.2 dB (40 pulses) gain 5.0 dB (40 pulses) gain 5.0 dB (40 pulses) gain 5.0 dB (40 pulses)		gain -8 dB or -3 dB (1 or 2 pulses) gain -8 dB or -4.5 dB (1 or 2 pulses) gain -8 dB or -4.5 dB (1 or 2 pulses) gain -8 dB or -4.5 dB (1 or 2 pulses) ** Noise, being uncorrelated pulse-to-pulse will be subject to the same gain/loss as uncorrelated clutter.

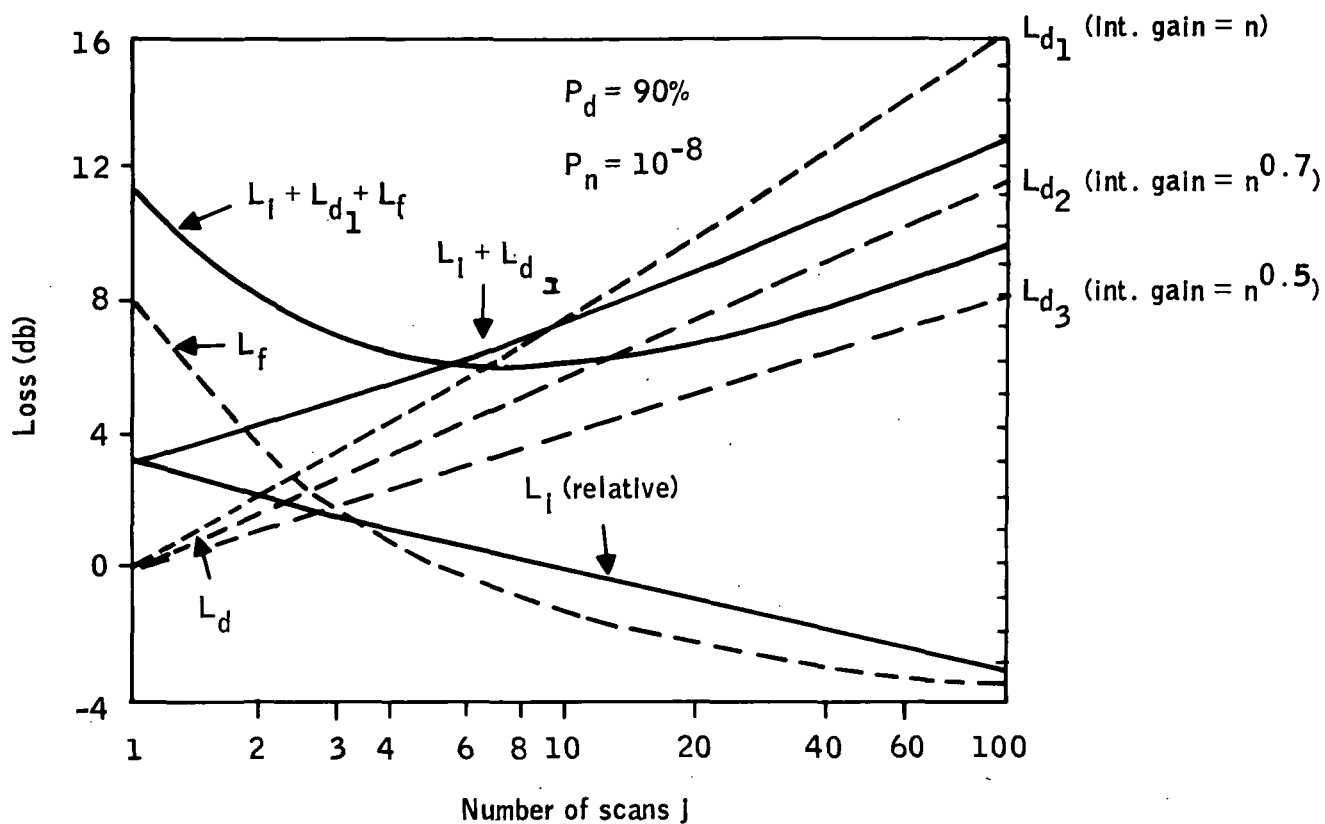


Figure 9. Scan Distribution Loss and Related Losses vs. Number of Scans

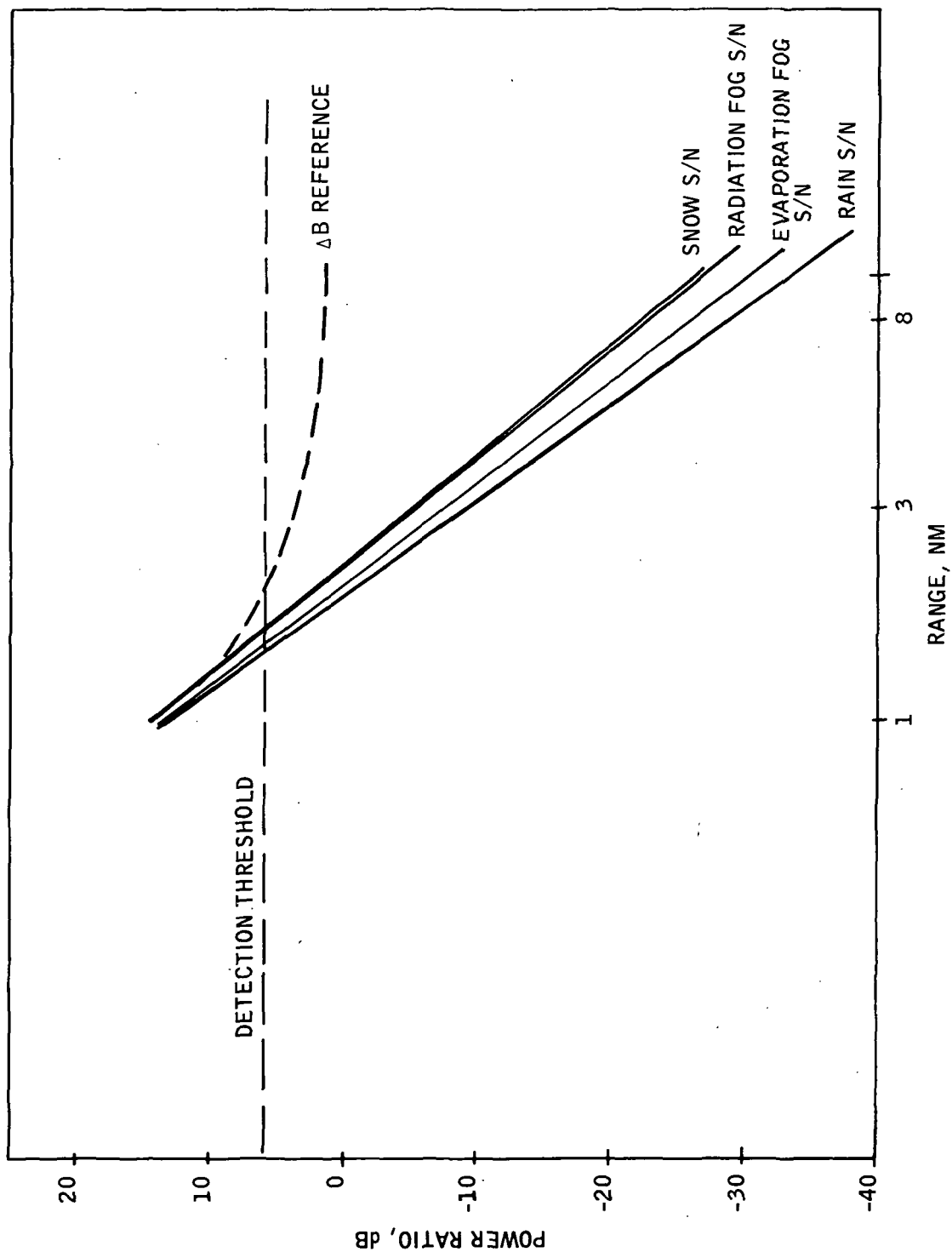


Figure 10. Summary of Power Detection Ratio $\frac{S+B_g}{C+N}$ for Marconi LN-66 Bistatic System (Minimum γ X-RADAR Modification with Circular Polarization)

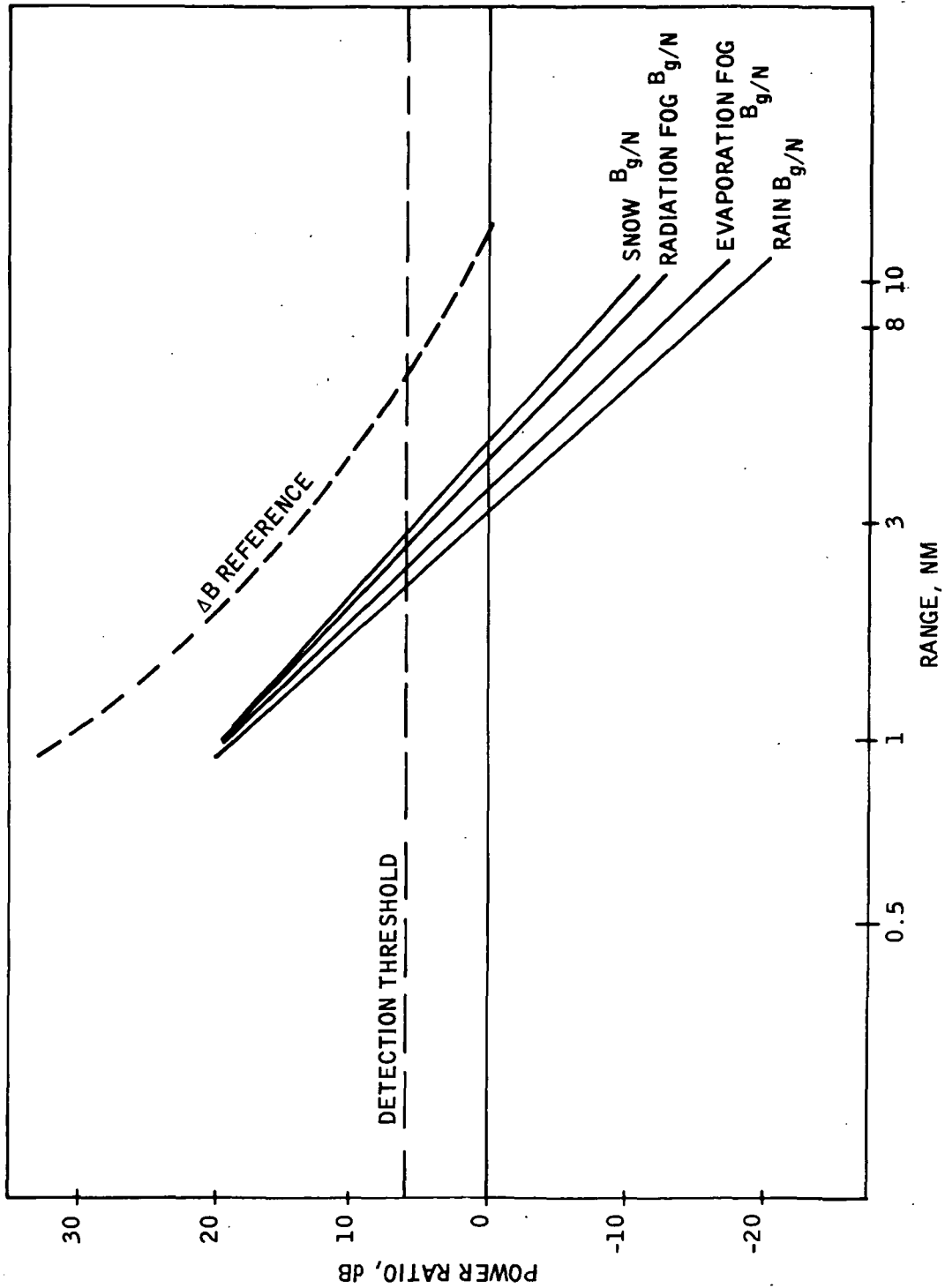


Figure 11. Summary of Power Detection Ratio $\frac{S+B_g}{C+N}$ for Marconi Bistatic System (Maximum γ)

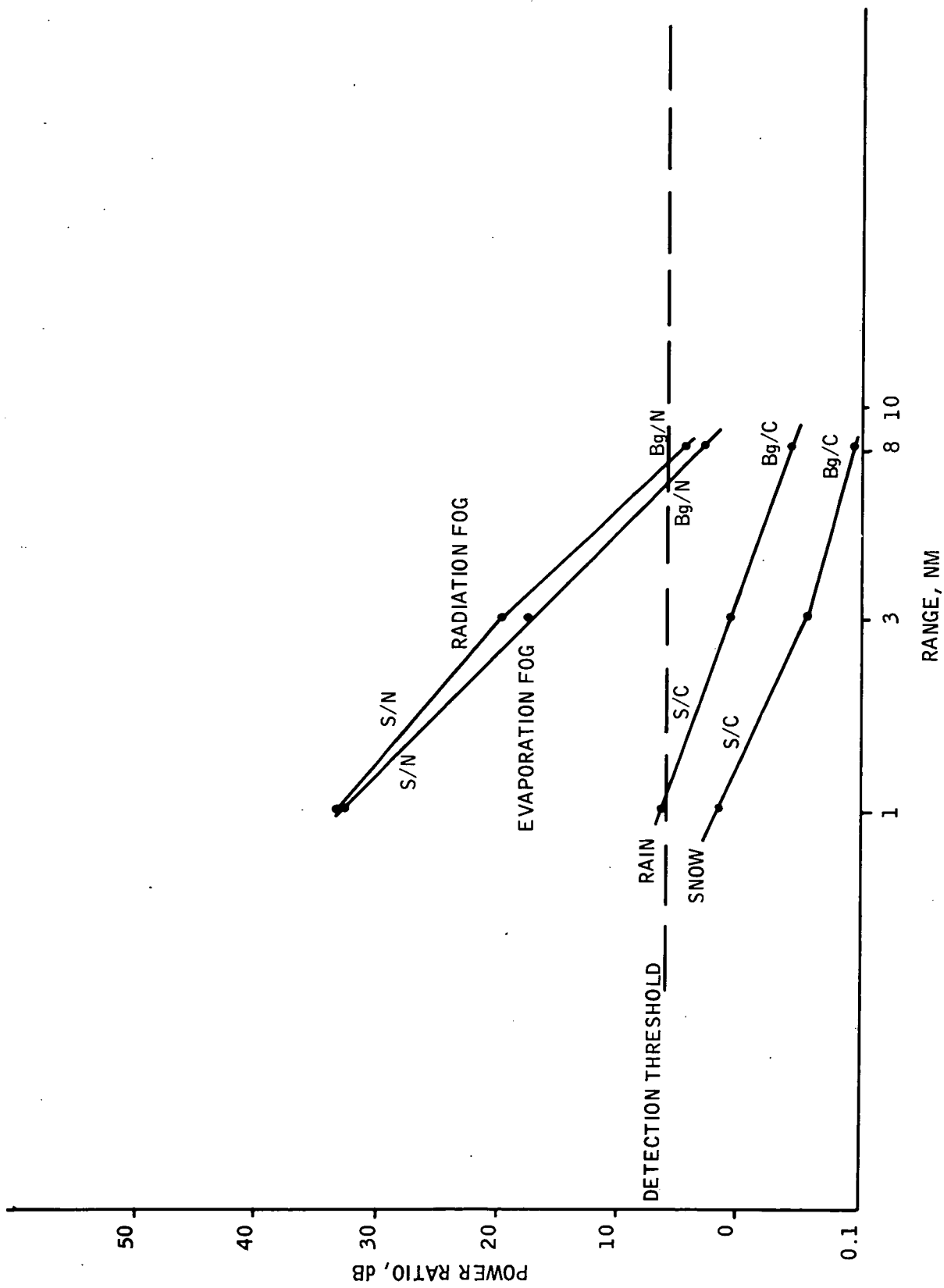


Figure 12. Summary of Power Detection Ratio $\frac{S+B_g}{C+N}$ for RCA AVQ-30X Bistatic System (Minimum γ , Circular Polarization Used)

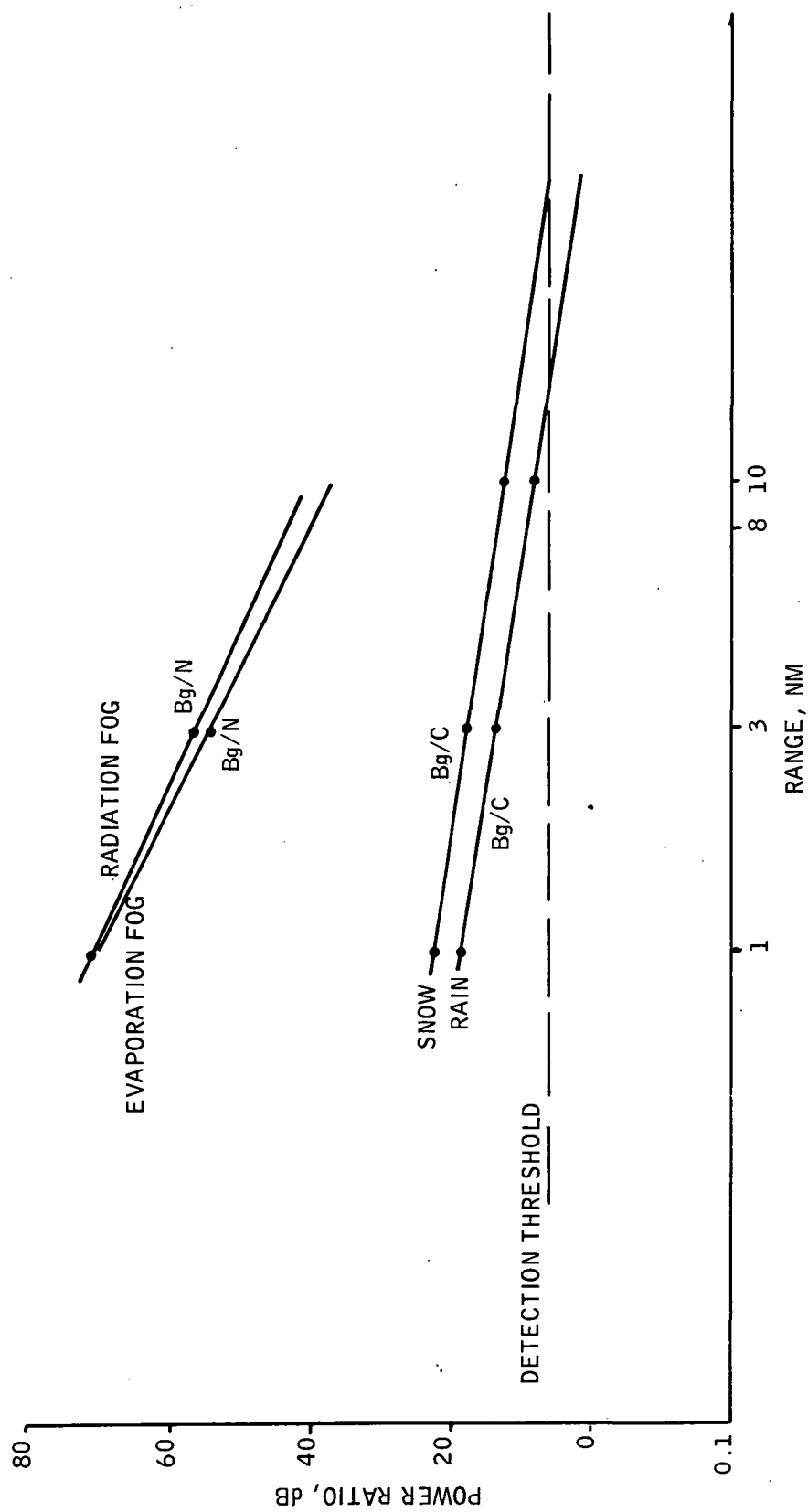


Figure 13. Summary of Power Detection Ratio $\frac{S+B_g}{C+N}$ for RCA AVQ-30X Bistatic System (Maximum γ)

2. Runway images derived by passive reflector enhancement or imaging of cultural objects such as runway lights or other objects with approximately 1 square meter scattering cross-sections can be detected with the extended detection ranges shown:

Weather	Detection Range, 23m Runway
16 mm/hr Rain	(2.6 km)
9 mm/hr Snow	(3.0 km)
Fog, zero visibility	(2.8 km)

3. Higher backscattering cross-sections allow further utilization of the high resolution capabilities of the Marconi illuminator with the array receiving system. For this case, a runway to background contrast of 35 dB was analyzed. The approximate detection ranges are:

Weather	Detection Range, 23m runway
16 mm/hr Rain	(4.1 km)
9 mm/hr Snow	(5.4 km)
Fog, zero visibility	(4.4 km)

4. The limitations above for the 23 meter runway are due to the runway to background contrast. This contrast of 35 dB is approximately the maximum allowable based on the 33 dB sidelobes measured for the array (Reference 2). Using this as the limiting case, assuming 6 dB Bg/C minimum required for detection, the maximum precipitation rates may be derived for the detection of a 23 meter runway at 1 n.mi. and 2 n.mi. These maximum rates are derived from the approximate expression $C \propto R^{1.6}$, where R is the precipitation fall rate in mm/hr. (Reference 1)

Maximum Precipitation Rates for 23 meter Runway Detection

1 NM	Rain	67 mm/hr
	Snow	59 mm/hr Equivalent Water
2 NM	Rain	20 mm/hr
	Snow	17 mm/hr Equivalent Water

COMMENTS ON ILM APPLICATION

The application of the bistatic concept as a ILM would require a system consisting of a short pulsewidth, high PRF illuminator similar to the Marconi LN-66 with a phased array receiving antenna with narrow beamwidth resolution, essentially the system proposed in Reference 2. Due to high resolution (small resolution cell) capability of the system, extensive display processing (such as with a digital scan converter) would not be beneficial since the complexity imposed by the large number of possible image locations would make a digital application very time consuming and costly in mass storage. The correlation functions of the signal returns do not indicate the potential for significant power ratio enhancement by utilizing such a processing capability beyond that which can be achieved with direct CRT display and nominal phosphor persistence to minimize flicker.

The bistatic system is shown in block diagram form in Figure 14.

The physical equipment requirements of this system are large requiring modification of existing radar equipment (if a suitable radar is available as an illuminator) or installation of a suitable radar illuminator, installation of a receiver, installation of a cockpit display subsystem, and installation of a large external receiving array with internal routing of signal information. The system obviously requires an extensive aircraft retrofit. Additionally, since the array is rigidly mounted to the aircraft, a "tie-in" to motion sensors is required to stabilize the high precision imagery. The

use of existing instrument sensors or the addition of instrument motion sensors would be necessary for accuracies of less than 1° . The list of equipment/modifications necessary for high accuracy utilization of a BISTAR-type system are listed below with their functions.

Transmitter (illuminator) (i.e., modified LN-66)

Narrow Scan	- high sample rate
Narrow Pulsewidth	- high resolution
High PRF	- short range, high sample rate
Staggered PRF or Pulse-to-Pulse Frequency Agility	- interference suppression
Narrow Beamwidth (a few degrees)	- interference and sidelobe suppression

Weather Radar Modification (i.e., AVQ-30X modification)

Decrease Scan Limits	- increases sample rate
Decrease Pulsewidth	- decrease clutter cell size
Increase PRF (coordinated with decreased pulsewidth to provide the same duty cycle)	- increase sample rate
Staggered PRF or Frequency Agile Transmitter	- enhances interference suppression

Receiver

L.O. Locked to Transmitter	- maximize received signal
Heterodyning performed at Array	- minimize RF loss
Fast Receiver Blanking	- minimize nearest effective range and protection of components
Manual and/or Automatic Gain, Threshold, and Linearity Controls	- optimize receiver to scenario

Array, Receiving (at least 20 to 30 elements)

Electronically Phase Scanned and Focused	- highest scan rates and resolution
Wing Mounted (underside)	- maximize array length

Directional Elements	- higher gain and interference immunity
Thinned Array Element Spacing matched to Transmitting Antenna	- suppresses receiving pattern grating lobe ambiguities

Display and Processor

Direct CRT Display for High Pulse Rates	- near real-time
Perspective Display	- real-world similarity
Stabilized Display	- more accurate viewing, less "jitter" and "ghosting"

Mutual interference effects are reduced by using staggered pulses or a frequency agile transmitter and the highly directional antennas. The very small backscattering cross-sections (-40 to -60 dBSM) typical of highly specular surfaces (e.g., concrete, asphalt, snow) will necessitate a large dynamic range for the receiver such that direct interference signals do not disrupt the reception of following cultural returns. With sufficient dynamic range, the cultural returns will integrate to effectively reduce the sporadic interference effects.

The production costs of the bistatic radar (Figure 1) are based on use of a standard weather radar, such as the RCA AVQ-30X with small modifications for adding a second mode of operation, and the addition of the thinned array antenna. Projected cost of the X-band radar with modifications is \$30,000. Cost of the thinned array antenna is \$1,000 per element including phase shifters and phase shifting logic. For the 32-element antenna, this corresponds to \$32,000. Total cost per aircraft for this ILM concept is estimated at \$62,000.00. This concept is totally contained on the aircraft with no additional ground system costs. Estimated weight of the airborne system is 82 kgms. It should be noted that approximately \$25,000 of this figure could be attributed to the weather radar mode. Aircraft installation costs were not estimated. A major cost add-on for this system is the non-recurring installation design costs for each specific aircraft type to install a thinned array antenna in the wings.

ANALYSIS OF SPACE DIVERSITY INTERFEROMETERS FOR ILM

INTRODUCTION

A space diversity interferometer utilizes a number of interferometer pairs spaced different distances from the multipath sources. Since multipath-caused errors in an interferometer can be positive or negative depending on the path length difference between the direct and multipath signal, averaging the results over multiple interferometer pairs can yield an increase in accuracy over that obtainable with a single interferometer.

The particular application being analyzed here is the MADGE system, developed by the MEL Equipment Co. Ltd, Sussex, England. It utilizes a space diversity interferometer to obtain elevation data, a standard interferometer with a special array ambiguity resolution technique to obtain azimuth, and a pulse DME to obtain range. The previous analysis of Independent Landing Monitor techniques employing interferometers (Reference 1) concluded that they could not be used, due to the extreme phase distortions caused by multipath reflections. These distortions prevented correct ambiguity resolution of a long baseline interferometer with a short baseline interferometer, since the short baseline unit did not have enough accuracy to determine the correct grating lobe of the long baseline unit.

By using an array of interferometer pairs, and recursively resolving ambiguities from a shorter baseline to a slightly longer baseline, correct ambiguity resolution can be obtained for arrays of any length. Further reduction in multipath caused errors can then be obtained by averaging the results of interferometers at different positions.

Since the previous analysis showed that specular multipath was the major problem with interferometry, it is the only area addressed in this analysis.

Various flight paths and terrain scenarios were used to establish different multipath situations. Specific parameters for the various situations are given in following discussion.

ANALYSIS

The primary effort in this analysis was directed toward the creating of a computer program general enough to handle the MADGE space diversity array and to create multipath situations which could challenge its capabilities. The previous analysis (Reference 1) showed that only specular multipath prevented interferometry from being effective, so specular multipath was the only factor considered in this report.

A detailed description of the MADGE concept is contained in Reference 4. Only key factors will be repeated here.

A. MADGE Parameters

The MADGE system consists of three interferometer arrays, one for azimuth and two for elevation.

The azimuth array consists of seven horn antennas, spaced such that a pair of antennas is available with spacings increasing in a 2:1 ratio from $\frac{1}{2}$ wavelength to 16 wavelengths.

The azimuth angle data is derived completely from the 16 wavelength long interferometer. All the other antenna pairs are used to resolve ambiguities. Assuming a high signal to noise ratio, ambiguities can be correctly resolved assuming multipath phase distortion remains less than 60° with a 2 to 1 ratio interferometer array.

The main elevation array consists of eight antennas arranged in a linear vertical array with 3.6 wavelengths between antennas. Since the main array has a 5 degree grating lobe width, a smaller array is also provided. It is a linear array of four antennas with a 1.8 wavelength spacing providing unambiguous angle measurement to 25.6 degrees elevation.

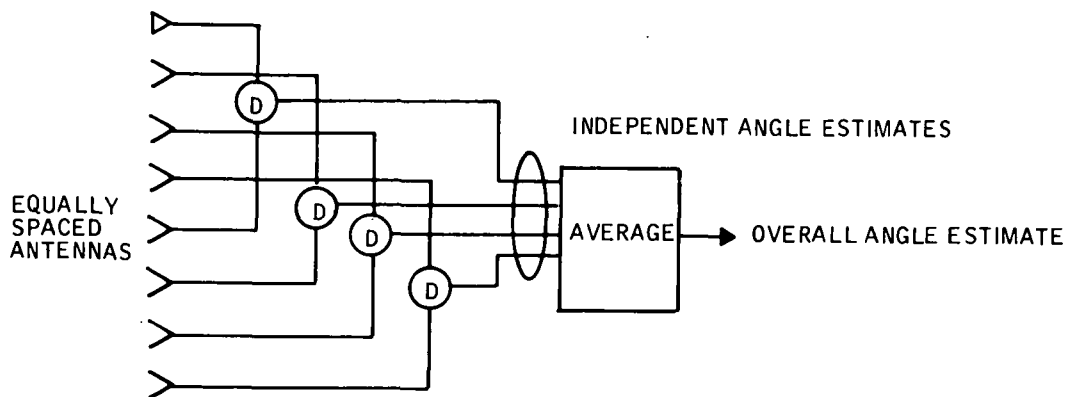


Figure 15. Effective Elevation Array Connection

The elevation angle data is the average of the estimates from 4 pairs of interferometers as shown in Figure 15. Figure 15 does not represent the actual connection of the equipment, but rather the manner in which the information is used. The array is divided into 4 pairs, each pair with a separation of 14.4 wavelengths between antennas. Ambiguity resolution is accomplished first by using the data from the antennas as a recursive array using the 3.6 separation to resolve the 7.2, then using the 7.2 to resolve the 10.8, etc., and by using an additional array with smaller spacing to resolve the ambiguities in the 3.6 wavelength interferometer. This technique will correctly resolve ambiguities in the presence of multipath phase distortions up to 90° . Assuming this condition to be met, each of the four pairs provides an independent measurement with different multipath. The average of the 4 measurements may therefore be better than any individual measurement.

Other equipment parameters are given in Table 8.

B. Software Scenario

The software described in Appendix B was exercised for fifteen different situations (Table 9). The first twelve are related to the elevation

TABLE 8

MADGE SYSTEM PARAMETERS

Band	C-Band
Frequency	12 channels from 5-5.25 GHz interferometer for angle measurement, pulse DME for range measurement, ground derived and data linked.
Power	200 watts
Bandwidth	3 MHz
Minimum Operating SNR	15 dB
Size	<p>Aircraft Unit</p> <p>2 - 3/8 ATR short</p> <p>8 Kg</p> <p>Ground Unit</p> <p>Azimuth Antenna</p> <p>1.5 M x .3 M x .4 M</p> <p>38 Kg</p> <p>Elevation Antenna</p> <p>1.9 M x .4 M x .3 M</p> <p>40 Kg</p> <p>Transponder</p> <p>.6 M x .3 M x .4 M</p> <p>23 Kg</p>

Table - 9 Scenario Test Situations

<u>RUN</u>	<u>TYPE</u>	<u>FOCUSSED</u>	<u>ENVIRONMENT</u>	<u>ARRAY CONFIGURATION</u>
1	Elevation	No	Figure 16	Standard MADGE
2	Elevation	Yes	Free Space	Standard MADGE
3	Elevation	Yes	Figure 16	Standard MADGE
4	Elevation	Yes	Figure 16	Standard MADGE
5	Elevation	Yes	Figure 16	Standard MADGE
6	Elevation	Yes	Figure 17	Standard MADGE
7	Elevation	Yes	Figure 17	Standard MADGE
8	Elevation	Yes	Figure 17	Standard MADGE
9	Elevation	Yes	Figure 17	Standard MADGE
10	Elevation	Yes	Figure 17	Stuffed Array
11	Elevation	Yes	Figure 17	Stuffed Array
12	Elevation	Yes	Figure 17	Extended Array
13	Elevation	Yes	Figure 17	Extended Array
14	Azimuth	Yes	Figure 18	Simple Interferometer
15	Azimuth	Yes	Figure 19	Simple Interferometer
15	Azimuth	Yes	Figure 19	Elevation Array Rotated 90°

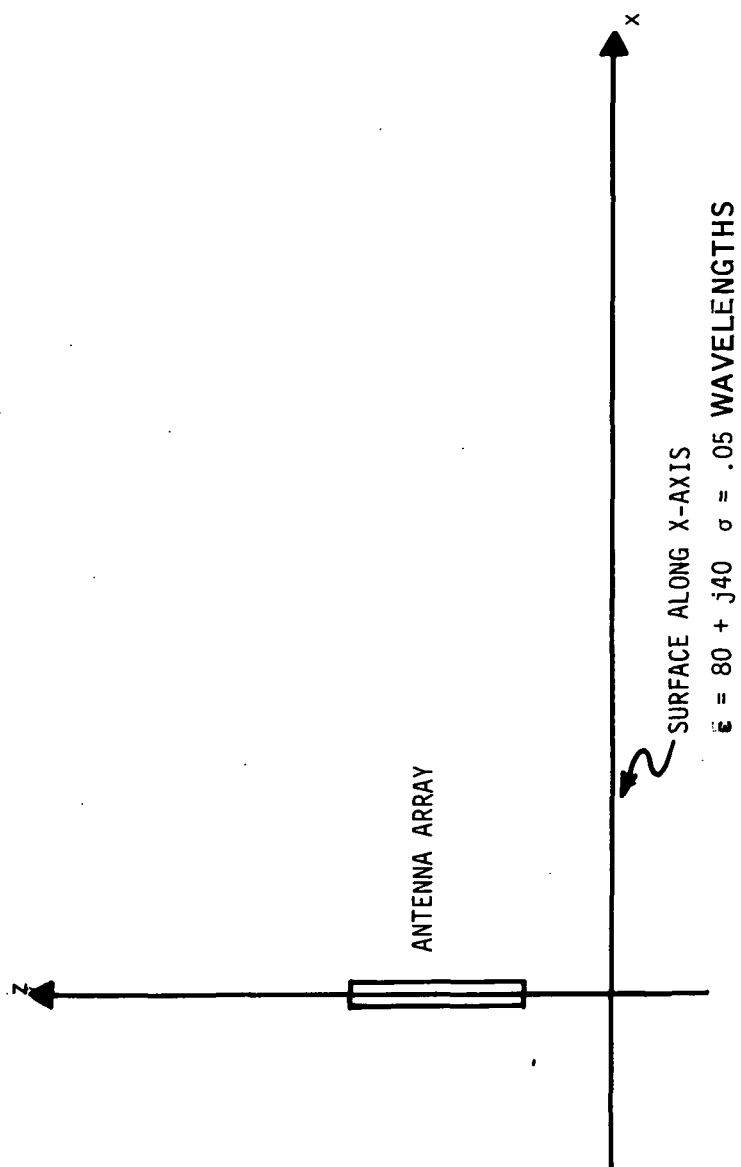


Figure 16. Flat Surface

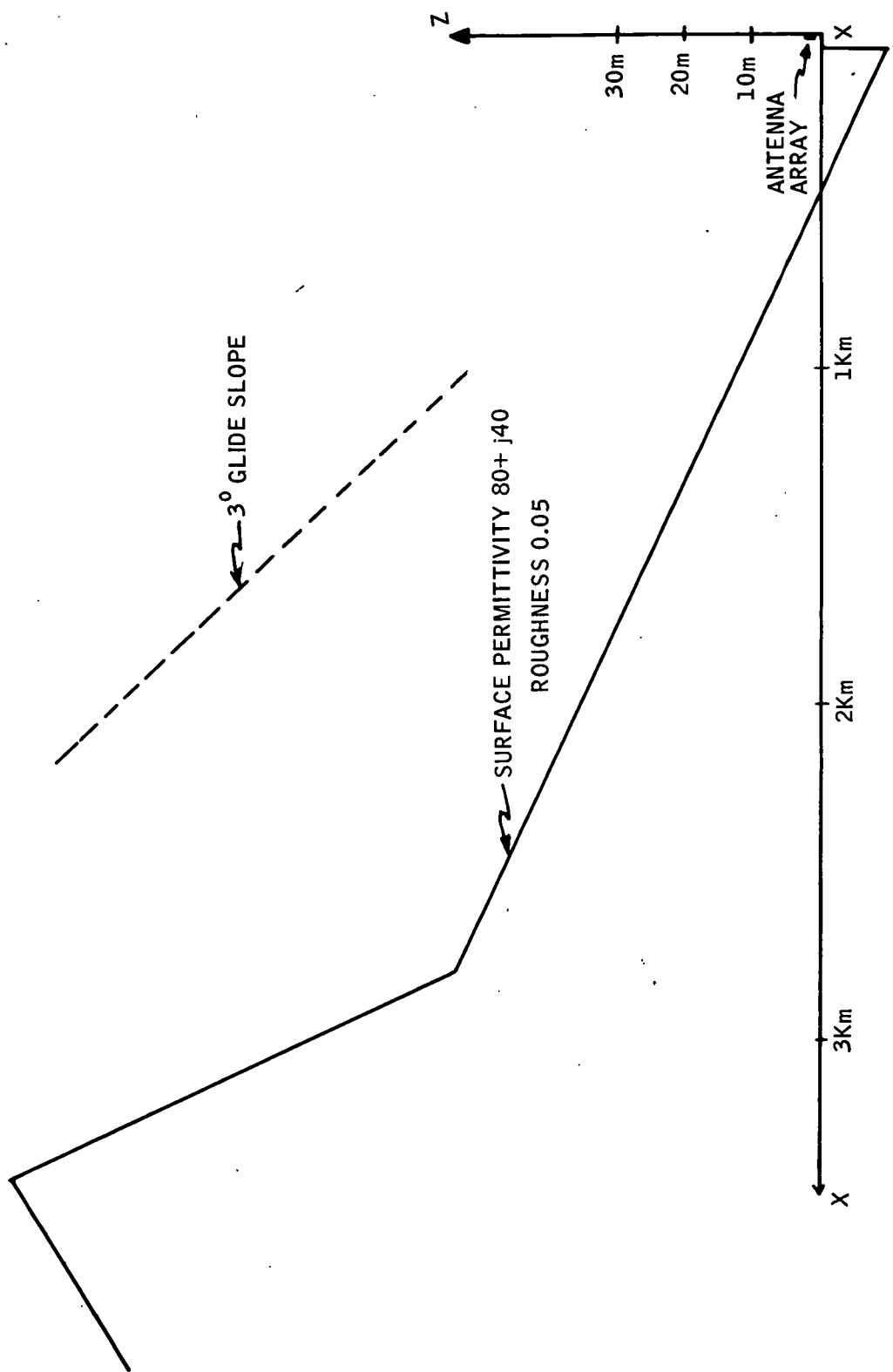


Figure 17. Samoa Airport

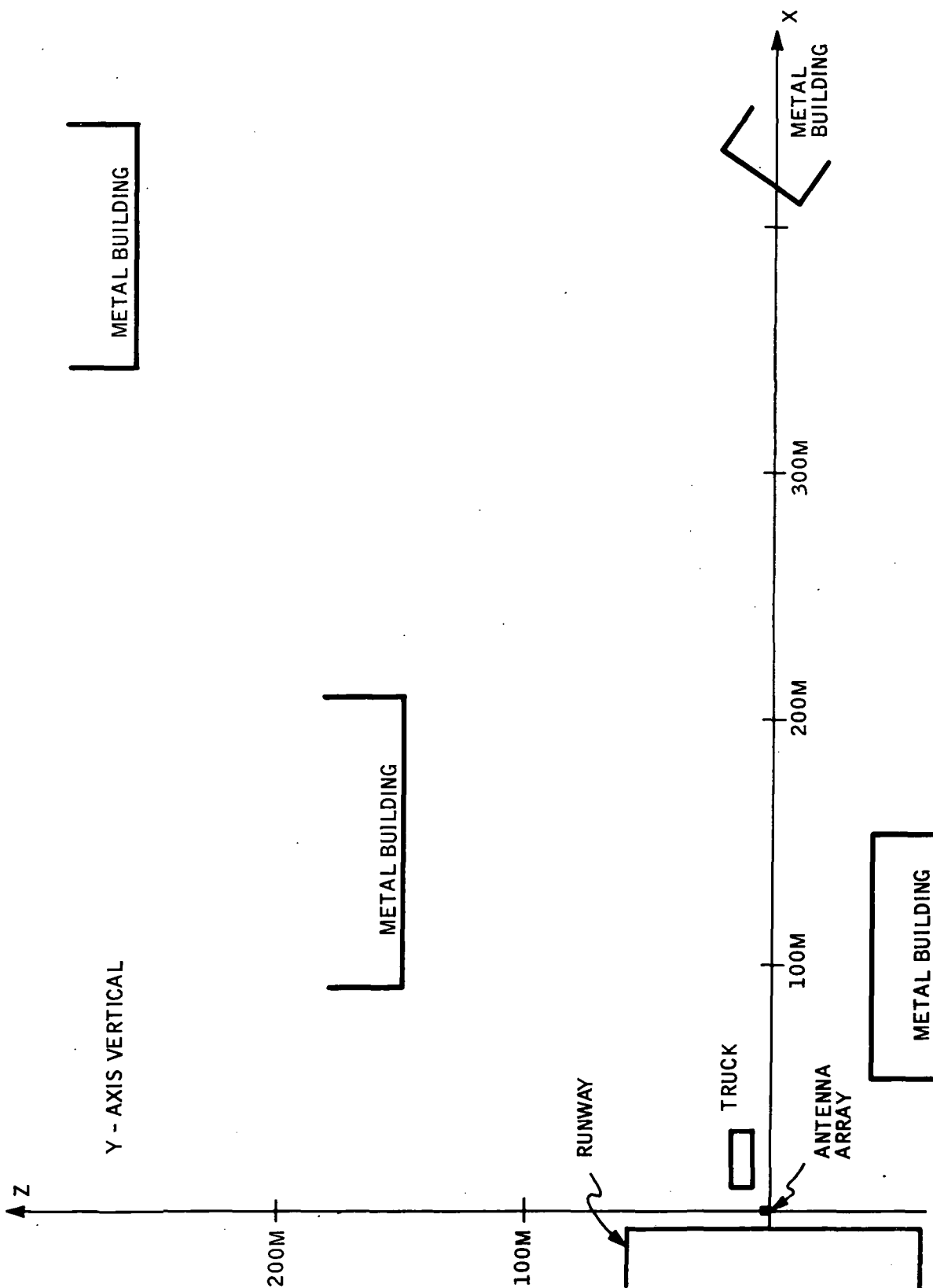


Figure 18. Hangar Scenario

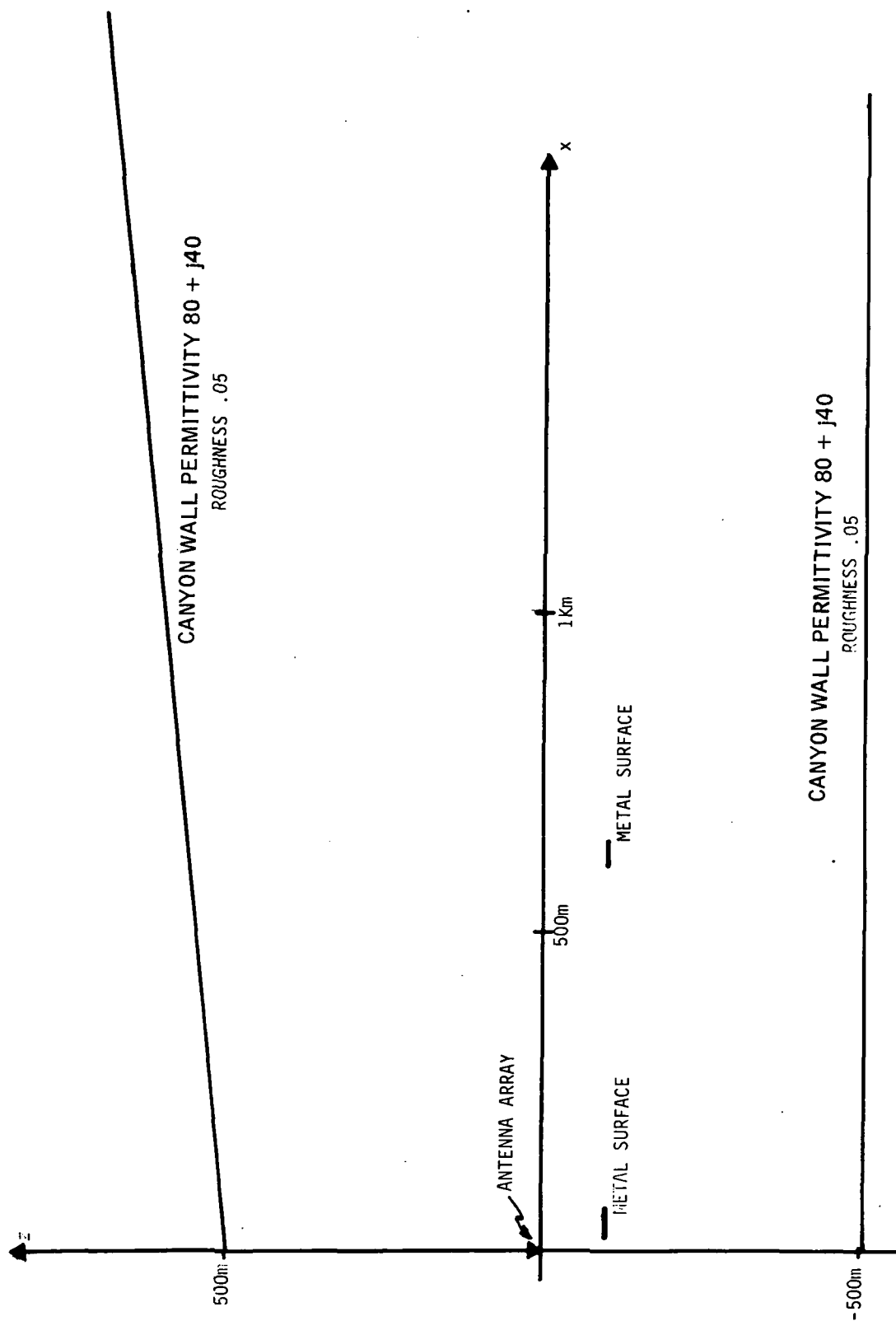


Figure 19. Box Canyon or Fjord

array and the last three are related to the azimuth array. Each run is divided into two segments, the first from a range of 5000m to 1000m, the second segment from 1000m to 20m.

Runs 1, 3, 4, and 5 were done using a rough flat surface, of permittivity $80 + j 40$ and surface RMS deviation of .05 wavelengths. Run 2 had no multipath and is a check on residual errors. Runs 6 through 12 use the actual approach path to Pago Pago airport in Samoa, and is an attempt to provide an extreme multipath situation. Run 13 is a hangar scenario where the aircraft approaches between rows of hangars, and is the situation which MEL claims to have tested its equipment in. Run 14 is an imaginary box canyon or fjord, with two aircraft on a taxiway in front of the system. Both run 13 and run 14 are extreme multipath situations. Run 15 is the box canyon environment again, using a space diversity array in place of the MADGE azimuth unit.

Three pages of output are provided for each run. The first page provides the setup of the system and the environment. The data titled "ANTENNA PAIRS" is the height of each antenna above the reference plane in meters. FLIGHT PATH SEGMENTS provides the starting and ending coordinates of the aircraft in meters relative to the reference coordinates. On those pages where the setup for two runs is made, the first two columns of flight path data refer to the first run number, and the second two columns refer to the second run number. Any surfaces which could cause multipath have their parameters listed under the heading "REFLECTING SURFACES". The second page of the output is a plot of angular error in radians versus range in meters from 5000m to 1000m. The third page is a similar plot from 1000m to 20m. These plots are automatically scaled by the computer routine, and thus the long range and short range data usually have different scales.

C. Analytical Considerations

The program developed for this analysis computes the effect of specular

reflections on a space diversity interferometer of up to ten pairs of antennas, for up to ten flight path segments, with up to ten reflecting surfaces. The program description is given in Appendix B.

Simple large target reflection is all that is considered. At each increment of each flight path segment for each surface and each antenna, a computation is made to determine whether or not a point exists on the surface such that the angle of incidence from the aircraft equals the angle of reflection to the antenna. If such a point exists, the rough surface modified complex Fresnel reflection coefficient is computed, and used in the determination of that surface's contribution to multipath errors. If no such point exists within the bounds of the surface, no multipath contribution from this surface (for this antenna at this increment on the flight path) is computed. All surfaces are assumed to lie normal to the plane of interferometer operation, i.e., for the azimuth interferometer, all surfaces are assumed vertically oriented and of infinite extent in the vertical direction. In the plane of operation, surfaces are represented by a line segment.

Diffraction is ignored, except that no test of blockage of a surface reflection by another surface is performed. Hence, some diffraction effects are included unintentionally.

The analysis mechanized in the program is basically the technique described in Reference 1 under the section Azimuth Channel Multipath, with a few modifications. Logic is included to average the errors over an array, and actual reflection coefficients are computed. Since a range estimate is available, provision for focusing of the interferometer array is included as an option. Focusing compensates for the spherical nature of arriving wavefronts, and the displacement of the individual interferometer pairs from the reference datum and each other.

Reflected signal strengths are modified by the ratio of the direct range to the antenna from the aircraft to the range via the reflecting surface,

the magnitude of the reflection coefficient, and the ratio of the antenna pattern in the direct direction to the pattern in the direction of the reflected ray. A very simple approximation to the antenna pattern was used, since the only available data was the 3dB beamwidth. The patterns used are shown in Figures 20 and 21. Polarization is assumed to be vertical relative to the surface of the earth at the point of reflection.

A total vector sum of the field strengths at each antenna is computed, and an estimate of physical angle is made, using a focused or unfocused algorithm as specified by the data and assuming ambiguity resolution can be properly obtained. This angle is compared to the actual (physical) angle, and the resulting error is output.

D. Evaluation (See pages 71 through 111 for computer runs)

Run 1

The first run is the basic MADGE elevation array measuring an aircraft on a 3° glide slope in an environment consisting of a single flat reflecting surface. The results show that multipath distortions are smoothed quite well, but errors of up to 7.5 mrad are still present. These errors occur at short ranges of 200 m or less. Thus, with careful siting this could be acceptable.

Run 2

The focused algorithm was run without any multipath distortions to determine the residual errors inherent in using range to the antenna rather than range to the reference point and errors due to truncation in the computer. The results show errors on the order of a few micro-radians, so the program was judged acceptable.

Run 3, 4 and 5

The next three runs are the focused MADGE elevation array operating in a flat reflecting surface environment, measuring aircraft on 1° , 3° , and 6° glide slopes for runs 3, 4 and 5 respectively.

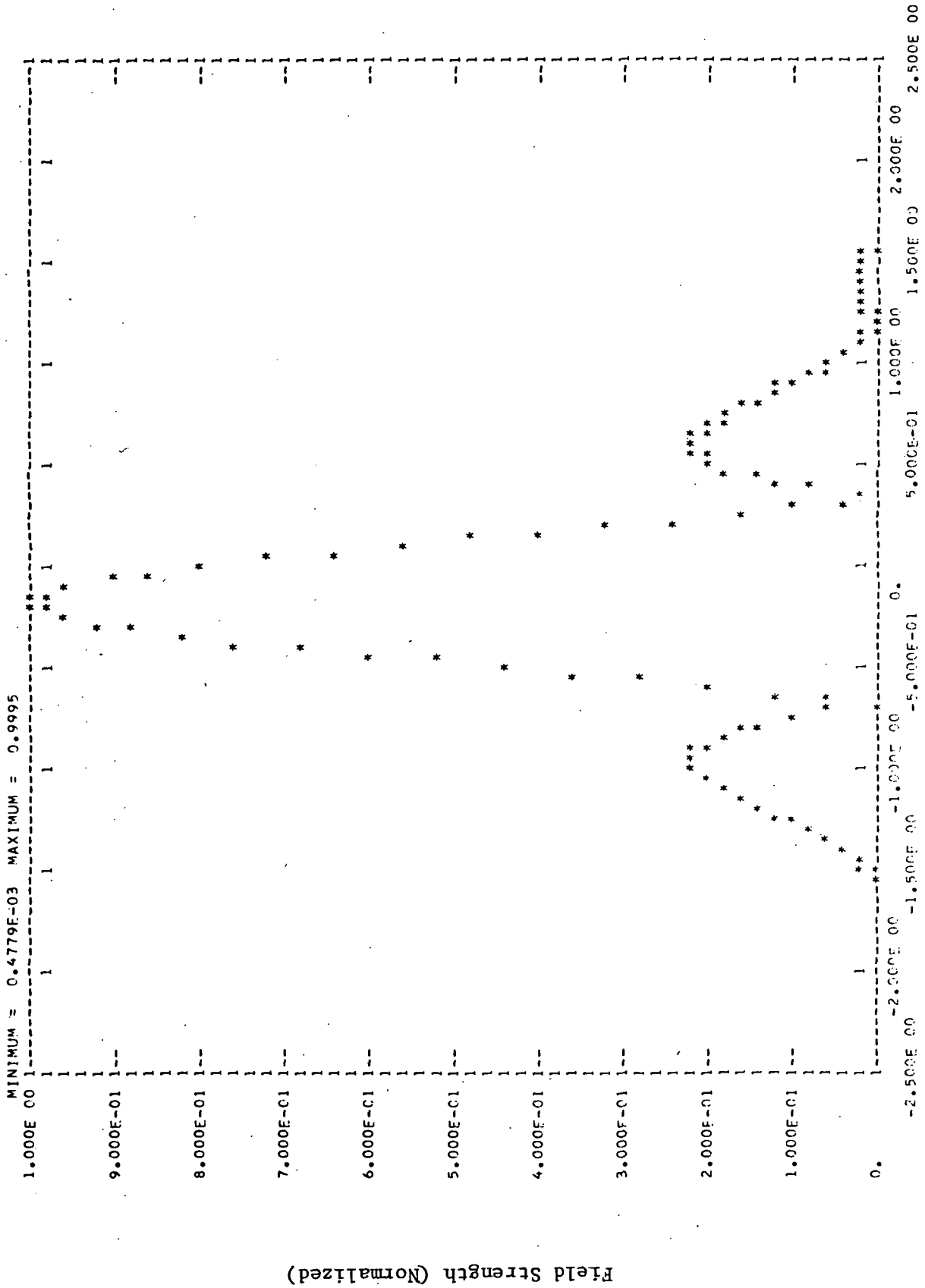


Figure 20. Antenna Field Pattern Plot
Vertical Array

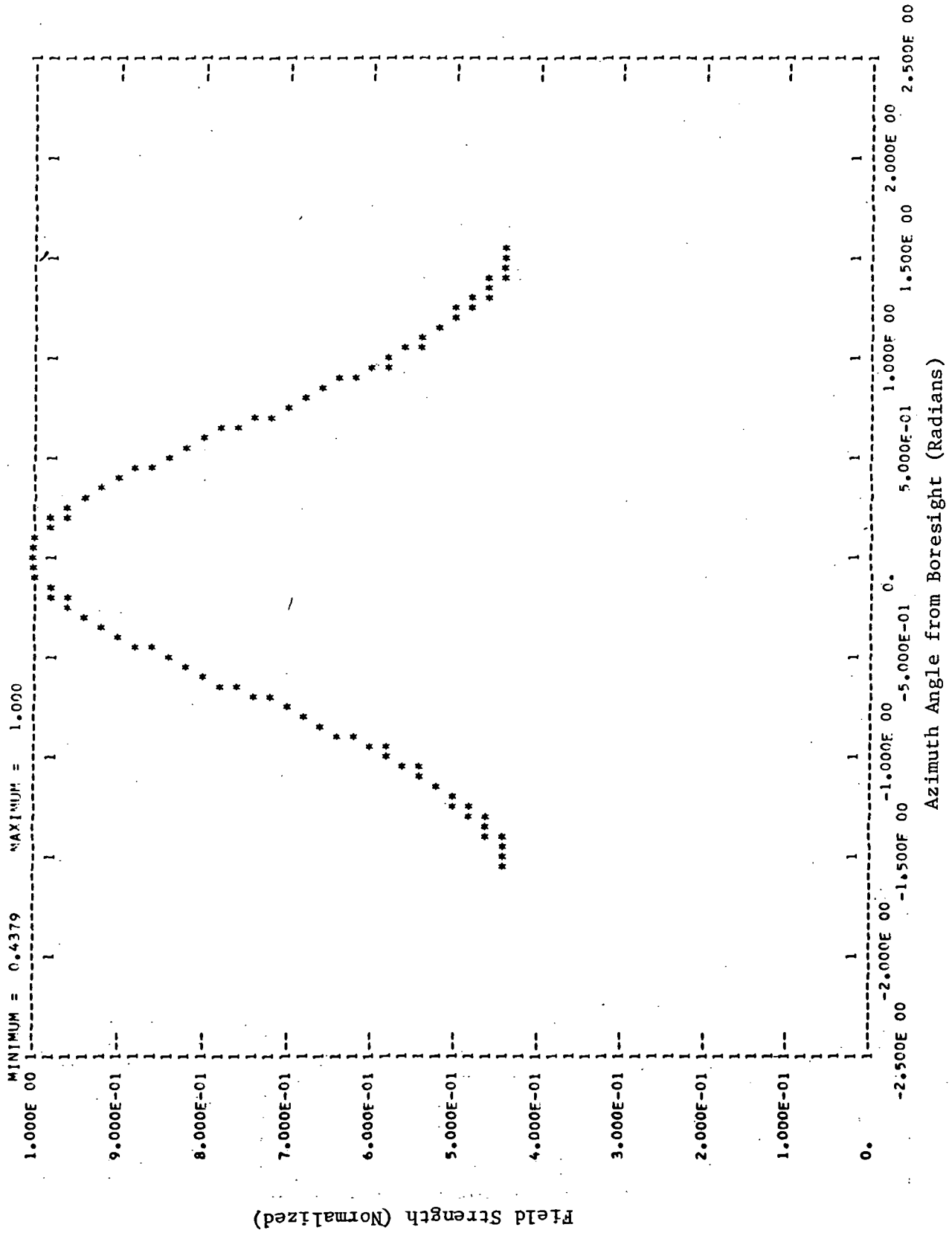


Figure 21. Antenna Field Pattern Plot Horizontal Array

The results are as could be expected in that at very low elevation angles which correspond to high reflection coefficients and inability to obtain any reduction in multipath signal strength via antenna patterns, the errors are highest, running about 10 mrad at 1° , 2.5 mrad at 3° , and less than 1 mrad at 6° , all at long range.

The runs at 1° and 6° show an increasing error at short range. These runs were offset 55m to the side of the elevation array however, and the magnitude of the error is similar to the difference between the elevation angle from the reference datum at the base of the interferometer array and the elevation angle from a reference point at the intersection of the ground with the flight path. That this is a purely geometrical effect is shown by the 3° run, which has no offset. In the 3° run, the errors decrease with decreasing range as the incidence angle to the reflecting surface becomes greater and the antenna pattern becomes more effective in reducing the multipath signal strength.

Runs 6, 7 and 8

The runs use the MADGE elevation array in the Samoan airport scenario at elevation angles of 1° , 3° , and 6° . Although a 1° glide slope is not possible at this airport, those surfaces which would interfere with a 1° glide slope are excluded from reflecting by the specular angle logic included in the program, so that for the 1° case the situation is effectively an airport with a 10m cliff at the approach end of the runway. In all of these runs, the aircraft flight path is offset 55m from the elevation array horizontally.

In run 6, the long range data shows a small error. The multipath indicators show that only surface number 2 is reflecting, so this is to be expected. In the short range data, both surface 1 and surface 2 are reflecting and oscillations in the multipath error of ± 10 mrad are observed in the data.

Runs 7 and 8 show oscillations in the multipath errors on the order of 1.2 mrad, which is still within the specification. In addition, the geometrical effects of the offset are again observed.

Runs 9 and 10

Runs 9 and 10 are again the Samoa airport at 3° and 6° glide slopes. The interferometer used here is a MADGE array, stuffed with 8 more antennas (4 more pairs) in between the antennas of the basic MADGE. The results are almost identical to runs 7 and 8, so this is not an effective modification.

Runs 11 and 12

For runs 11 and 12, four additional antennas were added to the top of the elevation array, and antenna pairs are defined as every sixth antenna rather than every fourth antenna as in the existing MADGE system. Run 11 is a 1° glide slope and Run 12 is a 3° glide slope. Some improvement in accuracy can be noted relative to runs 6 and 7.

Run 13

Run 13 was made with a single interferometer pair in azimuth. This is effectively the configuration used by the MADGE system, as all the remaining antennas are used only for ambiguity resolution. The multipath scenario consisted of 4 hangars near the interferometer and a truck.

At long range, the data is very good on the order of microradians. The multipath indicators show that none of the objects are influencing the measurement. At short ranges, various objects are reflecting over part of the path, and oscillations of ± 18 mrad are shown in the data. However, these oscillations correspond to phase distortions of ± 100 degrees. Since, for proper resolution of ambiguities, the MADGE azimuth array cannot tolerate phase errors greater than ± 60 degrees, the MADGE azimuth unit could not operate in this scenario.

Run 14

Run 14 was also made with a single interferometer pair, with a scenario representing a box canyon or fjord.

The results are similar to run 11, except that the multipath problem exists at all ranges. Rapid oscillations in measurement error of ± 18 mrad occur over the entire flight path. As with run 11, errors of this magnitude cannot be accommodated by the ambiguity resolution technique so that actual error would be much larger, on the order of several degrees due to improper ambiguity resolution.

Run 15

Run 15 is an identical environment to run 14, but the basic MADGE elevation array is turned on its side to use as an azimuth unit in place of the regular interferometer MADGE uses in azimuth.

Oscillatory errors on the order of ± 13 mrad exist in the data. The significant difference from Run 14 is that the space diversity array can function properly with errors this large, whereas the regular interferometer cannot.

RESULTS

Space diversity has been shown to be an effective technique for the reduction of specular multipath errors in an interferometer. The MADGE elevation array shows errors of less than 10 mrad even in severe multipath conditions when operated as a focused array. The current MADGE system is apparently operated in an unfocused manner, but range estimates to allow focusing could be made available with minor change in system operation. The 10 mrad error exceeds the allowable 1.2 mrad error for a MLS elevation unit, but is close enough that further effort on the array would probably yield an acceptable system.

Two fixes were attempted.

- o Stuffing the array with additional antennas, keeping the spacing between antennas of a pair constant.

- o Extending the array by 4 more antennas, maintaining the array spacing constant and thereby increasing the spacing between antennas of a pair by a ratio of 3/2.

Stuffing the array did not yield any improvement in performance. Extending the array provided a slight increase in accuracy, bounding the error below 7.5 mrad rather than 10 mrad. Thus, neither of these particular fixes are sufficient to provide Category III performance in a severe multipath environment.

The MADGE azimuth unit does not utilize space diversity for multipath protection. In the cases examined, which were severe multipath situations, the azimuth unit had errors large enough to cause ambiguity resolution errors. The azimuth unit does have some multipath protection, and would probably be adequate in a less severe environment. It would be better to use a space diversity array similar to the elevation unit to insure operation in any multipath environment.

In the box canyon environment, an elevation type array operated as an azimuth showed better performance, holding peak errors to 13 mrad rather than the 18 mrad of the normal MADGE azimuth unit. More importantly, the space diversity array is capable of providing correct ambiguity resolution in the presence of multipath distortions of this magnitude, whereas the standard MADGE azimuth is not.

In all cases using a space diversity array, large multipath errors tend to be highly oscillatory with a mean error much smaller than the peaks of the oscillation. Since no filtering is employed in the computation of these multipath errors, it is likely that the errors could be reduced to a much more acceptable value if filtering were employed. For example, in the case of the extended elevation array at a 1° glide slope in the Samoan airport environment, the peak errors are about ± 7.5 mrad, whereas the mean error is .02 mrad. Errors on the order of .02 mrad are certainly acceptable multipath error components.

SNUMR = GID05. ACTIVITY # = 01. REPORT CODE = 12. RECORD COUNT = 000270

ANTENNA PAIRS

UPPER	1.22	1.40	1.58	1.76	0.	0.	0.	0.	0.
LOWER	0.50	0.68	0.86	1.04	0.	0.	0.	0.	0.

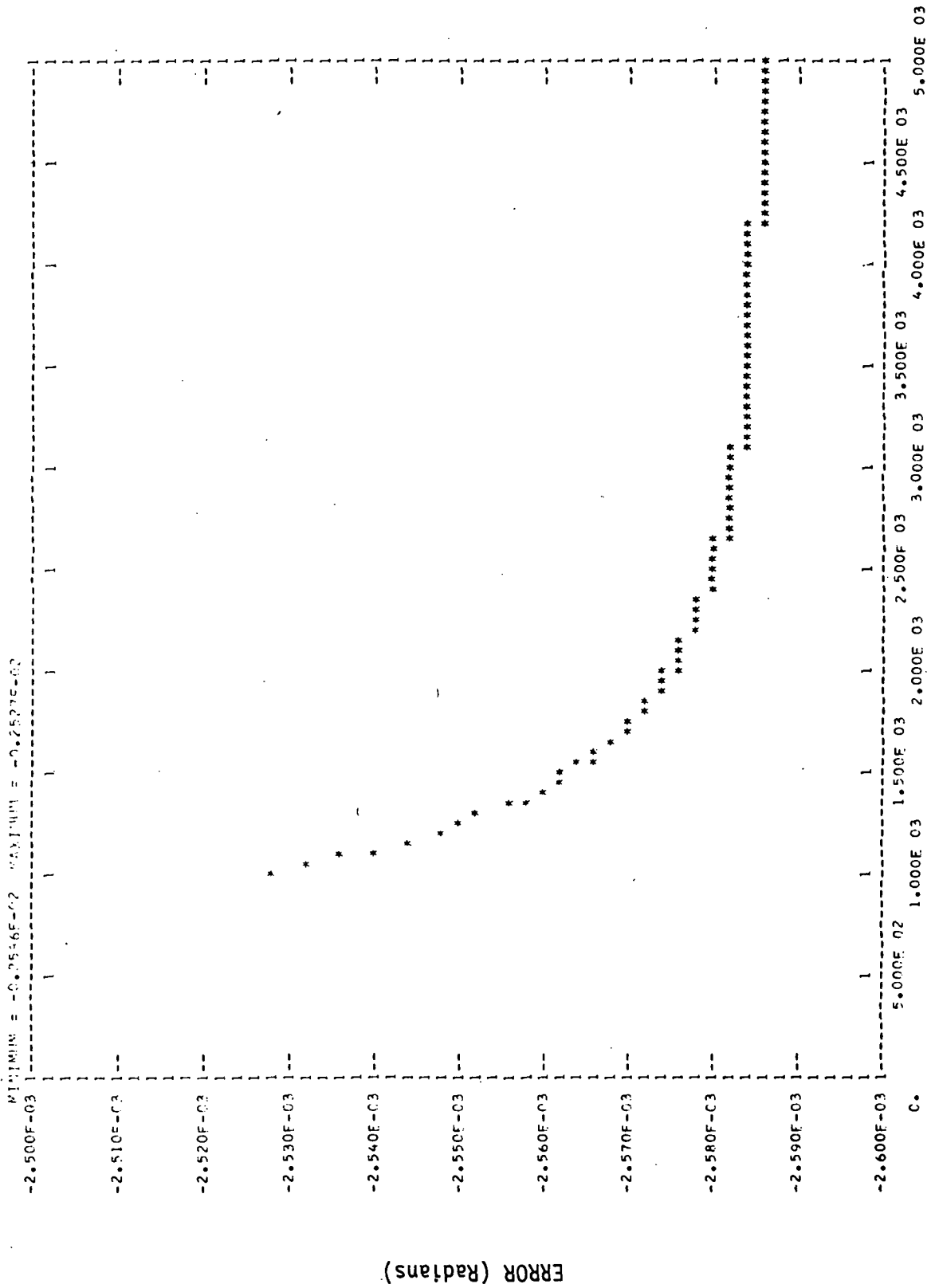
AIRCRAFT FLIGHT PATH SEGMENTS

X AT START	0.499E 04	0.999E 03	0.	0.	0.	0.	0.	0.	0.
Y AT START	0.550E 02	0.550E 02	0.	0.	0.	0.	0.	0.	0.
Z AT START	0.262E 03	0.523E 02	0.	0.	0.	0.	0.	0.	0.
X AT FINISH	0.999E 03	0.200E 02	0.	0.	0.	0.	0.	0.	0.
Y AT FINISH	0.550E 02	0.550E 02	0.	0.	0.	0.	0.	0.	0.
Z AT FINISH	0.523E 02	0.105E 01	0.	0.	0.	0.	0.	0.	0.
NUMBER OF INCREMENTS	50	50	0	0	0	0	0	0	0

REFLECTING SURFACES

SURFACE NUMBER	STARTING COORDINATES	ENDING COORDINATES	PERMITTIVITY	ROUGHNESS
1	-0.10000E 03	0.60000E 04	0.80000E 02	0.50000E-01
2	0.	0.	0.	0.
3	0.	0.	0.	0.
4	0.	0.	0.	0.
5	0.	0.	0.	0.
6	0.	0.	0.	0.
7	0.	0.	0.	0.
8	0.	0.	0.	0.
9	0.	0.	0.	0.
10	0.	0.	0.	0.

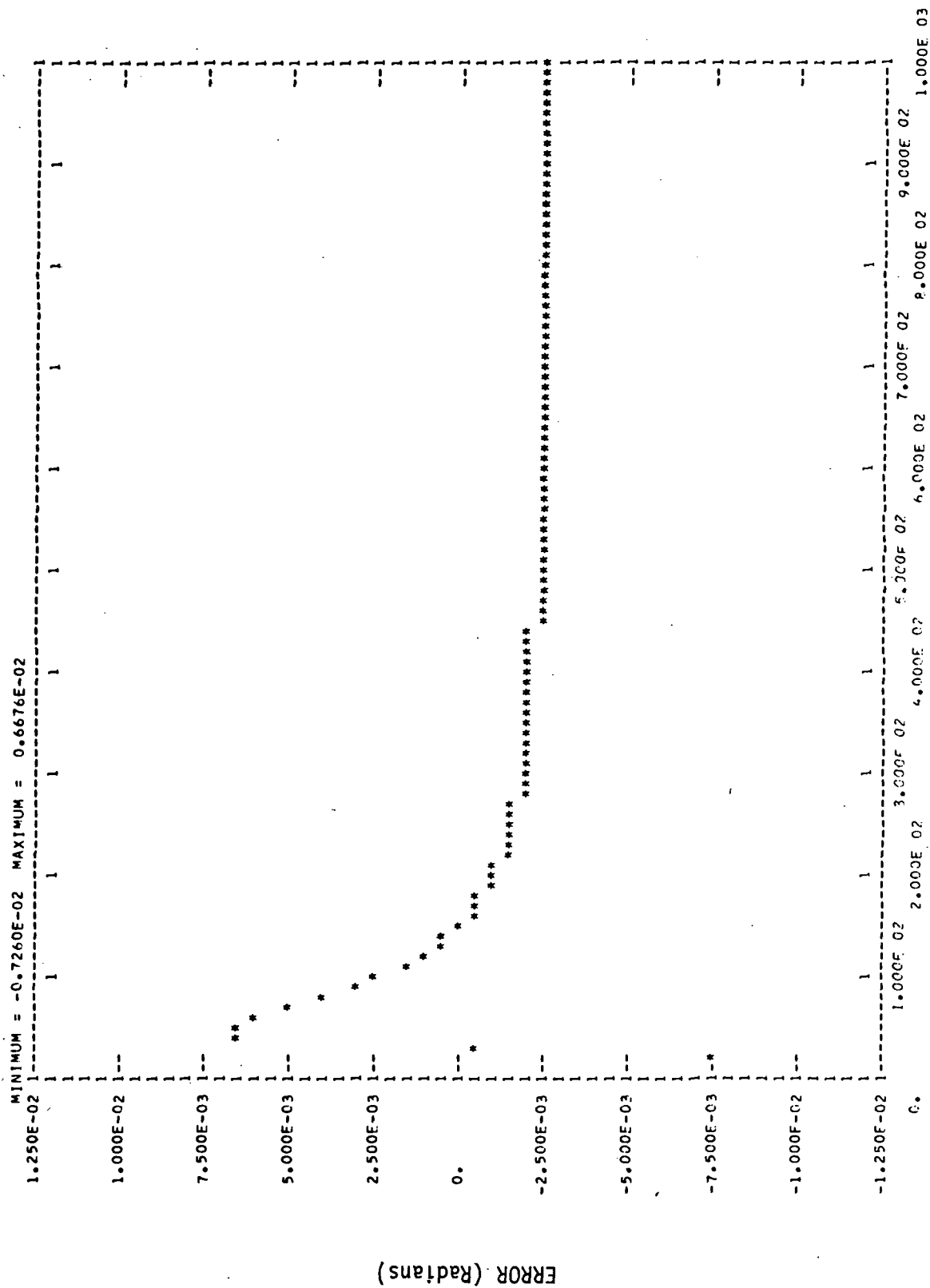
PLOT OF ANGULAR ERROR VERSUS RANGE



RANGE (Meters)

RUN 1

PLOT OF ANGULAR ERROR VERSUS RANGE

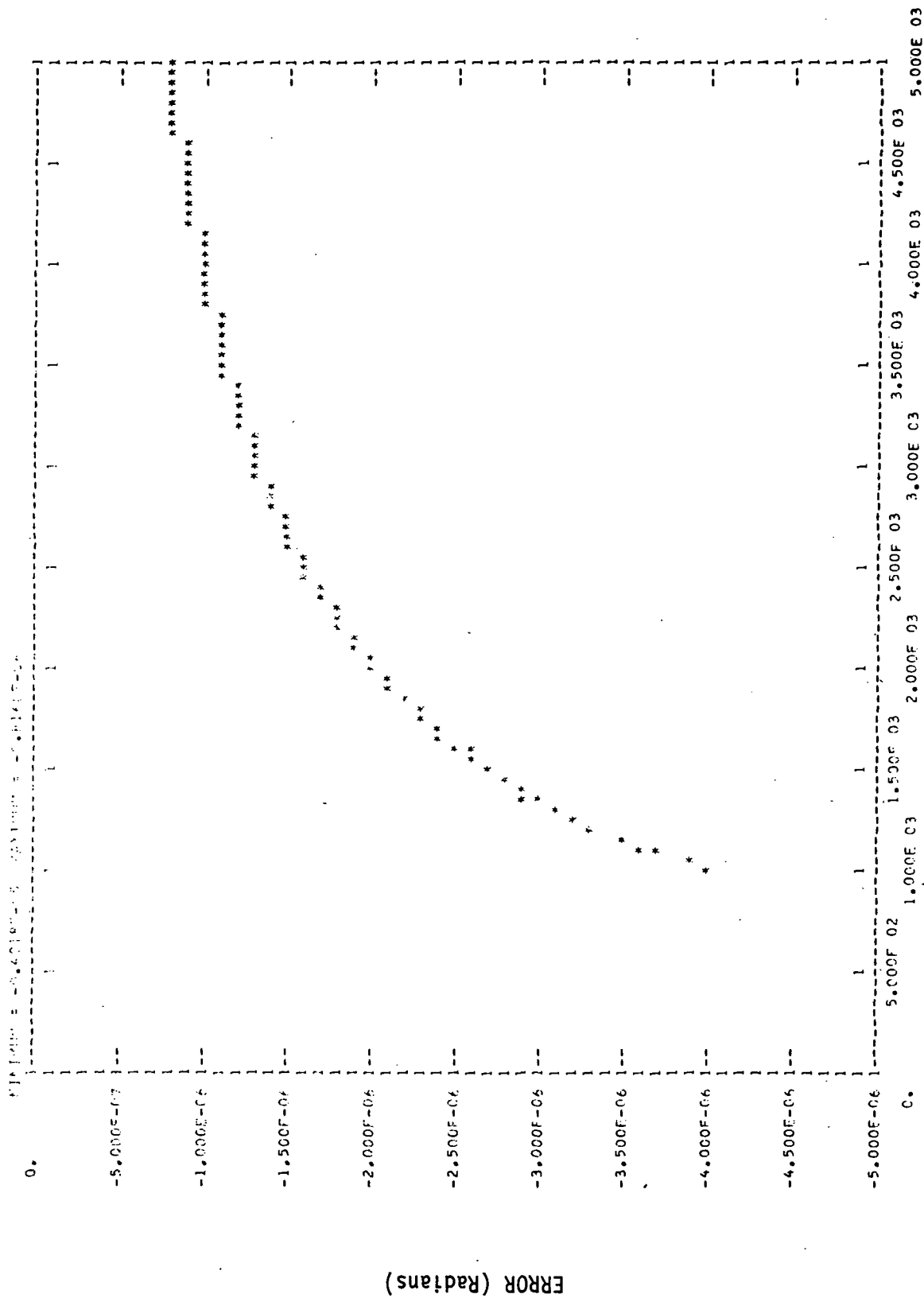


RANGE (Meters)

RUN 1

RUN 2

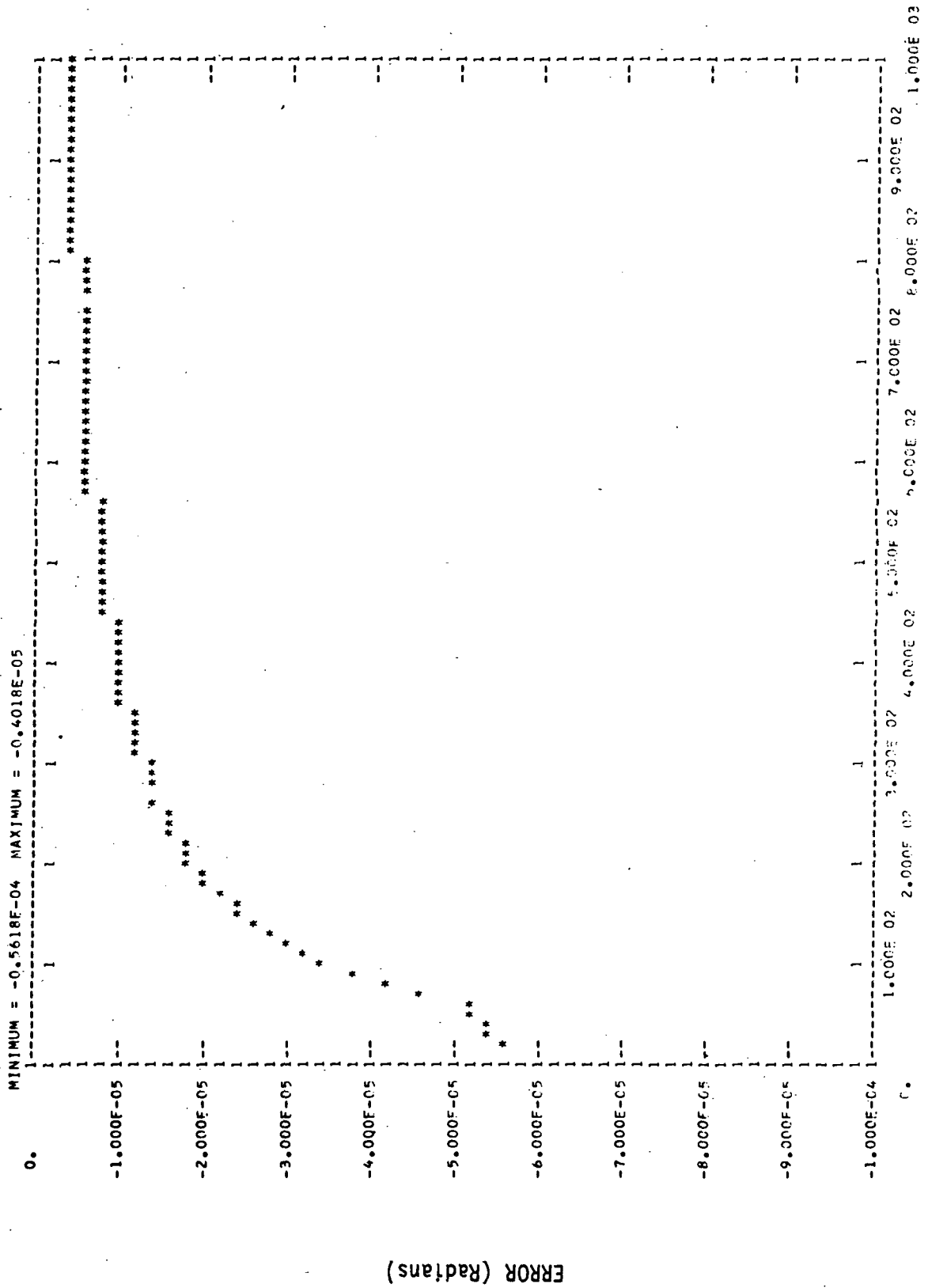
PLOT ANGULAR ERROR VERSUS RANGE



RANGE (Meters)

RUN 2

PLOT OF ANGULAR ERROR VERSUS RANGE



RANGE (Meters)

RUN 2

ERROR (Radians)

SNUPR = DED00, ACTIVITY # = 01, REPORT CODE = 12, RECORD COUNT = 000514

ANTENNA PAIRS

	1.22	1.40	1.58	1.76	0.	0.	0.	0.	0.	0.
UPPER	0.50	0.68	0.86	1.04	0.	0.	0.	0.	0.	0.
LOWER										

AIRCRAFT FLIGHT PATH SEGMENTS

	0.500E 04	0.100F 04	0.497E 04	0.995E 03	0.	0.	0.	0.	0.	0.
X AT START	0.550E 02	0.550E 02	0.550E 02	0.550E 02	0.	0.	0.	0.	0.	0.
Y AT START	0.873E 02	0.175E 02	0.523E 03	0.105E 03	0.	0.	0.	0.	0.	0.
Z AT START	0.100E 04	0.200F 02	0.995E 03	0.199E 02	0.	0.	0.	0.	0.	0.
X AT FINISH	0.550E 02	0.550E 02	0.550E 02	0.550E 02	0.	0.	0.	0.	0.	0.
Y AT FINISH	0.175E 02	0.349E 00	0.105E 03	0.209E 01	0.	0.	0.	0.	0.	0.
Z AT FINISH										
NUMBER OF INCREMENTS	50	50	50	50	0	0	0	0	0	0

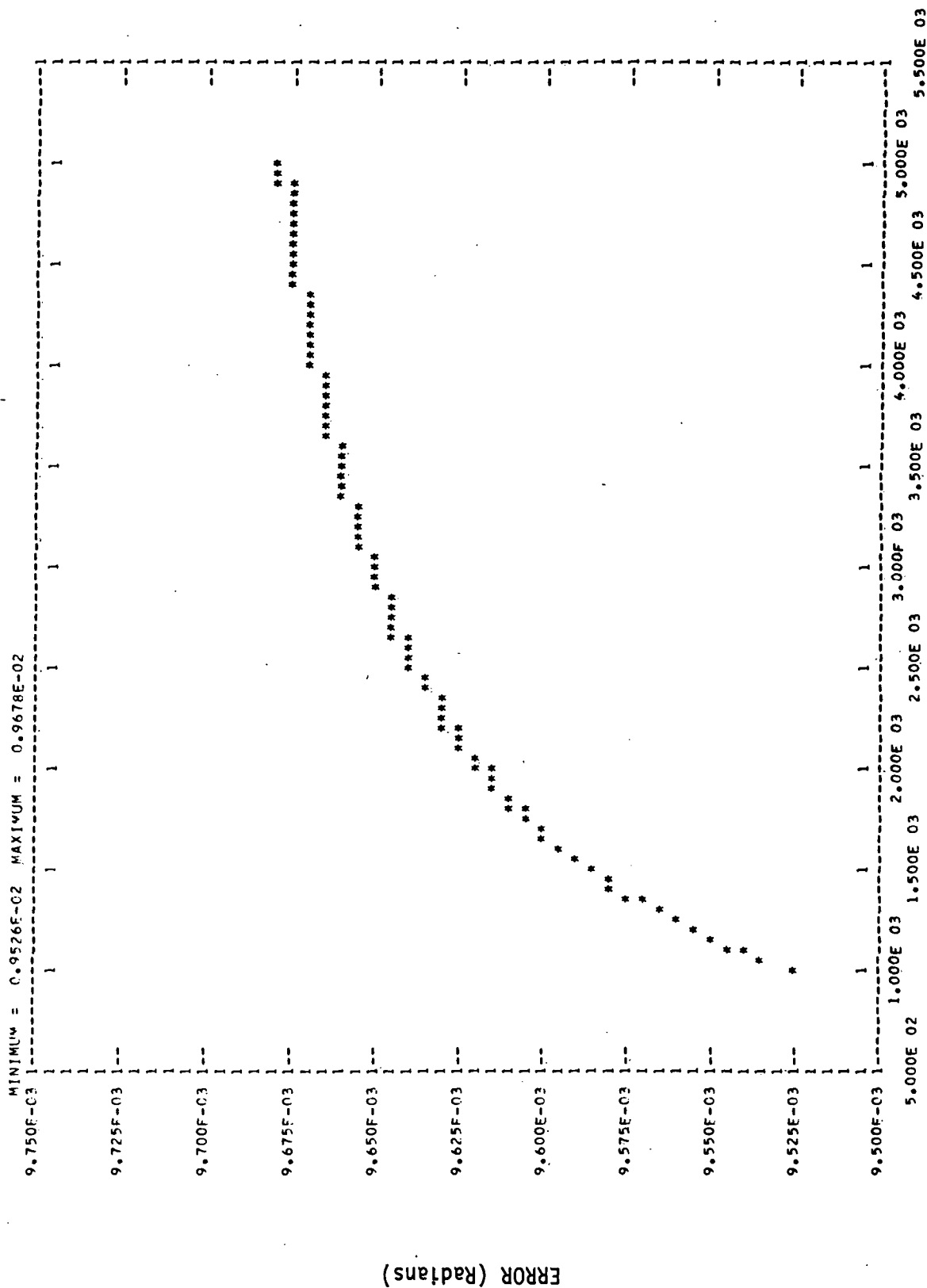
REFLECTING SURFACES

SURFACE NUMBER	STARTING COORDINATES			ENDING COORDINATES			PERMITTIVITY	ROUGHNESS
	X	Y	Z	X	Y	Z		
1	-0.10000E 02	0.	0.	0.60000E 04	0.	0.	0.80000E 02	0.40000E 02
2	0.	0.	0.	0.	0.	0.	0.	0.50000E-01
3	0.	0.	0.	0.	0.	0.	0.	0.
4	0.	0.	0.	0.	0.	0.	0.	0.
5	0.	0.	0.	0.	0.	0.	0.	0.
6	0.	0.	0.	0.	0.	0.	0.	0.
7	0.	0.	0.	0.	0.	0.	0.	0.
8	0.	0.	0.	0.	0.	0.	0.	0.
9	0.	0.	0.	0.	0.	0.	0.	0.
10	0.	0.	0.	0.	0.	0.	0.	0.

RUN 3 Segments 1 & 2

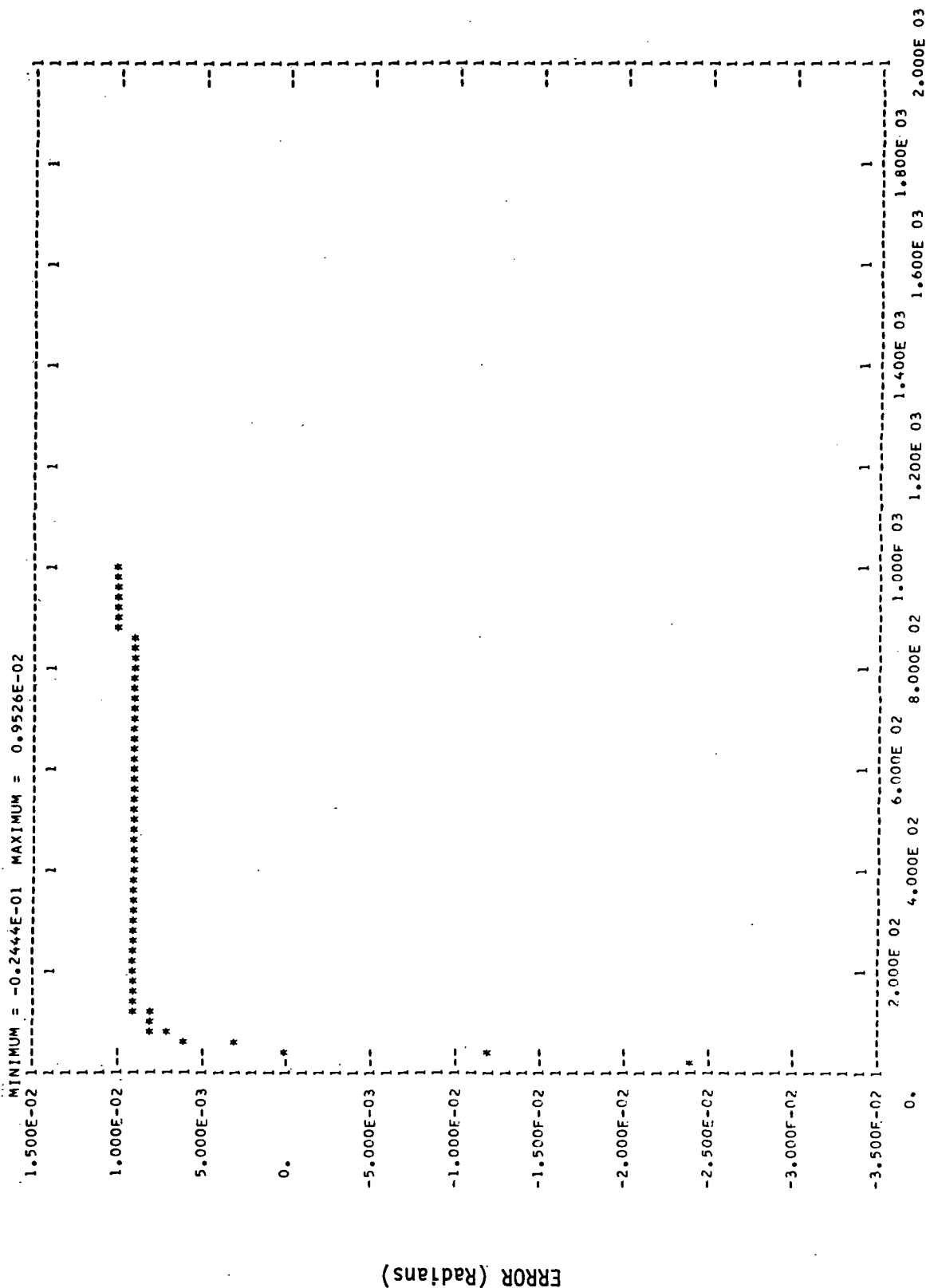
RUN 5 Segments 3 & 4

PLOT OF ANGULAR ERROR VERSUS RANGE



RANGE (Meters)
RUN 3

PLOT OF ANGULAR ERROR VERSUS RANGE



RANGE (Meters)
RUN 3

SNUMR = GID05, ACTIVITY # = 01, REPORT CODE = 12, RECORD COUNT = 000270

ANTENNA PAIRS

	UPPER	1.22	1.40	1.58	1.76
LOWER	0.50	0.68	0.86	1.04	1.22

AIRCRAFT FLIGHT PATH SEGMENTS

	X AT START	0.499E 04	0.999E 03	0.
Y AT START	0.	0.	0.	0.
Z AT START	0.262E 03	0.523E 02	0.	0.
X AT FINISH	0.999E 03	0.200E 02	0.	0.
Y AT FINISH	0.	0.	0.	0.
Z AT FINISH	0.523E 02	0.105E 01	0.	0.
NUMBER OF INCREMENTS	50	50	50	50

REFLECTING SURFACES

SURFACE STARTING COORDINATES

SURFACE NUMBER	STARTING COORDINATES			ENDING COORDINATES			Z
	X	Y	Z	X	Y	Z	
1	-0.10000E 03	0.	0.	0.60000E 04	0.	0.	0.
2	0.	0.	0.	0.	0.	0.	0.
3	0.	0.	0.	0.	0.	0.	0.
4	0.	0.	0.	0.	0.	0.	0.
5	0.	0.	0.	0.	0.	0.	0.
6	0.	0.	0.	0.	0.	0.	0.
7	0.	0.	0.	0.	0.	0.	0.
8	0.	0.	0.	0.	0.	0.	0.
9	0.	0.	0.	0.	0.	0.	0.
10	0.	0.	0.	0.	0.	0.	0.

PERMITTIVITY

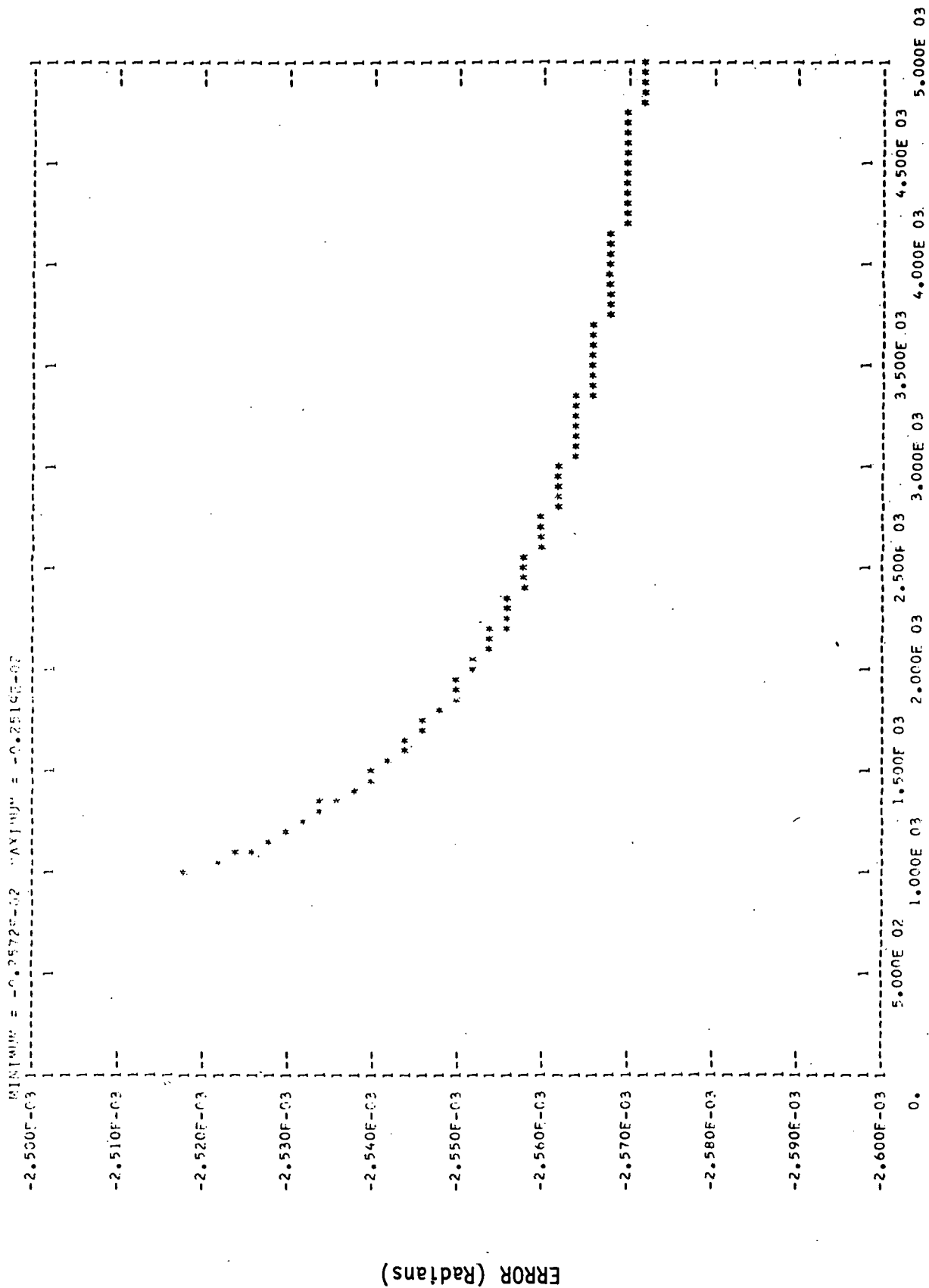
ROUGHNESS

	0.80000E 02	0.40000E 02	0.50000E-01
0.	0.	0.	0.
0.	0.	0.	0.
0.	0.	0.	0.
0.	0.	0.	0.
0.	0.	0.	0.
0.	0.	0.	0.
0.	0.	0.	0.
0.	0.	0.	0.
0.	0.	0.	0.
0.	0.	0.	0.

0.
0.
0.
0.
0.
0.
0.

0

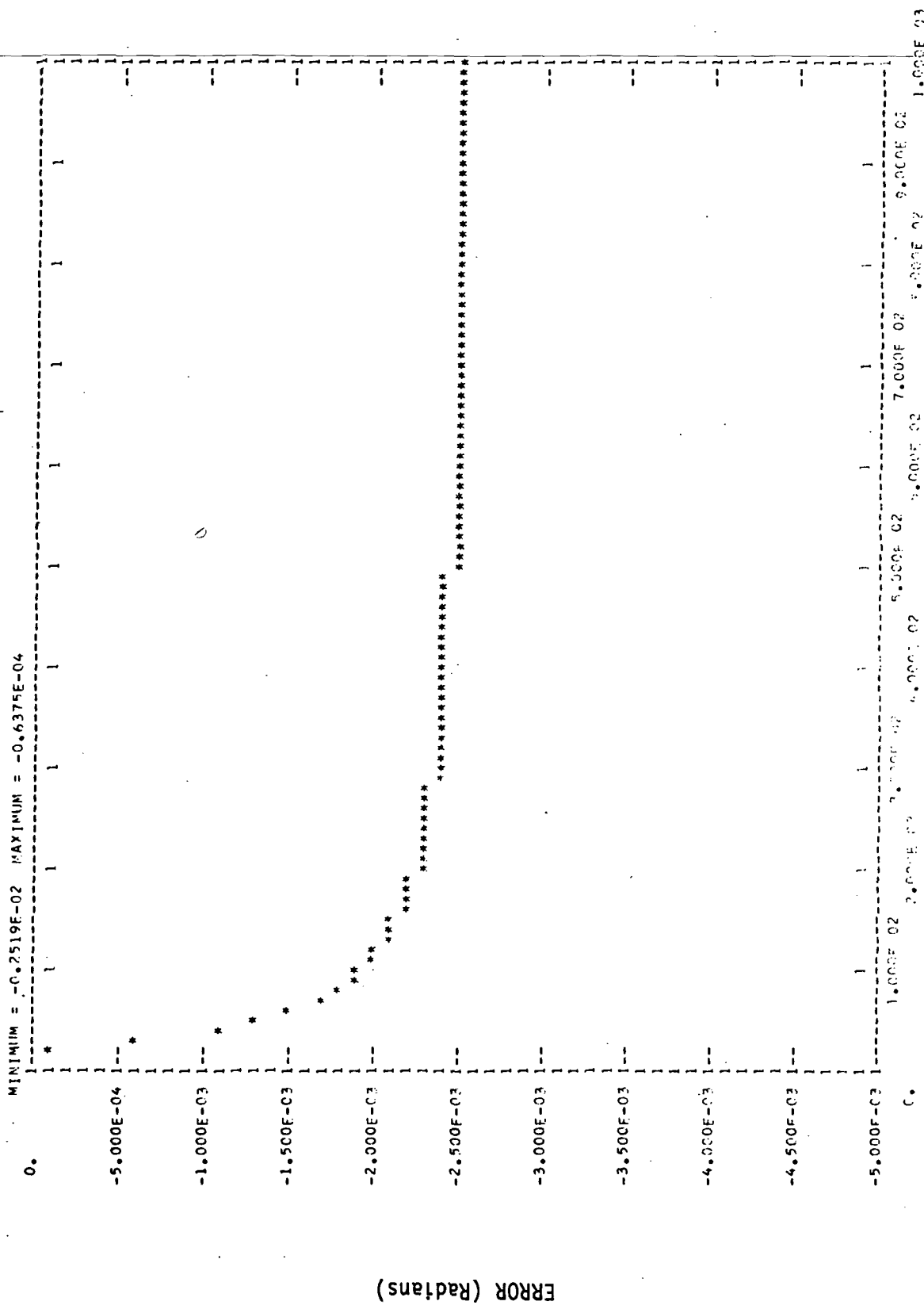
PLOT OF ANGULAR ERROR VERSUS RANGE



RANGE (Meters)

RUN 4

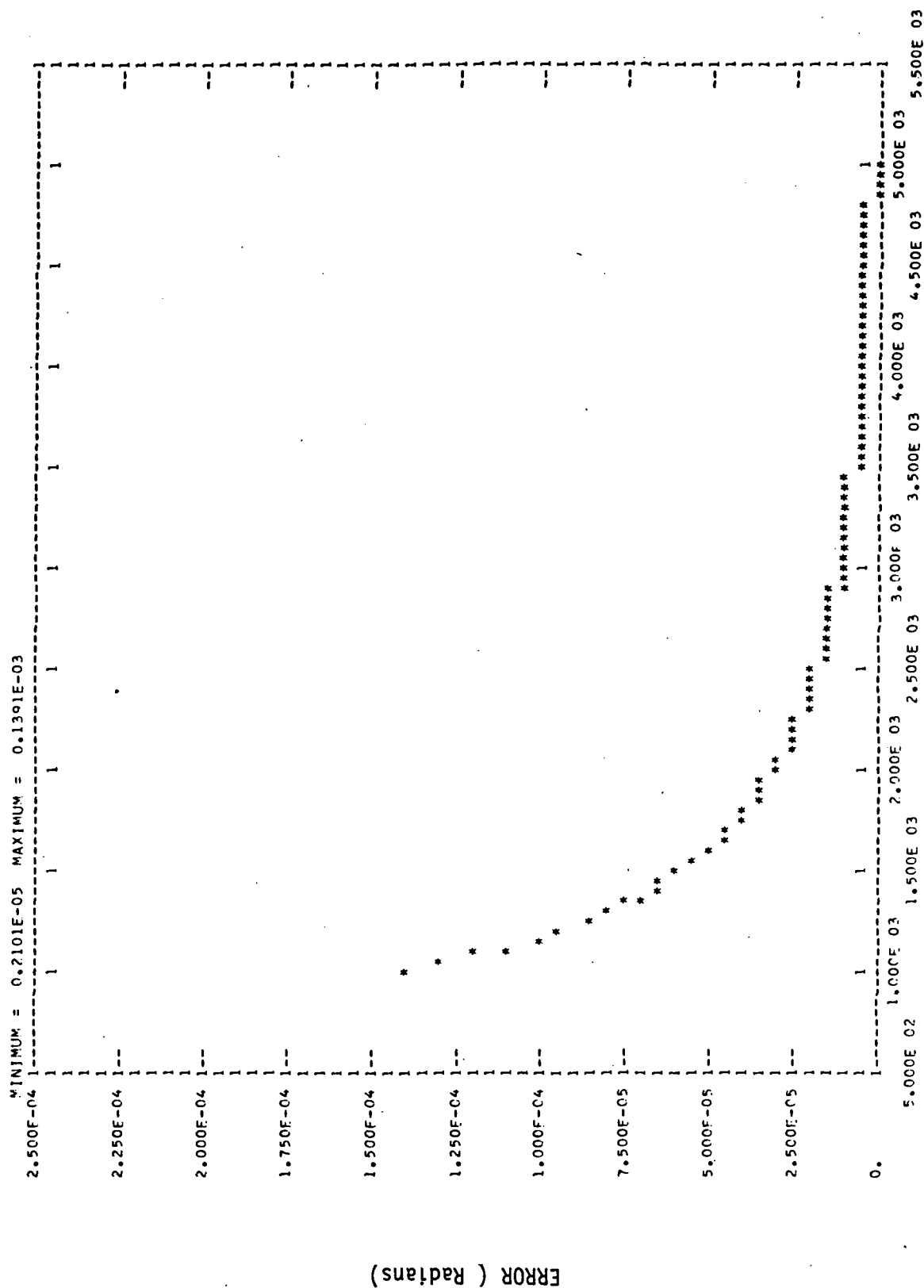
PLOT OF ANGULAR ERROR VERSUS RANGE



RANGE (Meters)

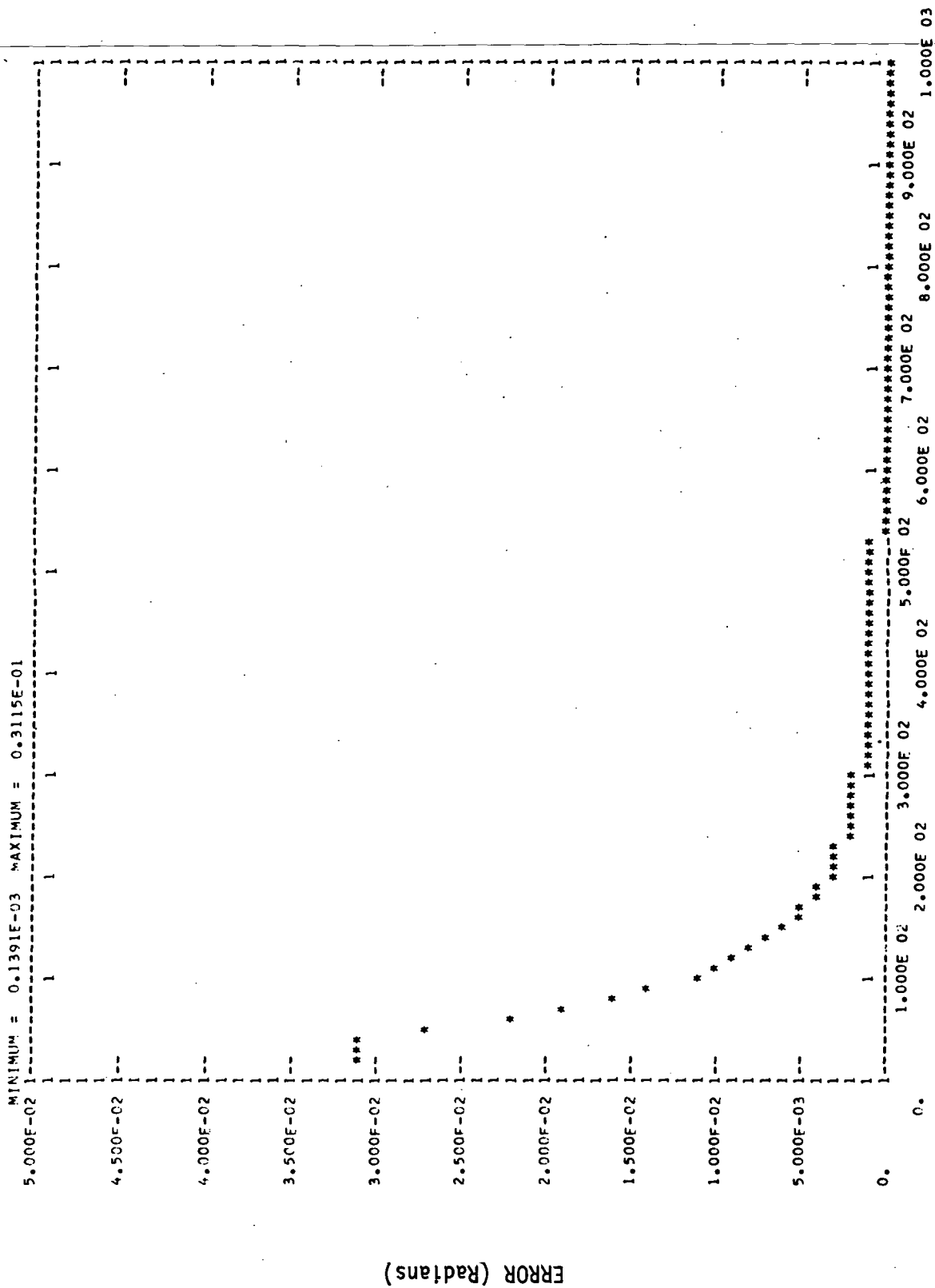
RUN 4

PLOT OF ANGULAR ERROR VERSUS RANGE



RANGE (Meters)
RUN 5

PLOT OF ANGULAR ERROR VERSUS RANGE



RANGE (Meters)
RUN 5

SNUMB = DED02. ACTIVITY # = 01. REPORT CODE = 12. RECORD COUNT = 000270

ANTENNA PAIRS

UPPER	1.22	1.40	1.58	1.76	0.	0.	0.	0.	0.
LOWER	0.50	0.68	0.86	1.04	0.	0.	0.	0.	0.

AIRCRAFT FLIGHT PATH SEGMENTS

X AT START	0.499E 04	0.999E 03	0.	0.	0.	0.	0.	0.	0.	0.	0.	0.	0.	0.	0.	0.	0.	0.	0.
Y AT START	0.	0.	0.	0.	0.	0.	0.	0.	0.	0.	0.	0.	0.	0.	0.	0.	0.	0.	0.
Z AT START	0.262E 03	0.523E 02	0.	0.	0.	0.	0.	0.	0.	0.	0.	0.	0.	0.	0.	0.	0.	0.	0.
X AT FINISH	0.999E 03	0.200E 02	0.	0.	0.	0.	0.	0.	0.	0.	0.	0.	0.	0.	0.	0.	0.	0.	0.
Y AT FINISH	0.	0.	0.	0.	0.	0.	0.	0.	0.	0.	0.	0.	0.	0.	0.	0.	0.	0.	0.
Z AT FINISH	0.523E 02	0.105E 01	0.	0.	0.	0.	0.	0.	0.	0.	0.	0.	0.	0.	0.	0.	0.	0.	0.
NUMBER OF INCREMENTS	50	50	0	0	0	0	0	0	0	0	0	0	0	0	0	0	0	0	0

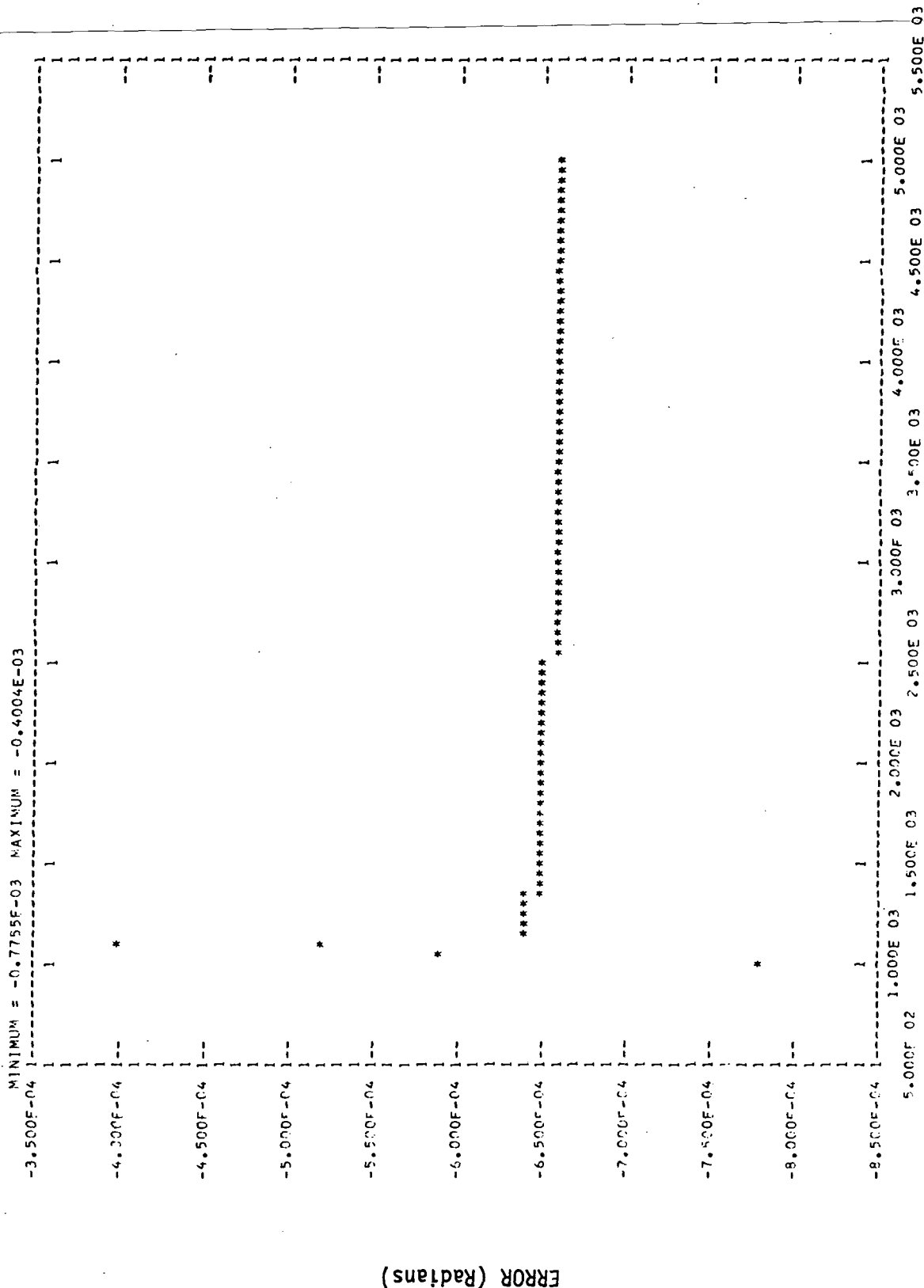
REFLECTING SURFACES

SURFACE NUMBER	STARTING COORDINATES X	STARTING COORDINATES Z	ENDING COORDINATES X	ENDING COORDINATES Z	PERMITTIVITY	ROUGHNESS
1	0.	0.	0.30000E 02	0.30000E 02	0.80000E 02	0.20000E-01
2	0.30000E 02	-0.10000E 02	0.28000E 04	0.65000E 02	0.40000E 02	0.50000E-01
3	0.28000E 04	0.65000E 02	0.31000E 04	0.97000E 02	0.40000E 02	0.50000E-01
4	0.31000E 04	0.97000E 02	0.34000E 04	0.13000E 03	0.40000E 02	0.50000E-01
5	0.	0.	0.	0.	0.	0.
6	0.	0.	0.	0.	0.	0.
7	0.	0.	0.	0.	0.	0.
8	0.	0.	0.	0.	0.	0.
9	0.	0.	0.	0.	0.	0.
10	0.	0.	0.	0.	0.	0.

RUN 6 Segments 1 & 2

RUN 8 Segments 3 & 4

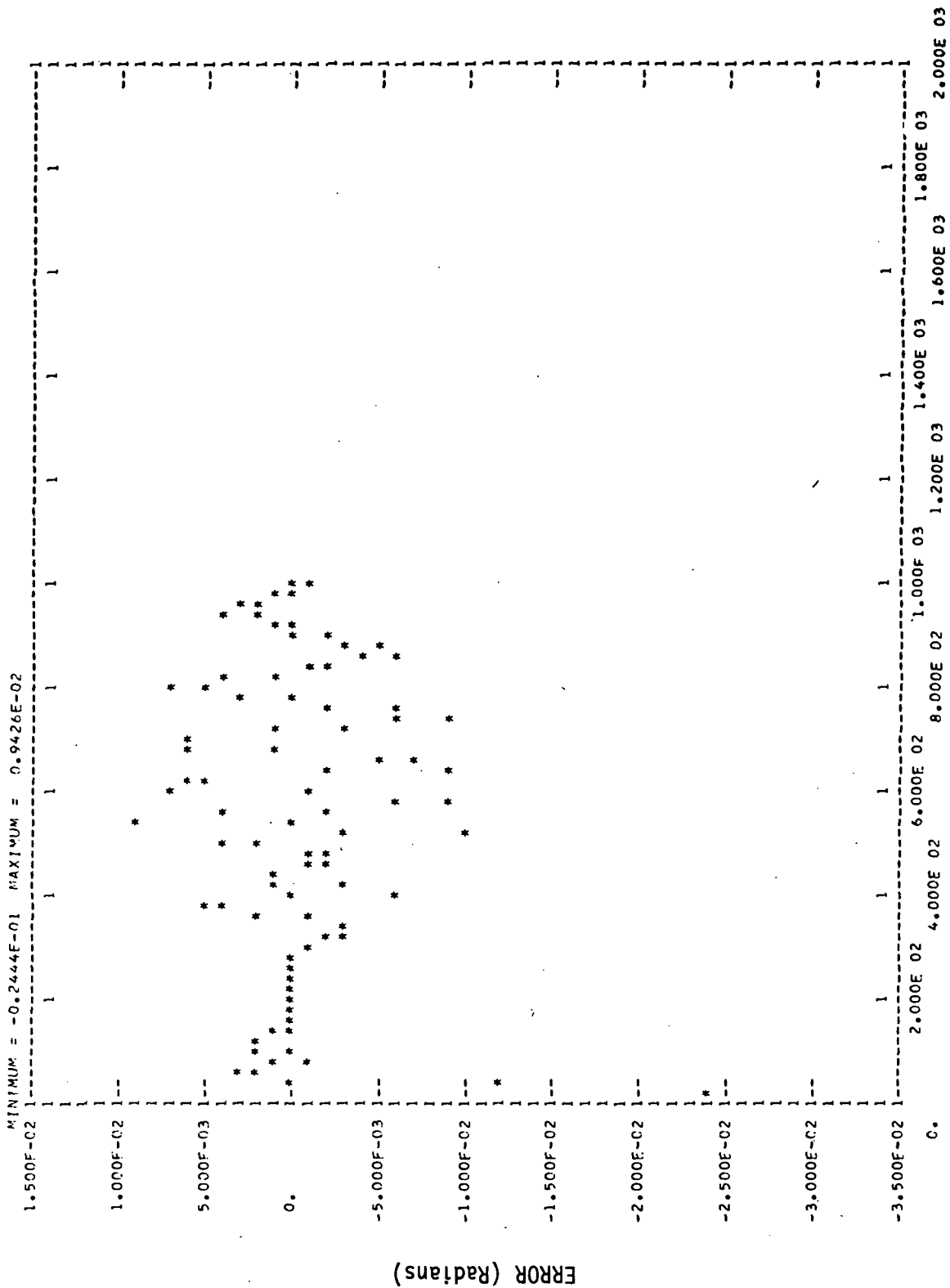
PLOT OF ANGULAR ERROR VERSUS RANGE



RANGE (Meters)

RUN 6

PLOT OF ANGULAR ERROR VERSUS RANGE



RANGE (Meters)

RUN 6

SNUMB = DED02, ACTIVITY # = 01, REPORT CODE = 12, RECORD COUNT = 000270

ANTENNA PAIRS

UPPER	1.22	1.40	1.58	1.76	0.	0.	0.	0.	0.	0.	0.
LOWER	0.50	0.68	0.86	1.04	0.	0.	0.	0.	0.	0.	0.

AIRCRAFT FLIGHT PATH SEGMENTS

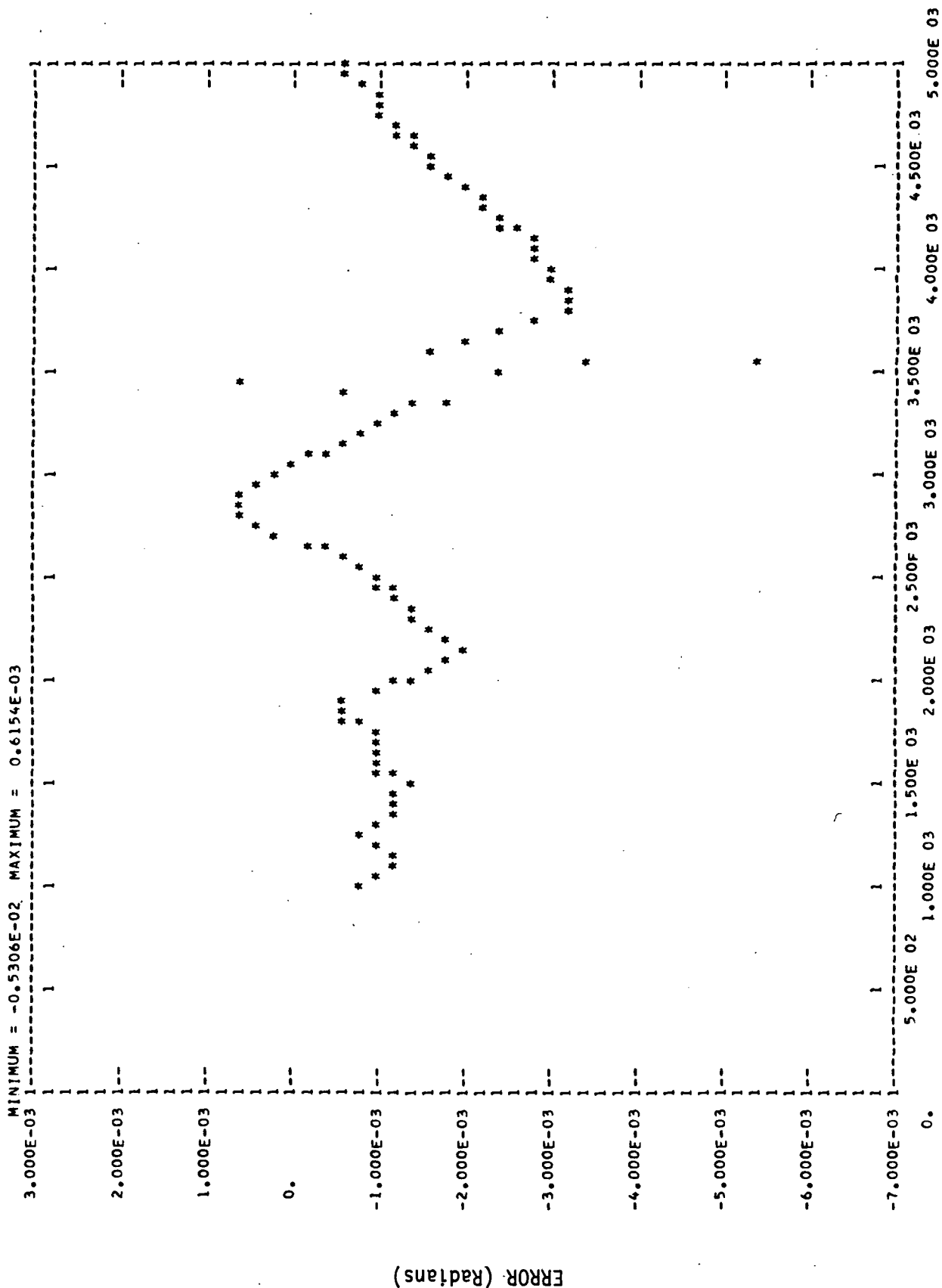
X AT START	0.499E 04	0.999E 03	0.	0.	0.	0.	0.	0.	0.	0.	0.
Y AT START	0.	0.	0.	0.	0.	0.	0.	0.	0.	0.	0.
Z AT START	0.262E 03	0.523E 02	0.	0.	0.	0.	0.	0.	0.	0.	0.
X AT FINISH	0.999E 03	0.200E 02	0.	0.	0.	0.	0.	0.	0.	0.	0.
Y AT FINISH	0.	0.	0.	0.	0.	0.	0.	0.	0.	0.	0.
Z AT FINISH	0.523E 02	0.105E 01	0.	0.	0.	0.	0.	0.	0.	0.	0.
NUMBER OF INCREMENTS	50	50	0	0	0	0	0	0	0	0	0

REFLECTING SURFACES

SURFACE NUMBER	STARTING COORDINATES X	STARTING COORDINATES Z	ENDING COORDINATES X	ENDING COORDINATES Z	PERMITTIVITY	ROUGHNESS
1	0.	0.	0.30000E 02	0.	0.80000E 02	0.20000E-01
2	0.30000E 02	-0.10000E 02	0.28000E 04	0.65000E 02	0.80000E 02	0.50000E-01
3	0.28000E 04	0.65000E 02	0.31000E 04	0.97000E 02	0.80000E 02	0.50000E-01
4	0.31000E 04	0.97000E 02	0.34000E 04	0.13000E 03	0.80000E 02	0.50000E-01
5	0.	0.	0.	0.	0.	0.
6	0.	0.	0.	0.	0.	0.
7	0.	0.	0.	0.	0.	0.
8	0.	0.	0.	0.	0.	0.
9	0.	0.	0.	0.	0.	0.
10	0.	0.	0.	0.	0.	0.

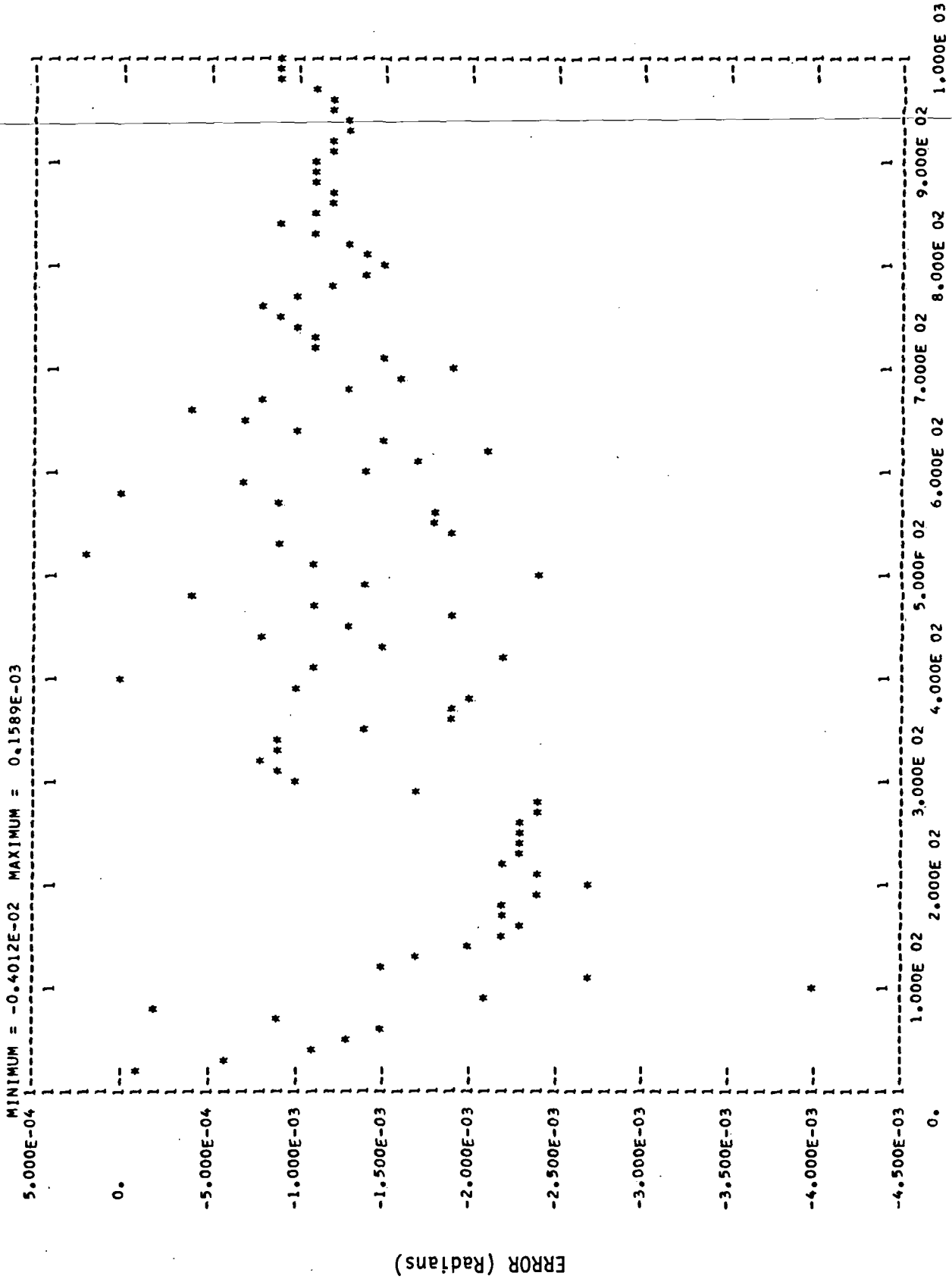
1
00
1

PLOT OF ANGULAR ERROR VERSUS RANGE



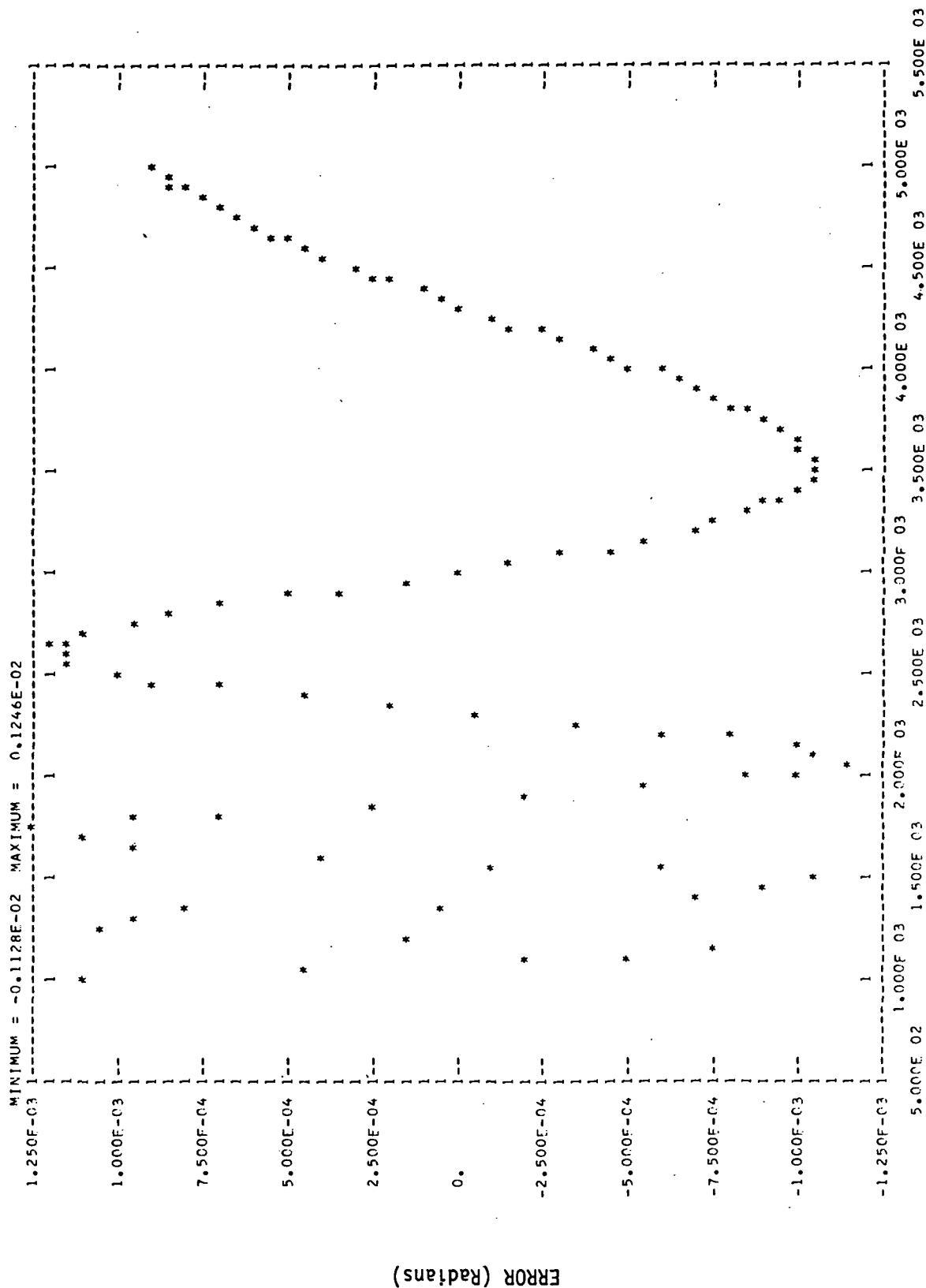
RANGE (Meters)
RUN 7

PLOT OF ANGULAR ERROR VERSUS RANGE



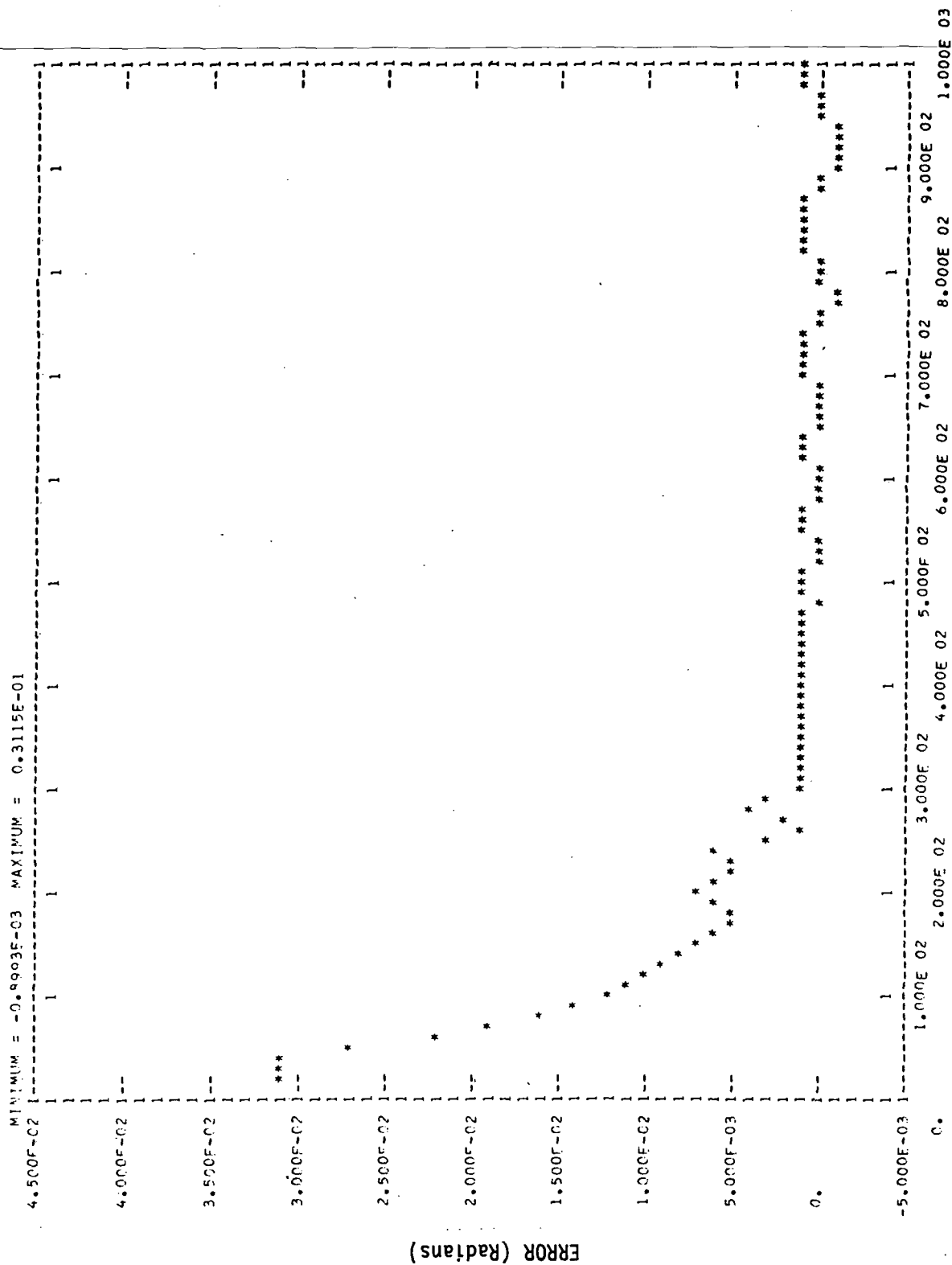
RANGE (Meters)
RUN 7

PLOT OF ANGULAR ERROR VERSUS RANGE



RANGE (Meters)
RUN 8

PLOT OF ANGULAR ERROR VERSUS RANGE



RANGE (Meters)
RUN 8

SNUM3 = G1004, ACTIVITY # = 01, REPORT CODE = 12, RECORD COUNT = 000514

ANTENNA PAIRS

UPPER	1.22	1.40	1.58	1.76	1.28	1.46	1.64	1.82	0.
LOWER	0.50	0.68	0.86	1.04	0.56	0.74	0.92	1.10	0.

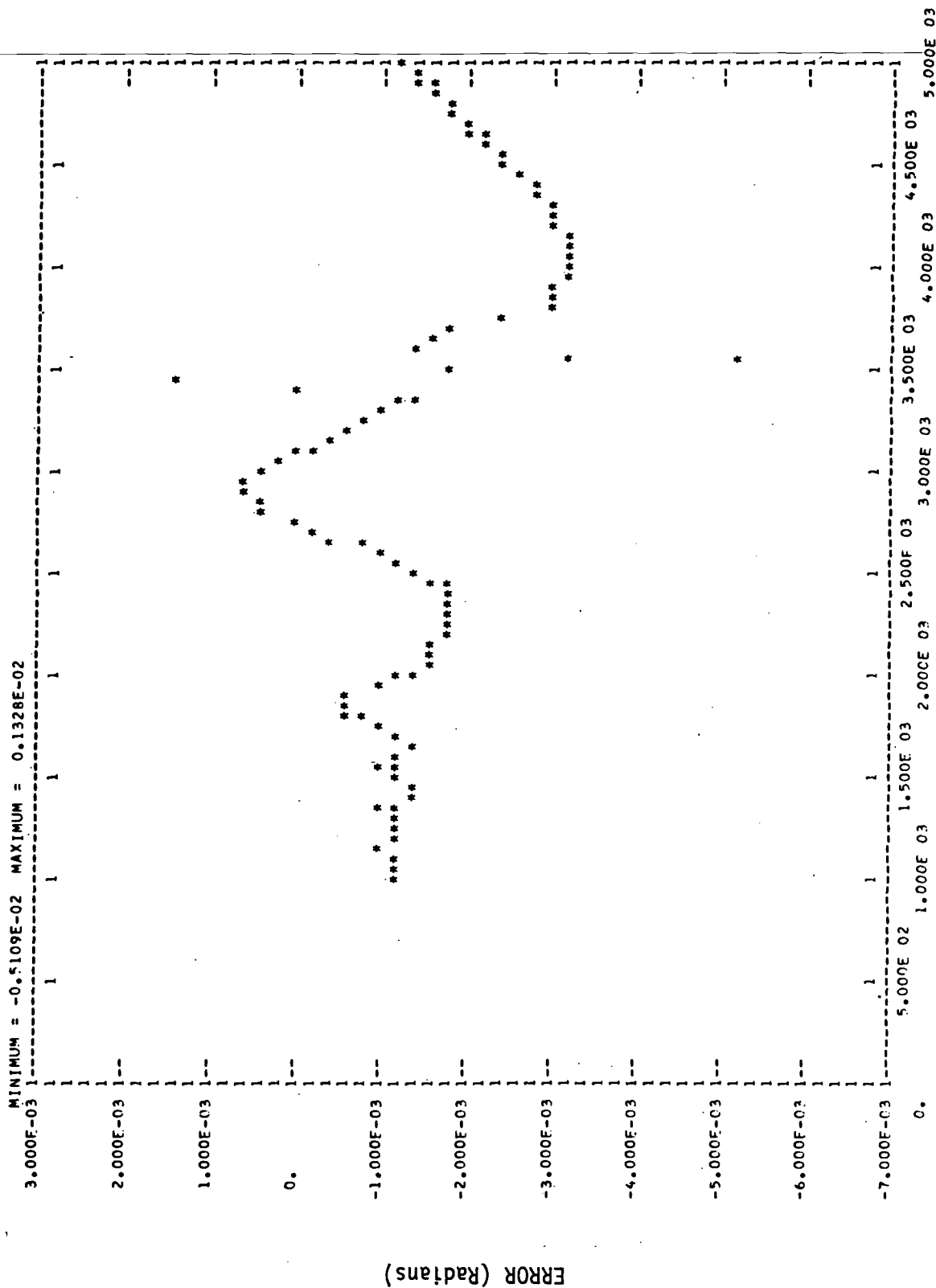
AIRCRAFT FLIGHT PATH SEGMENTS

X AT START	0.499E 04	0.999E 03	0.497E 04	0.995E 03	0.	0.	0.	0.	0.
Y AT START	0.550E 02	0.550E 02	0.550E 02	0.550E 02	0.	0.	0.	0.	0.
Z AT START	0.262E 03	0.523E 02	0.523E 03	0.105E 03	0.	0.	0.	0.	0.
X AT FINISH	0.999E 03	0.200E 02	0.995E 03	0.199E 02	0.	0.	0.	0.	0.
Y AT FINISH	0.550E 02	0.550E 02	0.550E 02	0.550E 02	0.	0.	0.	0.	0.
Z AT FINISH	0.523E 02	0.105E 01	0.105E 03	0.209E 01	0.	0.	0.	0.	0.
NUMBER OF INCREMENTS	50	50	50	50	0	0	0	0	0

REFLECTING SURFACES

SURFACE NUMBER	STARTING COORDINATES X	STARTING COORDINATES Z	ENDING COORDINATES X	ENDING COORDINATES Z	PERMITIVITY	ROUGHNESS
1	0.	0.	0.30000E 02	0.	0.80000E 02	0.20000E-01
2	0.30000E 02	-0.10000F 02	0.28000E 04	0.65000E 02	0.80000E 02	0.50000E-01
3	0.28000F 04	0.65000E 02	0.31000E 04	0.97000F 02	0.80000E 02	0.50000E-01
4	0.31000E 04	0.97000E 02	0.34000E 04	0.13000E 03	0.80000E 02	0.50000E-01
5	0.	0.	0.	0.	0.	0.
6	0.	0.	0.	0.	0.	0.
7	0.	0.	0.	0.	0.	0.
8	0.	0.	0.	0.	0.	0.
9	0.	0.	0.	0.	0.	0.
10	0.	0.	0.	0.	0.	0.

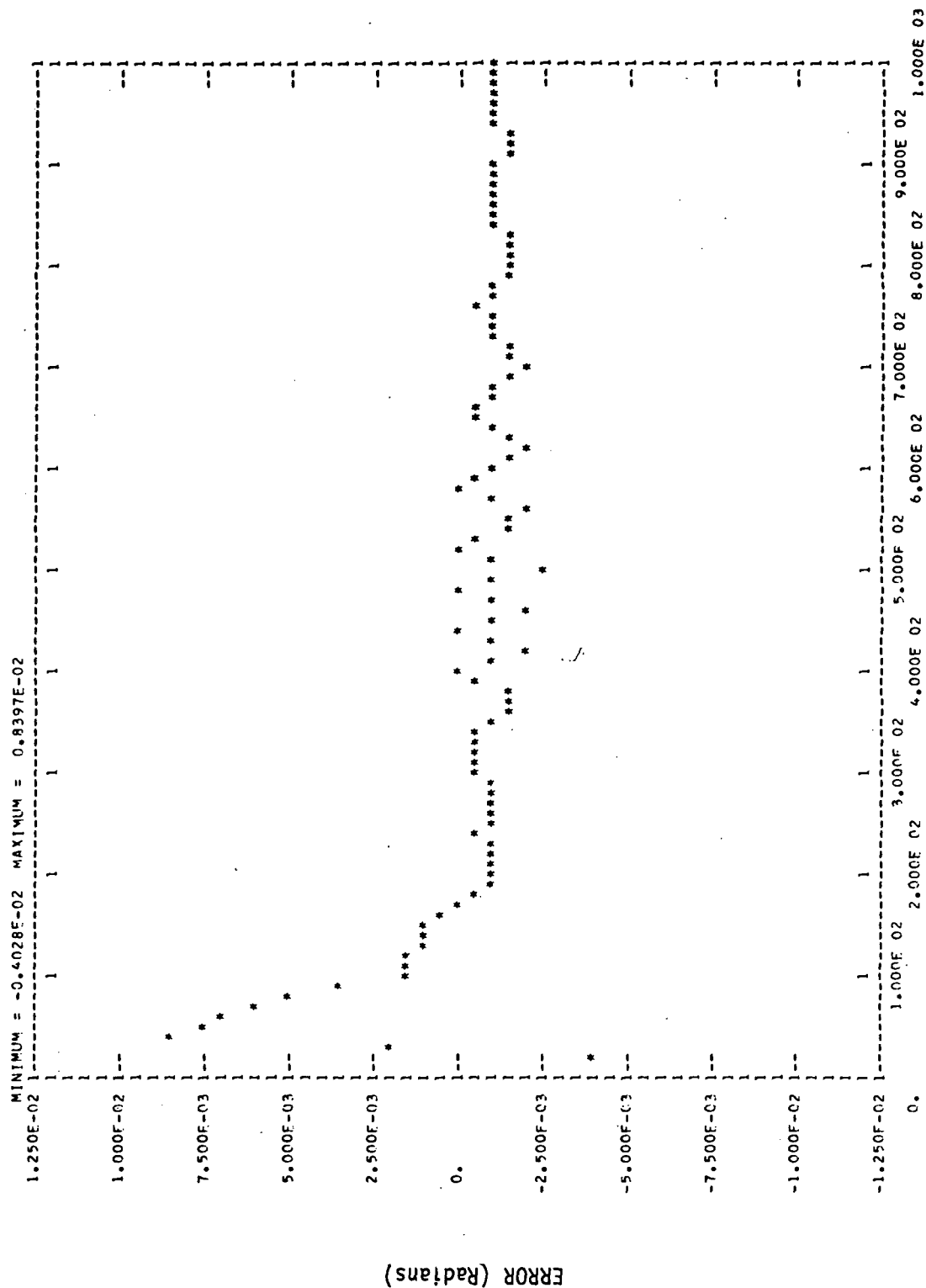
PLOT OF ANGULAR ERROR VERSUS RANGE



RANGE (Meters)

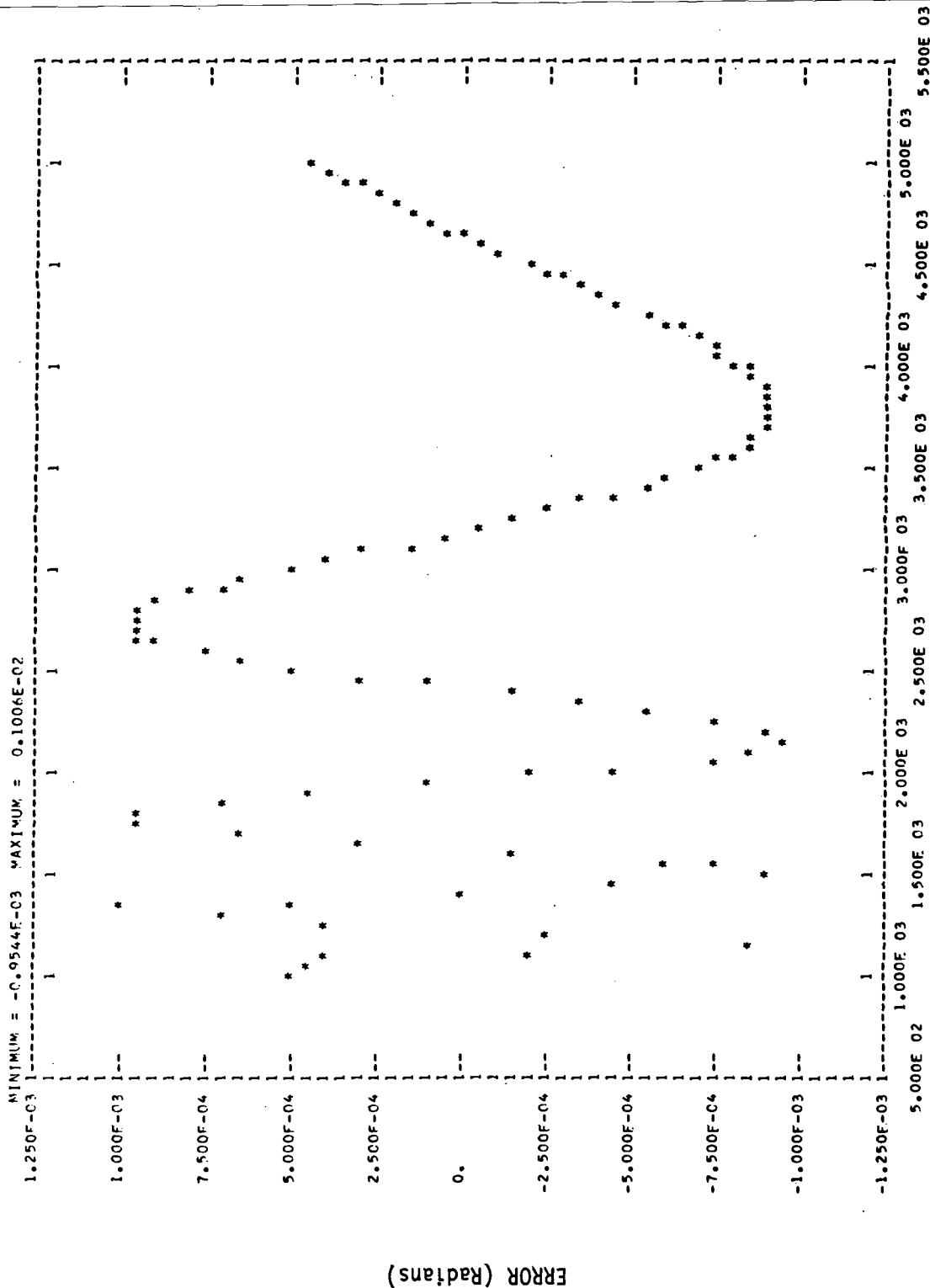
RUN 9

PLOT OF ANGULAR ERROR VERSUS RANGE

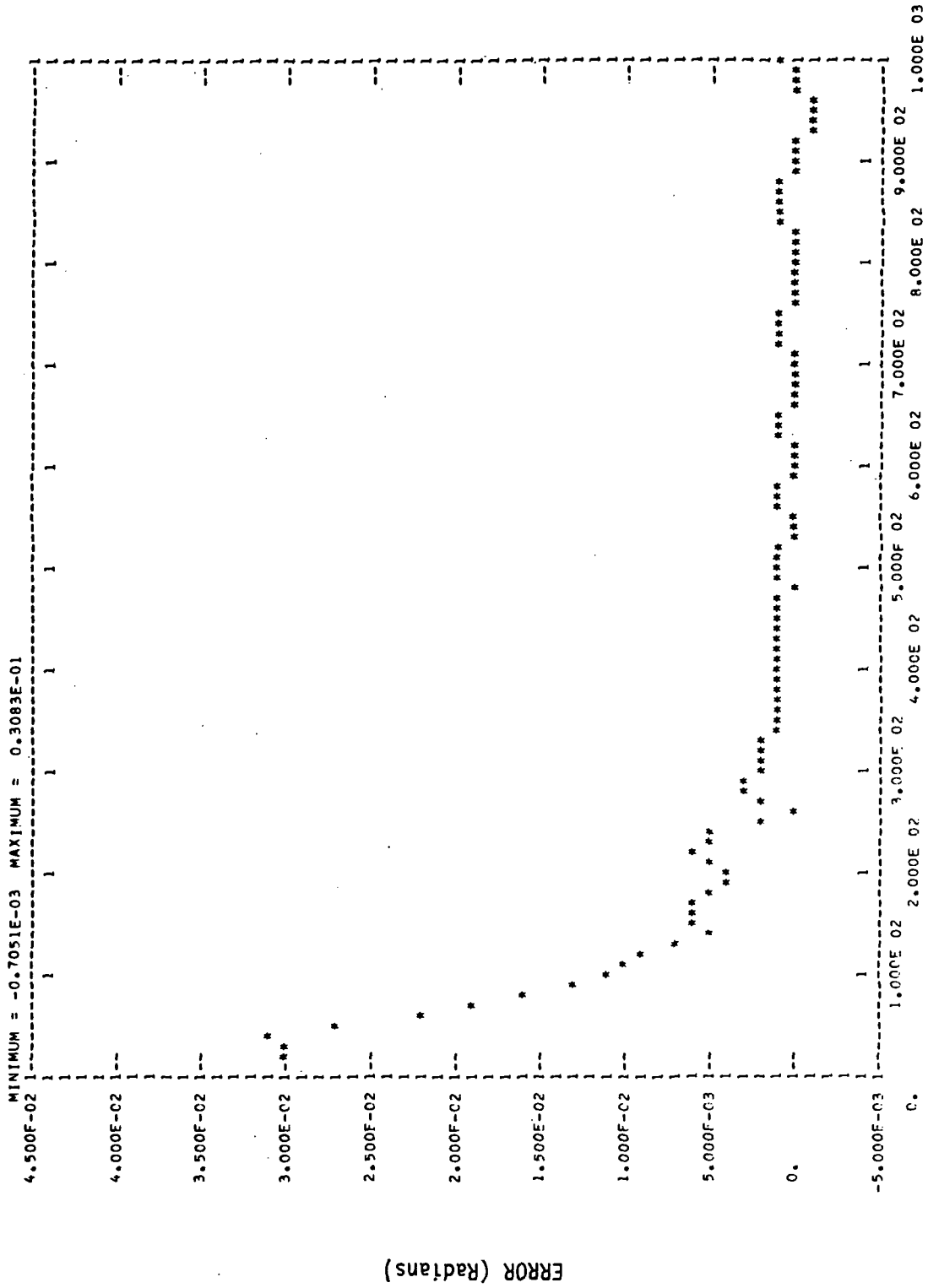


RANGE (Meters)
RUN 9

PLOT OF ANGULAR ERROR VERSUS RANGE



PLOT OF ANGULAR ERROR VERSUS RANGE



SNUMR = DED02, ACTIVITY # = 01, REPORT CODE = 12, RECORD COUNT = 000514

ANTENNA PAIRS

	1.58	1.76	1.94	2.12	2.30	2.48	
UPPER	0.50	0.68	0.86	1.04	1.22	1.40	0.
LOWER							0.

AIRCRAFT FLIGHT PATH SEGMENTS

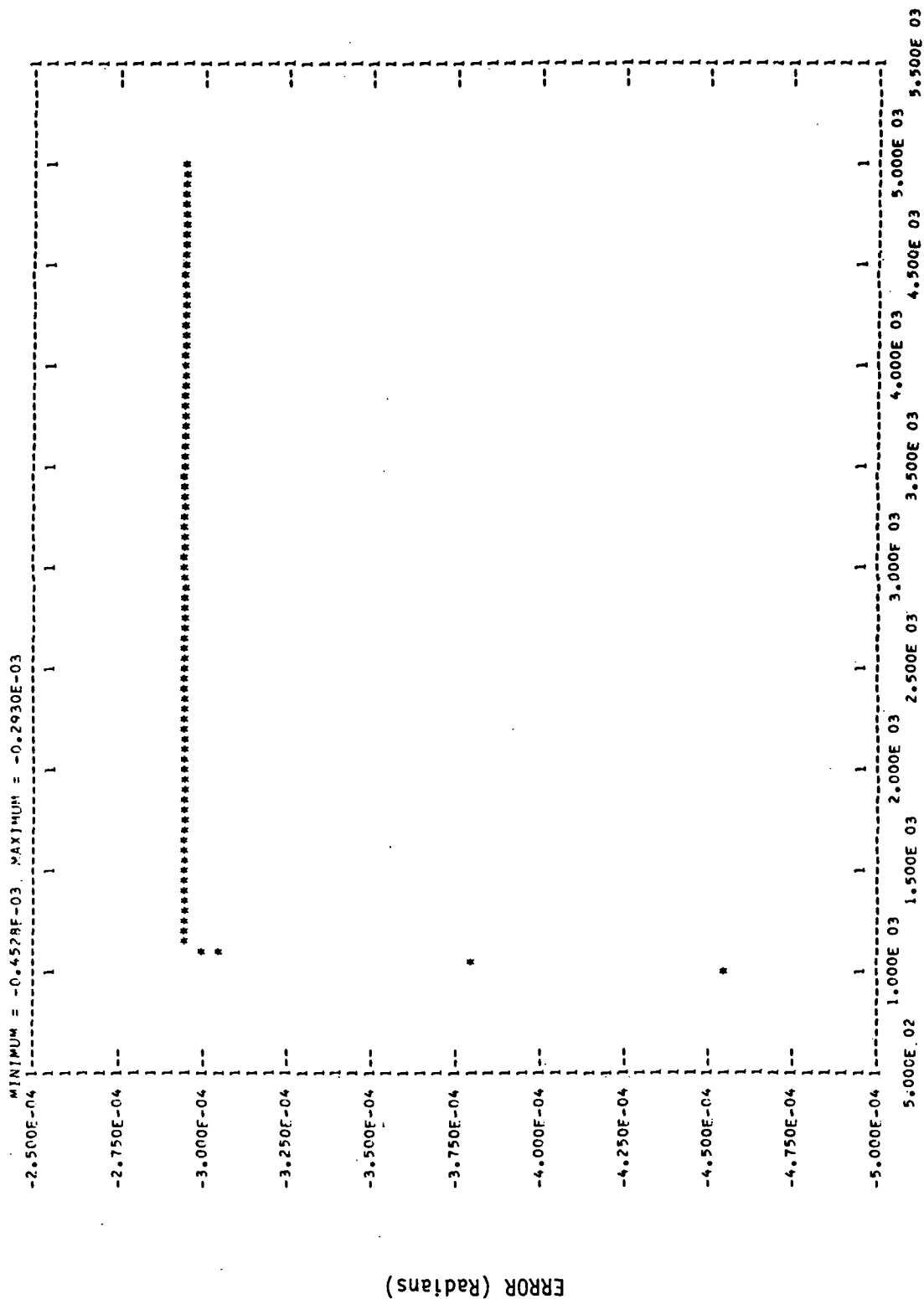
	X AT START	Y AT START	Z AT START	X AT FINISH	Y AT FINISH	Z AT FINISH	NUMBER OF INCREMENTS
	0.500E 04	0.	0.	0.100E 04	0.499E 04	0.999E 03	50
	0.873E 02	0.175E 02	0.262E 03	0.523E 02	0.999E 03	0.200E 02	50
	0.100E 04	0.200E 02	0.999E 03	0.	0.	0.	50
	0.	0.	0.	0.349E 00	0.523E 02	0.105E 01	50

REFLECTING SURFACES

SURFACE NUMBER	STARTING COORDINATES			ENDING COORDINATES			PERMITTIVITY	ROUGHNESS
	X	Y	Z	X	Y	Z		
1	0.	0.	0.	0.30000E 02	0.	0.80000E 02	0.40000E 02	0.20000E-01
2	0.30000E 02	-0.10000E 02	0.	0.28000E 04	0.65000E 02	0.80000E 02	0.40000E 02	0.50000E-01
3	0.28000E 04	0.65000E 02	0.	0.31000E 04	0.97000E 02	0.80000E 02	0.40000E 02	0.50000E-01
4	0.31000E 04	0.97000E 02	0.	0.34000E 04	0.13000E 03	0.80000E 02	0.40000E 02	0.50000E-01
5	0.	0.	0.	0.	0.	0.	0.	0.
6	0.	0.	0.	0.	0.	0.	0.	0.
7	0.	0.	0.	0.	0.	0.	0.	0.
8	0.	0.	0.	0.	0.	0.	0.	0.
9	0.	0.	0.	0.	0.	0.	0.	0.
10	0.	0.	0.	0.	0.	0.	0.	0.

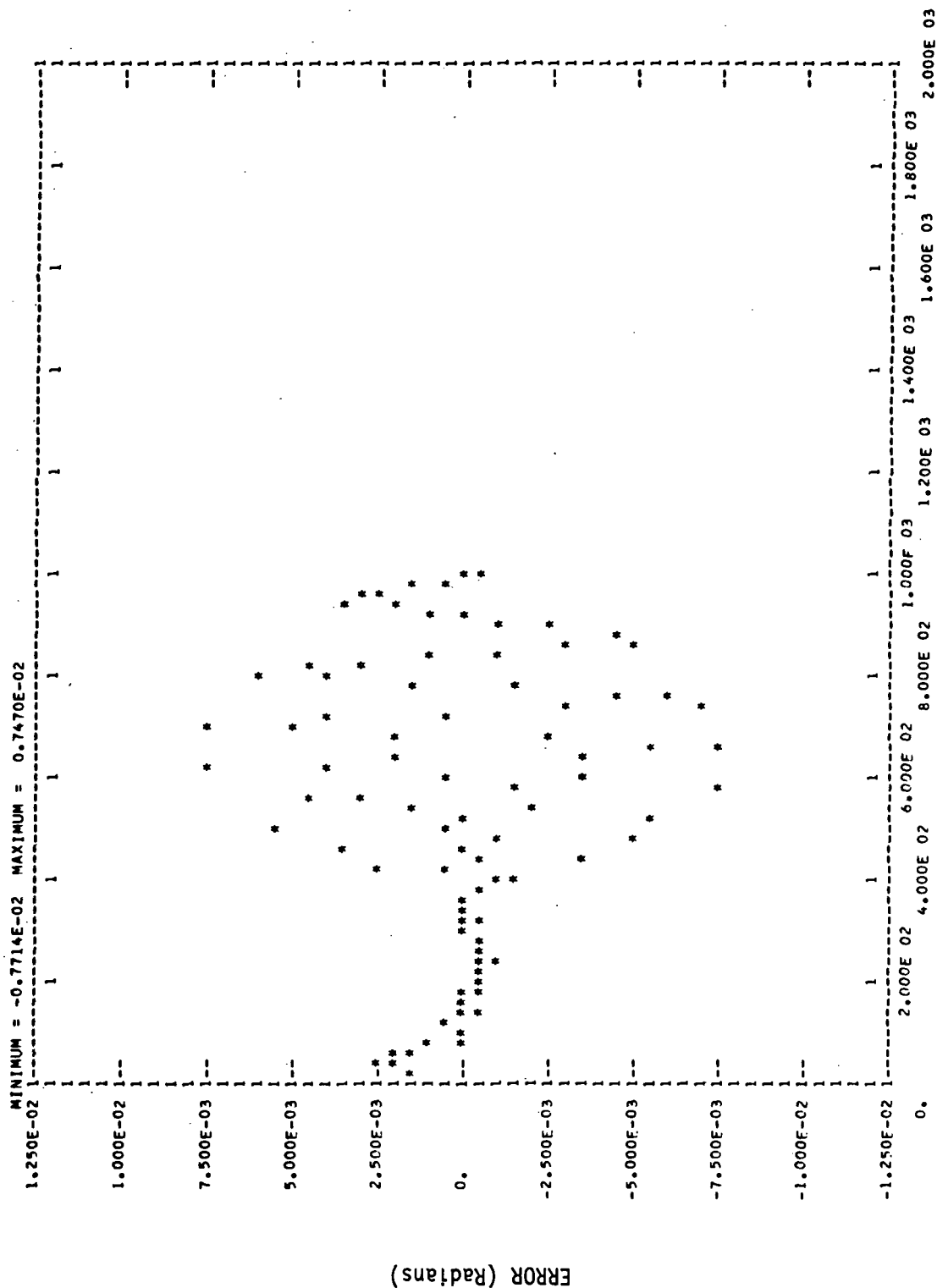
RUN 11 Segments 1 & 2
 RUN 12 Segments 3 & 4

PLOT OF ANGULAR ERROR VERSUS RANGE



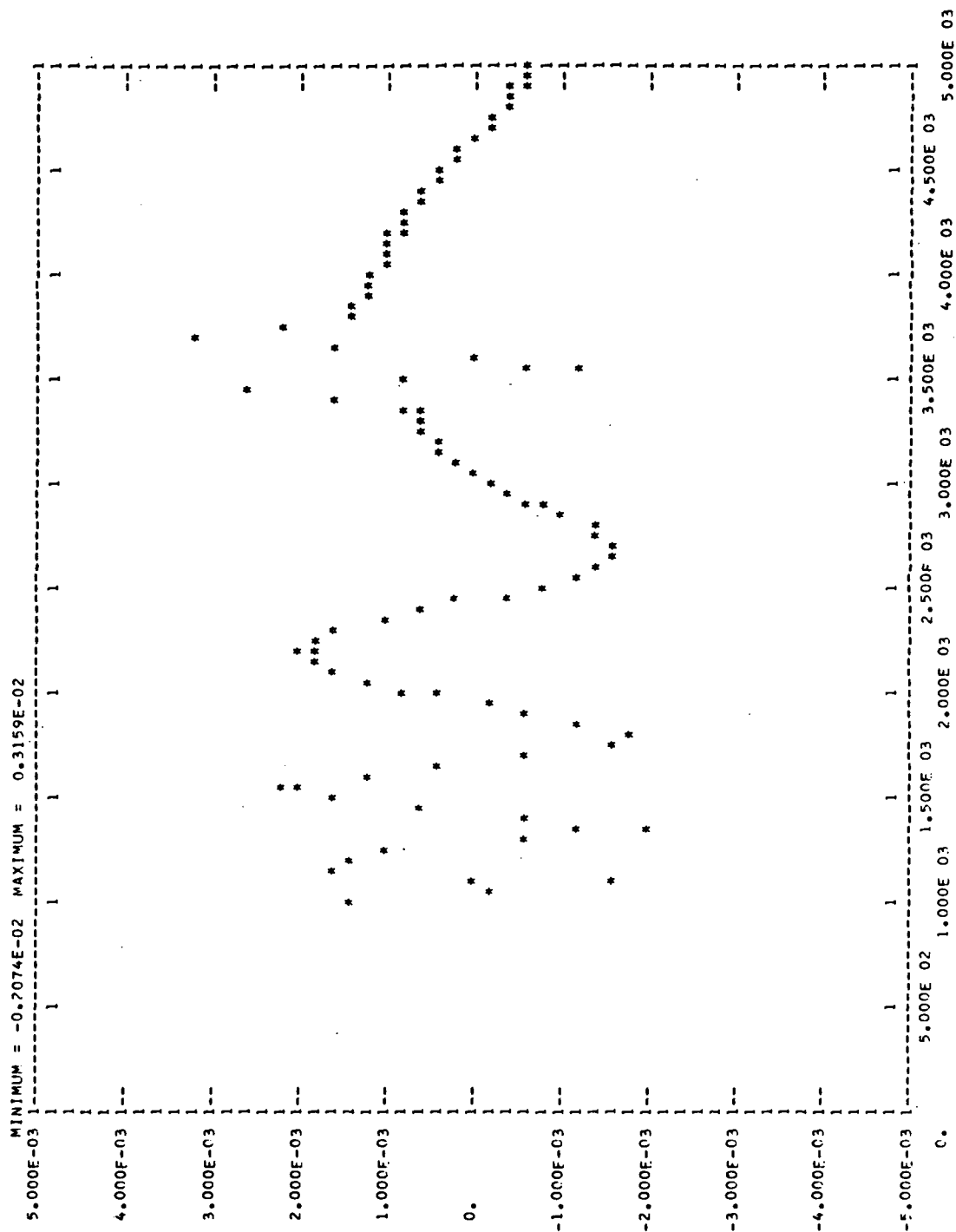
RANGE (Meters)
RUN 11

PLOT OF ANGULAR ERROR VERSUS RANGE



RANGE (Meters)
RUN 11

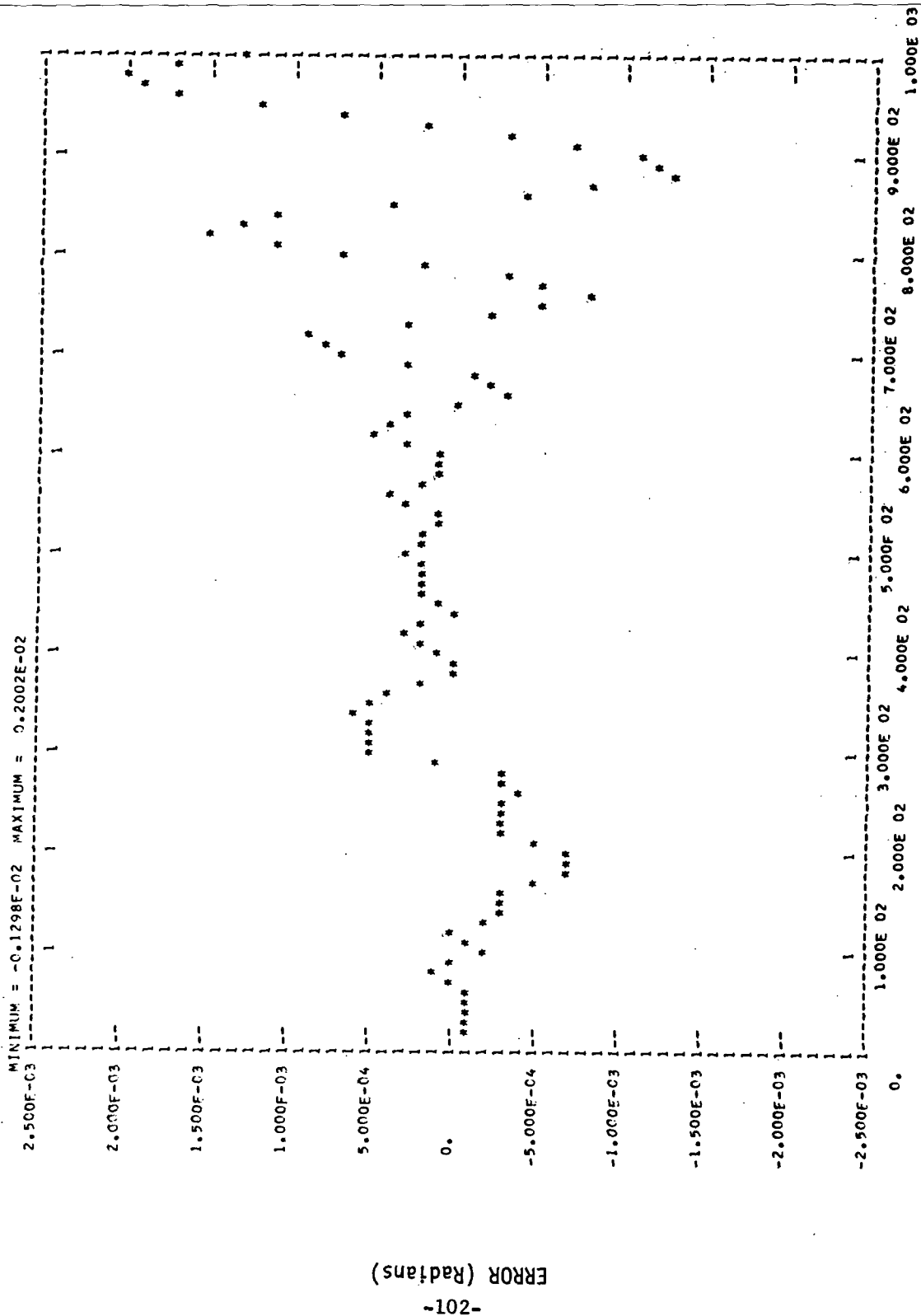
ERROR (Radians)



RANGE (Meters)

RUN 12

PLOT OF ANGULAR ERROR VERSUS RANGE



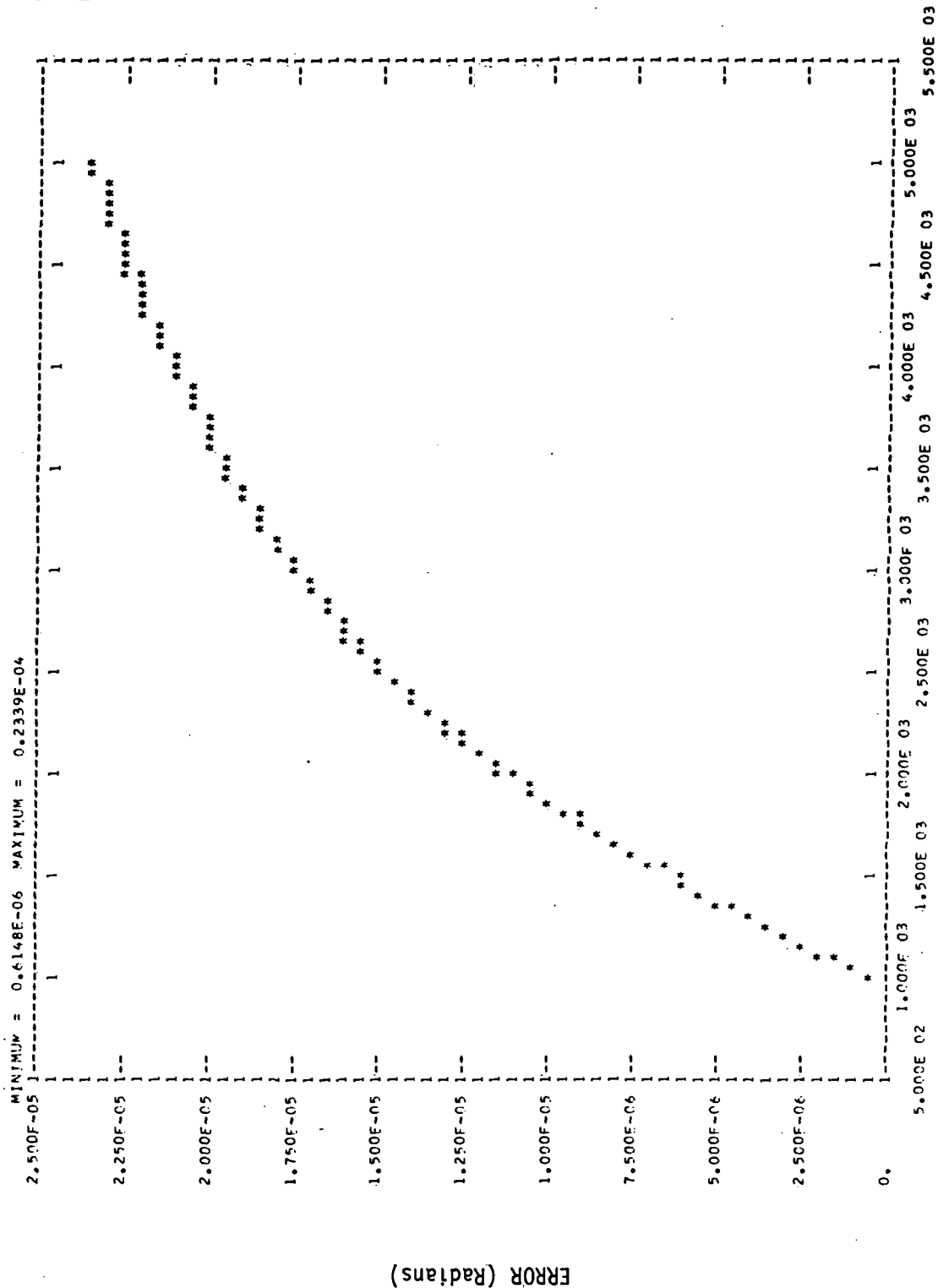
RANGE (Meters)

RUN 12

ANTENNA PAIRS					
UPPER	0.80	0.	0.	0.	0.
LOWER	0.	0.	0.	0.	0.
AIRCRAFT FLIGHT PATH SEGMENTS					
X AT START	0.500E 04	0.100E 04	0.	0.	0.
Y AT START	0.260E 03	0.550E 02	0.	0.	0.
Z AT START	0.873E 02	0.175E 02	0.	0.	0.
X AT FINISH	0.100E 04	0.200E 02	0.	0.	0.
Y AT FINISH	0.100E 02	0.550E 02	0.	0.	0.
Z AT FINISH	0.175E 02	0.349E 00	0.	0.	0.
NUMBER OF INCREMENTS	50	50	0	0	0

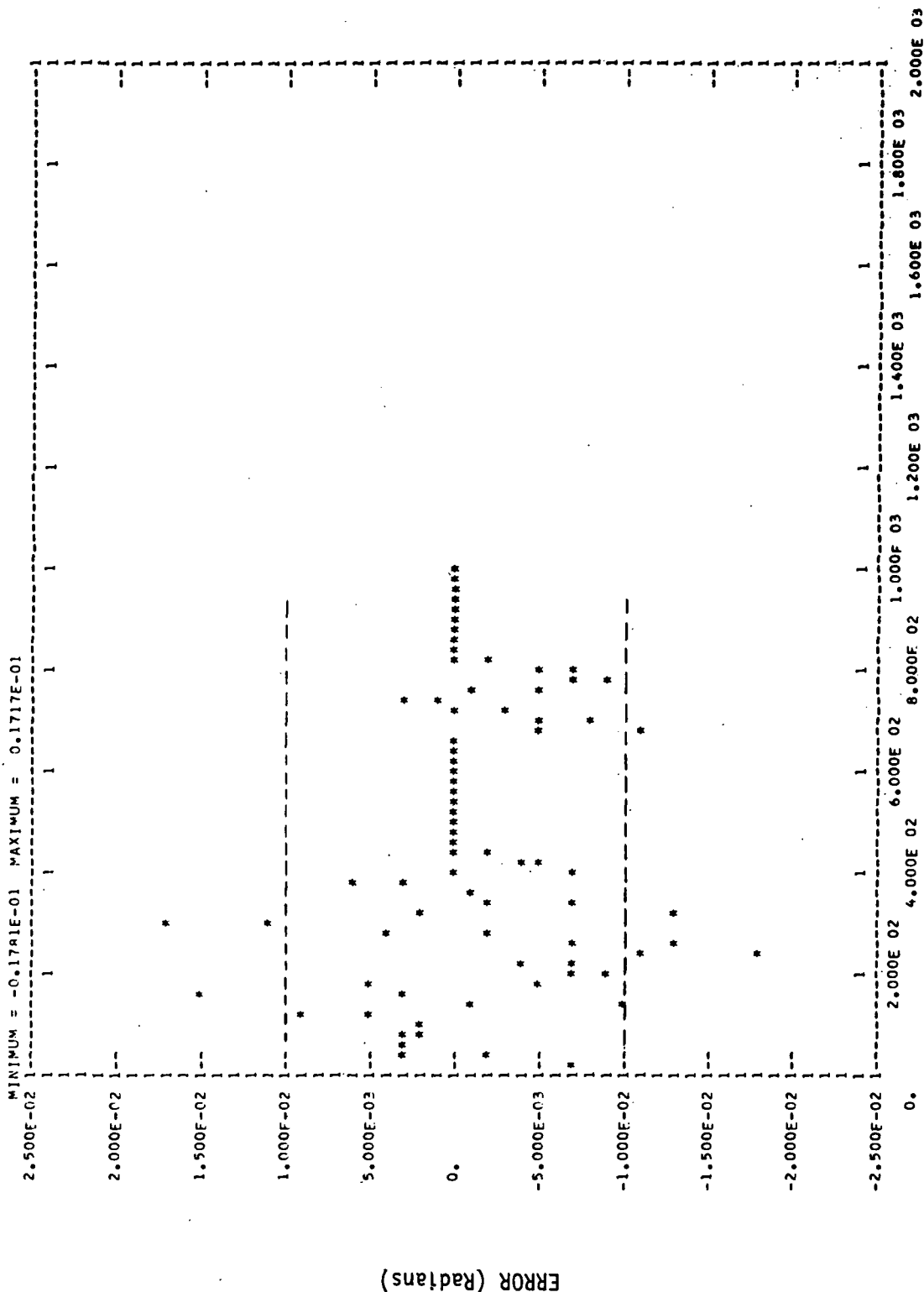
REFLECTING SURFACES						ENDING COORDINATES			PERMITIVITY			ROUGHNESS		
SURFACE NUMBER	X	Z	STARTING COORDINATES	X	Z									
1	0.9000E 02	0.1500E 03		0.2100E 03	0.1500E 03		0.2000E 02	0.1000E 03		0.1000E-02				
2	0.5500E 02	-0.4000E 02		0.1550E 03	-0.4000E 02		0.2000E 02	0.1000E 03		0.1000E-02				
3	0.3400E 03	0.2600E 03		0.4400E 03	0.2600E 02		0.2000E 02	0.1000E 03		0.1000E-02				
4	0.4100E 03	-0.1000E 02		0.4300E 03	0.2000E 02		0.2000E 02	0.1000E 03		0.1000E-02				
5	0.3000E 01	0.1000E 02		0.1000E 02	0.1000E 02		0.2000E 02	0.1000E 03		0.1000E-02				
6	0.	0.		0.	0.		0.	0.		0.				
7	0.	0.		0.	0.		0.	0.		0.				
8	0.	0.		0.	0.		0.	0.		0.				
9	0.	0.		0.	0.		0.	0.		0.				
10	0.	0.		0.	0.		0.	0.		0.				

PLOT OF ANGULAR ERROR VERSUS RANGE



RANGE (Meters)
RUN 13

PLOT OF ANGULAR ERROR VERSUS RANGE



ANTENNA PAIRS					
UPPER	0.80	0.	0.	0.	0.
LOWER	0.	0.	0.	0.	0.
 AIRCRAFT FLIGHT PATH SEGMENTS					
X AT START	0.500E 04	0.	0.100E 04	0.	0.
Y AT START	0.260E 03	0.	0.550E 02	0.	0.
Z AT START	0.873E 02	0.	0.175E 02	0.	0.
X AT FINISH	0.100E 04	0.200E 02	0.	0.	0.
Y AT FINISH	0.100E 02	0.550E 02	0.	0.	0.
Z AT FINISH	0.175E 02	0.349E 00	0.	0.	0.
NUMBER OF INCREMENTS	50	50	0	0	0

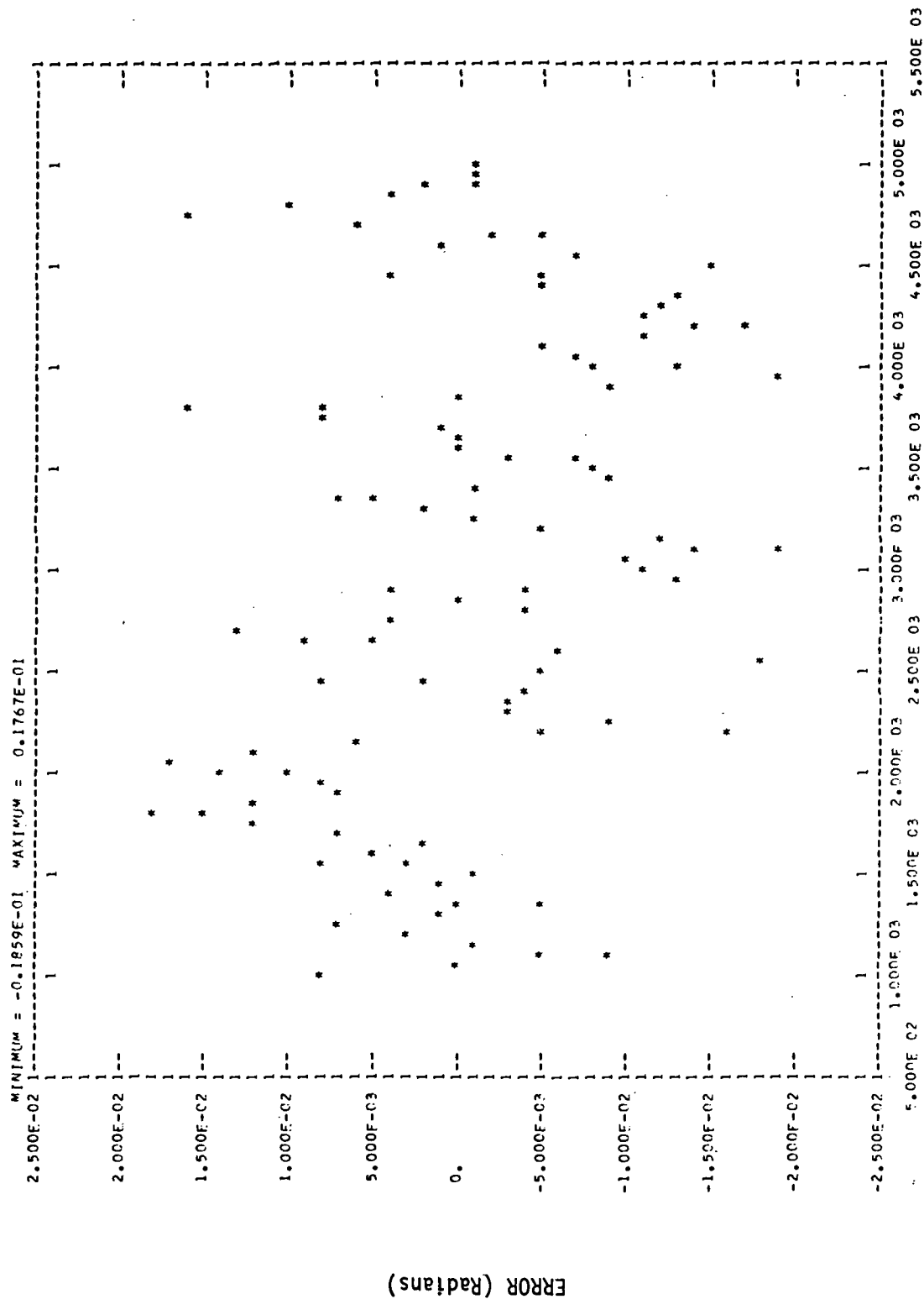
AIRCRAFT FLIGHT PATH SEGMENTS

NUMBER OF INCREMENTS	50	50	0.349E	00	0.
Z AT FINISH	0.175E	02			
X AT FINISH	0.100E	02			
X AT START	0.000E	04			
Z AT FINISH	0.873E	02			
X AT FINISH	0.100E	04			
X AT START	0.280E	03			
Z AT FINISH	0.175E	02			
X AT FINISH	0.200E	02			
X AT START	0.550E	02			
Z AT FINISH	0.100E	04			
X AT FINISH	0.100E	04			
X AT START	0.100E	04			

REFLECTING SURFACES

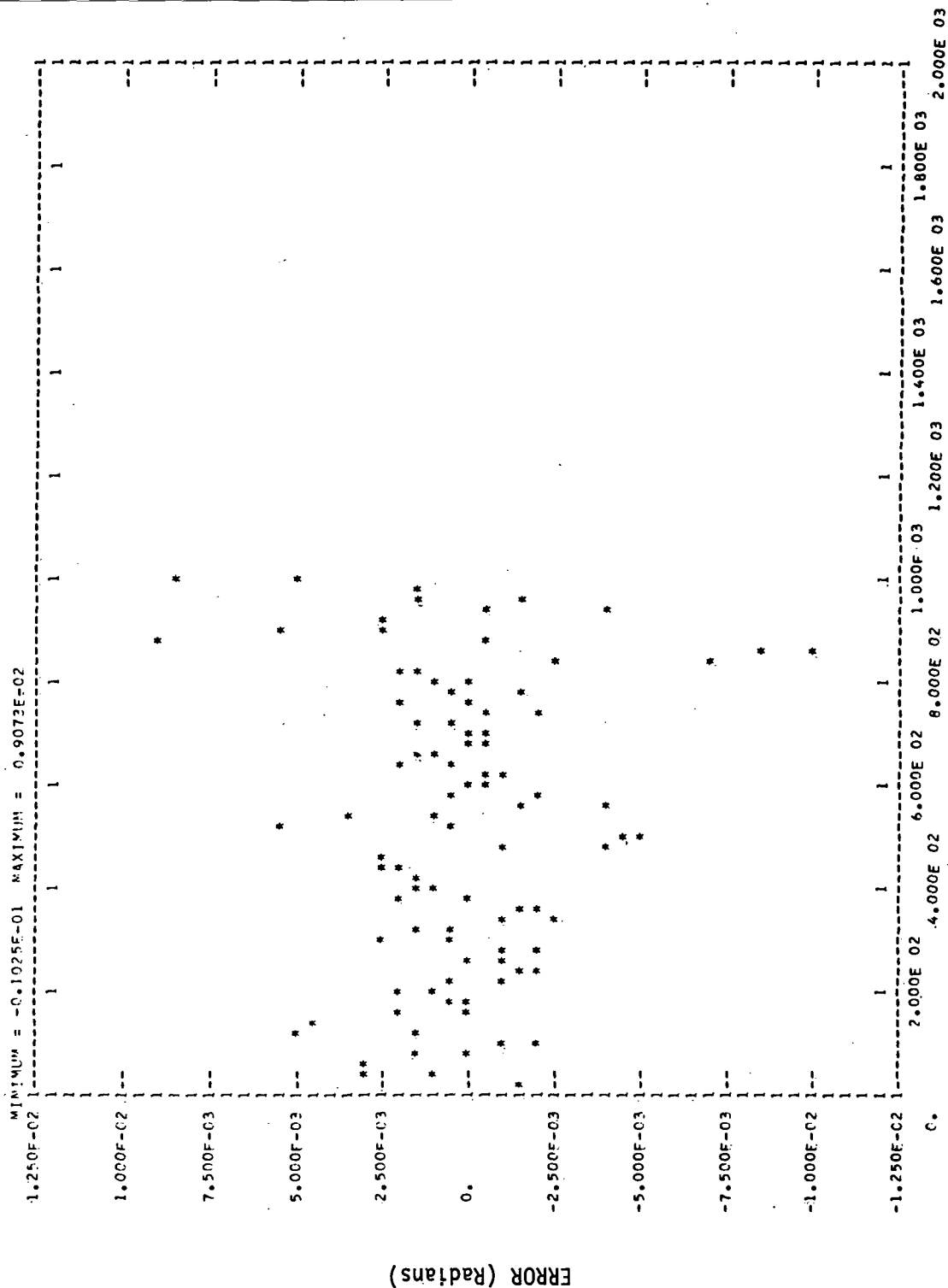
SURFACE NUMBER	STARTING COORDINATES		ENDING COORDINATES		PERMITTIVITY	ROUGHNESS
	X	Z	X	Z		
1	-0.1000E 04	0.5000E 03	0.7000E 04	0.8000E 03	0.8000E 02	0.5000E-01
2	-0.1000E 04	-0.5000E 03	0.7000E 04	-0.5000E 03	0.8000E 02	0.5000E-01
3	0.2000E 02	0.1000E 03	0.6000E 02	0.1040E 03	0.2000E 02	0.1000E-02
4	0.6000E 03	0.1000E 03	0.6300E 03	0.1010E 03	0.2000E 02	0.1000E-02
5	0.	0.	0.	0.	0.	0.
6	0.	0.	0.	0.	0.	0.
7	0.	0.	0.	0.	0.	0.
8	0.	0.	0.	0.	0.	0.
9	0.	0.	0.	0.	0.	0.
10	0.	0.	0.	0.	0.	0.

PLOT OF ANGULAR ERROR VERSUS RANGE



RANGE (Meters)
RUN 14

PLOT OF ANGULAR ERROR VERSUS RANGE



SNUMB = DED00, ACTIVITY # = 01, REPORT CODE = /12, RECORD COUNT = 000270

ANTENNA PAIRS

UPPER	1.22	1.40	1.58	1.76	0.	0.	0.	0.	0.	0.
LOWER	0.50	0.68	0.86	1.04	0.	0.	0.	0.	0.	0.

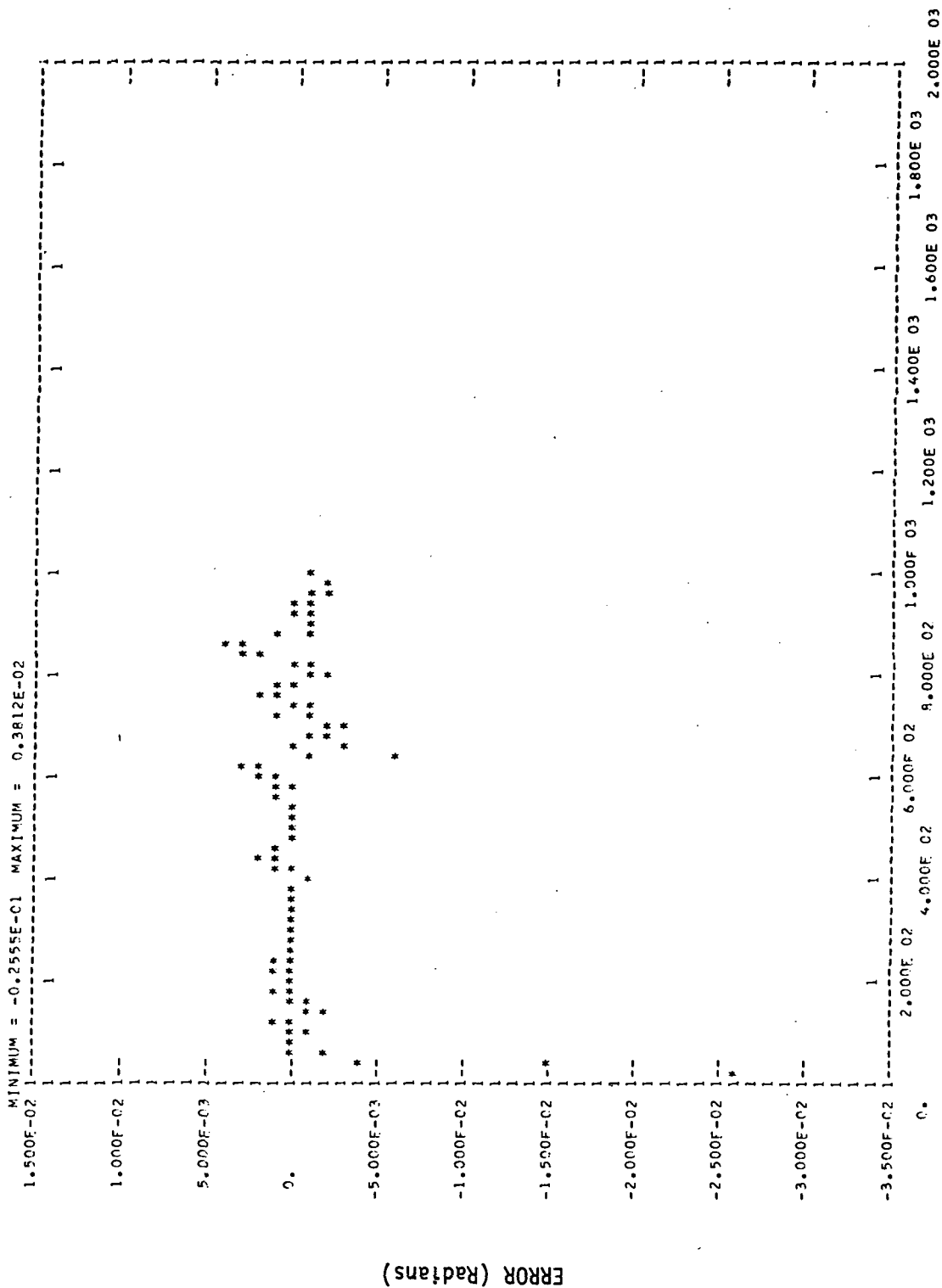
AIRCRAFT FLIGHT PATH SEGMENTS

X AT START	0.500E 04	0.100E 04	0.	0.	0.	0.	0.	0.	0.	0.
Y AT START	0.260E 03	0.550E 02	0.	0.	0.	0.	0.	0.	0.	0.
Z AT START	0.873E 02	0.175E 02	0.	0.	0.	0.	0.	0.	0.	0.
X AT FINISH	0.100E 04	0.200E 02	0.	0.	0.	0.	0.	0.	0.	0.
Y AT FINISH	0.100E 02	0.550E 02	0.	0.	0.	0.	0.	0.	0.	0.
Z AT FINISH	0.175E 02	0.349E 00	0.	0.	0.	0.	0.	0.	0.	0.
NUMBER OF INCREMENTS	50	50	0	0	0	0	0	0	0	0

REFLECTING SURFACES

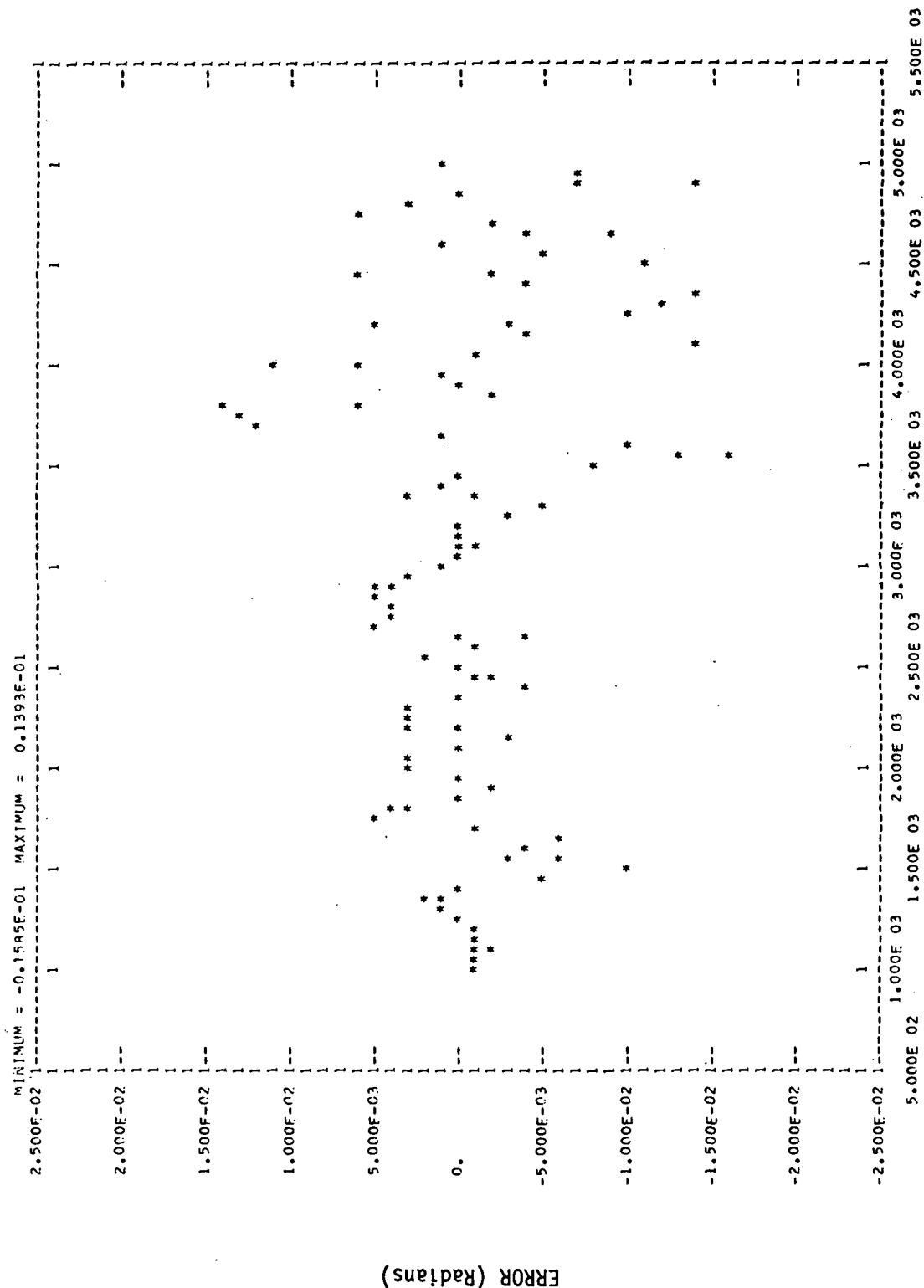
SURFACE NUMBER	STARTING COORDINATES	ENDING COORDINATES	PERMITIVITY	ROUGHNESS
	X	X		
1	-0.10000E 04	0.50000E 03	0.80000E 02	0.50000E-01
2	-0.10000E 04	-0.50002E 03	0.80000E 02	0.50000E-01
3	0.20000E 02	0.60000E 03	0.20000E 02	0.10000E-02
4	0.60000E 03	0.63000E 03	0.20000E 02	0.10000E-02
5	0.	0.	0.	0.
6	0.	0.	0.	0.
7	0.	0.	0.	0.
8	0.	0.	0.	0.
9	0.	0.	0.	0.
10	0.	0.	0.	0.

PLOT OF ANGULAR ERROR VERSUS RANGE



RANGE (Meters)
RUN 15

PLOT OF ANGULAR ERROR VERSUS RANGE



COMMENTS ON ILM APPLICATION

The MADGE equipment as it now exists is not capable of Category III operation. Severe multipath environments can cause errors to exceed the limits for Category III equipment, focusing errors cause excessive geometric biases, and the system is not configured to provide roll out guidance. The following changes should be made to MADGE to provide a workable Category III equipment:

- o The interferometer arrays should be focused.
- o The azimuth array should be replaced with a space diversity array.
- o The go-around azimuth unit should be mounted back to back with the regular azimuth unit, and the pair positioned at the approach end of the runway as shown in Figure 22.
- o The arrays should be extended to provide better multipath averaging.

By mounting the go-around unit back to back with the azimuth unit, its measurements can be used for roll out guidance.

A space diversity interferometer system employing these features can function successfully as a Category III independent landing monitor in extreme multipath environments.

The coverage of MADGE with these modifications would be unchanged from the basic MADGE system except that the extended array would allow elevation angles down to zero to be covered, i.e., the coverage is $\pm 45^\circ$ azimuth, 0° to 26° in elevation, and 50 Km in range. System saturation and mutual interference are approximately the same as any airborne controlled DME. The only significant difference between MADGE transmissions and normal (VORTAC) DME, is the extended reply code containing angle data. MADGE could thus be expected to saturate when about 180 aircraft are interrogating one system. The equipment as configured has 12 channels to prevent nearby installations from interfering. This would be sufficient until large numbers of MADGE units became operational. More channels could be allocated if necessary.

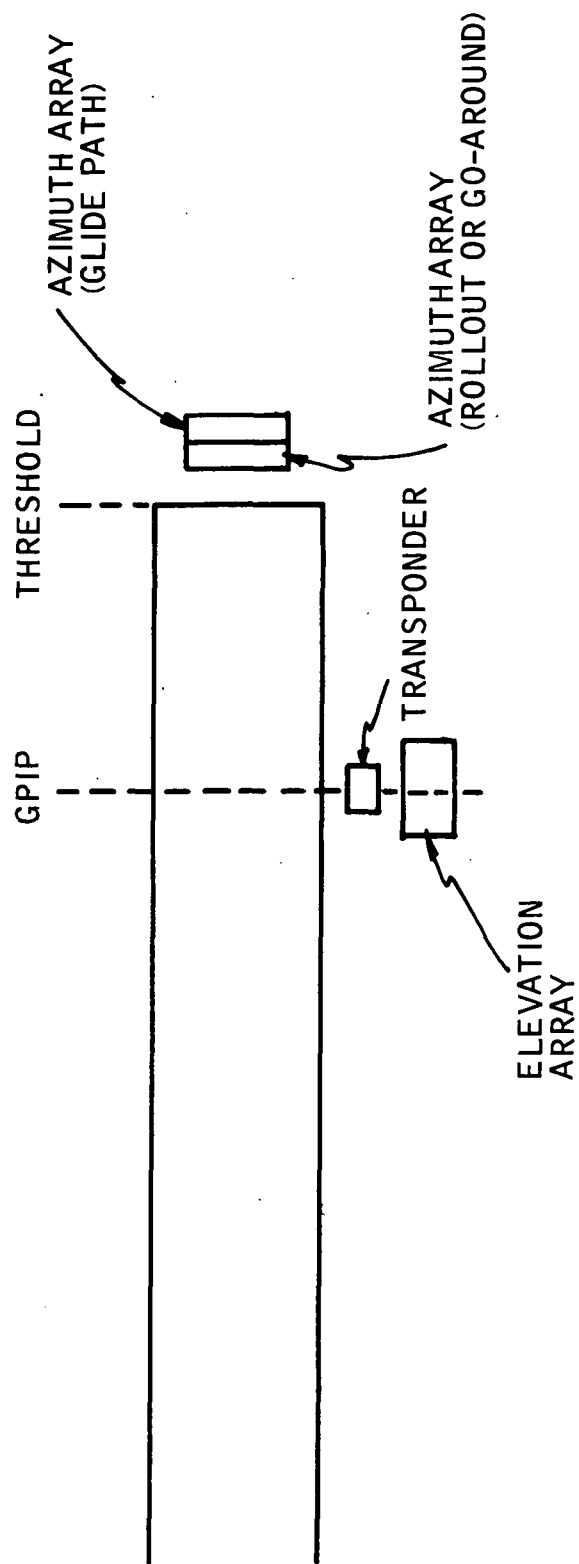


Figure 22. Location of Equipment for MADGE ILM Application

Some additional processing is required to focus the interferometer arrays.

Thus the transponder could be expected to be somewhat larger than the current MADGE system. Both elevation and azimuth antennas would have to be larger than the basic MADGE to allow Category III operations. The approximate parameters of a modified system are given in Table 10.

The production cost for the complex interferometer/DME concept (Figure 2) was estimated by breaking it into it's major components and estimating costs of these. Cost of the airborne unit is as follows:

DME and Antenna	- \$ 8,000.00
Data Link Decoding and Signal Averaging Logic	- \$ 4,000.00
Cross Pointer Display	- <u>\$ 1,000.00</u>
TOTAL	\$13,000.00

The cost of the ground unit for one azimuth and one elevation antenna is as follows:

20 Receivers at \$1,000 ea.	- \$20,000.00
20 Antennas at \$500 ea.	- \$10,000.00
Data Processing Logic	- \$ 5,000.00
Ground Transmitter	- <u>\$ 6,000.00</u>
TOTAL COST	\$41,000.00

A second set of azimuth/elevation antennas, if required for touchdown and rollout Category III operations would cost another \$35,000.00 or a total of \$76,000.00 for the ground system. Estimated weight of the airborne unit is 8 kgms.

Table 10

MODIFIED MADGE PARAMETERS

Band	C-Band
Power	200 W
Bandwidth	3 MHz
Size, Weight	
Aircraft Unit	2-3/8 ATR short 8 Kg
Ground Unit	
Azimuth Array	2 M x .3 M x .8 M 80 Kg
Elevation Array	3 M x .4 M x .3 M 50 Kg
Transponder	.6 M x .5 M x .5 M 30 Kg
Prime Power	
Aircraft Unit	100 W
Ground Unit	350 W

ANALYSIS OF A CIRCULAR SYNTHETIC APERTURE LOCATION SYSTEM FOR ILM

INTRODUCTION

This study analyzes a circular, synthetic aperture location system called "Astrolabe" being developed by the Office National d'Etudes et de Recherches Aeronautiques (ONERA), Chatillon, France. Although results are derived for the capabilities of this specific application, the analysis of the concept shows that the results are representative of the much broader class of synthetic aperture systems deriving resolution improvement by rotating antenna element pairs. The precision of the system is directly proportional to antenna element separation and has the potential for providing independent landing monitor (ILM) "back-up" or redundancy for low visibility landings with the adverse weather conditions and accuracies as specified in Reference 1.

CONCEPTUAL DESCRIPTION

The concept by which Astrolabe works is based on the grating lobe structure of a two element array where the elements are separated by a distance, R , much larger than the wavelength, λ , of consideration. A representative grating lobe pattern is shown in Figure 23. The pattern is shown in two dimensions although it should be considered that a similar pattern exists in the third dimension also. The phenomena that allows the Astrolabe system to resolve the grating lobe ambiguities is the non-uniform separation (in angle) of the grating lobe structure. More specifically, it is shown in Appendix C and Reference 5 that the multi-dimensional correlation function of the received grating lobe structure can be represented by a Bessel function. Appendix C shows the particular matched filter realization of the electro-optical system used in the Astrolabe receiving system and demonstrates how the apparatus can be altered to modify the correlation function shape and trade off correlation function anomalies.

The correlation processing may be visualized as the movement of a "mask" which is representative of the grating-lobe pattern signal being received. The movement of the mask to a position which optimizes the registration determines the angular coordinates of azimuth and elevation angle. The

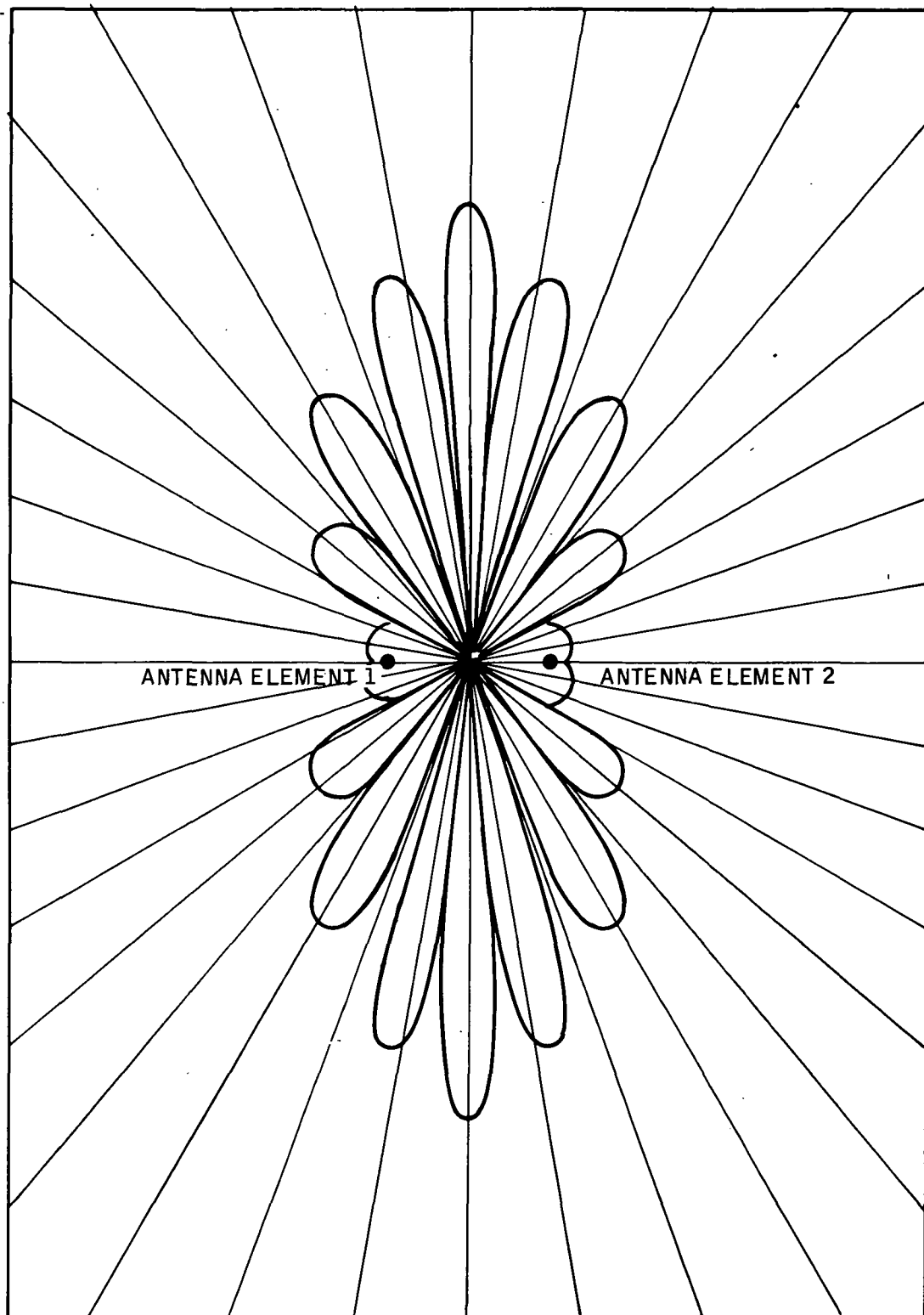


Figure 23. Antenna Grating Lobe Pattern Representation

analogy of a "mask" is used because the electro-optical apparatus in the Astrolabe system uses an optical transparency mask to perform the correlation by synchronizing the movement of the mask to the spinning of the antenna, uniformly illuminating the mask with a light source with intensity proportional to the square-law detected signal, and observing the correlation pattern produced as the eye integrates the light transmitted through the spinning mask.

The concept is valid for either a spinning transmitting or receiving antenna pair. This can be seen from the expressions in Appendix C for the two signals (one from each antenna) input to the detector.

$$A_1 \exp j(\Omega t - \Omega \frac{d_1}{c})$$

$$A_2 \exp j(\Omega t - \Omega \frac{d_2}{c})$$

The signals depend only on the absolute separations, d_1 and d_2 , between the transmitting and receiving elements. Similarly, doppler shift expressions (which modify Ω) depend only on relative motion between elements. The system concept is thus unchanged whether a single, fixed-gain receiving antenna detects a revolving, grating-lobe transmitting pattern or a single, fixed gain transmitting antenna is detected by a revolving, grating-lobe receiving antenna pattern.

GEOMETRICAL CONSIDERATIONS

The basic system concept described in Appendix C obtains angular information by interpreting the received signal produced by square-law detection of the superimposed signals from two revolving antenna elements. The geometries to be considered may consist of rotating transmitter or receiver antenna element pairs either on the ground or in the aircraft. The angular information is available only at the receiver unless a separate data link is provided.

The angular information consists of azimuth, θ_s , measured in the plane of rotation of the antenna pair (with an arbitrarily chosen "zero" reference)

and elevation angle, ψ_s , relative to the plane of rotation (plane of rotation is defined as the plane normal to the axis of rotation and containing the center of the array.)

Background

Reference 6 derives the expressions for the correlation function and relates each term of the expression to the correlation phenomena produced in the electro-optical receiving and display apparatus. The azimuth and elevation angle determination is made on the resolution of points with an intensity profile described by the Bessel function $J_0[\sqrt{A^2 + B^2}]$ and $J_0[\sqrt{A'^2 + B'^2}]$. The two terms correspond to a false target at $-\theta_s$ and ψ_s and the true location at θ_s , ψ_s . Assuming that the system is initialized to remove the false correlation point as per reference 6 (i.e., $\alpha + \beta = \pi/2$), we have as the expression for the true location point intensity profile: (See Appendix C for definition of terms.)

$$C_0 J_0[\sqrt{A'^2 + B'^2}]$$

$$\text{where } \sqrt{A'^2 + B'^2} = \left[\frac{\pi^2 P^2}{\delta^2} - \frac{8\pi^2 PR}{\delta \lambda} \cos \psi_s \cos(\theta_s - \theta_o) + \frac{16\pi^2 R^2}{\lambda^2} \cos^2 \psi_s \right. \\ \left. \cos^2(\theta_s - \theta_o) + \frac{16\pi^2 R^2}{\lambda^2} \cos^2 \psi_s \sin^2(\theta_s - \theta_o) \right]^{1/2}$$

$$= \left[\frac{\pi^2 P^2}{\delta^2} - \frac{8\pi^2 PR}{\delta^2} \cos \psi_s \cos(\theta_s - \theta_o) + \frac{16\pi^2 R^2}{\lambda^2} \cos^2 \psi_s \right]^{1/2} \quad (2)$$

Making the substitution $P = \frac{4\delta R}{\lambda} \cos \psi$,

$$\sqrt{A'^2 + B'^2} = \frac{4\pi R}{\lambda} [\cos^2 \psi - 2 \cos \psi \cos(\theta_s - \theta_o) \cos \psi_s + \cos^2 \psi_s]^{1/2} \quad (3)$$

ψ_s and θ_s are the desired angular references (actual values). $\theta_{ant} = \omega t + \theta_s$ is the time dependent reference of the spinning antenna. The disk which performs the cross-correlation is spinning with the same angular frequency, ω , such that its angular time expression is $\theta_{disk} = \omega t + \theta_o$. The relationship between θ_s and θ_o is thus some constant which allows expression of angular position, θ_o , on the disk to the true azimuthal position θ_s . The value

$\theta_s - \theta_o$ in the above expression is a constant value which is chosen to simplify calculations.

Reference 6 provides a description of the coefficients of the Bessel function. These coefficients, $\sqrt{A'^2 + B'^2}$ and $\sqrt{A'^2 + B'^2}$ are described as vector magnitudes. The magnitude, $\sqrt{A'^2 + B'^2}$, is represented as $|\vec{u} - \vec{v}|$ where \vec{v} describes the receiver location and \vec{u} describes the observed correlation point on the disk. These vectors are shown in Figure 24. To analyze the effects of spot size on the disk as a function of angular position, the vectors are set equal, $\vec{u} = \vec{v}$, such that $\theta_s = \theta_o$ and $|\vec{u} - \vec{v}|$ approaches 0 for ψ approaching ψ_s . The previously derived expression for $\sqrt{A'^2 + B'^2}$ becomes (for $\theta_s - \theta_o = 0$):

$$\sqrt{A'^2 + B'^2} = \frac{4\pi R}{\lambda} (\cos \psi - \cos \psi_s) \quad (4)$$

When the vectors are equal, $\vec{u} = \vec{v}$, the spot profile is independent of θ and the variation of $J_0 [\sqrt{A'^2 + B'^2}]$ as ψ approaches ψ_s is descriptive of the spot intensity variation with elevation angle. Since $\sqrt{A'^2 + B'^2} = 1.55$ corresponds to the 3 dB point of the Bessel function, this definition of resolution may be used to derive the value of ψ corresponding to the 3 dB point and thus derive the precision of the correlation function.

$$\text{Thus, } 1.55 = \sqrt{A'^2 + B'^2} = \frac{4\pi R}{\lambda} (\cos \psi_{3dB} - \cos \psi_s) \quad (5)$$

$$\text{or } \psi_{3dB} = \cos^{-1} \left[\frac{1.55 \lambda}{4\pi R} + \cos \psi_s \right] \quad (6)$$

Subtracting ψ_s we obtain the angular uncertainty corresponding to the 3 dB point of the correlation function.

$$\Delta\psi = \psi_{3dB} - \psi_s \quad (7)$$

The relationship of $\Delta\psi$ as a function of ψ_s is shown in Figure 25.

The precision of the correlation function in the θ , or azimuth position may be determined from the geometrical symmetry of the spot at distance P from the center of the disk. From the derivation of the correlation function in

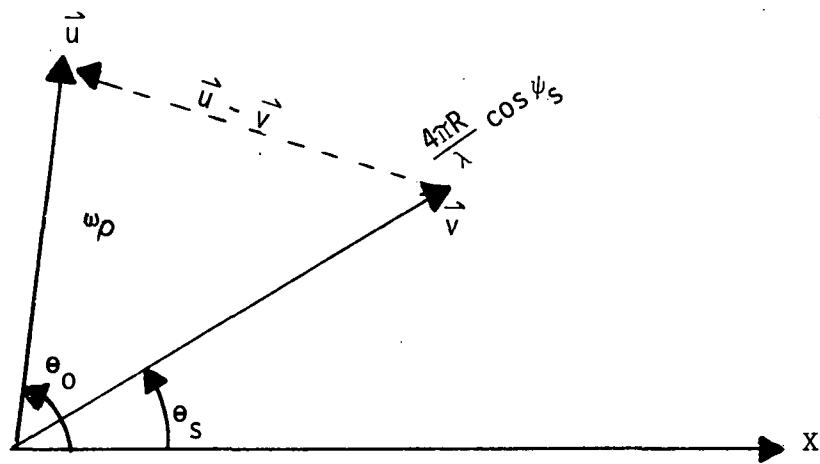


Figure 24. Vector Diagram of u and v

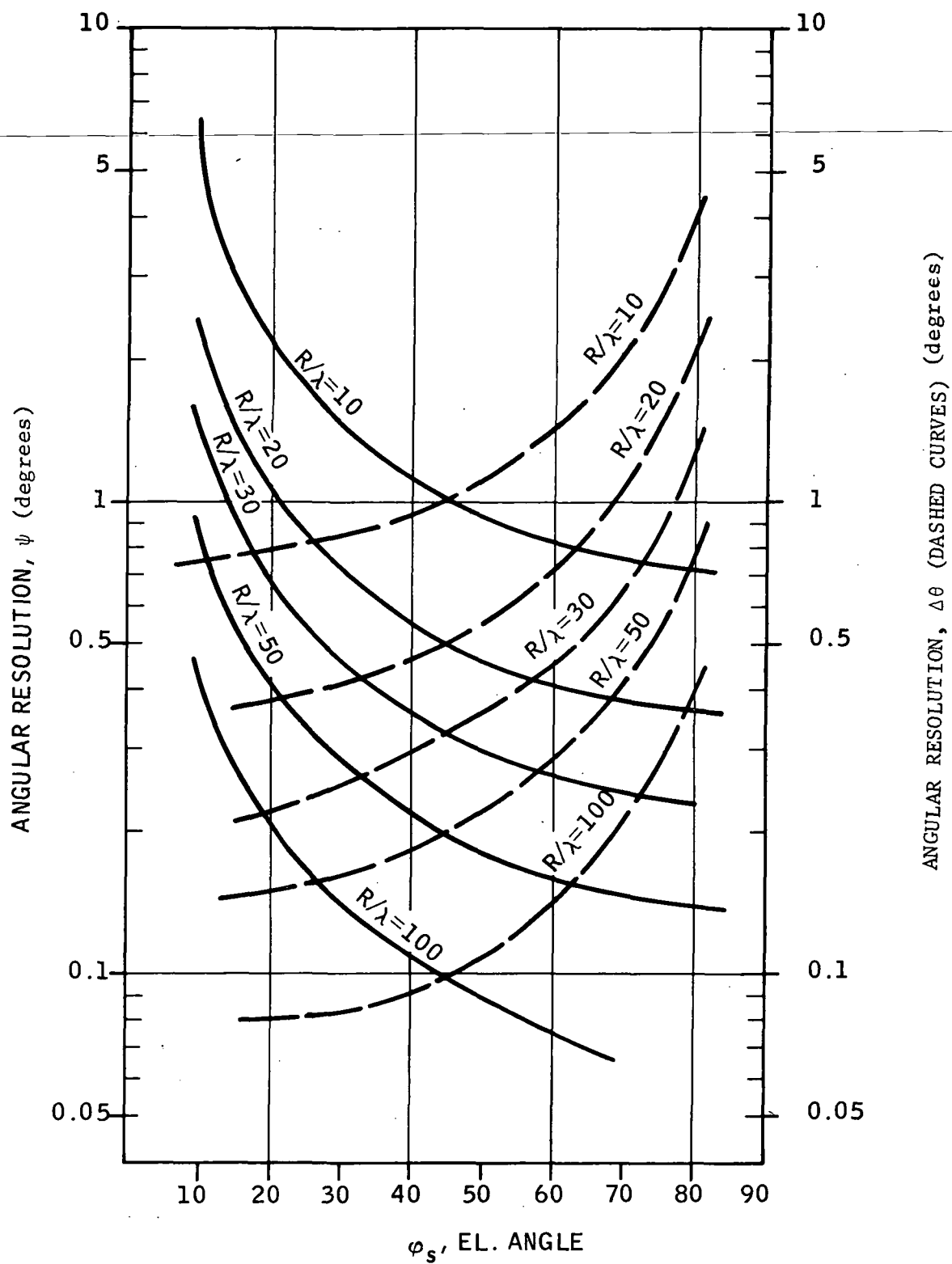


Figure 25. Angular Uncertainty as Function of Elevation Angle

Appendix C, it is known that the spot at the point (P, θ_0) is a circle. The dimension in the $\Delta\psi$ direction is the same as the dimension in the $\Delta\theta$ direction. The radius at the spot is:

$$\begin{aligned} \text{distance} &= \frac{4\delta R}{\lambda} \cos(\psi + \Delta\psi) \\ &\approx \frac{4\delta R}{\lambda} (\cos \psi - \Delta\psi \sin \psi) \\ &= \frac{4\delta R}{\lambda} \cos \psi - \frac{4\delta R}{\lambda} \Delta\psi \sin \psi \end{aligned} \quad (8)$$

The circumference at this elevation is

$$2\pi \cdot \text{Radius} = \frac{8\pi\delta R}{\lambda} \cos \psi \quad (9)$$

Thus

$$\frac{\Delta\theta}{2\pi} = \frac{\frac{4\delta R}{\lambda} \Delta\psi \sin \psi}{\frac{8\pi\delta R}{\lambda} \cos \psi} = \frac{\Delta\psi \sin \psi}{2\pi \cos \psi} \quad (10)$$

$$\Delta\theta \cos \psi = \Delta\psi \sin \psi \quad (11)$$

This relationship for the azimuthal uncertainty as a function of elevation angle and elevation uncertainty is also plotted in Figure 25 to show how the uncertainties relate.

Accuracies and Precision

Angular precision has been derived in the previous section to describe the repeatability of the correlation function spot position. The application of the electro-optical correlation apparatus described for the Astrolabe reference provides correlation function analysis and interpretation by human observer techniques. Operational tests of the Astrolabe concept using this apparatus for display and parameter retrieval have demonstrated 2σ accuracies comparable to the anticipated theoretical precision (Reference 5). The theoretical precisions derived in the previous section will thus be used as a baseline to analyze conceptual capabilities.

The study of the correlation function parameters identified angular deviations, $\Delta\theta$ and $\Delta\psi$, which are descriptive of the conceptual ability for measuring

direction with respect to the spinning antenna reference frame. The receiver processing is limited to deriving angular information referenced to the spinning antenna at the receiver. If the spinning antenna is the receiving antenna, the angles may be directly referenced to the receiver's reference frame. Otherwise, the angles derived are relative to the spinning transmitting antenna and additional reference angles may be required in order to orient the two separate reference frames. Table 11 provides a comparison of the different geometrical configurations for concept implementation. Systems consisting of one or more antenna placement geometries will derive guidance or position fixing by three techniques; location corridor, corridor triangulation, and geometrical shape orientation.

Location Corridor

The Location Corridor for monitoring consists of establishing directions, θ and ψ , within the angular uncertainties of $\Delta\theta$ and $\Delta\psi$. Linear uncertainties are $SR \cdot \Delta\theta$ and $SR \cdot \Delta\psi$ where SR is the unknown slant range between the receiving and transmitting antennas. θ and ψ are referenced to whichever antenna is spinning. Figure 26 shows the linear uncertainty as a function of antenna element separation and range.

Corridor Triangulation

Corridor Triangulation establishes location by intersection of two or more independent (separated) location corridors. The corridors defined by $SR_1 \cdot \Delta\theta_1$ and $SR_1 \cdot \Delta\psi_1$ and $SR_2 \cdot \Delta\theta_2$ and $SR_2 \cdot \Delta\psi_2$ may or may not intersect for each set of direction angles measured, $\Delta\theta_1$, $\Delta\psi_1$, and $\Delta\theta_2$, $\Delta\psi_2$. Assuming that sufficient integration time is available to provide corridor intersection as defined by the precision $\Delta\theta$, $\Delta\psi$ and eliminating non-intersections as false multipath targets, the volume defined by the intersection will have a maximum cross-sectional linear dimension of the larger of:

$$\begin{aligned} & SR \cdot \Delta\psi \\ & \frac{SR \cdot \Delta\theta}{\cos(\sin^{-1} \frac{D}{2SR})} \\ \text{and} \quad & \frac{2 \cdot SR^2 \cdot \Delta\theta}{D} \end{aligned} \quad \Delta \text{ angles in radians}$$

Table 11. Geometrical Configuration Consideration

Configuration		ψ, θ angles	Altitude, Range (one on many)	Position Derivation	Comments
Information Retrieval With Relay to the Aircraft 1. Ground Receiver(s), Airborne Transmitter, Ground Transmitter, Airborne Receiver, 2.	Spinning Receiving Antenna(s) A	Angles to aircraft relative to aircraft ψ_a, θ_a	Derived by triangulation based on known separations	Angular position only for single case Multiple case gives position estimate	Single transmitter on ground could provide aircraft with approach guidance on a radial into the airport. Multiple transmitters could provide additional range and altitude estimates for aircraft position relative to the runway.
	Spinning Receiving Antenna(s) B	Angles to aircraft relative to aircraft ψ_g, θ_g	Derived by triangulation based on known separations	No info beyond accuracy of instru- ments for single case Multiple case gives position estimate	Single transmitter on ground could provide direction of airport relative to the aircraft to the aircraft but estimates of airport approach radial and glide- slope would be dependent on and no more accurate than aircraft instruments.
	Spinning Transmitting Antenna A	Angles to airport relative to aircraft ψ_a, θ_a	Derived by triangulation based on known separations	No information without knowledge of aircraft instrument readings Multiple case gives position estimate	Multiple beacons could provide an image of the beacon geometry which would allow estimating the aircraft position on a radial and aircraft aspect.
	Spinning Transmitting Antenna(s) B	Angles to airport relative to aircraft ψ_g, θ_g	Derived by triangulation based on known separations	Angular position only for single case Multiple case gives position estimate	Single receiver provides only the direction from the aircraft to the airport which is of no value without knowledge of aircraft aspect. Multiple receivers could provide an estimate of aircraft position and aspect by image correlation similar to 2A above.
		Angles to aircraft relative to aircraft ψ_g, θ_g	Derived by triangulation based on known separations	Angular position only for single case Multiple case gives position estimate	Single receiver provides approach guidance (radial location) similar to 2B above except aircraft aspect information would not be available. Multiple receivers provides aircraft location similar to 2B above except no aircraft aspect information would be available.

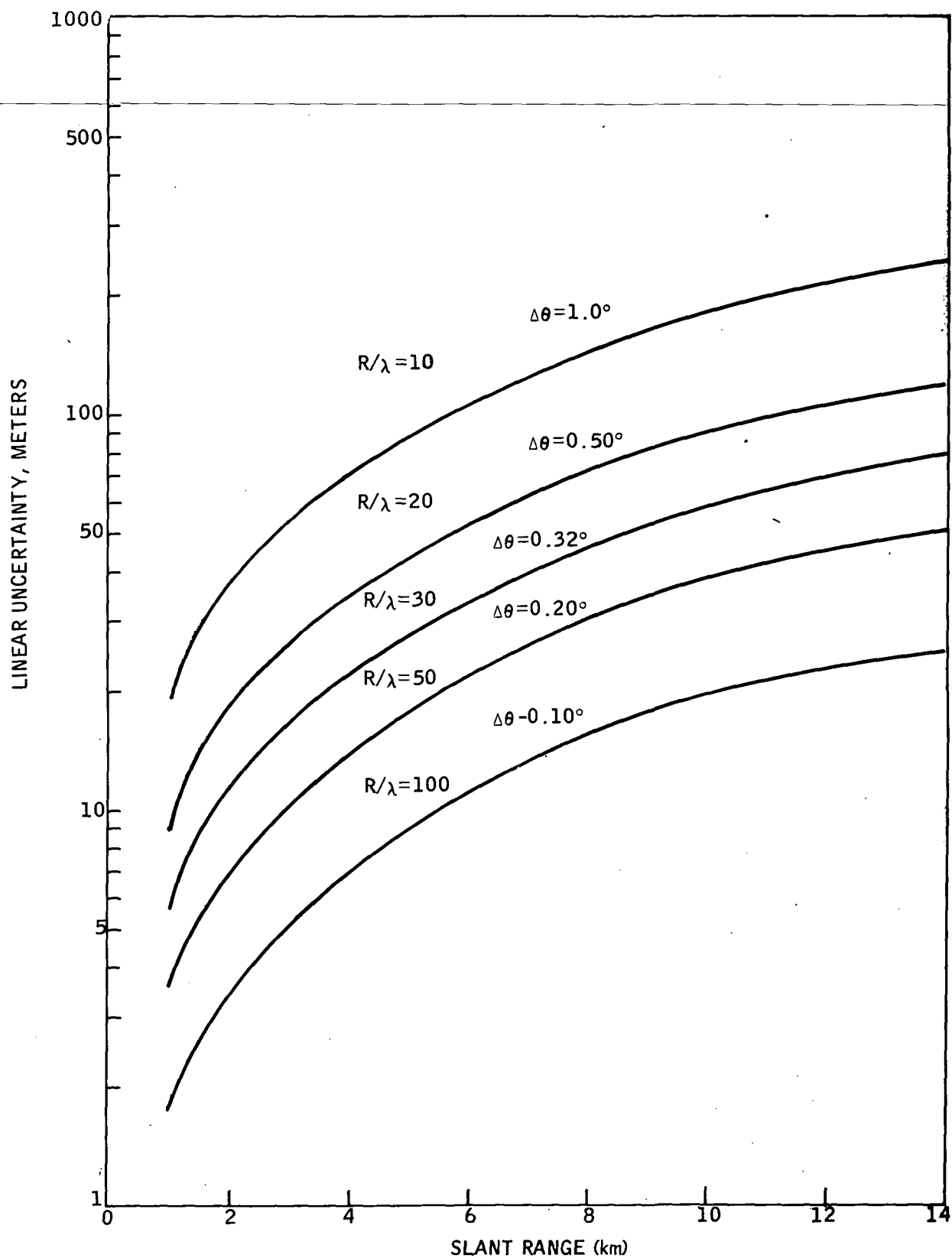


Figure 26. Linear Uncertainties for $\Delta\theta = \Delta\psi$ ($\psi = 45^\circ$)

These expressions are derived from Figure 27. An independent landing monitor will require resolving angular deviations in both horizontal position and altitude if dependence on other systems (such as a radar altimeter) are to be avoided. Equal azimuthal and elevation angle precisions will be assumed to provide comparable accuracies. Altitude accuracies (two σ values) within the $SR \cdot \Delta\psi$ precision should be expected with similar values for azimuth accuracy (See Figure 26) at longer ranges ($2 \cdot SR \gg D$) degrading as d_1 . Range accuracy for this assumed configuration with the location corridor sites straddling the runway would thus vary as d_2 . Figure 28 is a graph of the factor $\frac{d_2}{d_1}$ which relates range precision to azimuth precision (and similarly, the accuracies) so that expected ranging performance may be anticipated by using the graph of Figure 26 multiplied by the factor in Figure 28.

Geometrical Shape Orientation

The third possible technique for guidance or position fixing consists of determining aircraft location by measuring relative directions to a known geometry. An example of this would be beacons defining a runway edge. The two primary geometrical dimensions used for defining azimuthal (and elevation) angle deviation and range are shown in Figure 29. The angular deviations derived as a function of range will assume that point pairs used for range/roll attitude and azimuth/elevation angle derivation are known so that 90° approach ambiguities are not possible. Although the geometry is idealized, the results are indicative of guidance and positional capabilities.

The dimensions L and W represent the geometrical point separations. When $\theta_{\text{range}} \gg \Delta\theta$ (which may be assured by selecting W sufficiently large for the required detection ranges),

$$\sin \left(\frac{\theta_{\text{range}}}{2} \right) = \frac{W \pm 2 \cdot \text{Range} \cdot \Delta\theta}{2 \cdot \text{Range}} \quad (12)$$

$$\text{then Range} = \frac{\frac{W}{2} \pm \text{Range} \cdot \Delta\theta}{\sin \left(\frac{\theta_{\text{range}}}{2} \right)} \quad (13)$$

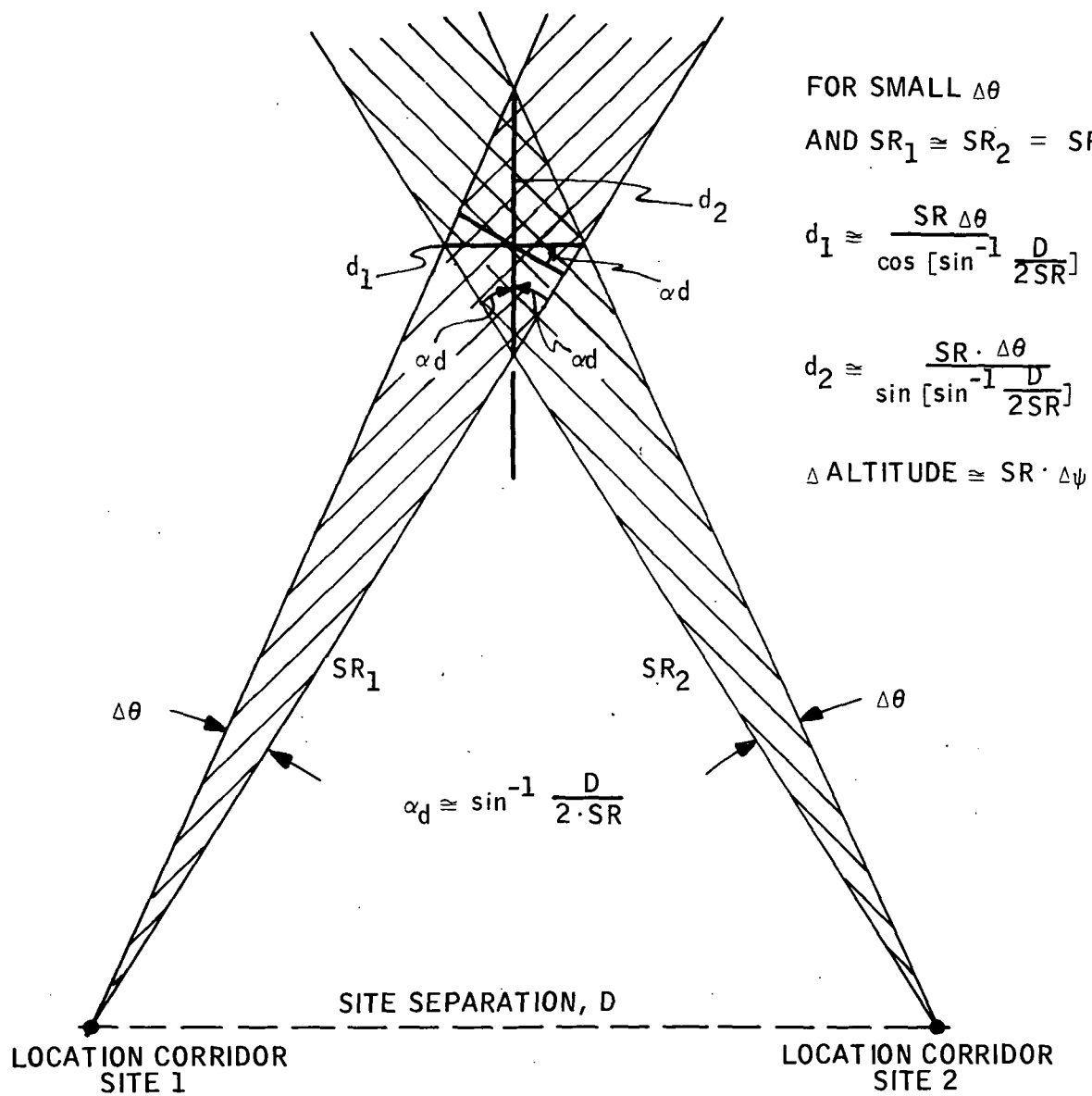


Fig. 27. Location Corridor Site Geometry for Corridor Intersection

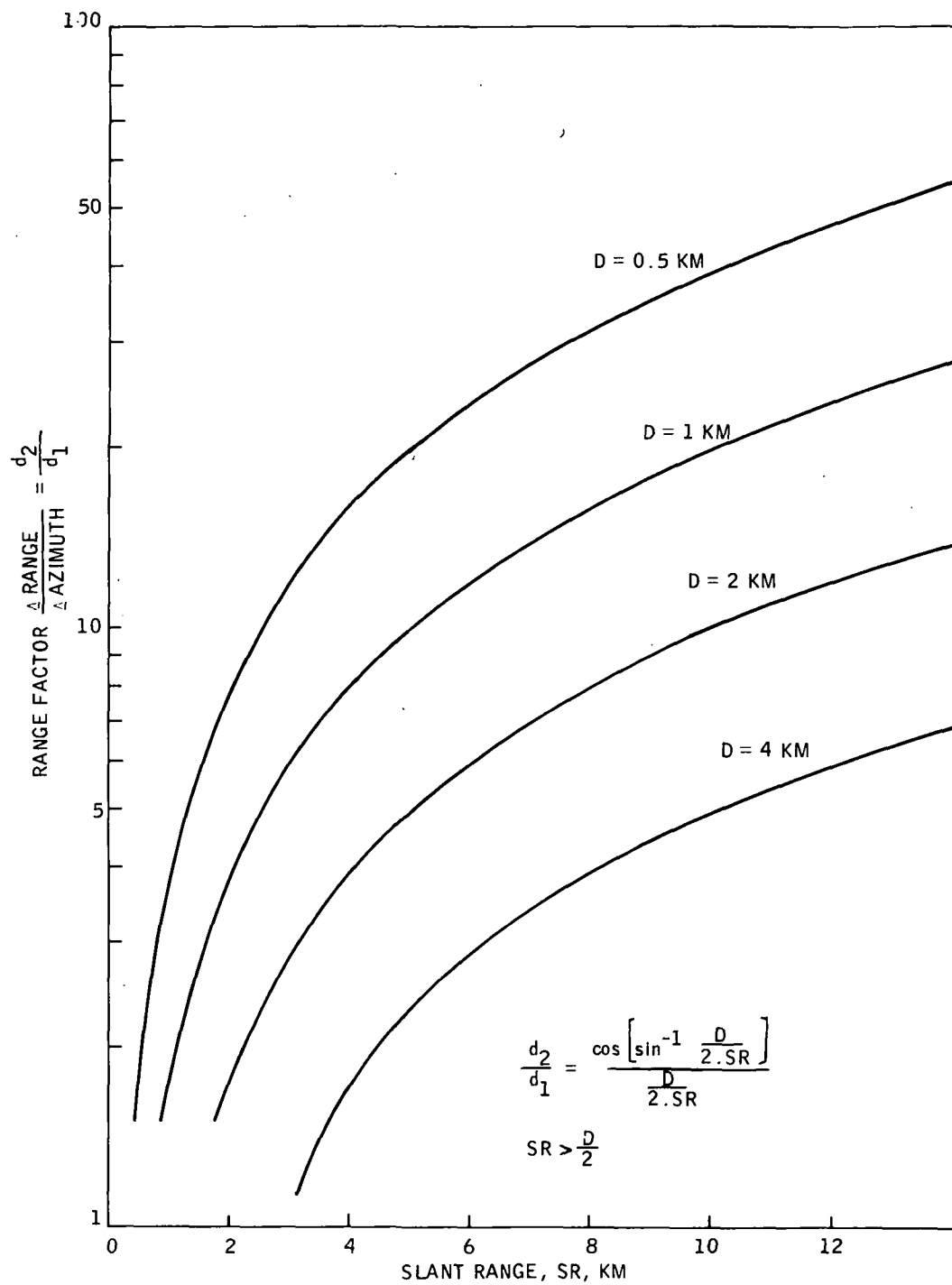


Figure 28. Relationship of Range and Azimuth Precision

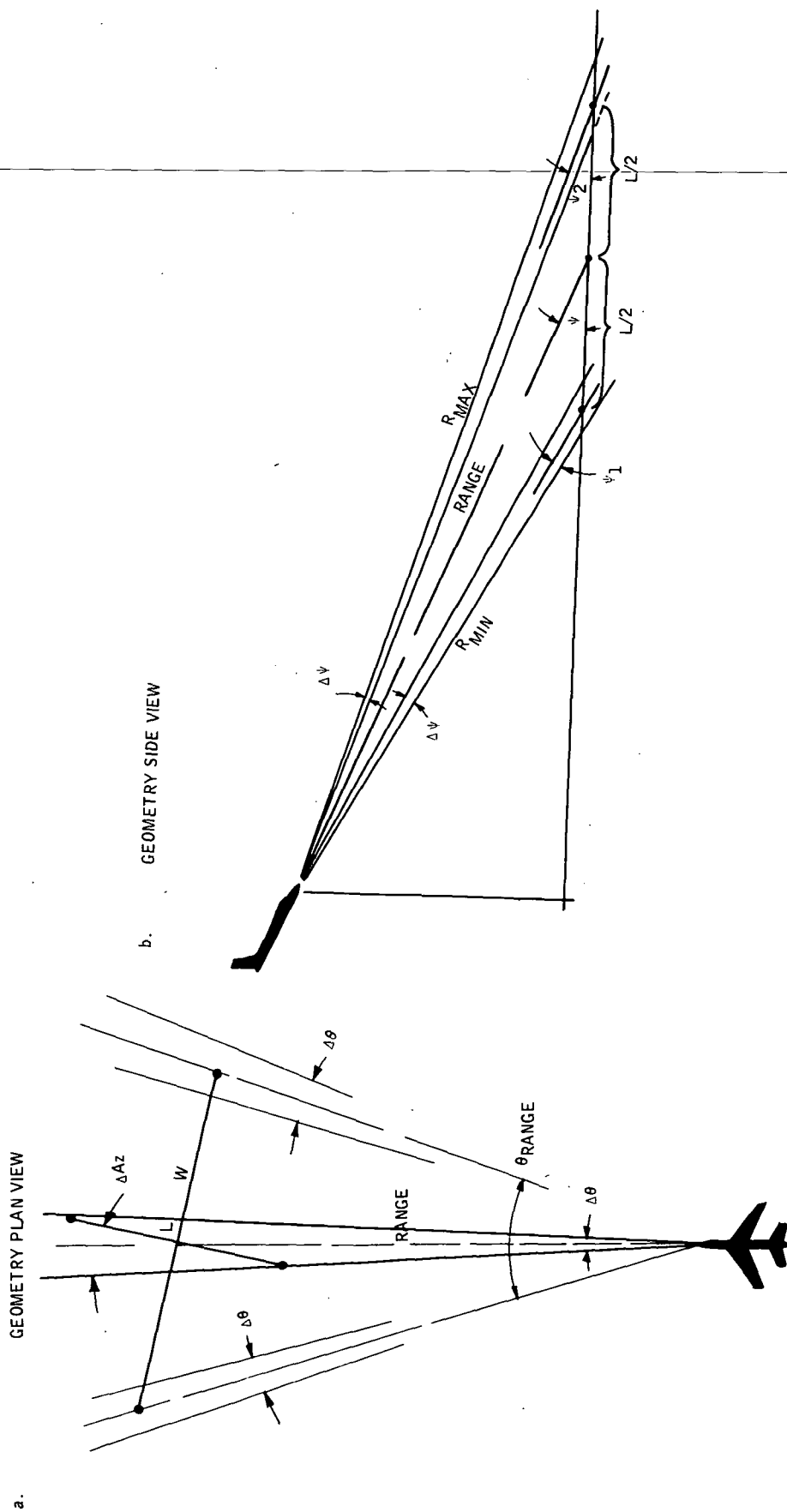


Figure 29. Geometry for Deviation of Guidance and Position from Known Ground Points

$$\text{or Range} \left[1 + \frac{\Delta\theta}{\sin\left(\frac{\theta_{\text{range}}}{2}\right)} \right] = \frac{W}{2 \sin \frac{\theta_{\text{range}}}{2}} \quad (14)$$

$$\text{Range} \left[1 + \frac{2 \cdot \text{Range} \Delta\theta}{W} \right] = \frac{W}{2 \sin\left(\frac{\theta_{\text{range}}}{2}\right)} \quad (15)$$

This expression may be evaluated to find the two ranges satisfying the limits. The total linear range variation, ΔRange , as a function of the actual range and the separation, W , may be defined as the difference of these two range values or:

$$\Delta \text{Range} \cong \frac{4 \cdot \text{Range}^2 \Delta\theta}{W} \quad (16)$$

The angular deviation from runway centerline, ΔAz is:

$$\Delta \text{AZ} \cong \sin^{-1} \frac{\left(\text{Range} + \frac{L \cos \psi}{2} \right) \Delta\theta}{L \cos \psi} \quad (17)$$

The elevation angle deviation, ΔEl is derived below.

$$R_{\min} = \left[(\text{Range} \cdot \cos \psi - \frac{L}{2})^2 + (\text{Range} \cdot \sin \psi)^2 \right]^{\frac{1}{2}} \quad (18)$$

and

$$R_{\max} = \left[(\text{Range} \cdot \cos \psi + \frac{L}{2})^2 + (\text{Range} \cdot \sin \psi)^2 \right]^{\frac{1}{2}} \quad (19)$$

For each of these ranges define an elevation angle ψ as shown on Figure 29b.

$$\psi_1 = \cos^{-1} \frac{\text{Range} \cdot \cos \psi - L/2}{R_{\min}} \quad (20)$$

$$\psi_2 = \cos^{-1} \frac{\text{Range} \cdot \cos \psi + L/2}{R_{\max}} \quad (21)$$

The deviation of the point locations within the envelopes of $\Delta\psi$ may vary the derived value of elevation angle, ψ_{der} , about the true value, ψ , such that:

$$\psi_{\text{der}} \cong \psi \pm \frac{\tan^{-1} \left[\frac{R_{\min} \cdot \Delta\psi}{L \cos \psi_1} + \frac{R_{\max} \cdot \Delta\psi}{L \cos \psi_2} \right]}{2} \quad (22)$$

$$\cong \psi \pm \frac{\tan^{-1} \left[\frac{\Delta\psi}{L} \left(\frac{R_{\min}}{\cos \psi_1} + \frac{R_{\max} \cdot \Delta\psi}{\cos \psi_2} \right) \right]}{2} \quad (23)$$

The total geometrical angular deviation is thus

$$\Delta\epsilon \cong \tan^{-1} \left[\frac{R_{\min} \cdot \Delta\psi}{L \cos \psi_1} + \frac{R_{\max} \cdot \Delta\psi}{L \cos \psi_2} \right] \quad (24)$$

Figure 30 shows the factor that is used to extend the results of Figure 26. It should be noted that the factor Δ Range is approximately twice the factor in Figure 28 such that range precision and accuracy of ranging for geometrical shape orientation is worst (approximately twice as large as location corridor intersection) for the same geometrical separation (W versus D).

Figure 31 shows ΔAz , the angular deviation from runway center line for 3° and 6° glide slope approaches. Guidance point separations, L, of 8 Km, 4 Km, and 2 Km are shown. The values are independent of ψ for $\psi \leq 6^\circ$. The error, or range of deviations, are $\pm \Delta Az$. For small angles, $\Delta Az < 10^\circ$, ΔAz is directly proportional to $\Delta\theta$, the azimuthal angle precision of the correlation function.

Figure 32 shows the elevation deviation. The curves are approximated in the region of sharp upsweep caused by overflight of the nearest geometrical reference point. The curves are insensitive to variations in ψ for $\psi < 10^\circ$ and are directly proportional to $\Delta\psi$ for $\Delta\psi < 1.0^\circ$. It becomes apparent that better elevation angle precision (almost by a factor of two) and a series of geometrical reference points are required to achieve the precision of a corridor location technique for glide slope guidance.

Conceptual Implementations

The applications for guidance or positioning by the three methods of corridor location, location corridor triangulation, and geometrical shape orientation are reviewed in Table 12. One conceptual implementation to achieve $\Delta\theta$ and $\Delta\psi$ angular precisions relative to each spinning antenna has been described as the Astrolabe system. Other implementations of this circular, synthetic

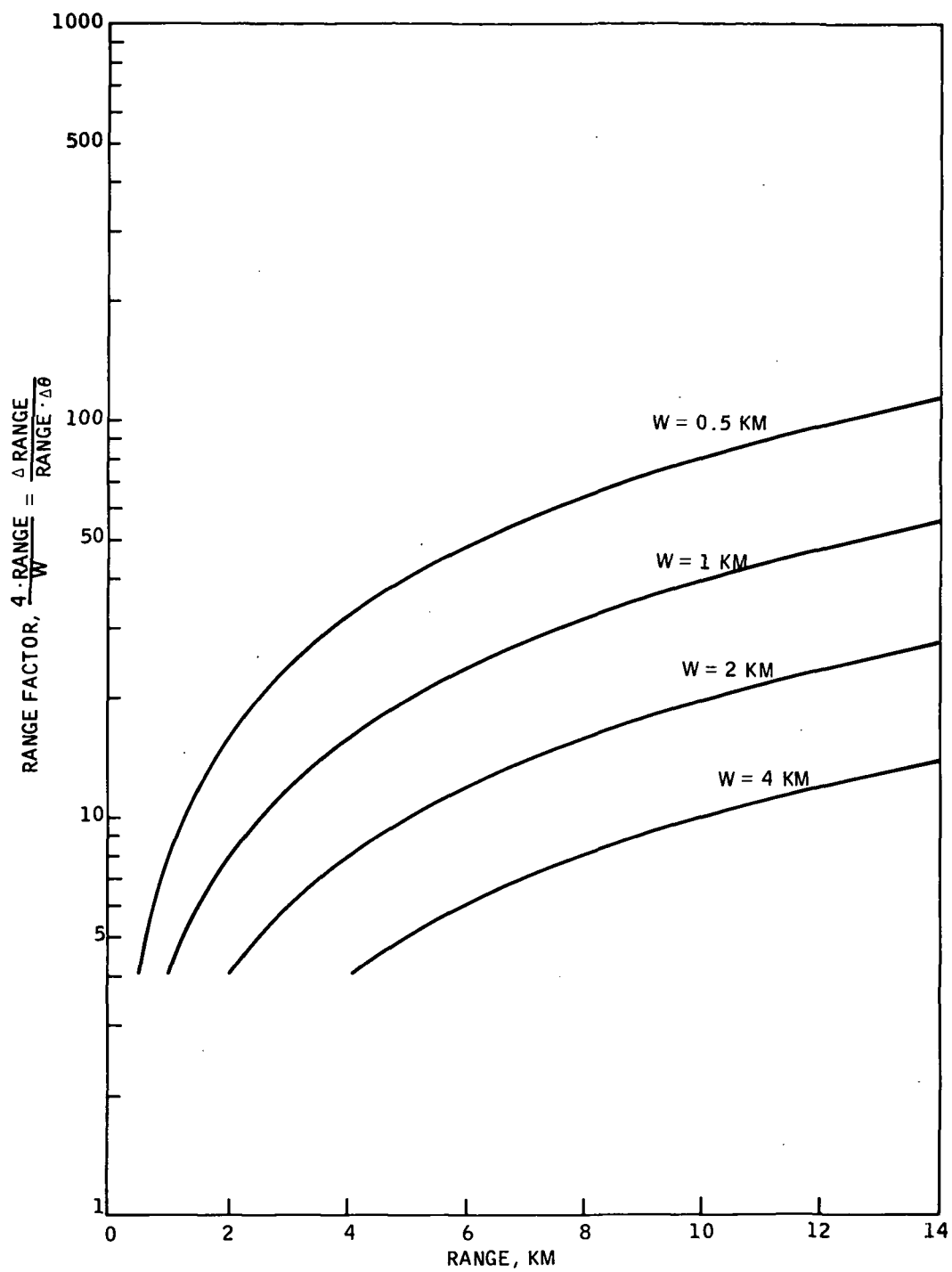


Figure 30. Factor to Derive Range Precision
for Geometrical Shape Orientation

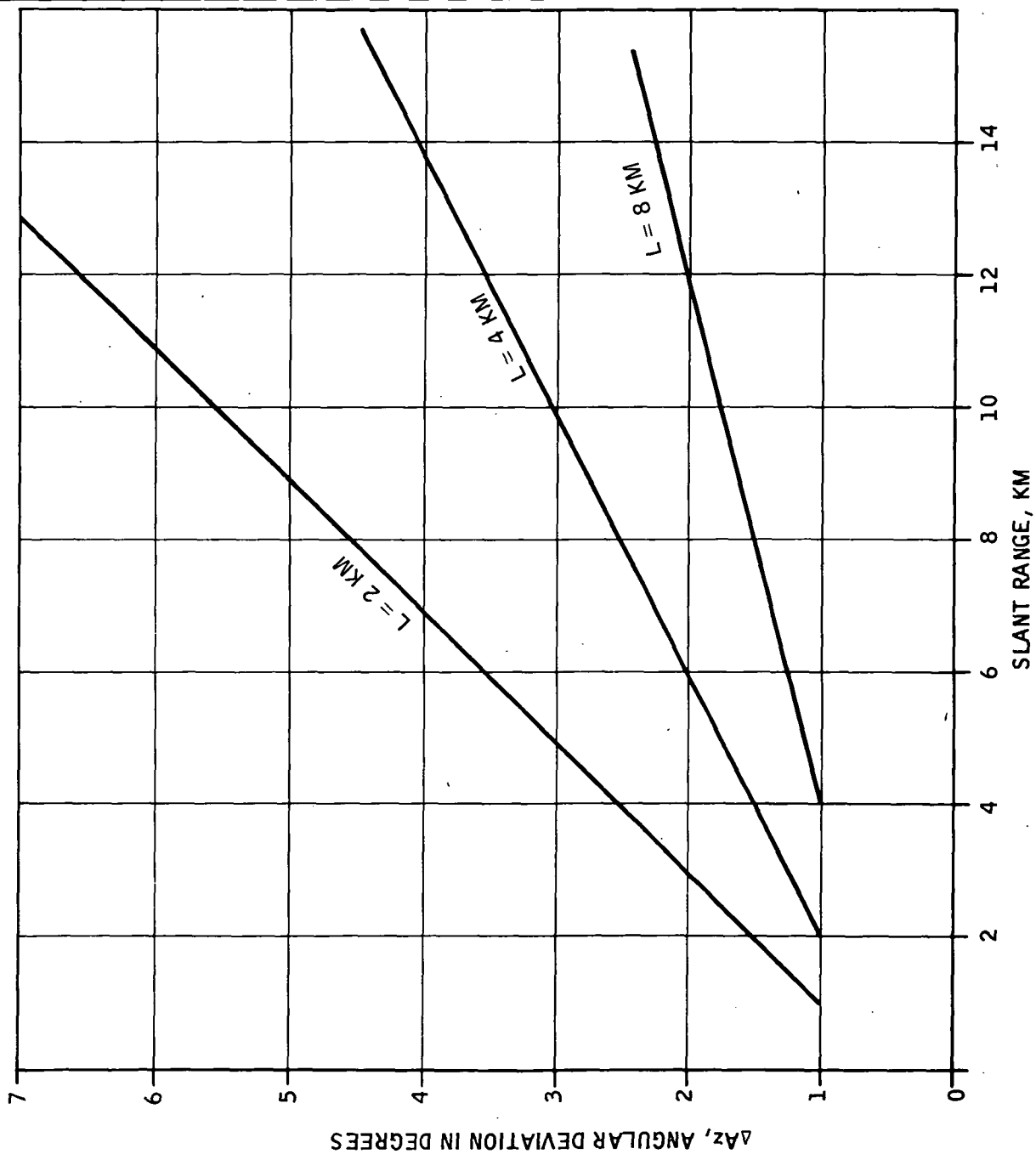


Figure 31. Azimuth Error as a Function of Geometry Point Separation, L and $\Delta\theta = 1.0^\circ$ ($\Delta Az \propto \Delta\theta$)

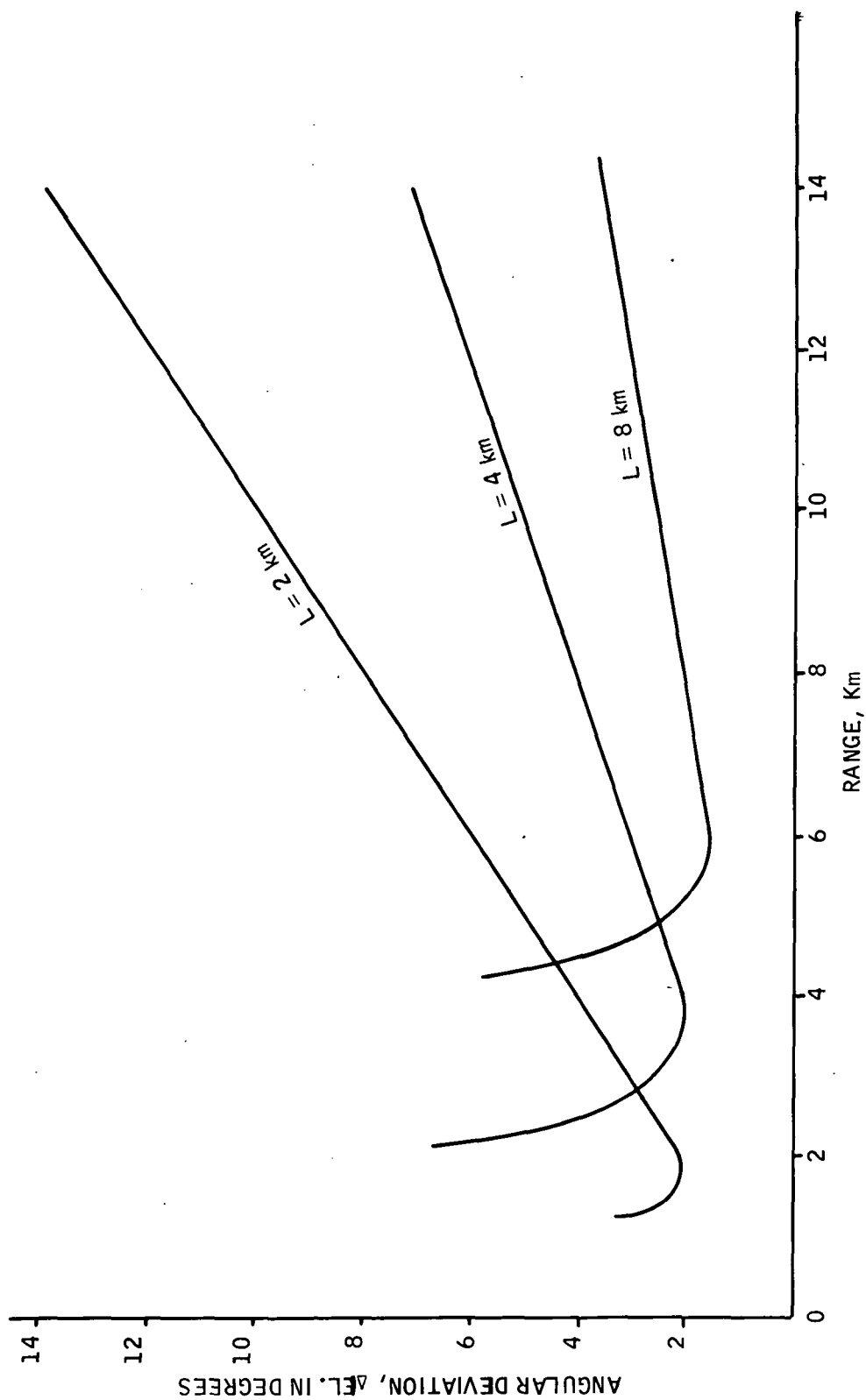


Figure 32. Elevation Angular Deviation as a
Function of Geometry Point Separation
 L , and $\Delta \psi = 1.0^\circ$ ($\Delta EL \propto \Delta \psi$)

Table 12. Mission Applications for Astrolabe Concept as an Independent Monitor

Mission	Astrolabe Configuration	Other System Inputs Required	Airborne Equipment Required	Ground Equipment Required	Comments
Cockpit information on approach corridor (azimuth and glide slope) to the ground based equipment	Configuration 2.B.1 (Airborne receiver, ground transmitter with spinning antenna) (corridor location)	Time reference to synchronize receiver processing with ground transmitting antenna rotational position	Receiving Antenna Receiver, Dual Channel Display for Az/EI Display Analyst	Spinning Antenna Fixed Antenna Transmitter, Dual Channel	Operation requires display interpretation by a crew member. System precision would approach SR-Δθ and SR-Δψ (SR is slant range between transmitting and receiving antennas)
	Configuration 1.A.1 (Airborne beacon, ground receiver with spinning antenna) (corridor location)	Data link to aircraft for directional information relay	Beacon Antenna Beacon Transmitter Data Link Antenna Data Link Receiver Az/EI Indicator	Spinning Antenna Receiver Receiver Processor Display for Az/EI Traffic Controller/Analyst Data Link Antenna Data Link Transmitter	Ground Personnel perform display interpretation. System precision approaches SR-Δθ and SR-Δψ
Cockpit information on aircraft position relative to the runway	Configuration 1.A.2 (Airborne beacon, ground receiver with multiple spinning antennas) (corridor triangulation)	Same as 1.A.1	Same as 1.A.1	Same as 1.A.1 1 additional spinning antenna	May have multipath limitations due to time multiplexing reducing integration time of the correlation function. Single receiver and processor limits the antenna spatial disposition. Multiple receivers, processors & analysts would be required for a system with SR-Δθ & SR-Δψ ranging precision. Angular precision in either case approaches Δθ and Δψ.
	Configuration 1.B.2 (Airborne transmitter with spinning antenna, multiple receiving antennas) (geometrical shape orientation)	Same as 2.B.1	Spinning Transmitting Antenna Fixed Antenna Transmitter, Dual Channel Data Link Antenna Data Link Receiver Az/EI/Range Indicator Optional Aircraft Aspect Indicator	4 Receiving Antennas Receiver Receiver Processor Display for Az/EI Traffic Controller/Analyst Data Link Antenna Data Link Transmitter Probable Computer Requirement	Same as 1.A.2 above with the additional considerations: <ul style="list-style-type: none"> Position precisions are degraded slightly compared to 1.A.2 above. Transmitting Antenna will require stabilization for precise measurements Display interpretation task will be much more difficult than 1.A.2 above since direct referencing to ground coordinates is not available until all angles received have been correlated with known geometry.
	Configuration 2.A.2 (Airborne spinning receiving antenna, multiple ground beacons) (geometrical shape orientation)	None	Spinning Receiving Antenna Receiver Receiver Processor Display for Az/EI Display Analyst	3 or 4 Beacon Antennas Transmitter, Commutated	Received image is somewhat geometrically similar to real-world perspective imagery. May have multipath limitations due to time multiplexing reducing integration time of the correlation function. Precisions of position measurements are similar to 1.B.2 above. Receiving antenna stabilization is necessary for maximum precision.
	Configuration 2.B.2 (Airborne Receiver, multiple spinning transmitting antennas) (corridor triangulation)	Same as 2.B.1	Receiving Antenna Receiver, Dual Channel Receiver Processor Display for Az/EI Display Analyst Possible Computer or Other Triangulation Aids Required	2 Spinning Transmitting Antennas 1 Fixed Antenna Transmitter, Dual Channel (Commutated)	Received image must be converted or interpreted by triangulation methods to derive position information. The imagery is not similar to real-world perspective imagery as the angle references are ground-to-aircraft. May have multipath limitations due to time multiplexing reducing the integration time of the correlation function. Precisions are similar to 1.A.2 above.

aperture concept would not differ substantially as far as transmitter, receiver, and antennas are concerned. The key parameter of the system would still be an antenna element separation of several wavelengths in a multi-element antenna which generates a multi-lobed antenna pattern which is rotated, or moved, in a predictable manner.

The number of lobes resulting from the multiple wavelength separation is directly a function of the separation distance so, similarly, the correlation function periodicity (and indirectly, the 3 dB point) are more a function of physical separation than individual element type or pattern. The Bessel function correlation characteristic is derived for a specific receiver processing application, however, it is apparent from Appendix C that other matched filter implementations would provide similar correlation characteristics (precision) differing only in relative strengths of the rings surrounding the correlation point, suppression of the ambiguous point, and biasing as a function of elevation angle (the same factors affecting the electro-optical apparatus). Spot size and ring diameter, which are related to precision, would be essentially independent of the processing scheme used.

The electro-optical processing described in the Astrolabe documentation is the most economical of several processing alternatives. The major objection to this application is the requirement for a trained observer to interpret the visual correlation function to derive necessary direction angles (location corridor descriptors of azimuth and elevation angle). This task involves rejection of multipath target angles which are unresolvable without knowledge of their time history. The unpredictability of this multi-path mechanisms makes automated processors difficult to implement due to the complex pattern recognition task of point pattern interpretation. Reference 5 describes how cross-terms (off-diagonal) of the multipath signal matrix are resolved by time integration, however the direct multipath terms are unresolvable in the same integration interval.

These multipath terms must be resolved from the true direction angles if precision guidance or positioning is to be achieved. Within the scope of this

~~analysis there is insufficient knowledge of the characteristics of the direct~~
multipath interference to specify the requirements of an automated decision processor. It can be assumed that such processing would not be more effective than a trained observer since the processing would be against the same correlation function as that viewed by the observer. For these reasons, the human observer/interpreter is proposed for the ILM application with an automated system as an alternative with greatly increased cost and complexity with no increase in system precision.

ILM APPLICATIONS

The concepts used in the Astrolabe system have potential for use as an ILM. Reference 1 contains the desired ILM angular accuracy specification of 0.10° to 0.12° for 2σ accuracy. Reference 5 presents some experimental results of measurement accuracy of a prototype Astrolabe system with an $R/\lambda=20$ normalized element separation. The empirical values for 2σ accuracy were within approximately 0.4° for azimuth and elevation angle determination. Relating these to the theoretical precision of 0.50° for $R/\lambda=20$, we can expect the 2σ accuracies of the application to be within the predicted precision for the respective R/λ value. To assure 2σ accuracy of 0.12° would require element separations of approximately $R/\lambda=80$ which would require spinning element separations of approximately 3 meters at X-band and 0.8 meters at K_a -band. The selection of frequency for the transmissions is somewhat arbitrary although it should be recalled from Reference 1 that approximately $(1.3 \times R_{\max} \text{ (Km)})$ dB more power is required for K_a -band operation than X-band operation in heavy rain (16 mm/hr) to compensate for path attenuation effects. For example, guidance or position determination at a range of 8 Km would require over 10 dB (10 times) more power at K_a -band than at X-band for the same receiver signal to thermal noise ratio.

It is conceivable, however, since an 80 cm element separation would be possible in the nose of a commercial aircraft, that K_a -band operation of a spinning antenna in the aircraft for high accuracy angle determination would be feasible for configuration 1.B.2 or 2.A.2 of Table 12. Both these configurations

would have the requirement for stabilization of the spinning antenna to eliminate high frequency roll, pitch, and yaw angular deviations to achieve the required high accuracies. A gimbaled system for the spinning antenna (with the spinning elements generating the gyroscopic stability platform) could be used with sensors to derive smooth aircraft to antenna reference angle to relate derived angles to the aircraft reference frame.

Several references have been made previously to multipath errors. These consist of two types: direct multipath terms which are unresolvable from true targets over short observation times and cross-product multipath terms that originate from the product detector which are resolvable over relatively short (less than one second at X-band) integration times. Reference 5 contains a detailed analysis of the effects on the correlation function for high reflection coefficients. In summary, the cross-product terms are reducible by at least 12 dB and the direct multipath terms are left to the expertise of the display analyst for removal. The multipath problem therefore favors ground receivers and analysts since the multipath geometry would be more familiar and predictable.

Comments on ILM applications up to this point have been general for nearly any configuration. When multiple systems are used in an effort to attain location by triangulation or geometrical shape orientation, several other considerations are necessary.

Multiple ground receiving locations have been shown to require large separations (2 to 4 Km). Range factors (the ratio of range uncertainty to linear azimuth uncertainty) are to be kept below 10 for ranges up to 10 Km.

Reference 1 specifications identify required range factors of 2 to 3. These wide separations seriously hinder displaced ground receiving sites (configurations 1.A.2 and 1.B.2 of Table 12) since the triangulation function must be performed centrally. Either multiple receivers, receiver processors, and analysts or multiple receivers with IF or detected IF signals relayed to a central processing and analysis center would be required which would be much more costly than some of the alternatives to be presented below.

~~Configurations 2.A.2 and 2.B.2 with airborne receivers and displaced ground~~ transmitters have the same problem of wide separation of ground antennas for high accuracy although the analysis is centralized to the aircraft. The wide separations necessary for ranging accuracies necessarily limit the linear accuracies to $D/2 \cdot \Delta\theta$, $D/2 \cdot \Delta\psi$, $W/2 \cdot \Delta\theta$, and $W/2 \cdot \Delta\psi$. This effect coupled with multipath problems will degrade performance such that any multiple configuration will be of questionable use for flare, touch-down, and roll-out information.

The multiple ground antenna configurations, although capable of providing high accuracy results prior to flare maneuvers is not an economical ILM configuration because of the complexity of the analysis, interpretation, and triangulation requirements. If the high accuracy requirements can be waived it would be feasible to use configuration 2.A.2 where the imagery (4 beacon points) would be representative of the four corners of the runway and presented to the aircrew in the form of a real-world perspective image for a VFR type of approach. This application would require the spinning (or a stepped Wollenweber array) receiving antenna in the aircraft. Decreased accuracy requirements to the order of 1 degree would negate the requirement for the stabilized antenna platform. Operation at lower frequencies and/or smaller element separations would also be possible.

A high accuracy ILM application at a reduced cost when compared to the multiple ground antenna configurations would consist of a combination of a single beacon transmitter on the aircraft, a spinning receiving antenna on the ground, and an interrogator /response DME (Distance Measuring Equipment) ranging capability incorporated into the ground-to-aircraft data link for relaying angular information to the aircraft (Configuration 1.A.1 extension). This system would provide high precision approach corridor information. (Azimuth and elevation angle along with precise range-to-go as described in Reference 1, ILM Multilateration Sensor section.) It should be pointed out that this combination of sensors would benefit from the most accurate capabilities of both techniques: Astrolabe precision angle referencing without triangulation techniques and its associated accuracy degradation and high precision ranging

by TOA (Time-of-Arrival) techniques without GDOP (Geometrical Dilution of Precision) inherent in multilateration angle determination.

Configuration 2.A.2 is a less precise system than Configuration 1.A.1 extension and provides a pseudo real-world perspective image for a visual back-up ILM. Point accuracies of the order of 1° allow a qualitative four-point image for flight crew reference. Configuration 1.A.1 extension is a high precision (2σ angular accuracies of approximately 0.1°) angular Astrolabe array with DME ranging accuracies of the order of a few meters.

The physical equipment requirements and functions of the two variations are summarized in Table 13.

Mutual interference of variation 1 is non existent when the beacons are commutated "on-off" in a cyclical pattern. Secondly, all the airborne equipment is passive (receiving only) so the same runway beacons may be used by all aircraft without conflict. Variation 2 would use coded airborne beacons with the ground station "repeating" or re-transmitting the code identifier so the appropriate aircraft may receive its coordinates. The only mutual interference would be in the multiple usage of the data link/DME data bus which would have to be maintained and controlled by the ground station to assure user coverage. This would be possible by using angle and range gating techniques. For example, a DME measurement exchange could be used to turn beacons on or off as required to derive angular coordinates and give update rate priorities to aircraft nearing touchdown.

Projected costs of these systems were generated by estimating major component costs. For variation one (Figure 3), the airborne costs are as follows:

Receiver	- \$ 2,000.00
Antenna	- \$ 5,000.00
Signal Processing and Display	- <u>\$ 4,000.00</u>
TOTAL	\$11,000.00

Table 13. Equipment Summary for ILM Applications

Variation 1 Cockpit Perspective Display (Configuration 2.A.2)

<u>Ground Equipment</u>	<u>Usage</u>
4 beacon transmitters with antennas	Outline runway
Commutated transmission control	Coordinate beacon transmissions
<u>Airborne Equipment</u>	<u>Usage</u>
Rotating array	Provide synthetic aperture
Receiver	Detect beacon signals
Electro-optical processor	Display correlation function
Analyst	Interpret position

Variation 2 Ground Station Analysis and Control (Configuration 1.A.1 extension)

<u>Ground Equipment</u>	<u>Usage</u>
Rotating array	Provide synthetic aperture
Receiver	Detect beacon signal
Electro-Optical processor	Display correlation function
Analyst	Interpret position and enter to data link/DME
Data link/DME	Measures range and transmits position information to aircraft
<u>Airborne Equipment</u>	<u>Usage</u>
Data link/DME	Measures range and receives position coordinates from ground
Instrumentation	Displays aircraft coordinates, range-to-go, and/or Az-El angles from runway
Beacon transmitter with antenna	Provides signal for ground fixation

This concept includes four ground beacons at each corner of the runway. The cost of each beacon was estimated at \$5,000 for a total ground system cost of \$20,000. It should be noted signal processing for this system consists of a mechanically spinning reference transparency with a light source driven by the received RF signal and a simple display of the cross-correlation function. This probably is not adequate for an operational configuration.

Variation two (Figure 4) consisted of an airborne beacon transmitter with ground receiver, processor/display and a DME/data link for ranging and transfer of guidance data back to the aircraft. Costs for the airborne unit for this variation were as follows:

Beacon	- \$ 6,000.00
DME/Data Link	- \$ 8,000.00
Cross Pointer Display	- <u>\$ 1,000.00</u>
TOTAL	\$15,000.00

Ground system costs are as follows:

Receiver	- \$ 4,000.00
Signal Processing/ Display	- \$ 4,000.00
Rotating Antenna	- \$ 5,000.00
DME Transponder and Data Link Logic	- <u>\$10,000.00</u>
TOTAL	\$23,000.00

Estimated weight of the airborne unit for this variation is 8 kgm. This variation also has the low cost mechanical signal processor at the ground site which probably would not be suitable for an operational configuration.

Page Intentionally Left Blank

SECTION IV
REFERENCES

1. Kirk, R.J.: Analytical Evaluation of ILM Sensors. NASA CR 132687, September 1975.
2. Hughes Aircraft Co.: Bistatic Thinned Linear Array (BISTAR Investigations). AFAL-TR-74-253, August 1974.
3. Barton, D.K.: Radar System Analysis. Prentice-Hall Inc., 1964.
4. Alcock, R.N., et al.: "MADGE", A Microwave Aircraft Digital Guidance Equipment. Phillips Technical Review, Vol. 34, No. 9.
5. Dorey, J. and Garnier, G.: Astrolabe, a Synthetic Circular Aperture System for Landing and Navigation. ONERA, 8th Annual Symposium on Aerospace Instrumentation, March 24-27, 1975.
6. Dorey, J., Guern, R. and Christophe, F.: Etude Sommaire de la Theorie Du System de Localisation Angulaire "Astrolabe". Office National D'Etudes et de Recherches Aerospatiales (ONERA), Document n^o 1/3135PN, September 26, 1974. (Translated version is included as Appendix C.)
7. Ma, M.T.: Theory and Application of Antenna Arrays. John Wiley & Sons, 1974.
8. Ramo, S., Whinnery, J. and VanDuzer, T.: Fields and Waves in Communication Electronics. John Wiley & Sons, 1967.

Page Intentionally Left Blank

Section V
 Appendices
 Appendix A

Determination of Array Gain Characteristics

The generalized expression for the distant field of each element of an array is (See Figure A-1)

$$E_i(\theta, \phi) = f(\theta, \phi) I_i \exp [j(kr_i \cos \psi_i + \delta_i)] \quad (A-1)$$

with:

$f(\theta, \phi)$ - the far-field function associated with the individual antenna element

I_i - amplitude excitation

δ_i - phase excitation

$k = 2\pi/\lambda$

$\cos \psi_i = \cos \theta \cos \theta_i + \sin \theta \sin \theta_i \cos(\phi - \phi_i)$

r_i = range

The total field contributed from an array is the summation of the individual contributions of the n elements.

$$\begin{aligned} E(\theta, \phi) &= \sum_{i=1}^n E_i(\theta, \phi) \\ &= f(\theta, \phi) \sum_{i=1}^n I_i \exp [j(kr_i \cos \psi_i + \delta_i)] \\ &= f(\theta, \phi) \cdot S \end{aligned} \quad (A-2)$$

$f(\theta, \phi)$ - element factor

S - array factor

The total field may be considered as consisting of the two separable factors, the element factor, $f(\theta, \phi)$ and the array factor, S . The power gain of the array may be expressed as the ratio of the squared field intensity in a particular direction to the average radiated power intensity.

Where P is the total power delivered to the array

$$G(\theta, \phi) = \frac{|E(\theta, \phi)|^2}{P/4\pi} = \frac{4\pi |f(\theta, \phi)|^2 |S|^2}{P}$$

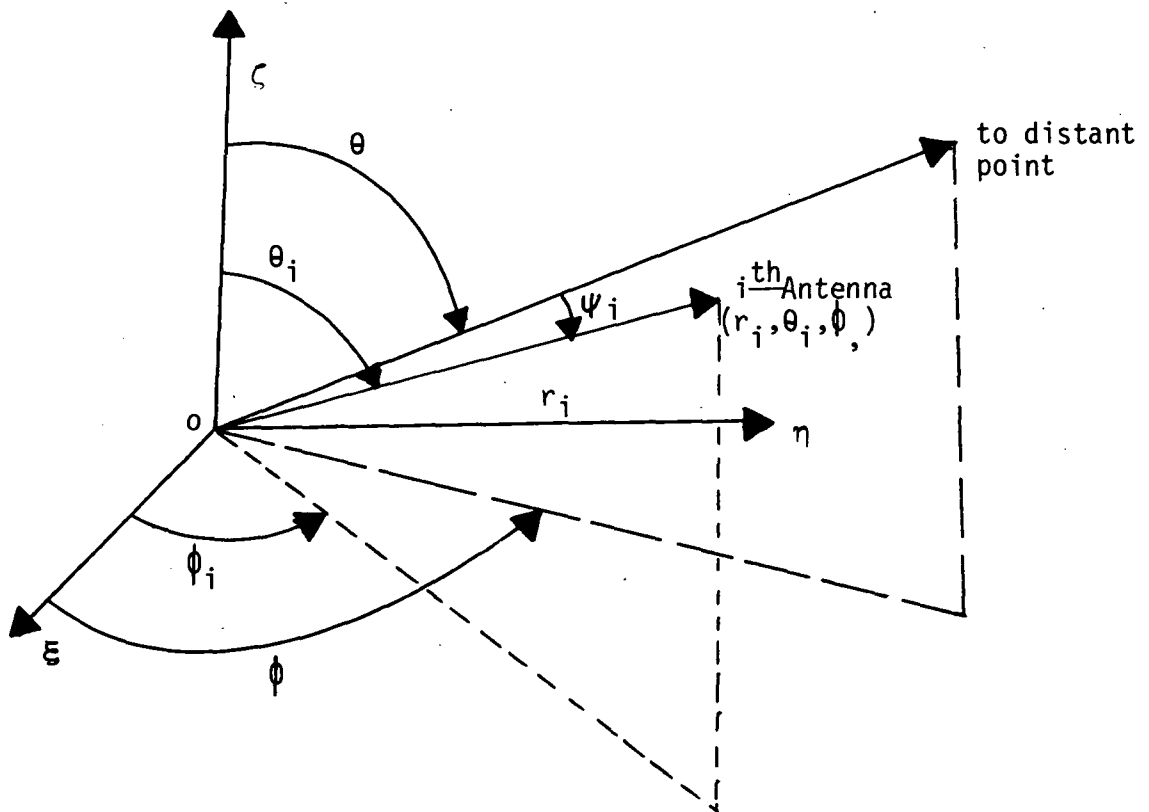


Figure A-1. 3-Dimensional Axis for Antenna Field Conventions

The element factor of a typical array element applicable to an ILM aircraft mounting is presented in Reference 2. A linear approximation of the vertical and horizontal gain curves presented in Reference 2 are shown in Figure A-2 and A-3. These curves were numerically integrated to derive the lossless antenna maximum element gain as 20 dB. The element factor, $|f(\theta, \phi)|^2$ has the normalized gain characteristics shown in Figures A-2 and A-3 with a maximum gain of 20 dB at boresight ($f_{\max}(\theta) = 8.2$ dB and $f_{\max}(\theta) = 11.8$ dB). The additional gain due to the array factor, S, will be analytically derived in the following sections.

The concept of a thinned array dictates that elements are removed or "thinned" from a conventional array with element spacings less than the wavelength, λ . Removal of these elements creates grating lobes.

The uniform amplitude distribution, $I_i = 1$ has the unfortunate property of high sidelobes (only 13.2 dB below the main beam). A bistatic thinned array removes the grating lobes to null, or at least lower sidelobe, regions of the transmitting antenna, however, the receiving array with a beamwidth much narrower than the transmitting antenna, must sacrifice some mainlobe gain (and beamwidth) to reduce the sidelobes to an acceptable level. The amount of reduction is somewhat arbitrary, however, it can be assumed that if good runway edge resolution is required the sidelobes must be below expected edge contrast levels. The runway scenario of the previous studies of imaging radar ILM's (Reference 1) identified typical concrete runway to grass

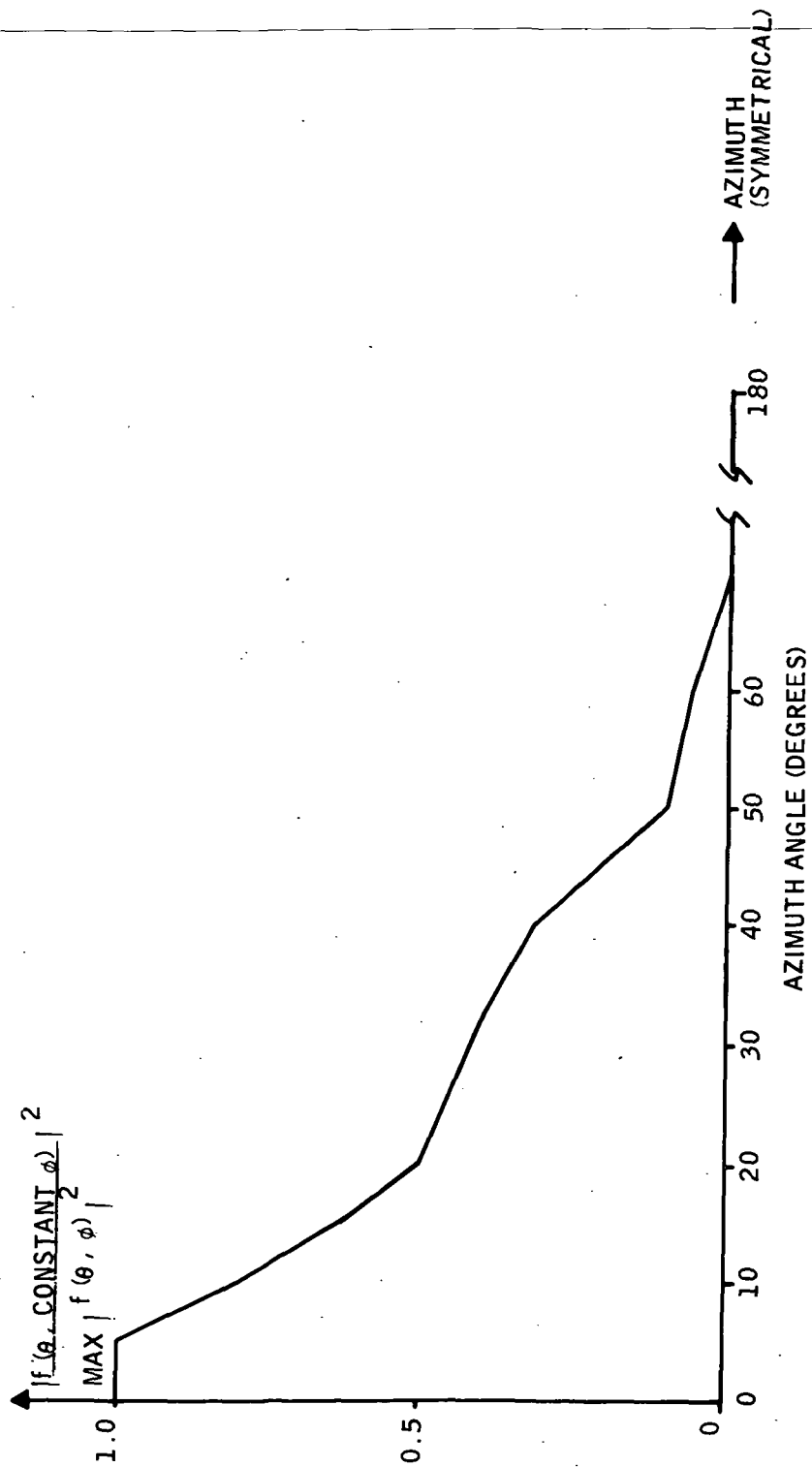


Figure A-2. Normalized Antenna Gain Profile (Azimuth)
Azimuth Profile (Referenced to direction of flight)

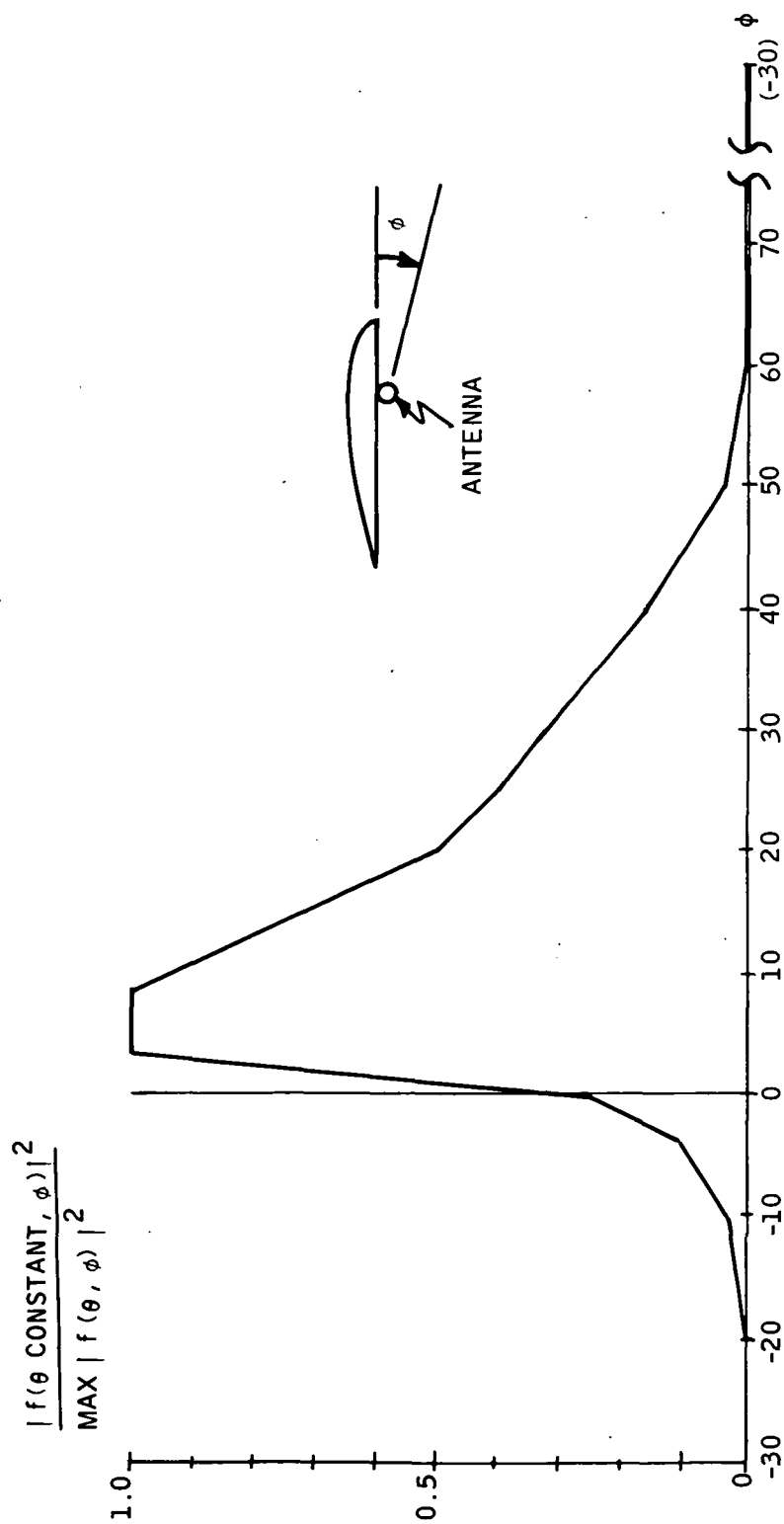


Figure A-3. Normalized Antenna Gain Profile (Elevation) Elevation Profile
(Reference to wing surface in the direction of flight, +angles
are down)

contrast ratios at X-Band in excess of 20 dB.

Assuming at least 6 dB additional differential for detection criteria, the sidelobes must be at least 26 dB down from the main beam. The proposed array in Reference 2 is in close agreement with Taylor weighting on the amplitudes for sidelobe suppression to approximately 33 dB below the mainlobe. The effect of this amplitude weighting is to produce a slight decrease in the maximum theoretical mainlobe gain of 2 to 3 dB.

This factor will be incorporated later.

$$\begin{aligned}
 G_{A_{\max}} &= \frac{\max |E(\theta, \phi)|^2}{P/4\pi} \\
 &= \frac{4\pi \max |E(\theta, \phi)|^2}{\int_0^{2\pi} \int_0^{\pi} |E(\theta, \phi)|^2 \sin\theta \, d\theta \, d\phi}
 \end{aligned} \tag{A-4}$$

$$\text{or } G_{A_{\max}} = \frac{4\pi \max |f(\theta, \phi)|^2 |S|^2}{\int_0^{2\pi} \int_0^{\pi} |f(\theta, \phi)|^2 |S|^2 \sin\theta \, d\theta \, d\phi} \tag{A-5}$$

Previously we derived the maximum value of the element gain by:

$$\begin{aligned}
 G_{\max} &= \frac{\max |E(\theta, \phi)|^2}{P/4\pi} \\
 &= \frac{4\pi \max |f(\theta, \phi)|^2}{\int_0^{2\pi} \int_0^{\pi} |f(\theta, \phi)|^2 \sin\theta \, d\theta \, d\phi} = 20 \text{ dB}
 \end{aligned} \tag{A-6}$$

for $|S|^2 = 1$ (one element only)

This expression was evaluated on the assumption that $|f(\theta, \phi)|^2 = |f(\theta)|^2 |f(\phi)|^2$

$$G_{\max} = 4\pi \frac{\max_{\phi} |f(\phi)|^2}{\int_0^{2\pi} |f(\phi)|^2 d\phi} \frac{\max_{\theta} |f(\theta)|^2}{\int_0^{\pi} |f(\theta)|^2 \sin\theta d\theta}$$

$$= 4\pi G_{\max}(\phi) G_{\max}(\theta) \quad (A-7)$$

When the element is used as an array element, the array factor must be derived. This gain will have a maximum value expressed by:

$$G_{A_{\max}} = \frac{4\pi \max_{\theta, \phi} [|f(\theta, \phi)|^2 |S|^2]}{\int_0^{2\pi} \int_0^{\pi} |f(\theta, \phi)|^2 |S|^2 \sin\theta d\theta d\phi} \quad (A-8)$$

When $f(\theta, \phi)$ and S are maximum in the same direction:

$$G_{A_{\max}} = \frac{4\pi \max_{\theta, \phi} |f(\theta, \phi)|^2 \max_{\theta, \phi} |S|^2}{\int_0^{2\pi} \int_0^{\pi} |f(\theta, \phi)|^2 |S|^2 \sin\theta d\theta d\phi} \quad (A-9)$$

Previously it was described how the pattern of the array has narrow beamwidths with several grating lobes, the number, m , of lobes being determined by the element spacing. The array factor effectively shapes the array pattern since the array beamwidth in θ is very narrow. Thus, for each lobe the variation of $f(\theta)$ across the beamwidth is small such that (since S is independent of θ for the array geometry chosen):

$$\int_0^{2\pi} \int_0^{\pi} |f(\theta, \phi)|^2 |S|^2 \sin\theta d\theta d\phi \approx \int_0^{2\pi} |f(\phi)|^2 \int_0^{\pi} |f(\theta)|^2 |S|^2 \sin\theta d\theta d\phi$$

Continued

$$\cong \int_0^{2\pi} |f(\phi)|^2 d\phi \sum_{i=1}^m |f_i(\theta)|^2 \int_{\theta_i - \xi_i}^{\theta_i + \xi_i} |S|^2 \sin\theta d\theta \quad (\text{A-10})$$

where

$f_i(\theta)$ is the element factor constant for the i^{th} lobe

θ_i is the angle corresponding to the i^{th} lobe
($0 < \theta_i < \pi$)

ξ_i is an angle chosen sufficiently larger than the respective lobe beamwidth such that negligible power is radiated beyond this angle until the next lobe is encountered.

Then

$$G_{A\max} \cong 4\pi \frac{\max |f(\phi)|^2}{\int_0^{2\pi} |f(\phi)|^2 d\phi} \frac{\max |f(\theta)|^2 \max |S|^2}{\sum_{i=1}^m |f_i(\theta)|^2 \int_{\theta_i - \xi_i}^{\theta_i + \xi_i} |S|^2 \sin\theta d\theta} \quad (\text{A-11})$$

Recall that:

$$G_{\max} = 4\pi \frac{\max |f(\theta)|^2}{\int_0^{\pi} |f(\theta)|^2 \sin\theta d\theta} \frac{\max |f(\phi)|^2}{\int_0^{2\pi} |f(\phi)|^2 d\phi} \quad (\text{A-12})$$

So

$$G_{A\max} = G_{\max} \frac{\max |S|^2 \int_0^{\pi} |f(\theta)|^2 \sin\theta d\theta}{\sum_{i=1}^m |f_i(\theta)|^2 \int_{\theta_i - \xi_i}^{\theta_i + \xi_i} |S|^2 \sin\theta d\theta} \quad (\text{A-13})$$

The lobes are very similar over the range of the $f(\theta)$ function when

$f(\theta)$ has a narrow beamwidth (less than 40° to 60°) such that:

$$G_{A\max} = G_{\max} \frac{\max |S|^2}{\int_{\theta - \xi}^{\theta + \xi} |S|^2 \sin\theta d\theta \left[\frac{|f_1(\theta)|^2}{\int_0^{\pi} \dots} + \frac{|f_2(\theta)|^2}{\int_0^{\pi} \dots} + \dots \right]} \quad (\text{A-14})$$

Dividing through by the term $\frac{\max |f_i(\theta)|^2}{\int_0^{\pi} \dots} = G_{\max}(\theta)$

$$G_{Amax} = \frac{G_{max}}{G_{max}(\theta)} \frac{\frac{\max |S|^2}{\int_{\theta-\xi}^{\theta+\xi} |S|^2 \sin\theta d\theta}}{\frac{G_1(\theta)}{G_{max}(\theta)} + \frac{G_2(\theta)}{G_{max}(\theta)} + \dots + 1 + \dots + \frac{G_m(\theta)}{G_{max}(\theta)}} \quad (A-15)$$

where $G_i(\theta)$ is the gain associated with the i^{th} lobe.

When the array is thinned such that the element spacings, although uniform, are in excess of one wavelength, the summation becomes the value K' and the expression for G_{Amax} becomes:

$$\begin{aligned} G_{Amax} &= \frac{G_{max}}{G_{max}(\theta)} \frac{1}{K'} \frac{\max |S|^2}{\int_{\theta-\xi}^{\theta+\xi} |S|^2 \sin\theta d\theta} \\ &= \frac{G_{max}}{G_{max}(\theta)} \frac{K''}{K'} \end{aligned} \quad (A-16)$$

The values of K' are only a function of element spacing since it is this characteristic that generates and places the grating lobes. Values of K' as a function of element spacing for the array element azimuth characteristic of Figure A-2 are shown in Figure A-4.

The factor K'' , with the denominator integral limited to one lobe is the same as the integral expression for an unthinned array of length ℓ with no grating lobes. $\max |S|^2$ is the normalizing value associated with the $|S|^2$ term in the integral. K'' is thus indistinguishable from:

$$\frac{\max |S|^2}{\int_0^\pi |S|^2 \sin\theta d\theta} \quad \text{for a uniformly spaced array with no grating}$$

lobes which has been approximated in Reference 8 as:

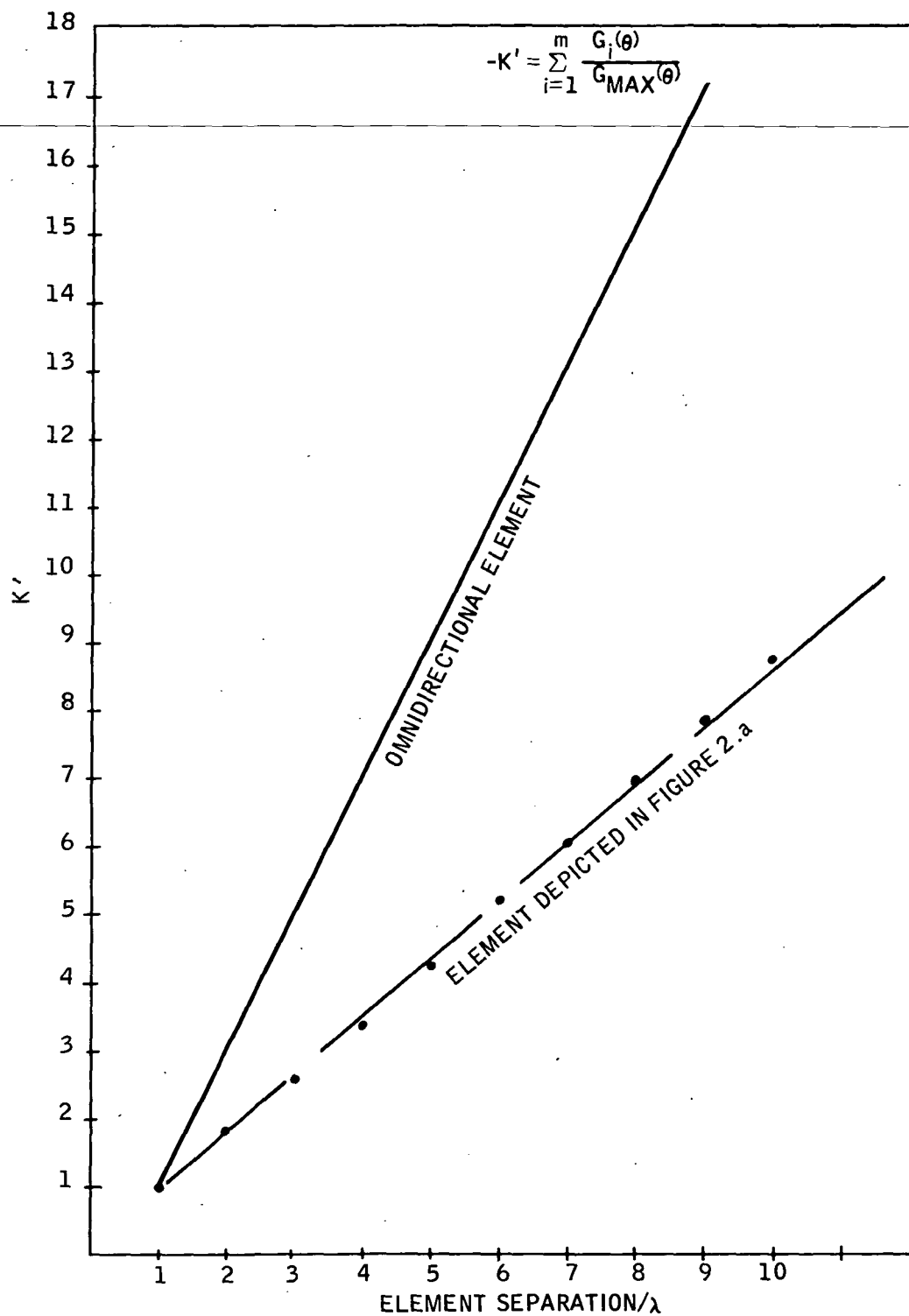


Figure A-4. K' as a Function of Element Spacing

$$\frac{4\pi \max |S|^2}{2\pi \int_0^\pi |S|^2 \sin\theta d\theta} \cong \frac{2L}{\lambda} \quad \text{for long arrays which is independent of the number of elements}$$

(A-17)

Thus, $K'' \cong \frac{L}{\lambda}$ for $L \gg \lambda$

The expression for maximum array gain becomes:

$$G_{A_{\max}} = \frac{G_{\max}(\theta, \phi)}{G_{\max}(\theta)} \frac{L}{K' \lambda} \quad (A-18)$$

For the array element shown in Figures A-2 and A-3 and assuming a 3 dB loss associated with amplitude weighting as per the previous discussion:

$$G_{A_{\max}} \text{ dB} \cong 5.8 \text{ dB} + 10 \log_{10} \left[\frac{L}{\lambda} \right] - 10 \log_{10} [K'] \quad (A-19)$$

Page Intentionally Left Blank

APPENDIX B

A COMPUTER PROGRAM FOR THE

ANALYSIS OF SPECULAR MULTIPATH IN AN INTERFEROMETER

I. ENVIRONMENT

The environment in which the interferometer is assumed to be working is a quasi-two dimensional. The antennas are positioned along the Z axis, and the aircraft flight path is in the X-Z plane. A flight path component is also allowed in the Y dimension. All reflecting surfaces are assumed to be finite line segments in the X-Z plane with infinite extent in the Y direction, and orientation perpendicular to the X-Z plane. The multipath geometry is as shown in Figure B-1.

The method of images is used to compute the reflection effects. For each antenna and each surface, the surface is extended to infinity and the image of that antenna about that surface is formed. A line is drawn from the aircraft to the image. If the line intersects the extended surface within the bounds of the real surface, and the extended surface does not separate the real antenna from the aircraft, a reflection is presumed to occur. The angle of incidence between the line and the surface is then computed, and the reflection coefficient computed from

$$R_V = \frac{\epsilon_r \cos\theta - \sqrt{\epsilon_r - \sin^2\theta}}{\epsilon_r \cos\theta + \sqrt{\epsilon_r - \sin^2\theta}} e^{-(2K\sigma\cos\theta)^2} \quad (B-1)$$

$$R_H = \frac{\cos\theta - \sqrt{\epsilon_r - \sin^2\theta}}{\cos\theta + \sqrt{\epsilon_r - \sin^2\theta}} e^{-(2K\sigma\cos\theta)^2} \quad (B-2)$$

where

R_V is the complex reflection coefficient for vertical polarization.

R_H is the complex reflection coefficient for horizontal polarization.

θ is the incidence angle

ϵ_r is the complex permittivity of the surface

σ is the RMS surface roughness,

K is the wave number.

The magnitude of the reflection coefficient is modified by the ratio of the range from the aircraft to the real antenna to the range from the aircraft to the image, and by an approximation to the antenna pattern. The phase of the reflection is modified by the difference in these ranges.

The reflection components for all surfaces are summed vectorially with the direct component to obtain a total field present at a given antenna. The direct vector is used as a magnitude and phase reference as shown in Reference 1, so that the normalized vector sum is a measure of the error in phase at the antenna. This is converted to a normalized range difference error by dividing by the wave number.

An estimate is then formed of the range difference between antennas of a pair using either a focused or unfocused algorithm. If the run is unfocused, the difference between range errors is added to the actual range difference. This range difference is divided by the distance between antennas to form an estimate of the sine of the angle between the aircraft and the x-axis. If the run is focused, the algorithm is

$$\hat{\phi} = \frac{R^2(2) - R^2(1)}{2R(1)(ZA(1) - ZA(2))} + \frac{ZA(1) + ZA(2)}{2R(1)} \quad (B-3)$$

where

$\hat{\phi}$ is the estimate of the sine of the angle.

$R(i)$ is the range from the aircraft to the i th antenna.

$ZA(i)$ is the height of the i th antenna from the x-axis.

The estimates for the various pairs of antennas in the array are averaged in an unweighted average. Since the sine of the angle rather than the angle is available, the error is computed via the approximation

$$\tilde{\theta} = \theta - \hat{\theta} = \sin^{-1} \sin(\theta - \hat{\theta}) \approx \sin\theta \cos\hat{\theta} - \sin\hat{\theta} \cos\theta \quad (B-4)$$

$$\approx (\sin\theta - \sin\hat{\theta}) \cos\hat{\theta} \text{ for small } \tilde{\theta} \quad (B-5)$$

where θ is the angle between the line from the aircraft to the origin and the x-axis.

$\hat{\theta}$ is the estimate of that angle.

$\tilde{\theta}$ is the error in that angle measurement.

These errors are computed at each increment along the flight path, and output both in tabular form and a plot.

GLOSSARY OF TERMS: PROGRAM MADGE

RGH	REAL	SURFACE RMS ROUGHNESS DIVIDED BY WAVELENGTH
RHO	REAL	MAGNITUDE OF FRESNEL REFLECTION COEFFICIENT
PHOR	REAL	MAGNITUDE OF REFLECTION COEFFICIENT MODIFIED BY RANGE AND ANTENNA PATTERN RATIOS
RR	DOUBLE	RANGE FROM AIRCRAFT TO IMAGE ANTENNA
RREF	DOUBLE	RANGE FROM AIRCRAFT TO REFERENCE POINT
SKP	REAL	
SMEAN	REAL	SAMPLE MEAN
SMSQ	REAL	SAMPLE MEAN SQUARE VALUE
SNTH	DOUBLE	SINE OF TRUE PHYSICAL ANGLE
SURFI	REAL	INTERCEPT OF SURFACE WITH Z AXIS
SURFS	REAL	SLOPE OF SURFACE
SVAR	REAL	SAMPLE VARIANCE
TEMP1	REAL	TEMPORARY INTERMEDIATE VARIABLE
TEMP2	REAL	TEMPORARY INTERMEDIATE VARIABLE
THETI	REAL	INCIDENCE ANGLE FOR SURFACE REFLECTION
THTILD	REAL	ERROR IN MEASUREMENT OF PHYSICAL ANGLE
TITLE	CHARACTER	HEADINGS FOR PRINTOUT
TWOPI	REAL	
WAVLTH	REAL	WAVELENGTH
X1	REAL	START OF SURFACE
X2	REAL	END OF SURFACE
XAC	REAL	POSITION OF AIRCRAFT
XAC1	REAL	STARTING POINT OF FLIGHT PATH SEGMENT
XACF	REAL	ENDING POINT OF FLIGHT PATH SEGMENT
YAI	REAL	POSITION OF IMAGE ANTENNA
XC	REAL	INTERCEPT OF SURFACE WITH LINE FROM AIRCRAFT TO ANTENNA
XI	REAL	INTERCEPT OF SURFACE WITH NORMAL FROM ANTENNA
XREF	REAL	REFERENCE POINT (NORMALLY=0.0)
X5	REAL	SPECULAR POINT ON SURFACE
YAC	REAL	POSITION OF AIRCRAFT
YAC1	REAL	STARTING POSITION OF FLIGHT PATH SEGMENT
YACF	REAL	ENDING POSITION OF FLIGHT PATH SEGMENT
Z1	REAL	START OF SURFACE
Z2	REAL	END OF SURFACE
ZA	REAL	POSITION OF ANTENNA (X=0.0)
ZAC	REAL	POSITION OF AIRCRAFT
ZAC1	REAL	START OF FLIGHT PATH SEGMENT
ZACF	REAL	END OF FLIGHT PATH SEGMENT
ZAI	REAL	POSITION OF ANTENNA IMAGE
ZI	REAL	INTERCEPT OF SURFACE WITH NORMAL FROM ANTENNA
ZREF	REAL	REFERENCE POINT (NORMALLY=0.0)

UMR = 2549T, ACTIVITY # = 01, REPORT CODE = 21, RECORD COUNT = 000106

GLOSSARY OF TERMS: PROGRAM MADGE

AD	REAL	SLOPE OF LINE FROM AIRCRAFT TO ANTENNA
AIMAG	REAL	
AR	REAL	SLOPE OF LINE FROM AIRCRAFT TO ANTENNA IMAGE
AP	REAL	INTERCEPT OF LINE FROM AIRCRAFT TO ANTENNA IMAGE
COND	REAL	ARRAY PSEUDONYM FOR INPUT CONDITIONS
COND1	REAL	ARRAY PSEUDONYM FOR INPUT CONDITIONS
DELPHI	REAL	TOTAL PHASE ERROR DUE TO MULTIPATH
DFLX	REAL	FLIGHT PATH INCREMENT VALUE
DFLY	REAL	FLIGHT PATH INCREMENT VALUE
DFLZ	REAL	FLIGHT PATH INCREMENT VALUE
FFOCUS	REAL	INDICATOR OF FOCUSED INTERFEROMETER (1=FOCUSED)
FXCT	REAL	
I	INTEGER	
INC	INTEGER	FLIGHT PATH INCREMENT LOOP CONTROL
IPAIR	INTEGER	ANTENNA PAIR
IPOL	INTEGER	POLARIZATION INDICATOR (1=VERT., 2=HORIZ.)
IREFL	INTEGER	BINARY PACKED INDICATOR OF WHICH SURFACES ARE REFLECTING
ISFG	INTEGER	FLIGHT PATH SEGMENT LOOP CONTROL
ISURF	INTEGER	REFLECTING SURFACE LOOP CONTROL
ITTY	INTEGER	INDICATOR FOR PLOT SIZE
J	INTEGER	
L	INTEGER	
LOG1	LOGICAL	LOGICAL INDICATOR TO DETERMINE IF REFLECTION EXISTS
LOG2	LOGICAL	LOGICAL INDICATOR TO DETERMINE IF REFLECTION EXISTS
LOG3	LOGICAL	LOGICAL INDICATOR TO DETERMINE IF REFLECTION EXISTS
MCY	INTEGER	
MES1	CHARACTER	PRINTOUT HEADINGS
MES2	CHARACTER	" "
MES3	CHARACTER	" "
MES4	CHARACTER	" "
MES5	CHARACTER	" "
MINPH	REAL	INPHASE PORTION OF MULTIPATH
MQUAD	REAL	QUADRATURE " " "
NINC	INTEGER	NUMBER OF INCREMENTS THIS FLIGHT PATH SEGMENT
NOUT	INTEGER	FILE CODE FOR LINE PRINTER
NPAIR	INTEGER	NUMBER OF INTERFEROMETER ANTENNA PAIRS
NSEG	INTEGER	NUMBER OF FLIGHT PATH SEGMENTS
NSURF	INTEGER	NUMBER OF REFLECTING SURFACES
OR	BOOLEAN	ARRAY CONTAINING RESULTS FOR A FLIGHT PATH SEGMENT
OUT	REAL	ARRAY CONTAINING RESULTS FOR A FLIGHT PATH SEGMENT
OUTMAX	REAL	MAXIMUM VALUE FOR CORRESPONDING ELEMENT OF OUT
OUTMIN	REAL	" " " " " "
PATD	REAL	ANTENNA PATTERN VALUE IN DIRECTION OF AIRCRAFT
PATR	REAL	ANTENNA PATTERN VALUE IN DIRECTION OF REFLECTION
PHAS	REAL	PHASE OF GIVEN MULTIPATH AT GIVEN ANTENNA
PHI	REAL	PHASE OF FRESNEL COEFFICIENT
PHIRAR	REAL	AVERAGED ESTIMATE OF SINE OF PHYSICAL ANGLE
PHIHAT	REAL	ESTIMATE OF SINE OF PHYSICAL ANGLE FOR A GIVEN ANTENNA PAIR
PPMTIV	COMPLEX	PERMITTIVITY OF SURFACE
Q	REAL	DUMMY FLOATING VARIABLE FOR INPUT OF INTEGERS
R	COMPLEX	FRESNEL REFLECTION COEFFICIENT
RD	DOUBLE	RANGE FROM AIRCRAFT TO ANTENNA IN X-Z PLANE
RD3	DOUBLE	RANGE FROM AIRCRAFT TO ANTENNA
REAL	REAL	

SNUMS = 2179T, ACTIVITY # = 01, REPORT CODE = 21, RECORD COUNT = 000269

```

0010C PROGRAM WADGE COMPUTES THE ERRORS DUE TO SPECULAR REFLECTIONS
0020C AND FOCUSING IN A SPATIALLY AVERAGED INTERFEROMETER FOR UP TO
0030C 10 PAIRS OF ANTENNAE, 10 REFLECTING SURFACES, AND 10 FLIGHT PATH
0032C SEGMENTS
0033 COMMON/TAPES/MOUT
0034 COMMON/XCT/ITTY,WCY,SKP(4),FXCT(2)
0040 COMMON ZA(10,2),Z(10),X1(10),Z1(10),Y2(10),Z2(10),PRMTIV(10),
00456 EGH(10),XAC1(10),YAC1(10),ZAC1(10),XACF(10),YACF(10),ZACF(10),NINC(10)
0046 DIMENSION COND(10,7),COND1(10,4)
0048 EQUIVALENCE(COND,XAC1),(COND1,X1)
0049 DIMENSION PH1(10)
0050 DIMENSION SURF(10),SURF1(10),XAI(10,10,2),ZAI(10,10,2),
00556 DELP(1,2),OUT(100,15),OUTMIN(15),OUTMAX(15)
0056 DIMENSION IREFL(10)
0060 COMPLEX PRMTIV,R(2)
0062 CHARACTER MES1*60/' ANTENNA PAIRS'/,
00636 MES2*60/' AIRCRAFT FLIGHT PATH SEGMENTS'/,
00646 MES3*19/'REFLECTING SURFACES'/,
00656 MES4*60/' SURFACE STARTING COORDINATES ENDING COORDINATES'/,
00666 MES5*33/'PERMITIVITY ROUGHNESS'/
0067 CHARACTER TITLE*20(7)/'X AT START','Y AT START','Z AT START',
00686 'X AT FINISH','Y AT FINISH','Z AT FINISH','NUMBER OF INCREMENTS'/
0070 DATA WAVLTH,TWOPI/.05,6.2831853/
0071 REAL MINPH,MOUAD
0075 DOUBLE PRECISION PD(10,2),SMTH,QREF,PR
0076 DOUBLE PRECISION PD3(10,2)
0077 LOGICAL LOG1,LOG2,LOG3
0078 DATA IPOL/1/
0079 DATA XREF,ZREF/0.0,0.0/
0089C
0090C *****INPUT ANTENNA PARAMETERS
0100C
0105 READ(20,150)O,FFOCUS
0106 IPOL=O
0110 DO 190,IPAIR=1,10
0120 WRITE(11,130) IPAIR
0130 130 FORMAT('INPUT ANTENNA HIGHTS FOR ANTENNA PAIR NUMBER ',I2)
0140 READ(20,150)ZA(IPAIR,1),ZAI(IPAIR,2)
0150 150 FORMAT(5F10.5)
0160 IF(ZA(IPAIR,1).NE.0..OR.ZAI(IPAIR,2).NE.0.)GO TO 190
0170 NPAIR=IPAIR-1
0180 GO TO 230
0190 190 CONTINUE
0200C
0210C *****INPUT FLIGHT PATH PARAMETERS
0220C
0230 230 DO 300 ISEG=1,10
0240 WRITE(11,250) ISEG
0250 250 FORMAT('INPUT AIRCRAFT X AND Z COORDINATES AT START AND ',
02526 'FINISH OF SEGMENT ',I2,' AND NUMBER OF INCREMENTS THIS SFG')
0260 READ(20,150)XAC1(ISEG),ZAC1(ISEG),XACF(ISEG),ZACF(ISEG),
02626 Q
0264 NINC(ISEG)=Q
0265 WRITE(11,266) ISEG
0266 266 FORMAT('INPUT ST. AND FINISH Y COORDINATES, SEGMENT ',I2)
0267 READ(20,150)YAC1(ISEG),YACF(ISEG)
0270 IF(NINC(ISEG).NE.0) GO TO 300
0280 NSEG=ISEG-1
0290 GO TO 340

```

```

0300 300 CONTINUE
0310C
0320C *****INPUT REFLECTING SURFACE PARAMETERS
0330C
0340 340 DO 440 ISURF=1,10
0350 WRITE(11,360) ISURF
0360 360 FORMAT('INPUT X AND Z COORDINATES AT ENDS OF SURFACE ',I2)
0370 READ(20,150) X1(ISURF),Z1(ISURF),X2(ISURF),Z2(ISURF)
0380 IF(X1(ISURF).NE.X2(ISURF).OR.Z1(ISURF).NE.Z2(ISURF))
03826 GO TO 410
0390 NSURF=ISURF-1
0400 GO TO 480
0410 410 WRITE(11,420) ISURF
0420 420 FORMAT('INPUT COMPLEX PERMITIVITY AND ROUGHNESS OF SURFACE ',
04226 I2)
0430 READ(20,150)PRMTIV(ISURF),FGH(ISURF)
0440 440 CONTINUE
0450C
0460C *****COMPUTE SURFACE PARAMETERS
0470C
0471 480 DO 610 ISURF=1,NSURF
0473 IF(X1(ISURF).NE.X2(ISURF)) GO TO 486
0475 SURFS(ISURF)=1.E37
0477 SURFI(ISURF)=1.E37
0478 DO 484 IPAIR=1,NPAIR
0479 DO 483 L=1,2
0480 XAI(ISURF,IPAIR,L)=2.*X1(ISURF)
0482 ZAI(ISURF,IPAIR,L)=ZA(IPAIR,L)
0483 483 CONTINUE
0484 484 CONTINUE
0485 GO TO 610
0486 486 IF(Z1(ISURF).NE.Z2(ISURF))GO TO 490
0487 SUPFS(ISURF)=0.0
0488 GO TO 500
0490 490 SUPFS(ISURF)=(Z1(ISURF)-Z2(ISURF))/(X1(ISURF)-X2(ISURF))
0495 500 CONTINUE
0500 SURFI(ISURF)=Z1(ISURF)-SUPFS(ISURF)*X1(ISURF)
0510 TEMP1=1.+SURFS(ISURF)**2
0520 DO 600 IPAIR=1,NPAIR
0530 DO 590 L=1,2
0540 TEMP2=(ZA(IPAIR,L)-SURFI(ISURF))/TEMP1
0550 XI=SUPFS(ISURF)*TEMP2
0560 ZI=ZA(IPAIR,L)-TEMP2
0570 XAI(ISURF,IPAIR,L)=2.*XI
0580 ZAI(ISURF,IPAIR,L)=2.*ZI-ZA(IPAIR,L)
0590 590 CONTINUE
0600 600 CONTINUE
0610 610 CONTINUE
0612C *****OUTPUT RUN CONDITIONS
0614 WRITE(10,616)MES1,7A,MES2,(TITLE(I),(COND(J,I),J=1,10),I=1,7),
06156 MES3,MES4,MES5,(J,(COND1(J,I),I=1,4),PRMTIV(J),FGH(J),J=1,10)
0616 616 FORMAT(A60/' UPPER ',10(F6.2,4X)/' LOWER ',10(F6.2,4X)/
06176 A60/6(A20,10(F9.3,2X)/),A20,10(I5,6X)//A20/A56,14X,A35/
06186 ' NUMBER',6X,2('Y',14X,'Z',14X)/10(3X,
06196 I2,7(2X,E12.5)/))
0620C
0630C *****INCREMENT A/C POSITION AND COMPUTE RANGE TO REFERENCE POINT
0640C
0650 DO 1530 ISEG=1,NSEG
0660 DELX=(XAC1(ISEG)-XAC(ISEG))/(NINC(ISEG)-1)
0665 DELY=(YAC1(ISEG)-YAC(ISEG))/(NINC(ISEG)-1)
0670 DELZ=(ZAC1(ISEG)-ZAC(ISEG))/(NINC(ISEG)-1)
0672 SMFAN=0.0
0674 SMSQ=0.0
0675 DO 678 IPAIR=1,10
0676 IREFL(IPAIR)=0

```

```

0678 678 CONTINUE
0680 DO 1470 INC=1,NINC(ISEG)
0686 PHIBAR=0.0
0690 XAC=XAC1(ISEG)-(INC-1)*DELX
0695 YAC=YAC1(ISEG)-(INC-1)*DELY
0700 ZAC=ZAC1(ISEG)-(INC-1)*DELZ
0710 RREF=DSORT((XAC-XREF)**2+(ZAC-ZREF)**2)
0712 PATD=PAT(0.0+1.570796-ZAC/RREF,IPOL)
0720C
0730C *****SELECT ANTENNA PAIR AND COMPUTE DIRECT RANGE
0740C
0750 DO 1200 IPAIR=1,NPAIR
0760 DO 1140 L=1,2
0770 RD(IPAIR,L)=DSORT(XAC**2+(ZAC-ZA(IPAIR,L))**2)
0772 RD3(IPAIR,L)=DSORT(RD(IPAIR,L)**2+YAC**2)
0775 MQUAD=0.0
0777 MINPH=0.0
0780C
0790C *****SELECT SURFACE
0800C
0810 DO 1120 ISURF=1,NSURF
0820 RR=DSORT((XAC-XAI(ISURF,IPAIR,L))**2+(ZAC-
0830 ZAI(ISURF,IPAIR,L))**2)
0840 AR=(ZAI(ISURF,IPAIR,L)-ZAC)/(XAI(ISURF,IPAIR,L)-XAC)
0850 BR=ZAI(ISURF,IPAIR,L)-AR*XAI(ISURF,IPAIR,L)
0860 XS=(SURFI(ISURF)-BR)/(AR-SURFS(ISURF))
0870 AD=(ZAC-ZA(IPAIR,L))/XAC
0880 XC=(SURFI(ISURF)-ZA(IPAIR,L))/(AD-SURFS(ISURF))
0881 IF(SURFS(ISURF).LT.1.E37)GO TO 920
0883 XC=X1(ISURF)
0885 XS=X1(ISURF)
0890C
0900C *****DETERMINE IF REFLECTION OCCURS
0910C
0911 CONTINUE
0920 920 LOG1=X1(ISURF).GT.X2(ISURF)
0930 LOG2=XS.GT.X2(ISURF)
0940 LOG3=XS.GT.X1(ISURF)
0950 IF((LOG1.AND.LOG2.AND..NOT.LOG3.OR..NOT.LOG1.AND..NOT.LOG2
0960 .AND.LOG3).AND.((XC.GT.0..OR.XC.LT.XAC).AND.XAC.LT.0..OR.
0970 (XC.LE.0..OR.XC.GT.XAC).AND.XAC.GE.0.)) GO TO 1000
0972 IREFL(IPAIR)=OR(IREFL(IPAIR),2**(9-ISURF))
0980 GO TO 1120
0992C
0994C *****FIND REFLECTION COEFFICIENTS
0996C
1000 1000 THETI=ATAN((1.+AR*SURFS(ISURF))/(AR-SURFS(ISURF)))
1010 THETI=APS(THETI)
1020 CALL CFRSNL (PRMTIV(ISURF),RGH(ISURF),THETI,R(1),R(2))
1030 RHO=CABS(R(IPOL))
1031 IREFL(IPAIR)=OR(IREFL(IPAIR),2**(ISURF-1))
1040 PHI=ATAN2(AIMAG(R(IPOL)),REAL(R(IPOL)))
1050 PHAS=PHI+(RR-RD(IPAIR,L))*TWOPI/WAVLTH
1052 PATP=PAT(SURFS(ISURF),THETI,IPOL)
1060 RHOR=RHO*RD(IPAIR,L)*PATR/(PATD*RR)
1070C
1080C *****ACCUMULATE MULTIPATH ERRORS
1090C
1100 MQUAD=MQUAD+RHOR*SIN(PHAS)
1110 MINPH=MINPH+RHOR*COS(PHAS)
1120 1120 CONTINUE
1130 DELPHI(L)=ATAN(MQUAD/1.+MINPH)
1140 1140 CONTINUE
1150C
1160C *****AVERAGE PHASE ERRORS
1170C

```

```

1180      PHIHAT(IPAIR)=(RD3(IPAIR,1)-RD3(IPAIR,2)-WAVLTH/TWOPT*
11826      (DELPHI(1)-DELPHI(2)))/(ZA(IPAIR,2)-ZA(IPAIR,1))
1184      IF (FFOCUS.EQ.1.) PHIHAT(IPAIR)=PHIHAT(IPAIR)*(1.-.5*PHIHAT(IPAIR)
11856      *(ZA(IPAIR,2)-ZA(IPAIR,1))/RD(IPAIR,1))+.5*(ZA(IPAIR,1)+
11886      ZA(IPAIR,2))/RD(IPAIR,1)
1190      PHIBAR=PHIBAR+PHIHAT(IPAIR)/NPAIR
1200 1200 CONTINUE
1220C
1230C      *****PHIBAR IS THE REDUCED PHASE MEASUREMENT SUCH THAT THE
1240C      ESTIMATE OF POSITION IS ARCSIN(PHIBAR)
1250C
1260C      *****COMPUTE ANGULAR ERROR
1280      SNTH=ZAC/RREF
1320 1320 THTILD=(SNTH-PHIBAR)*SORT(1.0-PHIBAR**2)
1330C
1340C      *****STORE DATA FOR FUTURE OUTPUT
1350C
1360      DO 1380 J=5,NPAIR+4
1370      OUT(INC,J)=PHIHAT(J-4)
1380 1380 CONTINUE
1390      OUT(INC,1)=RREF
1400      OUT(INC,2)=THTILD
1410      OUT(INC,3)=SNTH
1420      OUT(INC,4)=PHIBAR
1430      OUTMIN(1)=-1.E-37
1440      OUTMIN(2)=-1.E-37
1450      OUTMAX(1)=-1.E-37
1460      OUTMAX(2)=-1.E-37
1462      SMEAN= SMEAN+THTILD/NINC(ISEG)
1464      SMSQ=SMSQ+THTILD**2/NINC(ISEG)
1470 1470 CONTINUE
1480C
1490C      *****OUTPUT RESULTS THIS SEGMENT
1500C
1505      SVAR=SMSQ-SMEAN**2
1510      WRITE(10,1520) ISEG, ((OUT(I,J), J=1,15), I=1, NINC(ISEG))
1512      WRITE(10,1514) SMEAN, SVAR, IREFL
1514 1514 FORMAT(' MEAN EPROP='E11.4,4X, 'VARIANCE='E11.4//
15166      ' MULTIPATH INDICATORS'//2X,10(17.4X))
1520 1520 FORMAT(1H1// ' RESULTS FOR FLIGHT PATH SEGMENT ',12//3X,
15226      ' RANGE SPACE ERROR SIN TP SIN EST',20X,
15246      ' UNAVERAGED ESTIMATES'/50(1X,F9.3,2X,E11.4,13(1X,F7.4))//1H1//
1530      WRITE(10,1532)
1532 1532 FORMAT(1H1// ' PLOT OF ANGULAR ERROR VERSUS RANGE'/3X, 'ERROR(RADIANS)')
1534      NOUT=10
1536      ITTY=0
1538      CALL STUF(OUT(1,2),OUT(1,1),NINC(ISEG))
1540      CALL PRNPLT(OUT(1,2),OUT(1,1),OUTMIN(2),OUTMIN(1),OUTMAX(2),
15426      OUTMAX(1),NINC(ISEG),1,1,50,2)
1544      WRITE(10,1546)
1546 1546 FORMAT(50X, 'RANGE')
1548 1530CONTINUE
1550      STOP
1552      END
1560C
1570C      *****SUBROUTINE TO COMPUTE FRESNEL COEFFICIENT
1580C
1590      SUBROUTINE CFPSNL(PRM,RGH,TH,RV,RH)
1600      COMPLEX RV,RH,PRM,A1
1610      A1=CSORT(PRM-SIN(TH)**2)
1620      RV=(PRM*COS(TH)-A1)/(PRM*COS(TH)+A1)
1630      RH=(COS(TH)-A1)/(COS(TH)+A1)
1640      RED=EXP(-157.9137*(RGH*COS(TH))**2)
1650      RV=RV*RED
1660      RH=RH*RED
1670      RETURN

```

```

1680      END
1690C
1700C      *****FUNCTION TO COMPUTE ANTENNA PATTERNS
1710C
1720      FUNCTION PAT(SL,TH,I)
1722      DIMENSION BW(2)/.3,1.2/,TILT(2)/.18,0.0/
1730C      *****.18 IS UPTILT OF ANTENNA
1740      ALPH=1.570796-TH-ATAN(SL)+TILT(I)
1750C      *****PATTEPN FOR OPTIMUM HORN
1760      T=1.9*SIN(ALPH)/SIN(BW(I))
0001770      PAT=SIN(T)/T
0001780      IF(PAT.LT.0.)PAT=-PAT
0001790      RETURN
0001800      END
1850C
1860C      *****MAKE MORE POINTS TO PLOT
1870C
1880      SUBROUTINE STUF(Y,X,N)
1890      DIMENSION X(1),Y(1)
1900      ISTUF=100/N
1910      IF(ISTUF.LE.1)GO TO 1980
1920      DO 1970 I=1,ISTUF-1
1930      DO 1960 J=1,N-1
1940      Y(N+J+(N-1)*(I-1))=(Y(J+1)-Y(J))/ISTUF*I+Y(J)
1950      X(N+J+(N-1)*(I-1))=(X(J+1)-X(J))/ISTUF*I+X(J)
1960 1960 CONTINUE
1970 1970CONTINUE
1975      N=(N-1)*ISTUF+1
1976      WRITE(11,1978)N,ISTUF
1978 1978FORMAT(' POINTS=',I4,2X,'ISTUF=',I4)
1980 1980 RETURN
1990      END

```

Page Intentionally Left Blank

APPENDIX C

(English Translation of Reference 6)

1.0 INTRODUCTION

Two transmitting antennas are symmetrically oriented on a platform which revolves about a fixed point, O, as shown in Figure C-1. A receiver located at a point in space, S, (at a range much larger than the transmitting antennas separation) receives the superimposed signals from the two antennas. The superimposed signals contain information (which when compared with a separate coherent reference signal) provide information on the azimuth and elevation angle of the point S relative to the transmitting antennas. By an optical processing scheme, a cross-correlation is performed between a transparent film with a transmittance function imposed on it and an illumination function amplitude modulated by the product of the two signals received at S. The optical cross-correlation produces luminous spots on a viewing screen such that the position of the spot in a two-dimensional vector polar coordinate system of angle and magnitude of the vector corresponds to azimuth and elevation angle respectively.

2.0 CALCULATIONS

2.1 Receiver Signals

The antennas are located at points M₁ and M₂ and the receiver at point S (See Figure C-1) such that separations d are:

$$d_1 = SM_1 \quad (C-1)$$

$$d_2 = SM_2 \quad (C-2)$$

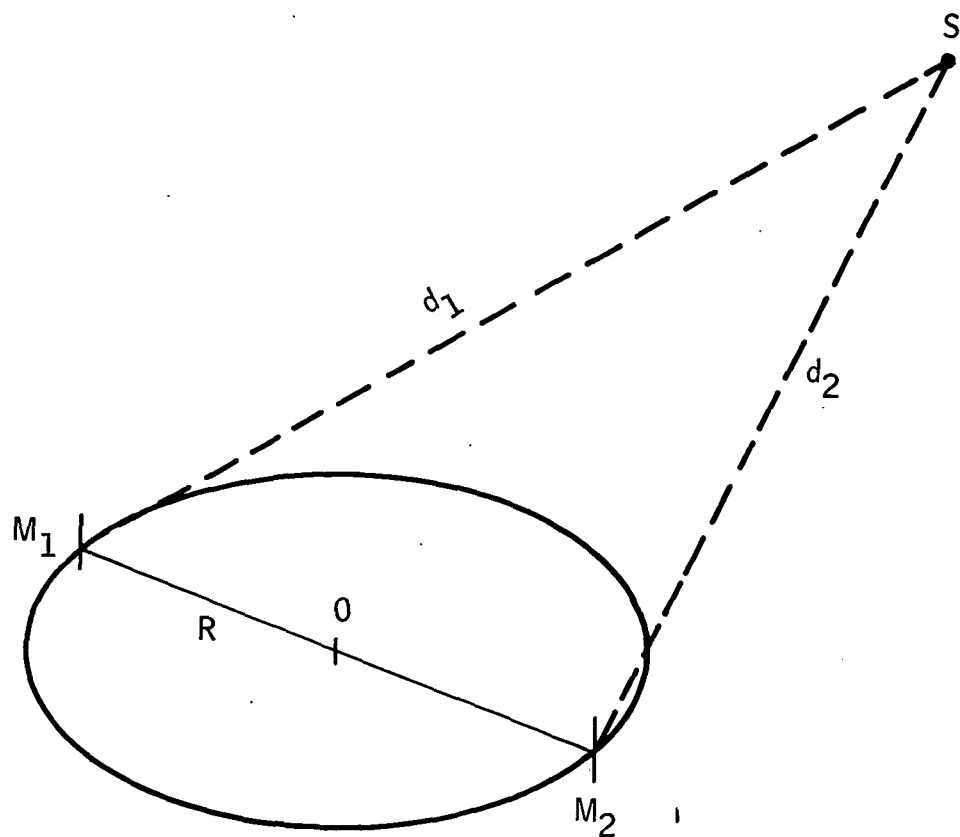


Figure C-1. Rotating Antenna Geometry

2.1 Receiver Signals (Cont'd)

The signals transmitted at the antennas have radian frequency
($\Omega = 2\pi F$, F the frequency in Hertz) and phase difference, β .

At S the two signals received are:

$$A_1 \exp\{j(\Omega t - \Omega \frac{d_1}{c})\}$$

$$A_2 \exp\{j(\Omega t - \Omega \frac{d_2}{c} + \beta)\}$$

The product of these signals is:

$$\frac{A_1 A_2}{2} \cos\{2\Omega t - \frac{\Omega}{c} (d_1 + d_2) + \beta\} + \cos\{\frac{\Omega}{c} (d_1 - d_2) + \beta\}$$

The low-pass filtered part of this product is:

$$P(t) = A_0 \cos\{\frac{\Omega}{c} (d_1 - d_2) + \beta\} = A_0 \cos\{\frac{2\pi}{\lambda} (d_1 - d_2) + \beta\} \quad (C-3)$$

where: λ = transmitter wavelength

c = propagation velocity (speed of light)

Calculating $d_1 - d_2$

In the three-dimension reference frame located at the transmitting antenna, the point S is described by the angles θ and ψ_S and the distance $d = OS$ (Figure C-2). Then:

$$d_1^2 - d_2^2 = \vec{SM}_1^2 - \vec{SM}_2^2 = 4Rd \cos\psi_S \cos\theta \quad (C-4)$$

When the point S is far from the transmitting antennas ($d \gg R$)

$$2d \approx d_1 + d_2 \quad (C-5)$$

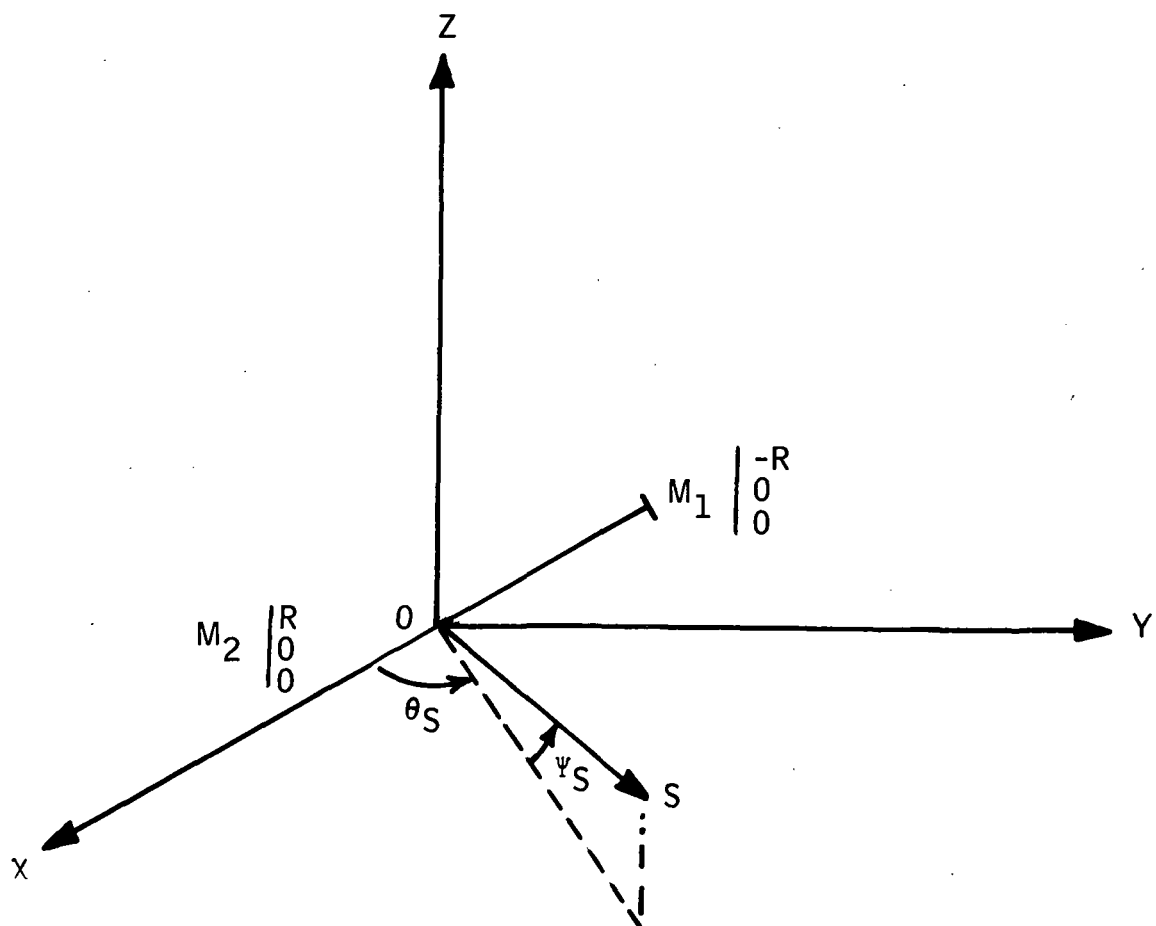


Figure C-2. Transmitting Antenna Reference Frame

2.1 Receiver Signals (Cont'd)

Thus:

$$d_1^2 - d_2^2 = (d_1 - d_2) (d_1 + d_2) \approx 2d (d_1 - d_2) \quad (C-6)$$

And from equation C-4 we get:

$$d_1^2 - d_2^2 = 2R \cos\psi \cos\theta \quad (C-7)$$

When the two antennas are turning around the point O with radian frequency ω , the time dependent angle θ can be reference such that:

$$\theta = \omega t + \theta_s \quad (C-8)$$

Equation C-3 then becomes

$$P(t) = A_0 \cos\left\{\frac{4\pi R}{\lambda} \cos\psi \cos(\omega t + \theta_s) + \beta\right\} \quad (C-9)$$

2.2 Transparency Function

Consider a disk with equally spaced, alternating bands of opaque and transparent material. (Figure C-3). Also, consider the disk turning around the center O with the same angular frequency ω as the two antennas.

To simplify the equations, assume that the transmissivity of the disk is sinusoidal (instead of square) such that along the x-axis the transmissivity function may be described as:

$$O(x) = B_0 \left\{ 1 + \cos \left(\frac{\pi x}{\delta} + \alpha \right) \right\} \quad (C-10)$$

where:

α is the angular position corresponding to the transparency band maximum opaquesness relative to the center of the disk.

$O(X)$ is always positive

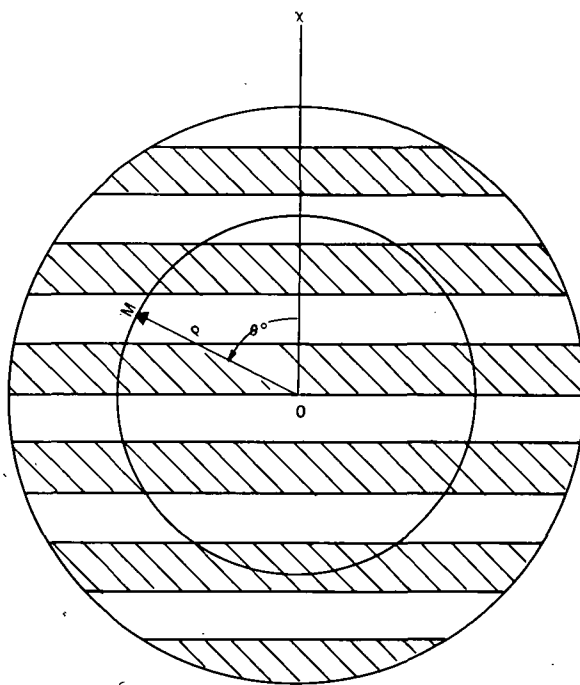


Figure C-3. Transparency Function

2.2 Transparency Function (Cont'd)

This disk turns with the same angular frequency w as the antennas and, therefore, does not introduce an erroneous phase difference which would result in erroneous θ_s and ρ_s spot references. The orientation of the disk will be chosen with the bands perpendicular to the x-axis at $t = 0$.

Consider the point, $M(\rho, \theta)$, when the disk turns past this point the transmittance function is: (for $x = \rho \cos \theta (wt + \theta_0)$)

$$L(t) = B_0 \{ 1 + \cos \left(\frac{\pi \rho}{\delta} \cos(wt + \theta_0) \right) + \alpha \} \quad (C-11)$$

3.0 STUDY OF THE CORRELATION (SIGNAL PRODUCT AND TRANSMITTANCE)

Preliminary:

$J_0(Z)$ is the Bessel function of the zeroth order with the following relationships:

$$\frac{1}{\pi} \int_0^\pi \cos(z \sin \theta) d\theta = \frac{1}{\pi} \int_{-\pi}^{\pi} \cos(z \sin \theta) d\theta = \frac{1}{2\pi} \int_0^{2\pi} \cos(z \sin \theta) d\theta = J_0(z) \quad (C-12)$$

$$\frac{1}{\pi} \int_0^\pi \sin(z \sin \theta) d\theta = \frac{1}{\pi} \int_{-\pi}^{\pi} \sin(z \sin \theta) d\theta = \frac{1}{2\pi} \int_0^{2\pi} \sin(z \sin \theta) d\theta = 0 \quad (C-13)$$

The disk is illuminated with a single source of light with amplitude, or intensity, $P(t)$ proportional to the product of the two antenna signals. Biasing the original signal $P(t)$ so that the illumination function is never negative, we obtain for $A_0 > 0$:

$$A_0 \{ 1 + \cos \left[\frac{4\pi R}{\lambda} \cos \psi_s \cdot \cos(wt + \theta_s) + \beta \right] \}$$

3.0 STUDY OF THE CORRELATION (Signal Product and Transmittance) (Cont'd)

On the other side of the disk, at point M(P, θ_0), we can observe the product of that function with the disk's transmissivity function. Integrating the two functions as the disk revolves (which is what the eye sees) generates the two dimensional cross-correlation function

$$G(\rho, \theta_0) = \frac{A_0 B_0}{T} \int_0^T \{ 1 + \cos[\frac{4\pi R}{\lambda} \cos \psi_s \cdot \cos(\omega t + \theta_s) + \beta] \} \cdot \{ 1 + \cos[\frac{\pi \rho}{\delta} \cos(\omega t + \theta_0) + \alpha] \} dt \quad (C-14)$$

On setting $\omega t = \theta$, and $T = \frac{2\pi}{\omega}$, we get:

$$G(\rho, \theta_0) = A_0 B_0 [1 + I_1 + I_2 + I_3] \quad (C-15)$$

a) Calculating I_1 :

$$I_1 = \frac{1}{2\pi} \int_0^{2\pi} \cos \alpha \cos [\frac{\pi \rho}{\delta} \cos(\theta + \theta_0)] d\theta - \frac{1}{2\pi} \int_0^{2\pi} \sin \alpha \cdot \sin [\frac{\pi \rho}{\delta} \cos(\theta + \theta_0)] d\theta \quad (C-16)$$

we get:

$$I_1 = \cos \alpha \cdot J_0 \left(\frac{\pi \rho}{\delta} \right) \quad (C-17)$$

b) Calculating I_2 :

$$I_2 = \frac{1}{2\pi} \int_0^{2\pi} \cos \beta \cdot \cos [\frac{4\pi R}{\lambda} \cos \psi_s \cdot \cos(\theta + \theta_s)] d\theta - \frac{1}{2\pi} \int_0^{2\pi} \sin \beta \cdot \sin [\frac{4\pi R}{\lambda} \cos \psi_s \cdot \cos(\theta + \theta_s)] d\theta \quad (C-18)$$

we get:

$$I_2 = \cos \beta \cdot J_0 \left(\frac{4\pi R}{\lambda} \cos \psi_s \right) \quad (C-19)$$

c) Calculating I_3 :

$$I_3 = \frac{1}{2\pi} \int_0^{2\pi} \cos [\frac{4\pi R}{\lambda} \cos \psi_s \cdot \cos(\theta + \theta_s) + \beta] \cdot \cos [\frac{\pi \rho}{\delta} \cos(\theta + \theta_0) + \alpha] d\theta \quad (C-20)$$

I_3 is made up of four integrals:

$$I_3 = \cos \alpha \cdot \cos \beta \cdot I'_1 - \cos \alpha \cdot \sin \beta \cdot I_2 - \cos \beta \cdot \sin \alpha \cdot I'_3 + \sin \alpha \cdot \sin \beta \cdot I'_4 \quad (C-21)$$

3.0 STUDY OF THE CORRELATION (Signal Product and Transmittance) (Cont'd)

which are:

$$I_1' = \frac{1}{2\pi} \int_0^{2\pi} \cos \left[\frac{\pi \rho}{\delta} \cos (\theta + \theta_0) \right] \cdot \cos \left[\frac{4\pi R}{\lambda} \cos \psi_s \cdot \cos (\theta + \theta_s) \right] d\theta \quad (C-22)$$

$$I_2' = \frac{1}{2\pi} \int_0^{2\pi} \cos \left[\frac{\pi \rho}{\delta} \cos (\theta + \theta_0) \right] \cdot \sin \left[\frac{4\pi R}{\lambda} \cos \psi_s \cdot \cos (\theta + \theta_s) \right] d\theta \quad (C-23)$$

$$I_3' = \frac{1}{2\pi} \int_0^{2\pi} \sin \left[\frac{\pi \rho}{\delta} \cos (\theta + \theta_0) \right] \cdot \cos \left[\frac{4\pi R}{\lambda} \cos \psi_s \cdot \cos (\theta + \theta_s) \right] d\theta \quad (C-24)$$

$$I_4' = \frac{1}{2\pi} \int_0^{2\pi} \sin \left[\frac{\pi \rho}{\delta} \cos (\theta + \theta_0) \right] \cdot \sin \left[\frac{4\pi R}{\lambda} \cos \psi_s \cdot \cos (\theta + \theta_s) \right] d\theta \quad (C-25)$$

For all the integrals we make a change of variables, $\theta - \theta_0$ for θ and:

$$A = \frac{\pi \rho}{\delta} + \frac{4\pi R}{\lambda} \cos \psi_s \cdot \cos (\theta_s - \theta_0) \quad A' = \frac{\pi \rho}{\delta} - \frac{4\pi R}{\lambda} \cos \psi_s \cdot \cos (\theta_s - \theta_0) \quad (C-26)$$

$$B = \frac{4\pi R}{\lambda} \cos \psi_s \cdot \sin (\theta_s - \theta_0) \quad B' = - \frac{4\pi R}{\lambda} \cos \psi_s \cdot \sin (\theta_s - \theta_0)$$

$$\operatorname{tg} \psi = \frac{B}{A} \quad \operatorname{tg} \psi' = \frac{B'}{A'}$$

Calculating I_1' :

$$I_1' = \frac{1}{4\pi} \int_{-\theta_0}^{2\pi-\theta_0} \cos [\sqrt{A^2+B^2} \cdot \cos (\theta-\psi)] d\theta + \frac{1}{4\pi} \int_{-\theta_0}^{2\pi-\theta_0} \cos [\sqrt{A'^2+B'^2} \cdot \cos (\theta-\psi')] d\theta \quad (C-27)$$

we get:

$$I_1' = \frac{1}{2} [J_0(\sqrt{A^2+B^2}) + J_0(\sqrt{A'^2+B'^2})] \quad (C-28)$$

Calculating I_3'

$$I_3' = \frac{1}{4\pi} \int_{-\theta_0}^{2\pi-\theta_0} \sin [\sqrt{A^2+B^2} \cdot \cos (\theta-\psi)] d\theta - \frac{1}{4\pi} \int_{-\theta_0}^{2\pi-\theta_0} \sin [\sqrt{A'^2+B'^2} \cdot \cos (\theta-\psi')] d\theta \quad (C-29)$$

we get:

$$I_3' = 0 \quad (C-30)$$

Calculating I_3 :

$$I_3' = \frac{1}{4\pi} \int_{-\theta_0}^{2\pi-\theta_0} \sin [\sqrt{A'^2+B'^2} \cdot \cos (\theta-\psi)] d\theta + \frac{1}{4\pi} \int_{-\theta_0}^{2\pi-\theta_0} \sin [\sqrt{A'^2+B'^2} \cdot \cos (\theta-\psi')] d\theta \quad (C-31)$$

we get:

$$I_3' = 0 \quad (C-32)$$

Calculating I_4

$$I_4' = \frac{1}{4\pi} \int_{-\theta_0}^{2\pi-\theta_0} \cos [\sqrt{A'^2+B'^2} \cdot \cos (\theta-\psi')] d\theta - \frac{1}{4\pi} \int_{-\theta_0}^{2\pi-\theta_0} \cos [\sqrt{A'^2+B'^2} \cdot \cos (\theta-\psi)] d\theta \quad (C-33)$$

we get:

$$I_4' = \frac{1}{2} [J_0(\sqrt{A'^2+B'^2}) - J_0(\sqrt{A^2+B^2})] \quad (C-34)$$

Substituting these back into equation (C-21) we obtain:

$$I_3 = \frac{1}{2} \cos (\alpha-\beta) \cdot J_0(\sqrt{A'^2+B'^2}) + \frac{1}{2} \cos (\alpha+\beta) \cdot J_0(\sqrt{A^2+B^2}) \quad (C-35)$$

and finally, from equation C-15:

$$G(\rho, \theta_0) = A_0 B_0 [1 + \cos \alpha \cdot J_0(\frac{\pi \rho}{\delta}) + \cos \beta \cdot J_0(\frac{4\pi R}{\lambda} \cos \psi_s) + \cos(\alpha-\beta) J_0(\sqrt{A'^2+B'^2}) + \cos(\alpha+\beta) \cdot J_0(\sqrt{A^2+B^2})] \quad (C-36)$$

4.0 INTERPRETATION OF RESULTS

Equation C-36 shows that the cross-correlation function is composed of five parts:

a. Interpretation of the first term

The term, $A_0 B_0$, is a constant (independent of all parameters) and indicates uniform disk illumination of the observer.

b. Interpretation of the second term

$\left[J_0 \frac{\pi \rho}{\delta} \right]$ shows that the disk has a maximum illumination at 0.

According to the values of ρ , there are other maximums

and, since this term is independent of the angle θ_0 , we obtain concentric circles around the center of the disk at 0.

However, this term vanishes for $\alpha = \pi/2$.

c. Interpretation of the third term

$\left[J_0 \frac{4 \pi R}{\lambda} \cos \phi_s \right]$ does not depend on ρ or θ , so it also shows a uniform illumination of the disk with the intensity depending on ϕ_s . If we set β equal to $\pi/2$, this term goes to zero.

d. Interpretation of the fourth and fifth terms.

They are:

$$\frac{A_0 B_0}{2} \cos(\alpha + \beta) J_0(\sqrt{A^2 + B^2}) \quad (C-37)$$

We set the vectors u and v (Figure C-4) with the values

$$A, A', B, \text{ and } B' \text{ to get } \sqrt{A^2 + B^2} = |\vec{u} + \vec{v}| \quad (C-38)$$

$$\sqrt{A'^2 + B'^2} = |\vec{u} - \vec{v}|$$

The vector v , which is fixed, describes the point corresponding to the receiver at S. \vec{u} defines the observed point on the disk.

The illumination resulting from the cross-correlation, $G(\rho, \theta_0)$, then is a function of only u . This function is maximum for some values, such as $\sqrt{A^2 + B^2} = 0$ and $\sqrt{A'^2 + B'^2} = 0$, which corresponds to $J_0(0)$.

Consequently, when $\vec{u} = \vec{V}$, or $\vec{u} = -\vec{V}$ we observe spots at these points. Around these points we obtain concentric circles and an ambiguous spot with rings is symmetrically placed across the center of the disk. Only the spot corresponding to $\vec{u} = \vec{v}$ characterizes S as its position corresponds to θ_s and ϕ_s . The other point defines a false target at $-\theta_s$ and ϕ_s . In order to suppress this second spot we zero the coefficient of $J_0 \left[\sqrt{A^2 + B^2} \right]$ to get:

$$\cos \alpha + \beta = 0$$

$$\text{which means } \alpha + \beta = \pi/2$$

However, we cannot dispose of both parameters α and β , so it is impossible to suppress all of the following:

The concentric circles around 0

The uniform illumination with intensity dependent on ϕ_s .

The false spot

We therefore have to make a choice of which to remove.

CONCLUSIONS

Retaining the false targets (since we cannot remove or suppress all three of the above factors) we will obtain an illuminated spot on the disk whose angular position is representative of the azimuth and whose position relative to the center of the circle (distance = $\frac{4}{3} R \cos \phi$) allows us to calculate ϕ_s , the elevation angle.

5.0 APODIZATION BY AMPLITUDE MODULATION

We now study the case where the signals received at the point S are amplitude modulated by the rotation of the antennas located at M_1 and M_2 when we use horizontal dipoles (Figure C-5).

The received signal modulation is of the form $A_1 \cos (wt + \psi)$ and

equation C-3 becomes : $P(t) = A_0 [1 + \cos 2 (wt + \psi)] \cos \left[\frac{4\pi R}{\lambda} \cos \psi_S \cdot \cos (wt + \theta_S) + \beta \right]$

The product of the transmittance function $B(t)$ will have the same (C-39) terms as derived above in one part and the other part will have new terms originating from the development of:

$$I = \int_0^T \cos(2wt + 2\psi) \{1 - \cos \left[\frac{4\pi R}{\lambda} \cos \psi_S \cdot \cos (wt + \theta_S) + \beta \right]\} \cdot \{1 + \cos \left[\frac{\pi \rho}{\delta} \cos (wt + \theta_0) + \alpha \right]\} dt$$

We again find the same integrals as calculated above with the (C-40)

exception of the factor $\cos 2 (wt + \psi + \theta_S - \theta_0)$ under the integral sign. All of these integrations which yielded the Bessel function $J_0 [Z]$ now yield a term $\cos 2 (\psi + \theta_S - \theta_0) \cdot J_2 [Z]$. The result has the form:

$$\sum_i a_i [J_0(z_i) + \cos 2(\psi + \theta_S - \theta_0) J_2(z_i)]$$

We can now play with the coefficient $\cos 2 (\psi + \theta_S - \theta_0)$ to vary the form of the spots on the disk; in particular, the first sidelobe which is the most damped for the value:

$$\cos 2 [\psi + \theta_S - \theta_0] = 1$$

Apodization Effects

The width of the $J_0 [Z]$ curve at the 3 dB point is 1.55 and the first sidelobe is 50% and the width of the $J_0 [Z] + J_2 [Z]$ curve is 2.0 at the 3 dB point with a first sidelobe of 17%. Figure C-6 shows the

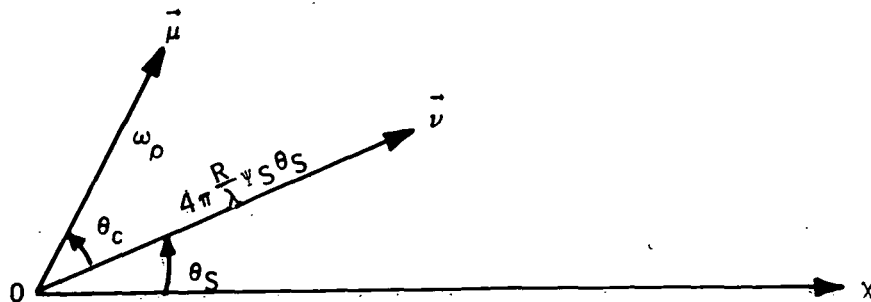


Figure C-4. Vector Relationship

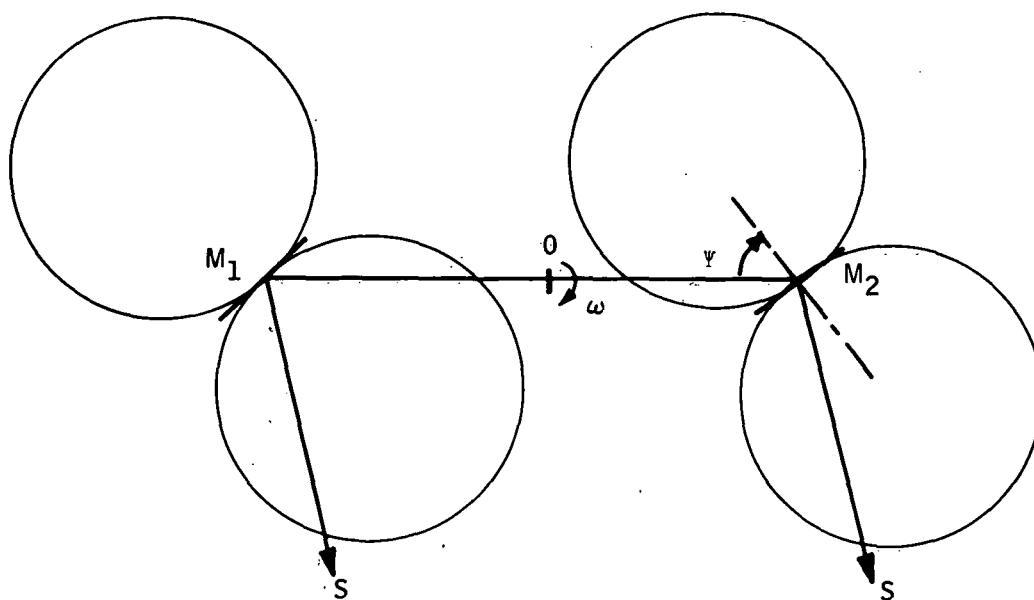


Figure C-5. Amplitude Modulation Through Antenna Rotation

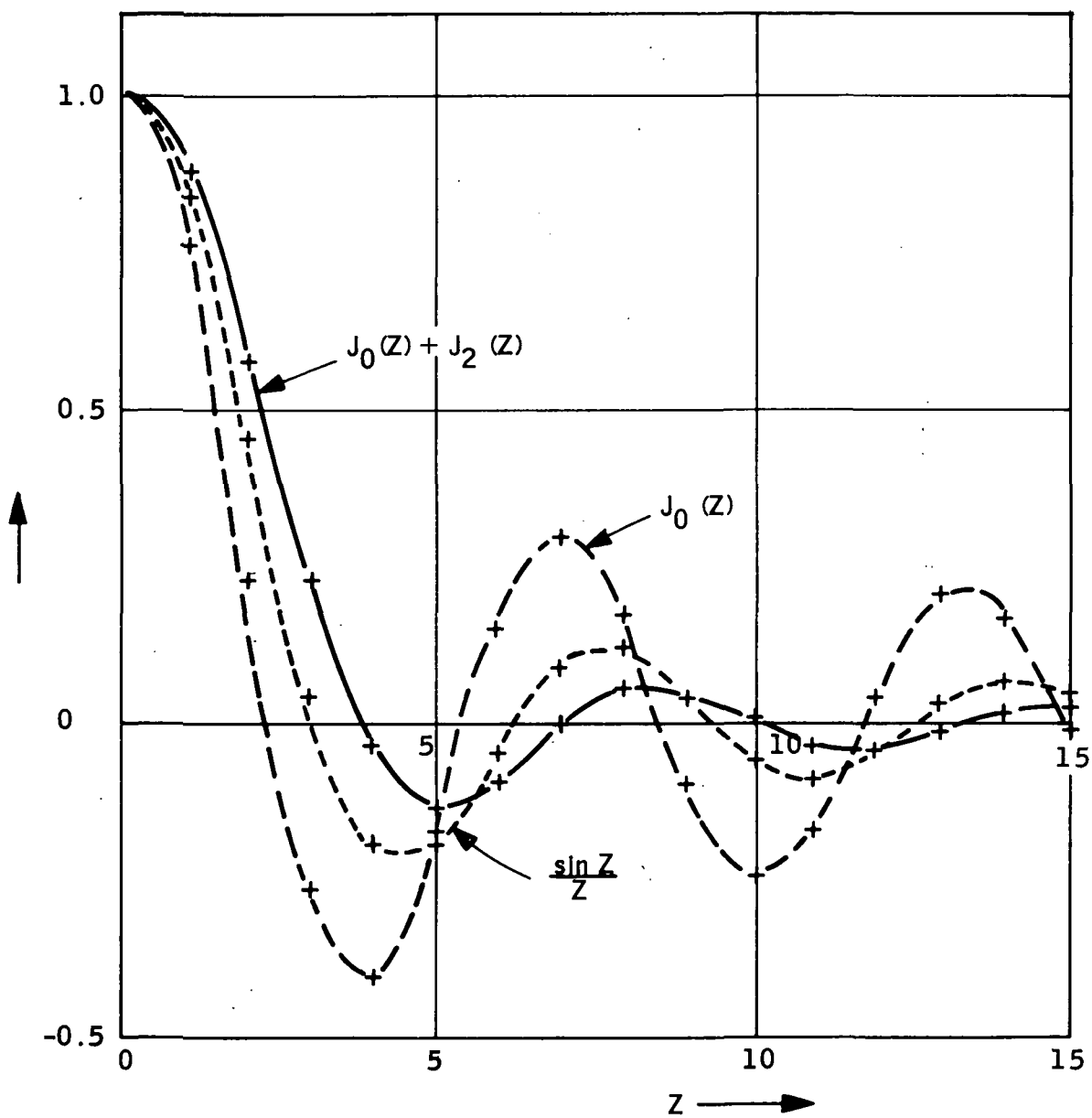


Figure C-6. Apodization Effects

behavior of the curves along with the classical $\frac{\sin Z}{Z}$ ambiguity

function. The ambiguity function obtained is not cyclic in the

optical plane; it is apodized in the direction $\psi + \theta_s - \theta_o = 0$.

When it is transformed to the direction $\psi + \theta_s - \theta_o = \pi/2$ it will equal

$J_0 [Z] - J_2 [Z]$ which has increased secondary sidelobes. The phase of the amplitude modulation (which can be electronically generated, such as, at the receiver) with respect to the antenna rotation defines the direction of apodization in the optical plane.